**The Synthesis and Surface Chemistry of Colloidal Quantum Dots**

*Fundamental and Applied Studies Enabled by Precursor Chemistry*

Michael Paul Campos

Submitted in partial fulfillment of the requirements for the degree of Doctor of Philosophy in the Graduate School of Arts and Sciences

Columbia University

2017

## ABSTRACT

**The Synthesis and Surface Chemistry of Colloidal Quantum Dots**

Michael Paul Campos

Colloidal semiconductor nanocrystals, also known as quantum dots, are an extraordinary class of material, combining many of the most attractive properties of semiconductors with the practicality of solution chemistry. As such, they lie at a unique interface between inorganic chemistry, organic chemistry, solid-state physics, and colloidal chemistry. The rapid advance in knowledge of quantum dots over the past 30 years has largely been driven by interest in their fundamental physical properties and their broad applicability to challenges in nanoscience. However, much less attention has been paid to the chemistry underlying these features. In this dissertation, we discuss the state of nanocrystal chemistry and new insights we have unlocked by taking a bottom-up, chemistry-based approach to nanocrystal synthesis. We will cover these in a case-by-case fashion in the context of four chapters.

Chapter 1 covers our CdTe nanocrystal synthesis surface chemistry studies with an eye toward CdTe photovoltaic technology, in which the role of CdTe surfaces is poorly understood. CdTe nanocrystals are traditionally a difficult material to synthesize, particularly with well-defined surface chemistry.

In order to enable quantitative surface studies, we looked upstream and re-evaluated CdTe synthesis from the ground up. We identified a CdTe precursor largely overlooked since 1990, cadmium *bis*(phenyltellurolate) ($Cd(TePh)_2$), and harnessed its excellent reactivity toward a synthesis of CdTe nanocrystals solely bound by cadmium carboxylate ($Cd(O_2CR)_2$) ligands. We then use this well-defined material to show that $Cd(O_2CR)_2$ ligands bind less tightly to CdTe nanocrystals than CdSe nanocrystals. This finding holds promise for the development of photovoltaics from colloidal CdTe feedstocks.

Chapter 2 covers a tunable library of substituted thiourea precursors to metal sulfide nanocrystals. Controlling the size of nanocrystals produced in a given reaction is paramount to their use in opto-electronic devices, but the most widely used technique to control size is prematurely arresting crystal growth. We introduce a library of thiourea precursors whose organic substituents tune the rate of precursor conversion, which dictates the number of nanocrystals formed and the final nanocrystal size following complete precursor conversion. We use PbS as a model system to 1) demonstrate the concept of kinetically controlled nanocrystal size, 2) quantify substituent trends, and 3) optimize multigram scale syntheses. We then expand the thiourea methodology to a broad range of materials and nanocrystal morphologies. This work represents a

paradigm shift that will greatly accelerate the pace of progress in nanocrystal science as it transitions from academia to a multibillion-dollar industry.

Chapter 3 covers an analogously tunable library of substituted selenourea precursors, but focuses on the synthesis of PbSe nanocrystals. PbSe nanocrystal synthesis is notoriously low-yielding and poorly tunable, but the remarkable properties of PbSe nanocrystals in photovoltaics and electrical transport have driven interest in the material for decades. We develop a library of *N*,*N*,*N*′-trisubstituted selenourea precursors and leverage their fine conversion rate tunability to synthesize PbSe nanocrystals of many sizes in quantitative yields. Interestingly, the nanocrystals produced in this reaction are demonstrably less polydisperse than literature samples, exhibiting absorption linewidths approaching the single-particle limit. We quantify this narrowness using a transient absorption spectroscopy technique called spectral hole burning.

Chapter 4 covers our efforts to dig deeper into nanocrystal nucleation and growth and use that new knowledge to develop luminescent downconverters ready for on-chip integration into LED lighting. By studying early time points in PbS and PbSe nanocrystal synthesis, we estimate solute concentrations, nucleation thresholds, and nanocrystal growth rates. In particular, we find that metal selenides and sulfides have very different nucleation and growth behavior, as well as that PbS nucleation is a surprisingly slow process. The lessons learned

from these fundamental experiments have enabled us to rapidly develop red-emitting CdS/CdSe/CdS "spherical quantum well" emitters whose photoluminescence quantum yields are 90 – 95%.

## TABLE OF CONTENTS

## Acknowledgments

One of the best things about doing a chemistry Ph.D. in nanoscience is the chance to build relationships. If you're going to get anywhere in such a field full of siloed sub-fields that can barely understand each other speak, and in which lab personnel completely turns over every five years, you have to talk to people. So bear with me – I have a lot of people to thank.

First, I'd like to thank my thesis committee members for agreeing to accompany me on this journey. Dr. Mike Steigerwald, thanks for laying the groundwork for my first project back in 1990 and still being willing to talk it through with a naïve first-year graduate student in 2012. Every time I left your office the world felt a little fuller of possibility. Prof. Colin Nuckolls, thank you for your enduring creativity. You and your group have an uncanny ability to discover completely unknown systems using the tools of classic organic chemistry. Prof. Jack Norton, thank you for inspiring me to be rigorous in my kinetic studies, and for always showing up to Friday Synthesis Symposium and happy hour. Prof. Tianning Diao, thanks for agreeing to make the trip uptown from NYU to see me defend. I remember being impressed with your papers out of Shannon Stahl's group long before I knew who you were or that you had become a professor. I wish you all the best as you build up your lab.

Two collaborators stand for going above and beyond and welcoming me into their labs for weeks at a time. Emory Chan, thanks for going along with Mark, Iva and I as we tried our best to use WANDA without breaking things. Benjamin Abécassis, I can't thank you enough for inviting me to Lyon and the ESRF, finding me a place to stay in Lyon, and translating a lot of French for me.

This next batch of thank-yous covers the many lab mates I've had over five years in the Owen Lab, roughly chronologically. Peter and I joined the lab as its first generation of students was coming into its own, and we now leave the lab squarely in its second generation. There's been a ton of growth, change, and people who have made their mark on the lab in one way or another.

Nick Anderson was the heart of the lab, the one that took the first gamble on what Peter and I called the "Jon Owen rookie card." As a scientist, the two things I admire most about him are 1) his uncanny ability to get the most data from the fewest number of experiments possible, and 2) his willingness to go down the rabbit hole – in group meeting, chatting in the office about a strange NMR spectrum, or provoking Mark over sandwich definitions. The culture he instilled in lab is what I look for in a work environment. I would trust him with just about anything, and I hope we get the chance to work together again.

Mark Hendricks was my closest mentor in the Owen Lab and remains a great friend a few years later. I modeled most of my Ph.D. after his, and can't tell

you how many times I referred to his first paper in writing my own. I also can't tell you how many hours we spent troubleshooting and cursing a robotic arm late into the night.

Zak Norman was a clear leader of the lab and attacked what he saw as important with a single-minded focus. Since getting to know him, I've envied his clarity of thought and a willingness to learn new skills.

Alex Beecher recruited me to Columbia and the Owen Lab. Over the years he was always at the heart of our lab, friendly and flexible enough to share a hood with me before I knew what I was doing and still invite Peter and me out to a concert later that night. I think this also makes him uniquely good at explaining things, like phonon modes and pair distribution function analysis. Whenever I find myself trying to explain a strange new concept, I try to imagine how Beecher would do it.

Ava Kreider-Mueller was our master of fluorine NMR and set the standard of Parkin Group rigor that we always strove to match. Josh Choi is orders of magnitude smarter and harder working than me, but his humility sticks with me the most. When I was a first year and he was getting ready to start his own lab at UVA, he would ask ME questions as often as I would ask him questions. Abe Wolcott always brought a unique perspective to our group through his adventures into nanodiamonds, discussions during group meetings.

Brandi Cossairt left to start her own lab at UW before I got to the lab, but her legend preceded her. She's the queen of phosphorus, the first one in the group to start winning chemical arguments with Jon, the one to figure out you could distill octadecene following nanocrystal synthesis, and many other firsts I'm sure I'm not even aware of.

Aya Buckley and Rebecca Siegelman were the first two undergrads to graduate from the Owen Lab while I was there, and I think ever. Aya took on some challenging synthesis projects and always made the lab a more cheerful place. Rebecca is uniquely adept at forging her own path, working on gold nanocrystals at a time when nobody else in the lab was doing anything even close. I had the privilege of mentoring her before she didn't need me anymore. I'm overjoyed both of them have found their way in grad school at Berkeley.

A lot of people are student-athletes in high school, and many division-I athletes are "students" in college, but Bert Vancura is one of the few true student-athletes. But don't take it from me – in 2014 he was featured in the Wall Street Journal for studying while waiting for a plane to the NCAA tennis tournament.

Peter Chen and I have been a pair since day one of graduate school, when we figured out we were both from Rockville, MD. Graduate school can be a trying experience, but having a close friend and lab partner like Peter gets you

through it. To Peter and the rest of the friends I've made in the department – in particular, Josh Infantine, Stewart Mallory, Michael Gaschler, Joseph Harder, Nate Kim, Patrick Quinlivan, Nathan Daly, the rest of the Spicy Boyz softball team – thank you for making my time at Columbia great.

Tavi Semonin brought experience in solar to a lab of solar wannabes and fearlessly led us into areas we wouldn't have sought out on our own. He's also a worthy spikeball opponent – I think I was decent at it because I was used to running, fielding, and hitting from years playing baseball, but he was just a freak athlete and good at just about everything.

In this regard, Ilan Jen-La Plante is very similar – she has pure talent and practical expertise in both science and sports. I knew she was the real deal when she showed up and in a few weeks synthesized a dual-emitting nanocrystal sample that Leslie and I had spent a summer trying to make. She's one of the easiest people to get along with out there, and hope I get to work with her again.

Now for the undergraduates I had a hand in mentoring. Greg Cleveland is one of the most successful undergrads we've ever had. After a few years working with Mark he was basically a grad student, and I was fortunate enough to mentor him for a little bit once Mark graduated. I have no doubt he'll zip through his Ph.D. and become a professor if he still wants. Aidan Graham made an excellent addition to the thioureas team – he was always eager to synthesize

another precursor and run another test nanocrystal synthesis. I'm proud to have had some role in his ending up at Pacific Light Technologies. Robert Swain was a big help in getting selenoureas to the place they are now – we ran some of the early PbSe and CdSe reactions and navigated some pretty stinky selenourea syntheses together. Rajat Chandra boldly stepped across the boundary between chemical engineering and chemistry to take on the challenge of building a flow reactor for nanocrystal synthesis. I was impressed when he basically had it figured out on the first try!

The future of our precursor work is in capable hands with Leslie Hamachi and Iva Rreza. Leslie became a core member of the lab as soon as she arrived – the two of us worked together on a challenging nanocrystal synthesis her first summer, and a few days after moving to New York she bravely went on what turned out to be a wild group trip. Her combination of patience, drive, and cheerfulness is something I strive to match. Iva and I came to work closely together on the solid-state lighting project, which meant a trip to the Molecular Foundry to use WANDA. I want to thank her for putting up with me for two weeks and rolling with the punches that never seem to stop coming when you try to force chemistry to adhere to a schedule.

Trevor Hull has effortlessly taken over as the heart of the second-generation Owen Lab. In lab, he's always been fearless in taking on strange new projects. Outside of lab, he's one of my favorite people to hang out with.

Evelyn Auyeung boldly took on a range of projects during her time as a postdoc, and helped advance the work I had started on ZnSe synthesis and PbS superlattice formation – I'm just glad I had enough loose threads for her to pull on. I wish her all the best moving forward. Anthony Chesman was a pleasure to have join our lab for a few months, and his advice on cobbling together a CZTS nanocrystal synthesis for the SI of the thioureas paper was important to its eventual acceptance. Suk ho Hong made for a strong addition to the thiourea conversion mechanism project, as has Matt Greenberg in more recent months. I wish Matt the all the best in carrying that work forward – I think it's one of the most interesting unanswered questions in that area of research.

Jonathan De Roo had the unenviable task of replacing Ilan, but amazingly he's done it in his own way. I envy his skill at extracting meaning from chaos (as one has to do as a metal oxide surface chemist), and his relentless attention to detail. I was thrilled when he arrived and quickly assumed the role as cleanest person in lab! Willem Walravens added a great presence and know-how over his three months with us. In particular, he helped me out with some advanced TEM characterization during peer review on the PbSe paper while I was away for

three weeks. Brandon and Ellie are natural fits for the lab. Clearly passionate about what they're doing, interesting people to talk to, I'm proud to leave two of my projects in their capable hands.

To the current group of undergraduates – Victor Gordillo, Eric Reisel, Kevin Qian, Christian Joseph – I wish you all the best of luck and hope you find the research questions we've just begun to ask interesting enough to answer.

Growing up, I saw a lot of my friends' parents make them take up sports, musical instruments, volunteer work, test prep classes, and other resume boosters that they weren't really interested in. Mine never pushed me in any direction, but always provided a good environment for whatever I was interested in. Moreover, I was lucky enough to find coaches and mentors through the years who took a chance on me and allowed me to grow into ever larger roles. This level of trust is amazing to me – kids are dumb – but I'm forever thankful for it. I think this combination of leeway and support is probably the biggest reason I wove my way toward a Chemistry Ph.D. I know this is a chemistry dissertation, but these ideas make the most sense to me in terms of baseball, so bear with me for a moment.

In 7$^{th}$ grade, a friend from the neighborhood team encouraged me to try out for a select team he had joined. This was a whole different level; this team

had its eye on county championships. They lifted weights. They assigned homework. They traveled to tournaments in the summer and held practices in the winter. I was good for a recreational league catcher, but I was small and nowhere close to this level. I practiced with them that winter as an extended tryout and got my ass kicked over and over again. I'm not sure why, but they took me onto the team as a backup for that spring season. They didn't need an extra catcher and it showed. I rode the bench. Even if they had wanted to play me, I was sidelined with knee pain all season.

One practice that summer our first baseman was out, so I filled in for a round of "Ultimate Infield," which is a drill where the coaches hit the ball as hard as they can at the infielders, whose collective job is to make 21 outs without committing an error. An error means you start over from zero. Fun times. I had never played first base before, but to my surprise, I didn't suck! Turns out catching bad pitches in crappy gym lighting had taught me not to be afraid of the ball. The season on the bench had let me learn by osmosis. The knee issues turned out to be a symptom of growing three inches taller. Being the worst player on a good team was exactly where I'd needed to be. It's cheesy, but I was finally ready to repay the team for the risk they took on a scrawny 12 year-old trying out for catcher. I took over at first base and didn't look back.

Back to chemistry. As a senior in college, I applied to graduate schools pretty widely. Chemistry is a pretty small field and it's hard to know where you'll get accepted to Ph.D. programs in the same way that you can make some educated guesses for undergraduate or law school admissions. My grades weren't stellar and I didn't have the one thing that would almost certainly get you in anywhere: authorship on a paper. I started getting responses from schools that winter, spanning the spectrum from acceptance to wait listing to rejection. Columbia and one or two others put me on their wait lists, so throughout the spring I sent updates. Annoying try-hard things like "just wanted to update the admissions committee that I attended such-and-such conference in March," or "here are my Winter Quarter grades." When I did this with Columbia, they acknowledged receipt, but then sent me an outright rejection letter. Oh well. I enrolled at another school and made plans to do summer research.

Of course that's not the end of the story. Out of the blue one day in April, I got an email from Jon Owen and Luis Campos that I'll never forget, asking if I was still interested in the department. I'm not sure why it happened that way. The optimist in me thinks maybe there was some administrative mistake; the pessimist in me thinks they blew through all the waitlist spots without getting enough students to enroll and had to start taking people they'd rejected; the psychologist in me thinks maybe my last name caught Luis' eye in the same way

his last name caught my eye when I first visited the department website. I went through a range of emotions, but after initially taking offense that this department would toy with me like this, then worrying about how I could cancel my plans at the other school, then realizing I could spend most of my 20s in New York City, it became overwhelmingly clear where I was about to go. When I got to Columbia I used this experience as motivation to rise to the occasion again.

To my coaches – Mike Podhorzer, Scott Dunlap, J. D. Marchand, Joe Cassidy, and numerous others – thank you for seeing something in a skinny kid who didn't say much, and thank you for pushing me to achieve things I couldn't imagine. To Jon, thanks for taking a chance on a chemist with so-so grades and no papers. And to my mom and dad, and my brothers Brian and Will, thank you for always putting me in good environments and rolling with me as I've tried to carve my own path. I love you guys. To all of you, thank you for letting become part of something bigger than myself. I carry this responsibility on my shoulders and your trust in my heart. I won't let you down.

Last, I want to thank Sarah Eberspacher, my closest companion on this ride. Sarah, you're at the core of everything I do and it's hard to imagine having gone through all this without you by my side. By design, graduate school finds your limits and makes you push past them, and this kind of personal growth affects the people closest to you. So thanks for believing in me all this way, for

always lending an ear or a napkin so I can try out a wacky idea on you, for going on walks across Central Park just to watch the dogs, for always getting another Ben & Jerry's pint when we're out. I love you.

* * * *

# CHAPTER 1. Synthesis and Surface Chemistry of Cadmium Carboxylate-Passivated CdTe Nanocrystals from Cadmium *bis*(Phenyltellurolate)

## Table of Contents

Reproduced in part from:

Campos, M. P.; Owen, J. S. *Chem. Mater.* **2016**, *28*, 227-233.

## 1.1. Abstract

### *1.1.1. Technical Abstract*

We report the synthesis of cadmium telluride nanocrystals from cadmium *bis*(phenyltellurolate) ($Cd(TePh)_2$) and cadmium alkylcarboxylates ($Cd(O_2CR)_2$, $O_2CR$ = oleate, tetradecanoate). $Cd(TePh)_2$ reacts quantitatively with $Cd(O_2CR)_2$ at 220 °C over one hour with the concomitant elimination of diphenyl telluride ($Ph_2Te$) and CdTe nanocrystals. The nanocrystal diameter approaches 3.0–3.2 nm at full conversion, regardless of changes to the solvent, carboxylate chain length, heating conditions, and reactant concentration. Larger nanocrystals may be grown by slow addition of additional precursors to the crude product mixture. Isolated nanocrystals have carboxylate ligands (2.1–4.7 $nm^{-2}$) that can be displaced along with excess cadmium ions using low concentrations of N,N,N′,N′-tetramethylethylenediamine (TMEDA) (1.5–280 mM). Using $^1H$ NMR spectroscopy, we measure the extent of the displacement and show that the binding of $Cd(O_2CR)_2$ to CdTe is weaker than to CdSe nanocrystals of similar size. The weaker binding is proposed to arise from a lower polarity and greater stability of reconstructed CdTe surfaces.

*1.1.2. Plain English Abstract*

We developed a synthesis of cadmium telluride (CdTe) nanocrystals from $Cd(TePh)_2$, a bulk CdTe precursor discovered in the 1980s, and $Cd(O_2CR)_2$ surface ligands. This reaction is remarkable for two reasons. First, unlike most nanocrystal syntheses, which are "hot injection" methods that are exquisitely sensitive to reaction conditions, our synthesis is a "heat-up" method that is insensitive to many common changes such as reaction scale, heating rate, and precursor concentration, reliably producing 3.0-3.2 nm nanocrystals. This makes this reaction practical for scale-up. Second, this is the only CdTe nanocrystal synthesis to date to completely exclude all but one type of surface ligand. We exploit this fact to quantitatively show that $Cd(O_2CR)_2$ binds to CdTe more weakly than to CdSe, a finding we attribute to CdTe's less polar crystal lattice.

**1.2. Context**

*1.2.1. The Importance of Crystal Grain Boundaries in Photovoltaics*

CdTe is the only photovoltaic material on the market currently competitive with Si.[1] Broadly speaking, this is because while CdTe modules tend to be less efficient than Si modules, they are less expensive to manufacture and install, leading to faster energy payback times. The major producer of CdTe modules is a company called First Solar, which has focused its business on large-

area rural installations for grid-level electricity generation while continually breaking its own lab cell efficiency records (Figure 1.2.1).

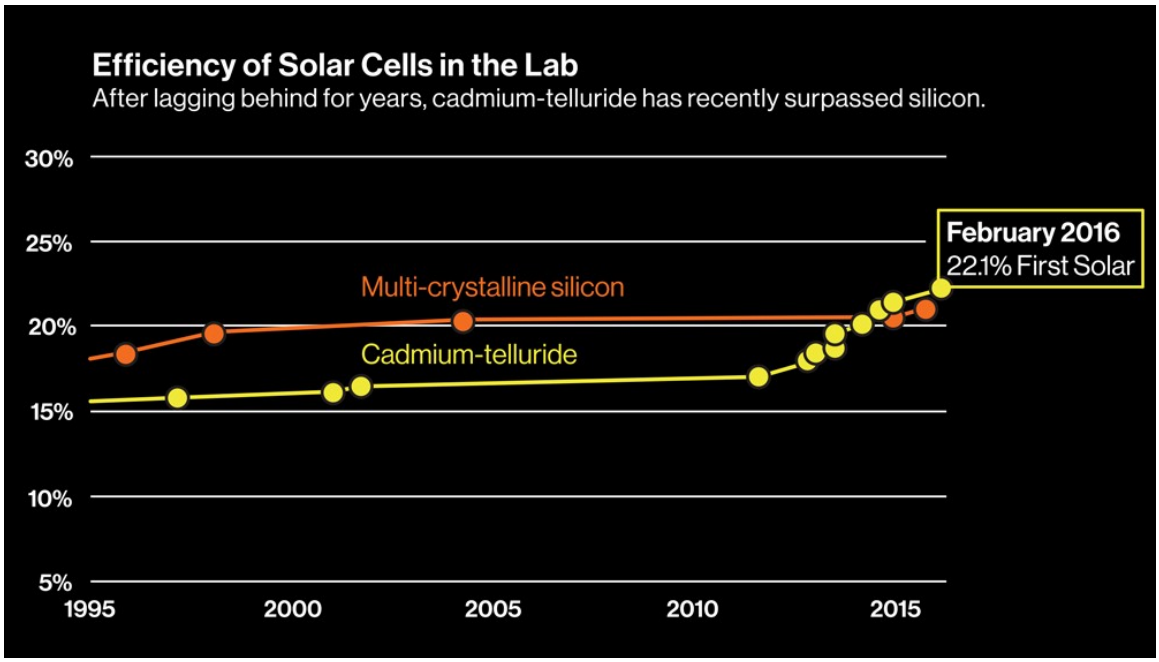


Figure 1.2.1. NREL-certified efficiencies of Si and CdTe PV cells.[1]

However, a number of important issues remain in CdTe PV.[2] The issue with the greatest potential impact on future cell efficiency is the open-circuit voltage. Crystal grain boundaries play an important, yet double-edged and poorly understood role in PV efficiency. From a first-principles perspective, grain boundaries represent breaks in the crystal lattice that should prevent charge collection at the electrical contacts. Further, under-coordination, reconstruction, and oxidation of surface atoms should introduce mid-gap "trap" states that decrease the operating voltage of a PV device while further exacerbating the issue of charge collection. Indeed, despite $CdCl_2$/heat treatments to catalyze

crystal grain growth, CdTe PV cells suffer from anomalously low open-circuit voltages when compared to GaAs PV cells, which have a similar band gap (Table 1.2.1).[2] Moreover, the best cells fabricated by close space sublimation (22.1% power conversion efficiency)[1] dramatically outperform the best cells fabricated by solution processing of CdTe nanocrystals (12.3%)[3,4] despite similar device geometries and treatments.

Table 1.2.1. Comparison of selected CdTe and GaAs PV characteristics.[2]

| Material | Band gap (eV) | Open-circuit voltage (V) |
|---|---|---|
| CdTe | 1.45 | 0.84-1.01 |
| GaAs | 1.42 | 1.10 |

Despite these issues, several benefits to grain boundaries have been clearly shown. While the grain boundary argument suggests that single-crystalline CdTe should be optimal, cells made from polycrystalline CdTe outperform those made from single-crystalline CdTe.[2] Recent work has shown that this may be due to surface dopants. Panthani et al. observed beneficial effects of Cu dopants arising from impurities in commercial Te samples.[3] Grecu et al. suggested that Cu migration from the device Cu back contact into the CdTe layer helps mitigate the impact of Cd vacancies.[5] Li et al. discovered a secondary effect of the common $CdCl_2$ treatment, Cl substitutions at Te sites near crystal surfaces.[6] Chemically, this results in localized *n*-doping, since Cl has more valence electrons than Te.

Given that CdTe is naturally *p*-type, or slightly deficient in Cd, these Cl substitutions create internal *p-n* junctions, resulting in dramatically higher photocurrent near crystal surfaces. Yan et al. argue that annealing under inert atmosphere facilitates S diffusion into the CdTe layer, which increases the photocurrent by actually *lowering* the device bandgap (due to a phenomenon called "bowing"[7]) and increasing spectral response at long wavelengths.[8] However, they also note that annealing under oxygen leads to Cd-O bonds at grain surfaces and suppresses S diffusion.

Despite these advances, our understanding of cadmium telluride interfaces, and nanostructured interfaces in general, is in its infancy. A reproducible and scalable synthesis of CdTe nanocrystals with well-defined chemical composition would 1) allow CdTe surface structure and its relationship to electronic structure to be studied using solution techniques and 2) create new pathways to solution-processed photovoltaic cells and photodetectors. These issues prompted us to investigate new methods to prepare colloidal CdTe nanocrystals with well-defined compositions on large reaction scales, and ideally, tunable conversion kinetics.[9–13]

*1.2.2. Issues Surrounding Tellurium Precursors to CdTe Nanocrystals*

Although ZnTe, CdTe, and PbTe nanocrystals can be prepared from phosphine tellurides, sodium telluride, and silyltelluride reagents, uncontrolled

reactivity of these tellurium precursors plagues the synthetic reproducibility.[14] In addition to their air and light sensitivity, many tellurium precursors are thermally unstable and release elemental tellurium at relatively low temperatures. Trioctylphosphine telluride, which is by far the most common tellurium precursor to CdTe nanocrystals, suffers from both of these problems. While phosphine sulfides and selenides have been synthesized and utilized in nanocrystal synthesis, phosphine tellurides are much less stable because of tellurium's greater resistance to reduction and the poorer overlap between the P *3s* and Te *5p* orbitals. Thus, phosphine telluride stability depends upon the reducing power of the phosphine's substituents (Scheme 1.2.1);[15–20] trioctylphosphine telluride is not a stable compound, eliminating tellurium even during storage at –78 °C. In order to use trioctylphosphine telluride as a CdTe precursor, most studies employ an excess of trioctylphosphine.[21–24] We will address this excess later in the section.

Scheme 1.2.1. Equilibrium between phosphine tellurides, phosphines, and elemental tellurium.

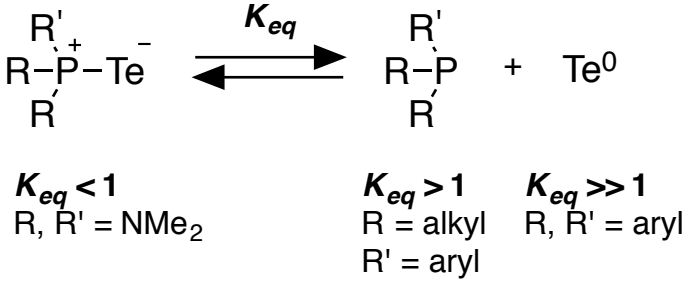

A few alternative tellurium precursors have been studied. Bawendi and Steigerwald wrote early reports on the use *bis*(trialkylsilyl)telluride reagents.[25,26] Notably, lower reaction temperatures were required for CdTe than CdSe or CdS, and bulkier trialkylsilyl protecting groups (*tert*-butyldimethylsilyl, triisopropylsilyl) were needed to stabilize the telluride than in the cases of *bis*(trimethylsilyl)sulfide and *bis*(trimethylsilyl)selenide. Both findings point to the extreme reactivity of silyl tellurides toward salt exchange and oxidation. Steigerwald et. al. explored the use of dialkyl ditellurides for organometallic vapor-phase epitaxial growth of CdTe quantum wells, noting that "the stench of the lower alkyls of tellurium made further study of this reaction inconvenient."[27] Shen et. al. utilized $TeO_2$ as a precursor by oxidizing impurities in commercial 90% trioctylphosphine oxide at 380 °C.[28]

Importantly, several strategies used for sulfur and selenium precursor preparation are ineffective for tellurium.[14] These include 1) oxidation of amine/alkene solvents as in the cases of S, Se, or $SeO_2$, 2) injection of finely powdered elemental chalcogen, 3) phosphinate salts, and 4) use of urea analogues (see Chapters 2 and 3).

*1.2.3. $M(EAr)_2$ complexes*

Metal *bis*(arylchalcogenolate) ($M(EAr)_2$) complexes (M = Zn, Cd, Hg; E = S, Se, Te) are a polymeric class of compounds that received attention from the

semiconductor community in the late 1980s and early 1990s. Early work by Steigerwald and others demonstrated a range of synthetic pathways to $M(EAr)_2$ derivatives including salt-exchange and redox reactions (Scheme 1.2.2, Scheme 1.2.3).[26,29–31]

Scheme 1.2.2. Synthesis of $M(EAr)_2$ from trimethylsilyl(aryl)chalcogenides.

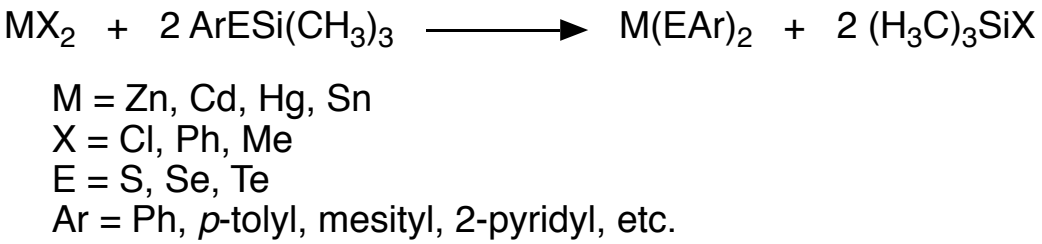


Scheme 1.2.3. Synthesis of $Hg(TePh)_2$ by redox and salt exchange reactions.

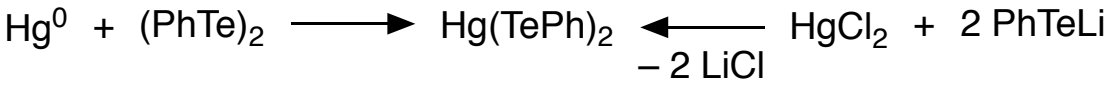


$M(EPh)_2$ complexes are polymeric, but highly sensitive to the presence of L-type ligands, which decrease the degree of polymerization. In the absence of L-type ligands, $Zn(SPh)_2$ forms a 3-dimensional network structure of adamantoid cages bridged by phenylchalcogenolates.[32] In the presence of methanol, the analogous $Cd(SPh)_2$ polymer is reduced to a 2-dimensional structure bound by L-type methanol ligands at vertices.[33] Upon treatment with 1,2-*bis*(diethylphosphino)ethane (DEPE), $Cd(SePh)_2$ forms a 1-dimensional polymer of $Cd(SePh)_2$ dimers bridged by DEPE.[30] When *N*,*N*,*N*′,*N*′-

tetramethylethylenediamine (TMEDA) is added, $Cd(SPh)_2$ and $Cd(SePh)_2$ form monomeric complexes bound by bidentate TMEDA ligands.[34]

It quickly became clear that these compounds converted cleanly to metal chalcogenide and diaryl chalcogenide under mild conditions (Scheme 1.2.4),[29,30,35] leading to more widespread interest in their use as chemical vapor deposition (CVD) precursors. Steigerwald, Brus, and coworkers also demonstrated that this efficient metal chalcogenide-forming reaction could be carried out in solution in the presence of coordinating ligands to afford nanocrystalline material with broad, yet discernible optical signatures of quantum-confined CdSe and CdTe (Scheme 1.2.5, Figure 1.2.2).[30,31]

Scheme 1.2.4. Disproportionation of $M(EAr)_2$.

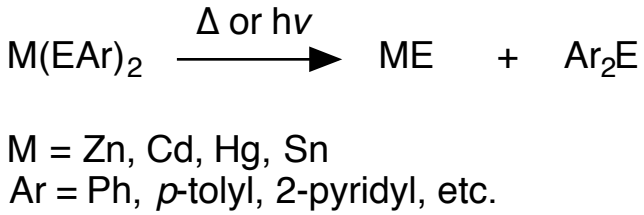


Scheme 1.2.5. Disproportionation of $Cd(EPh)_2$ (E = Se, Te) in coordinating media.

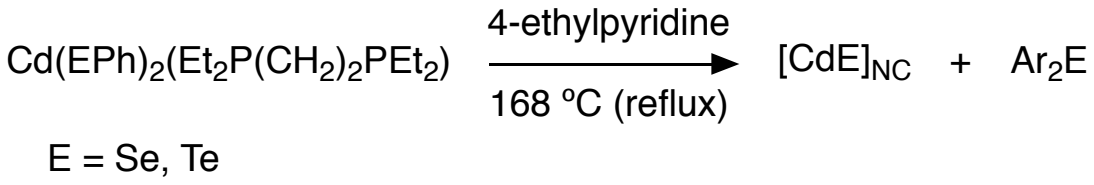

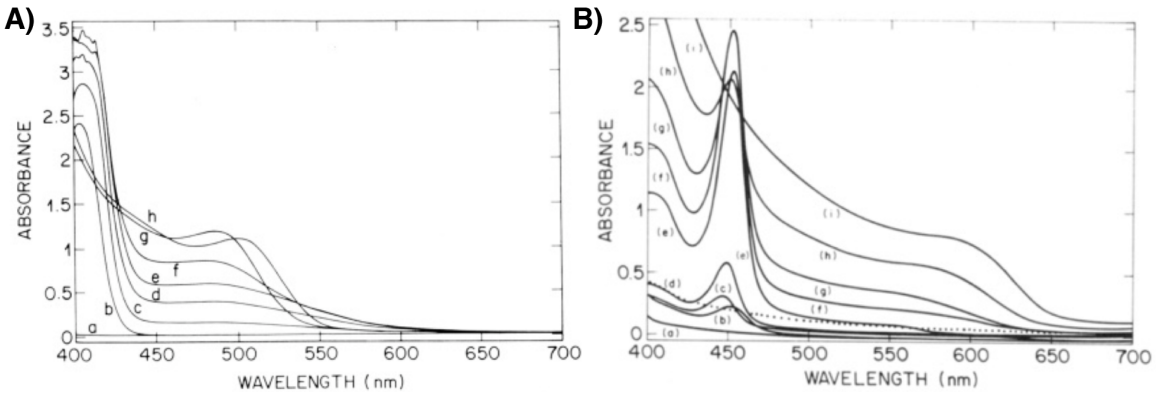


Figure 1.2.2. UV-vis absorbance spectra of first A) CdSe and B) CdTe nanocrystallites synthesized from $Cd(EPh)_2$.[30,31]

While promising, this work was soon overshadowed by the discovery of phosphine chalcogenide precursors, which most researchers preferred because of their ease of synthesis and utility at higher reaction temperatures. In 1993 this led to the first synthesis of nearly monodisperse CdE nanocrystals via hot injection of phosphine chalcogenide/dimethylcadmium solutions, an article that been cited nearly 9000 times at the time of this writing.[25] Thus, $Cd(EPh)_2$ precursors were largely forgotten for 25 years.

### 1.3. Synthesis of CdTe Nanocrystals from $Cd(TePh)_2$

Following this body of work, we developed a modern synthesis of CdTe nanocrystals from $Cd(TePh)_2$ and cadmium carboxylates ($Cd(O_2CR)_2$, $O_2CR$ = oleate, tetradecanoate). Given 1) their promising early CdTe synthesis, 2) previously raised issues with phosphine tellurides, and 3) encouraging discussions with Mike Steigerwald, we concluded that there was an enormous

opportunity to modernize this efficient precursor to better serve the traditionally difficult synthesis of CdTe, while carefully controlling its ligand chemistry for surface chemistry study and, down the line, photovoltaic cell fabrication.

*1.3.1. Synthesis of $PhTeSi(CH_3)_2R$ (R = Me, $^tBu$)*

We decided to pursue the cleanest possible, synthetic route to $Cd(TePh)_2$, given our knowledge of its sensitive coordination chemistry, which is likely to influence its utility and reproducibility as a CdTe nanocrystal precursor. Initial attempts to synthesize $Cd(TePh)_2$ from PhTeLi gave deeply colored mixtures of products likely containing di-/oligotellurides (for reference: diphenyl telluride is yellow while diphenyl ditelluride is red-orange) that would be nearly impossible to remove. This led us to phenyl(trialkylsilyl)tellurides. By adapting a known procedure,[36] we dissolved tellurium in phenyllithium (PhLi) solution and then quenched the lithium phenyltellurolate (PhTeLi) intermediate with either trimethylsilyl chloride or *tert*-butyldimethylsilyl chloride to give $PhTeSi(CH_3)_2R$ (R = Me, $^t$Bu). These also formed as deeply colored mixtures, but are readily purified by vacuum distillation to afford pale yellow oils. These oils can be stored indefinitely under nitrogen in a –40 °C freezer but rapidly degrade upon exposure to air with the formation of a deep red color.

Scheme 1.3.1. Synthesis of phenyl(trialkylsilyl)tellurides.

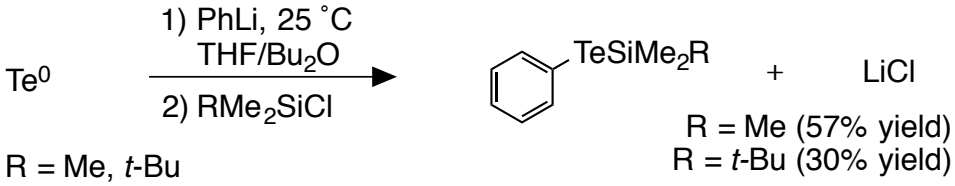


The synthesis and isolation of $PhTeSi(CH_3)_3$ balances yield versus side-product removal. When 1 equiv. PhLi is used, the tellurium does not completely dissolve, indicating the presence of a side reaction (perhaps base-promoted THF ring-opening). Following reaction with TMSCl, if $PhTeSi(CH_3)_3$ is vacuum distilled from this mixture, yields in the range of our reported 57% are obtained. To increase yield, an excess of PhLi (1 – 2 equiv.) may be employed to completely dissolve the tellurium. However, after reaction with TMSCl, a mixture of $PhTeSi(CH_3)_3$ and PhTMS remains. At this point, if the goal is to obtain analytically pure $PhTeSi(CH_3)_3$, a difficult fractional distillation must be performed to remove the slightly lower-boiling PhTMS. However, if the presence of PhTMS is tolerable, a more straightforward vacuum distillation will give higher yields of the target compound in a mixture. Since PhTMS is analogous to benzene/toluene (toluene being the solvent for the next step) the latter option is probably more practical.

While *tert*-butyldimethylsilyl protecting groups tend to impart greater stability to sensitive functional groups, we did not observe any differences in

stability between the two phenyl(trialkylsilyl)tellurides. Thus, we primarily pursued the trimethylsilyl derivative because of its higher yields and easier distillation. After several rounds of optimization, we were able to scale this reaction up to 15 g yields, which to the best of our knowledge is the largest ever reported.

*1.3.2. Synthesis of $M(TePh)_2$ (M = Cd, Zn)*

We next explored conditions for the conversion of $PhTeSi(CH_3)_3$ to $Cd(TePh)_2$. $PhTeSi(CH_3)_3$ reacts rapidly with many cadmium compounds to precipitate $Cd(TePh)_2$ as a fine yellow powder with the concomitant elimination of silylated anions. We have demonstrated this reaction across a variety of cadmium compounds and solvents (Table 1.3.1), eventually arriving at cadmium oleate and toluene as the preferred method.

Table 1.3.1. Optimization of $Cd(TePh)_2$ synthesis conditions.

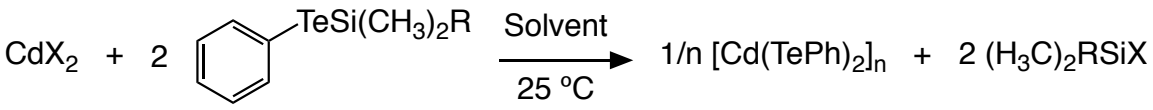


| Trial | X | Solvent | Yield | Comments |
|---|---|---|---|---|
| 1 | $O_2CPh$ | THF | 75-85% | Small THF impurity |
| 3 | Me | $CH_2Cl_2$ | Not recorded | Slower reaction (~24 h) |
| 4 | Oleate | Toluene | >95% | Small oleate, toluene impurities |

We chose these conditions for three reasons: 1) toluene is non-coordinating, 2) cadmium oleate is soluble in toluene at room temperature, and 3) in case of incomplete purification, left-over cadmium oleate is the most innocuous impurity possible, since our CdTe nanocrystal synthesis involves a 3-fold excess of cadmium oleate (see Section 1.3.3). After isolation and drying under vacuum, the chalky yellow powder can be handled briefly in air but should be stored under nitrogen or a red color will slowly develop.

Suitable donor ligands including trialkylphosphines, *n*-alkylamines, and chelating diamines such as TMEDA bind $Cd(TePh)_2$, allowing colorless solutions of the corresponding donor ligand complex to be prepared. Single crystals of ($\kappa^2$-TMEDA)$Cd(TePh)_2$ complex could be grown from a solution of TMEDA and $Cd(TePh)_2$, showing a four coordinate structure (Scheme 1.3.2, Figure 1.3.1, Section 1.6.15) analogous to the previously reported structures of ($\kappa^2$-TMEDA)$Cd(SPh)_2$ and ($\kappa^2$-TMEDA)$Cd(SePh)_2$.

Scheme 1.3.2. Synthesis of ($\kappa^2$-TMEDA)$Cd(TePh)_2$.

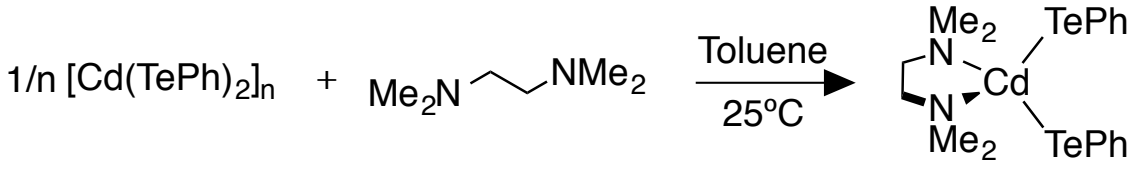

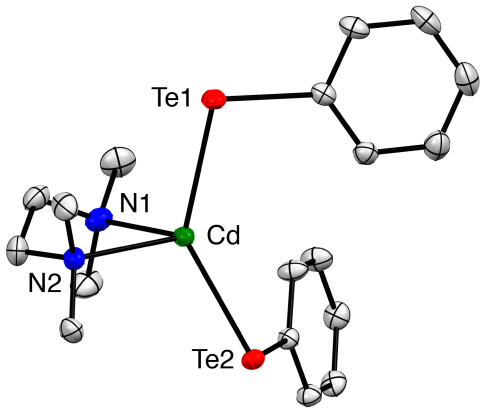


Figure 1.3.1. Molecular structure of ($\kappa^2$-TMEDA)Cd(TePh)$_2$. Selected bond lengths (Å): Cd–Te(1) 2.73873(19), Cd–Te(2) 2.74511(18), Te(1)–C(7) 2.1209(16), Te(2)–C(13) 2.1193(15), Cd–N(1) 2.4358(15), Cd–N(2) 2.3874(13). Selected bond angles: Te(1)–Cd–Te(2) = 139.217(6)°, N(1)–Cd–N(2) = 77.18(5)°, N(1)–Cd–Te(1) = 100.53(4)°, N(1)–Cd–Te(2) = 105.93(3)°, N(2)–Cd–Te(1) = 104.27(3)°, N(2)–Cd–Te(2) = 111.42(3)°. R1 [all data] = 0.0206, ωR2 [all data] = 0.0432. Ellipsoids are plotted at 50% probability level.

$^{125}$Te NMR spectra of Cd(TePh)$_2$ dissolved in the presence of *n*-octylamine reveal a concentration-dependent NMR line shape and frequency. The $^{125}$Te NMR signal sharpens and shifts upfield ($\delta$ = -246 ppm to -259 ppm) as the concentration of *n*-octylamine is increased (Figure 1.3.2). This behavior presumably results from rapid and reversible binding of the amine ligands to the cadmium centers on the NMR timescale. The rapid exchange of dative ligands bound to cadmium has been reported previously.[37,38]

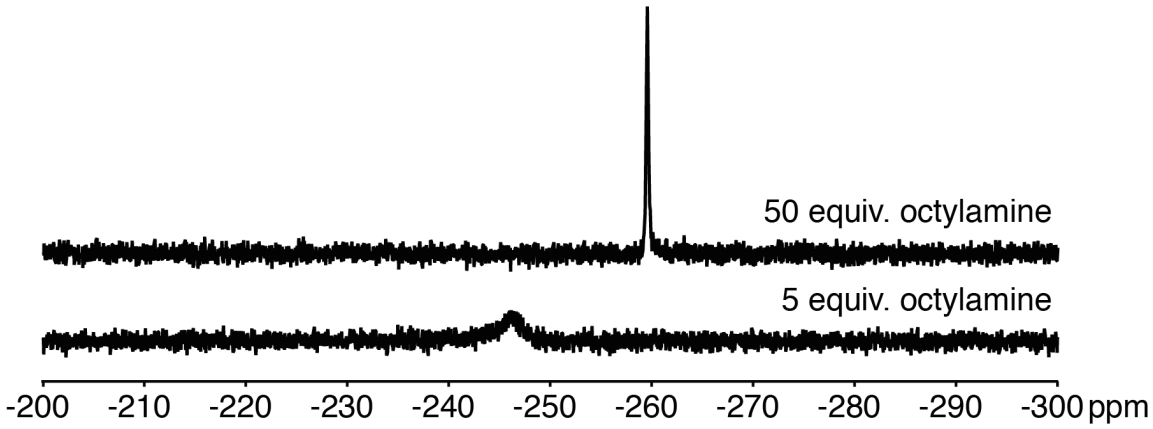


Figure 1.3.2 $^{125}$Te NMR spectra of $Cd(TePh)_2$ in benzene-$d_6$ upon addition of 5 and 50 equivalents of *n*-octylamine.

*1.3.3. Synthesis of CdTe Nanocrystals from $Cd(TePh)_2$ and $Cd(O_2CR)_2$*

Heating a suspension of $Cd(TePh)_2$ in hexadecane to 220 °C causes a color change from yellow to red to black beginning near 210 °C. An X-ray diffraction pattern taken from the black solid is characteristic of zinc blende CdTe, while $^1$H NMR spectroscopy demonstrates the formation of $Ph_2Te$ (Figure 1.3.3, Figure 1.3.5). Interestingly, in the presence of added cadmium oleate (3 equiv.), the $Cd(TePh)_2$ dissolves at lower temperatures (170 °C) and before the color darkens, suggesting that a complex is formed between the cadmium oleate and $Cd(TePh)_2$ precursors (Equation 1.3.1). After an hour at 220 °C, a red-brown solution of quasi-spherical nanocrystals with a zinc blende structure is formed (Figure 1.3.3, Figure 1.3.4). As the $Cd(TePh)_2$ precursor conversion reaches completion, the lowest energy absorbance feature approaches 530–550 nm with a full-width half-maximum of 44–50 nm. This corresponds to an average nanocrystal diameter of

3.0–3.2 nm according to published sizing formulas.[39,40] These linewidths are among the most narrow available at this size.[21–23,39,40] By measuring the absorbance of aliquots at $\lambda$ = 410 nm, the yield of CdTe was determined using a published extinction coefficient and exceeds 90% after an hour (Figure 1.3.4).[39] $^{1}$H NMR analysis of aliquots dissolved in benzene-$d_6$ and *n*-octylamine verified the complete conversion of $Cd(TePh)_2$ and the formation of $Ph_2Te$ in yields of 70-80% (Figure 1.3.5). No other aryl-containing products were observed.

Equation 1.3.1

$$1/n\ [Cd(TePh)_2]_n + m\ Cd(O_2CR)_2 \longrightarrow Cd(TePh)_2 \cdot (Cd(O_2CR)_2)_m$$

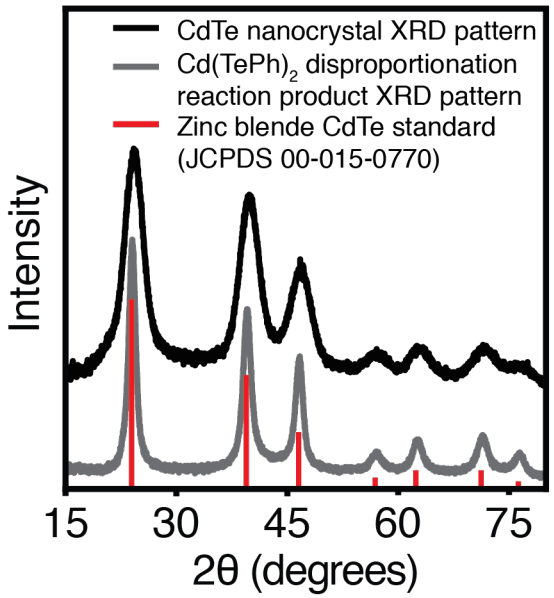


Figure 1.3.3. Powder X-ray diffraction pattern of CdTe nanocrystals (black) and polycrystalline CdTe produced by disproportionation of $Cd(TePh)_2$ at 220 °C in hexadecane (gray). Exponential baseline corrections were applied to the data to remove signal from scattering. The CdTe standard (red) was obtained from the Joint Committee on Powder Diffraction Standards (JCPDS) as coll. code 00-015-0770.

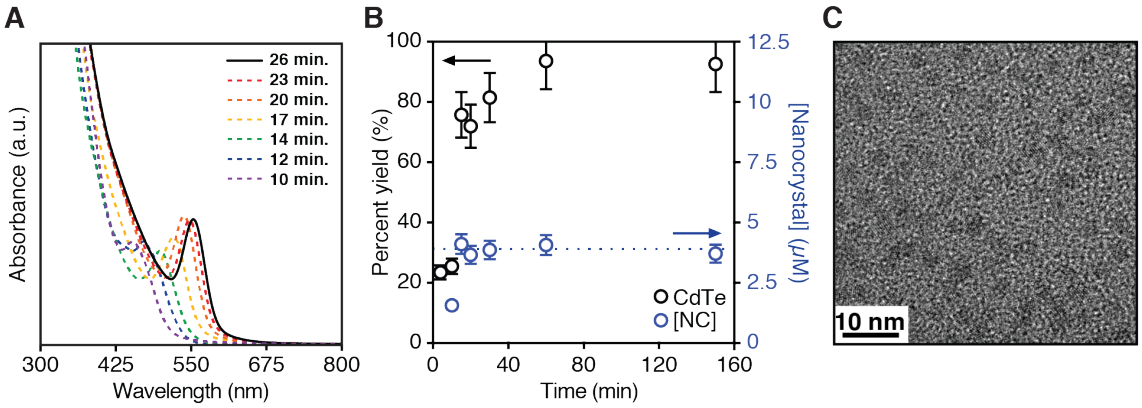


Figure 1.3.4. A) Time-dependent UV-visible absorption spectra. B) CdTe yield (black) and nanocrystal concentration (blue) over the course of a kinetics reaction. See the experimental section for reaction conditions and Figure 1.3.6 for corresponding absorption spectra. C) Transmission electron micrograph of isolated nanocrystals.

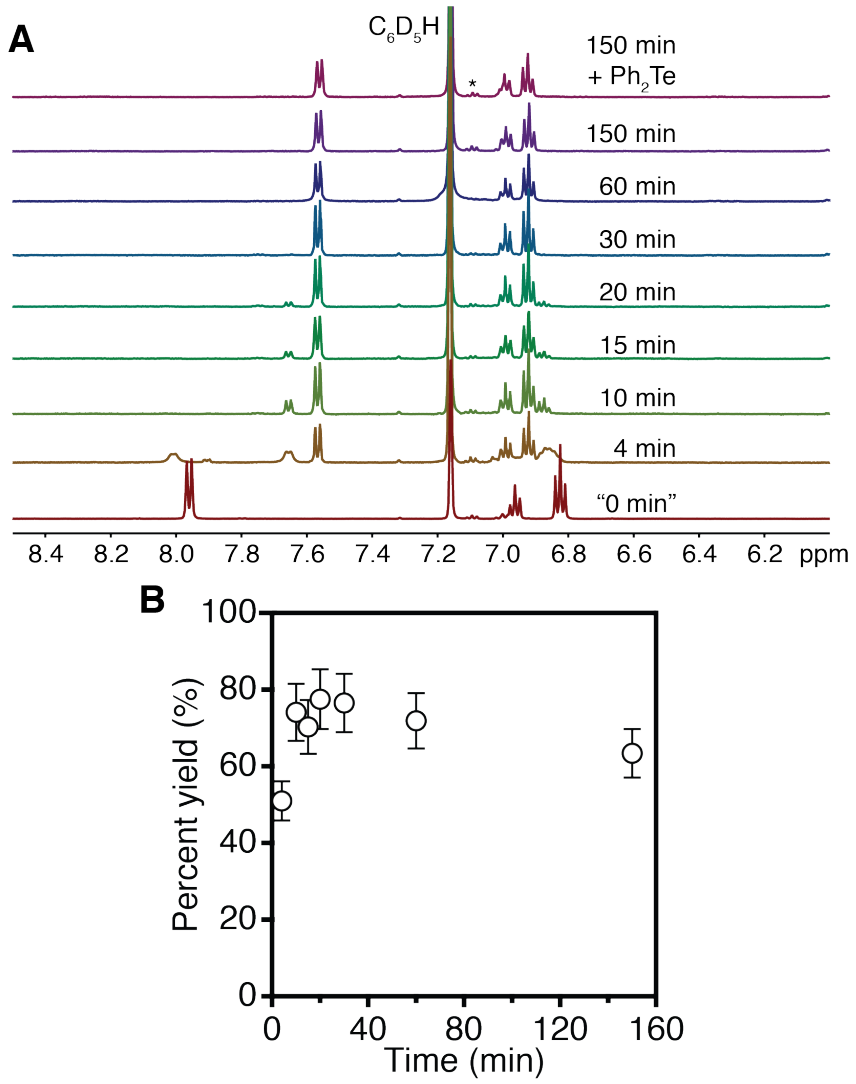


Figure 1.3.5. A) $^{1}$H NMR spectra of crude reaction mixture ("0 min"), aliquots removed during synthesis (4 min - 150 min), and the final aliquot with added diphenyl telluride prepared by the thermolysis of $Cd(TePh)_2$ in hexadecane (150 min + $Ph_2Te$). (*) denotes a toluene impurity. Additional signals in the $t$ = 4–20 min. aliquots may result from a complex between cadmium oleate and the diphenyl telluride, or a monocarboxylate-monotellurolate cadmium complex that results from comproportionation of the precursors. B) $Ph_2Te$ yield as measured by $^{1}$H NMR.

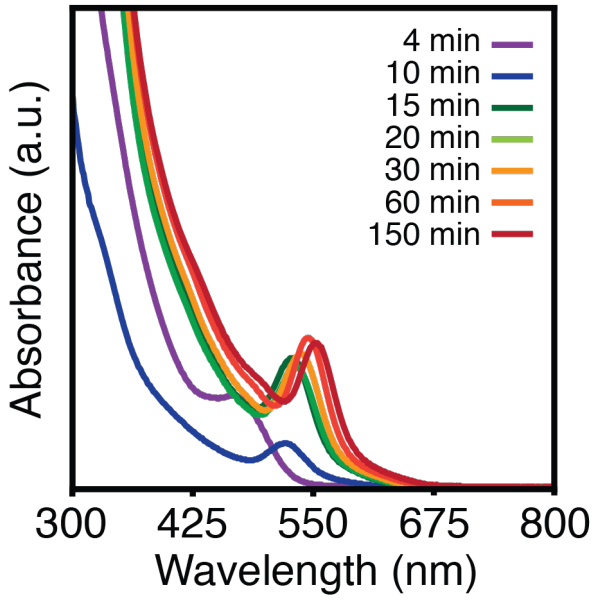


Figure 1.3.6. UV-vis absorbance spectra of aliquots removed from a nanocrystal kinetics reaction (4 min – 150 min).

*1.3.4. Synthetic Parameter Space*

Over many reactions, the final size reaches the same value regardless of changes in the heating rate, solvent, carboxylate chain length, oleic acid content, and over an order of magnitude change in the reaction concentration (16–160 mM (Cd)) (Figure 1.3.7). A similar invariance of the final size has been reported in a "heat-up" synthesis of CdS nanocrystals prepared from cadmium tetradecanoate and cadmium *bis*(diphenyldithiophosphinate).[9] The result is due, in part, to a slow Ostwald ripening rate and a nanocrystal concentration that is proportional to the concentration of the chalcogenide precursor during nucleation. In both this case and the previous report, this proportionality can be explained by first-order decomposition of a complex between cadmium oleate

and the chalcogen precursor, like the one in Equation 1.3.1 above. Because of the dramatic changes in temperature inherent to these reactions, however, precise determination of the kinetic rate law is not feasible. Attempts to influence the final size by adding *n*-alkylamines, tri-*n*-alkylphosphines, or varying the ratio of $Cd(O_2CR)_2$ to $Cd(TePh)_2$ all adversely affect the size distributions (Figure 1.3.8, Figure 1.3.9). However, larger nanocrystals with narrow size distributions can be obtained by the dropwise addition of $Cd(TePh)_2$ and cadmium carboxylate to the final reaction mixture (Figure 1.3.10).

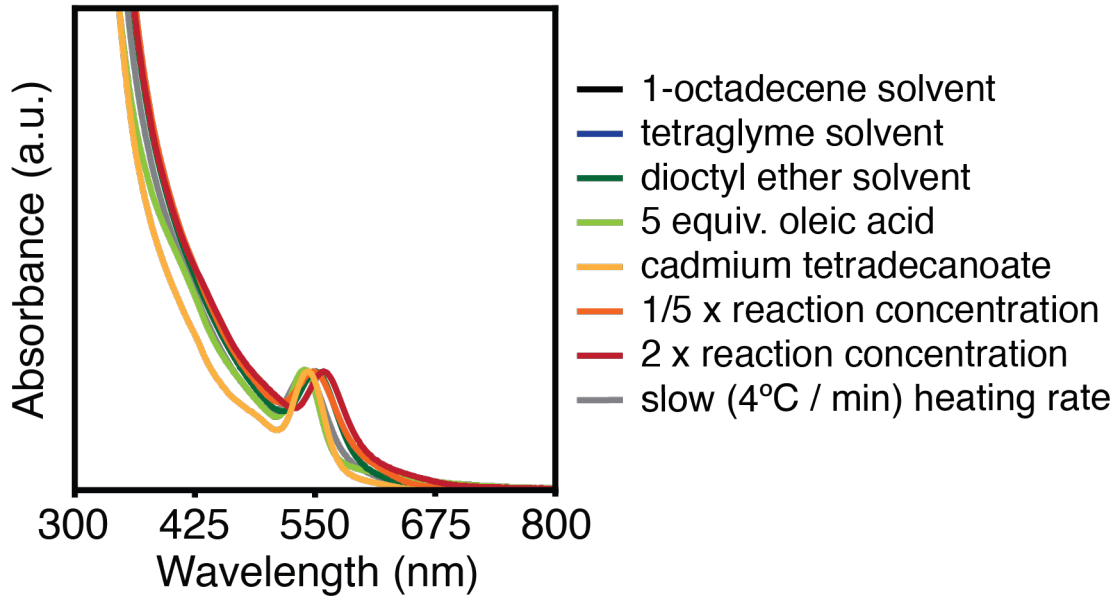


Figure 1.3.7. Absorbance spectra showing insensitivity of the final nanocrystal size to synthesis conditions. Spectra are normalized to the height of the excitonic band.

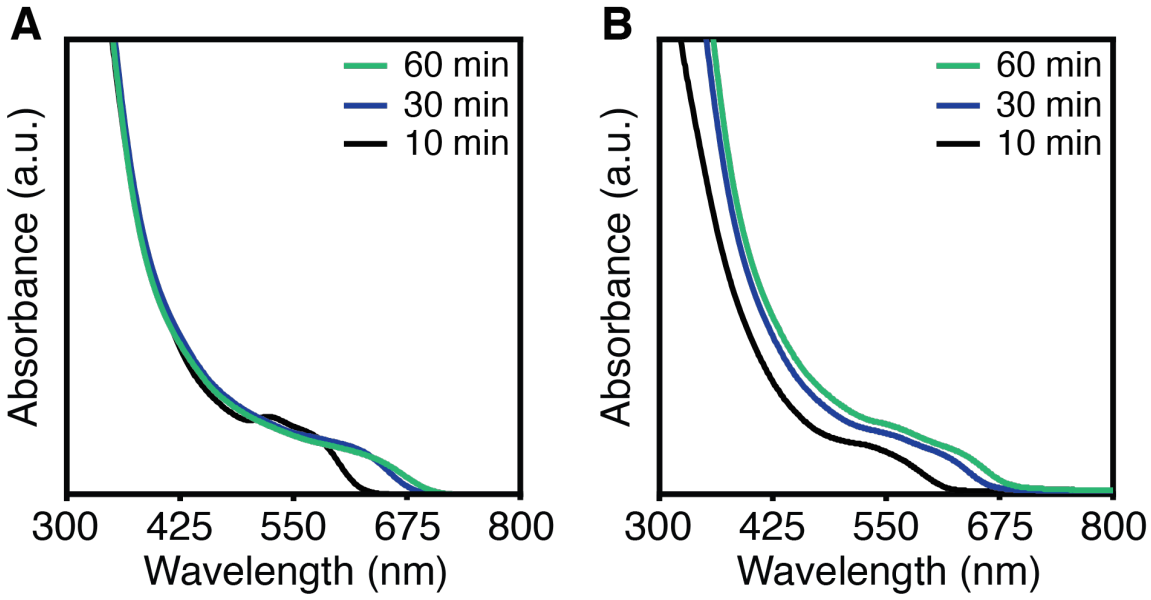


Figure 1.3.8. UV-visible absorbance spectra of nanocrystal synthesis reactions run in the presence of 5 equivalents of A) tributylphosphine and B) octadecylamine.

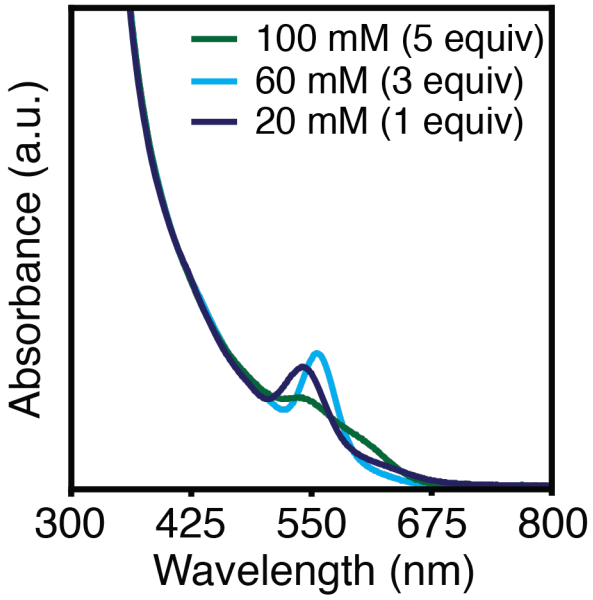


Figure 1.3.9. UV-visible absorbance spectra of nanocrystal synthesis reactions run in the presence of one, three, and five equivalents of cadmium oleate. Spectra are normalized to the absorbance at 410 nm.

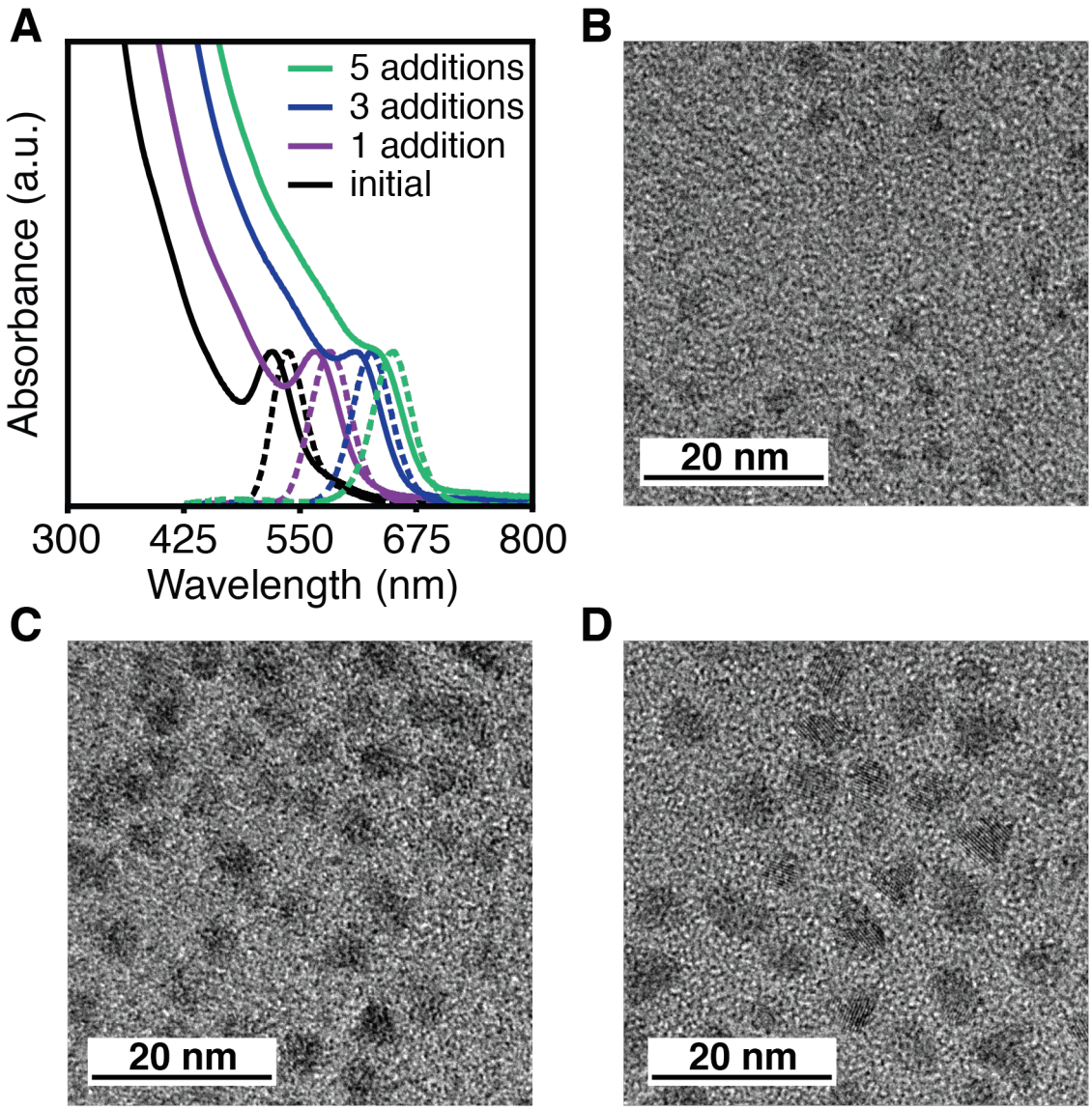


Figure 1.3.10. A) Absorbance and photoluminescence spectra of CdTe nanocrystals grown by successive additions of precursor mixture to a synthesis mixture at completion. Transmission electron micrographs of CdTe nanocrystals after A) one, B) three, and C) five additions of precursor mixture.

## 1.4. Surface Coordination Chemistry of CdTe Nanocrystals

### *1.4.1. Reversible Displacement of $Cd(O_2CR)_2$ complexes*

Nanocrystals isolated from the reaction mixture have $^1$H NMR signals characteristic of both bound and free oleate ligands (Figure 1.4.1, Figure 1.4.2, Figure 1.4.3). No signals from TePh fragments could be found. On the basis of these measurements we propose a balanced chemical equation for the conversion to CdTe nanocrystals bound by cadmium carboxylate (
Scheme 1.4.1).

By analyzing both the absorbance and $^1$H NMR spectra of nanocrystals dissolved in benzene-$d_6$ or toluene-$d_8$, ligand concentrations of 2.1–4.7 oleates/nm$^2$ surface area were found. Overlapping $^1$H NMR signals for free and bound oleate ligands were deconvoluted using a peak fitting routine (Figure 1.4.3) to better estimate the coverage of surface bound carboxylate ligands (2.1–3.1/nm$^2$), from which we estimate Cd:Te ratios of 1.1–1.2. Energy-dispersive X-ray spectroscopy confirms these estimations within error (Figure 1.4.4, Table 1.4.1). These ligand coverages are consistent with sub-monolayer passivation of available surface tellurium sites with cadmium carboxylate. The observed packing densities are 10–40% lower than typical carboxylate packing densities on as-prepared CdSe and CdS nanocrystal surfaces, and significantly lower than the packing density of crystalline *n*-alkanes (4.9 nm$^{-2}$) or the surface atom density of

CdTe facets ([111] = 5.50 $nm^{-2}$, [100] = 4.76 $nm^{-2}$; see Table 1.4.2).[41] The lower coverage suggests a relatively weak binding of cadmium oleate to CdTe compared to CdSe surfaces.

To measure the affinity of cadmium carboxylate for the CdTe surface, we studied its displacement from the nanocrystals using TMEDA. Following isolation from TMEDA solution (1.5 – 7.5 mM) both the carboxylate coverage and photoluminescence quantum yields decrease (Figure 1.4.1), much like was observed in a recent study on CdSe and CdS nanocrystals.[41] High concentrations of TMEDA (≥ 280 mM) completely displace the cadmium carboxylate ligand shell, leading to insoluble nanocrystal aggregates after exposure to methyl acetate or on prolonged standing at room temperature. Interestingly, the insoluble aggregates could be redispersed upon stirring the sample in cadmium oleate solution at room temperature. Both of these observations support a reversible binding of cadmium oleate to the CdTe nanocrystal surface.

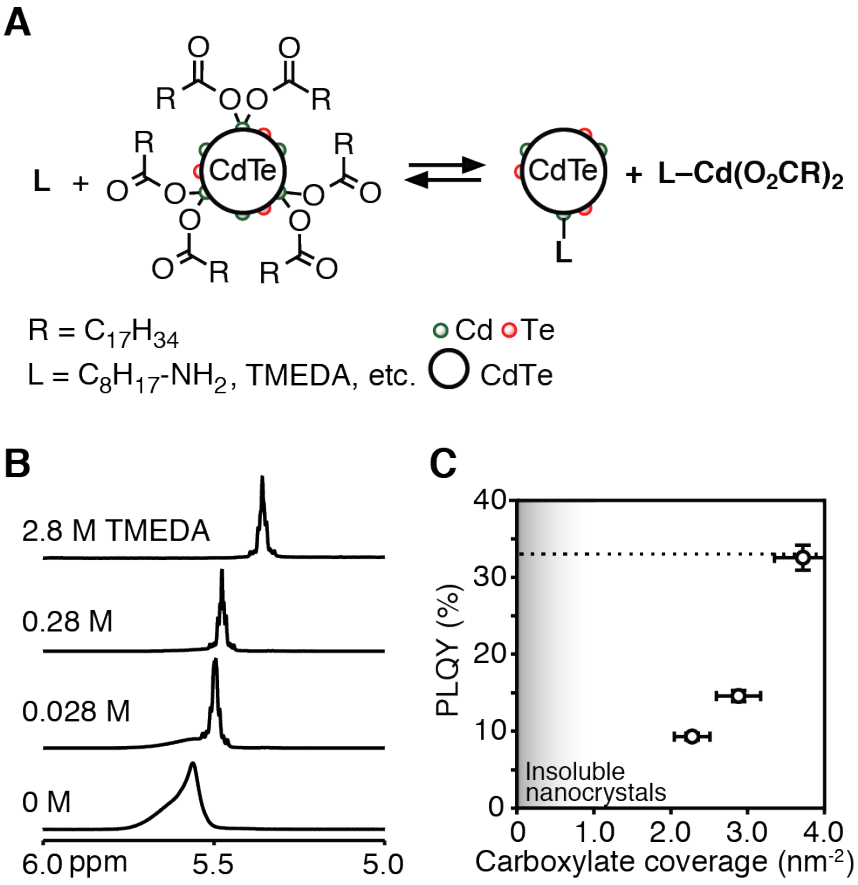


Figure 1.4.1. A) Reversible displacement of L-Cd($O_2CR$)$_2$ from CdTe nanocrystals promoted by L-type ligands. Descriptions of nanocrystal chemical formulas do not imply geometric structure. B) Vinyl region of $^1$H NMR spectra of CdTe nanocrystals showing displacement of Cd($O_2CR$)$_2$ upon treatment with increasing concentrations of TMEDA. Changes to the chemical shifts may be due to changes in the dielectric of the solvent medium. An analysis of the lineshape of the 0 M spectrum is shown in Figure 1.4.3. C) Dependence of the photoluminescence quantum yield on cadmium carboxylate coverage after treatment with TMEDA and isolation.

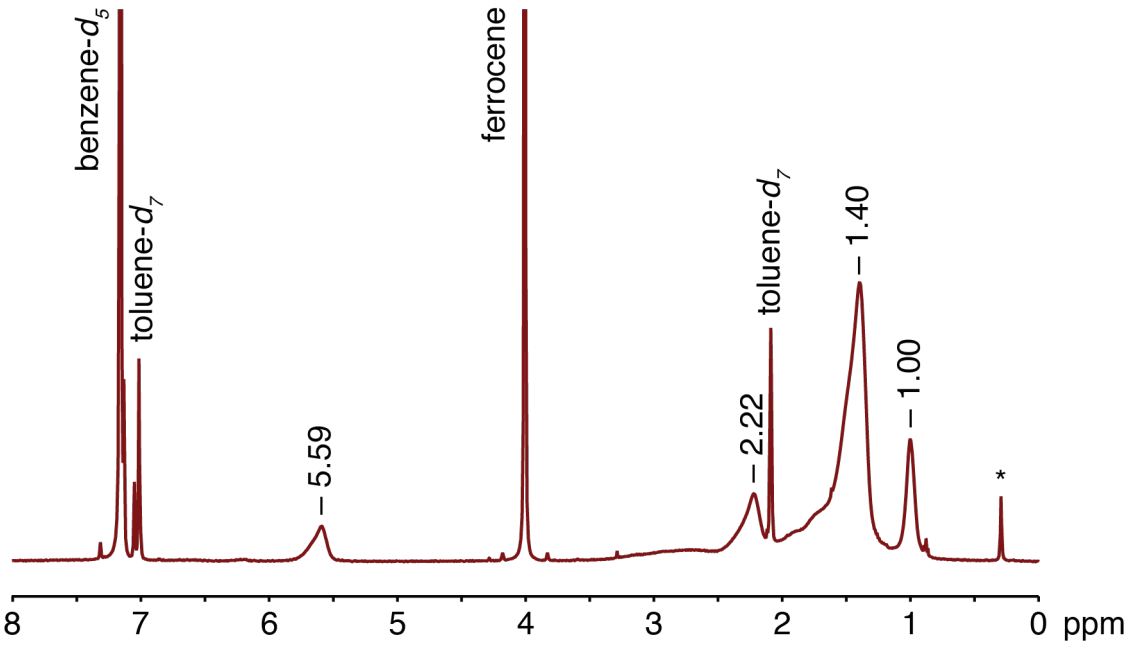


Figure 1.4.2. $^1$H NMR spectrum of CdTe nanocrystals dissolved in benzene-$d_6$ with addition of a ferrocene internal standard dissolved in toluene-$d_8$. (*) denotes a small silicone impurity leached from the silicone liner of the vial caps.

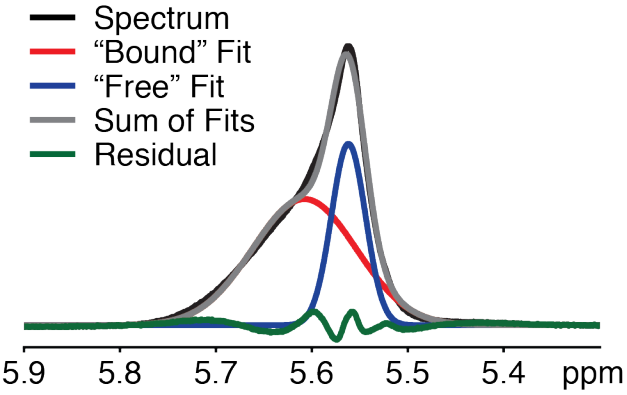


Figure 1.4.3. Vinyl region of $^1$H NMR spectrum of CdTe nanocrystals with 4.7 oleates/nm$^2$ shown in Figure 3B with an approximate fit to two Gaussians. The broad downfield peak represents surface-bound cadmium oleate (67.9% of total signal) and the sharper upfield peak represents free

cadmium oleate (32.1% of total signal). This analysis reduces the measured surface coverage to 3.1 oleates/nm$^2$.

Scheme 1.4.1. Balanced chemical equations for the formation of cadmium carboxylate-bound CdTe nanocrystals from $Cd(TePh)_2$ and cadmium carboxylates.

$$Cd(TePh)_2 \longrightarrow [CdTe]^i + TePh_2$$

$$m\,[CdTe]^i + n\,Cd(O_2CR)_2 \longrightarrow (CdTe)_m(Cd(O_2CR)_2)_n$$

$O_2CR$ = tetradecanoate, oleate

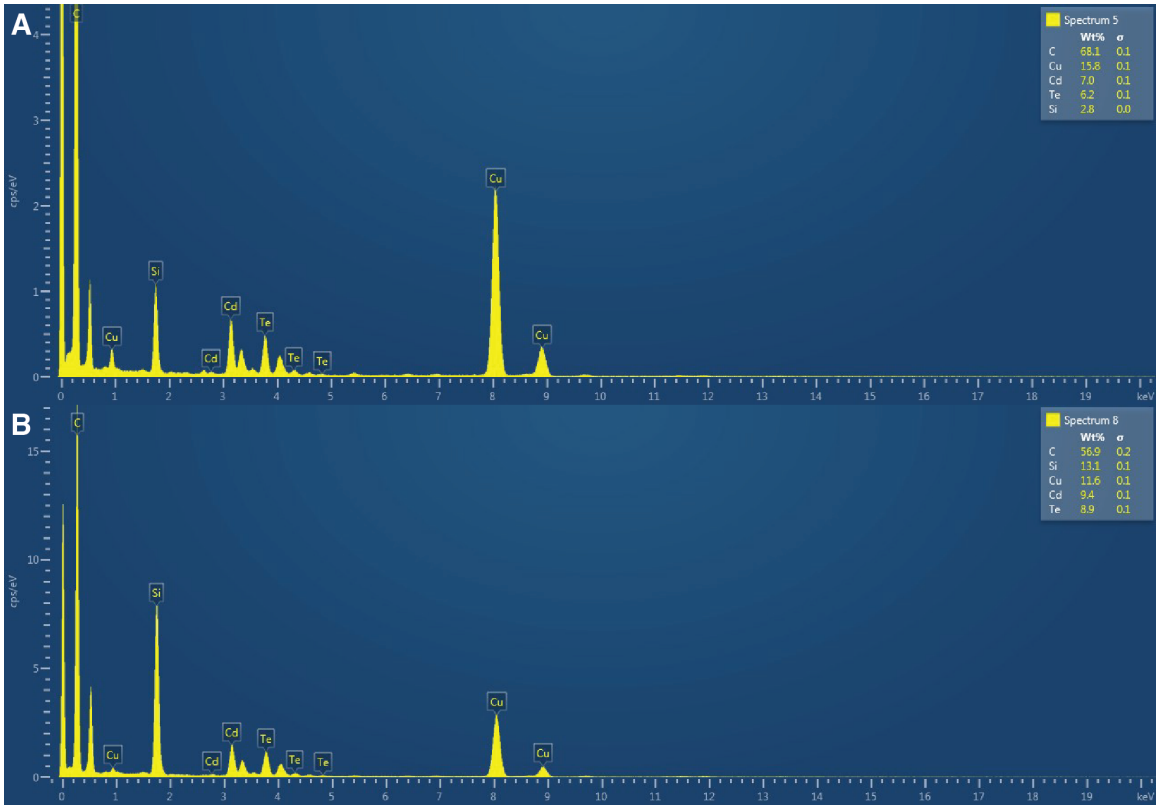


Figure 1.4.4. Energy-dispersive X-ray spectra of CdTe nanocrystal samples with A) 3.1 carboxylates/nm$^2$ and B) 2.3 carboxylates/nm$^2$.

Table 1.4.1. Cadmium-to-tellurium ratios in CdTe samples as measured by $^1$H NMR/UV-visible analysis of ligand-to-semiconductor ratios and energy-dispersive X-ray spectroscopy (EDX).

| Sample | Carboxylate coverage (nm$^{-2}$) | Cd:Te ratio by NMR/UV-vis | Cd:Te ratio by EDX |
|---|---|---|---|
| 1 | 3.7 | 1.25 ± 0.13 | - |
| 2 | 3.0 | 1.19 ± 0.12 | 1.28 ± 0.03 |
| 3 | 2.9 | 1.19 ± 0.12 | - |
| 4 | 2.6 | 1.17 ± 0.12 | - |
| 5 | 2.3 | 1.15 ± 0.12 | 1.20 ± 0.02 |

*1.4.2. Comparison with Analogous Study on CdSe Nanocrystals*

Given the relative ease with which the CdTe nanocrystals were made insoluble by the addition of TMEDA, we sought to compare the binding affinity of cadmium carboxylate to CdSe and CdTe nanocrystals. Cadmium carboxylate was displaced from CdTe nanocrystals of similar size, ligand coverage, and concentration to previously studied CdSe samples,[41] and the extent was monitored using $^1$H NMR spectroscopy ([TMEDA] = 0.020 – 2.000 M, [$Cd(O_2CR)_2$] = 0.10 M) (Figure 1.4.5). As the concentration of TMEDA is increased, sharp $^1$H NMR resonances corresponding to "free" cadmium oleate complexes increase in intensity at the expense of the broad signals from surface bound oleyl chains (Figure 1.4.1). The amount of free and bound cadmium carboxylate was measured by integrating the sharp and broad resonances in the vinyl region of the $^1$H NMR spectrum. This analysis clearly demonstrates a weaker affinity of cadmium carboxylate for CdTe nanocrystal surfaces.

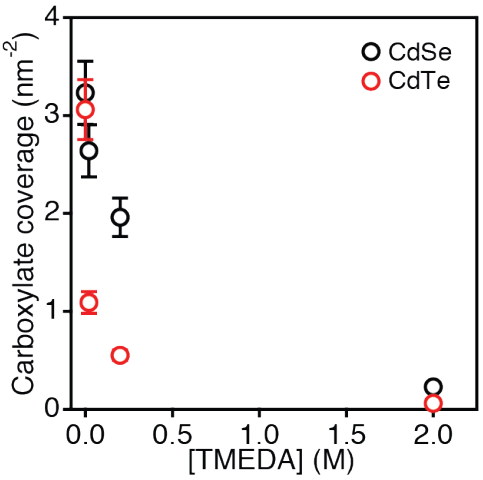


Figure 1.4.5. Carboxylate coverage per square nanometer of nanocrystal surface area in 3.2 nm CdTe (red) and 3.6 nm CdSe (black) nanocrystal samples with increasing concentration of TMEDA, as measured by $^{1}$H NMR and UV-visible absorption spectroscopies. CdSe data is re-plotted from literature data.[41]

Table 1.4.2. Surface site and ligand density values calculated for $Cd(O_2CR)_2$-bound CdSe and CdTe nanocrystals. CdSe nanocrystal data is obtained from the same literature data plotted in the main text.[41] Lattice constants are obtained from the Joint Committee on Powder Diffraction Standards (JCPDS) as coll. codes 00-019-0191 (CdSe) and 00-015-0770 (CdTe) and atom densities are calculated geometrically from the zinc blende unit cell.

| **Nanocrystal sample** | **CdSe** | **CdTe** |
|---|---|---|
| Zinc blende lattice constant (nm) | 0.6077 | 0.6481 |
| Atom density on {100} facet ($nm^{-2}$) | 5.42 | 4.76 |
| Atom density on {111} facets ($nm^{-2}$) | 6.25 | 5.50 |

| | | |
|---|---|---|
| Average surface atom density ($nm^{-2}$) | 5.83 | 5.13 |
| Average surface chalcogen density ($nm^{-2}$) | 2.92 | 2.56 |
| | | |
| Peak position (nm) | 571 | 552 |
| Peak position (eV) | 2.17 | 2.25 |
| Average nanocrystal diameter (nm) | 3.57 | 3.25 |
| Surface area per nanocrystal ($nm^2$) | 39.9 | 33.2 |
| Surface chalcogen sites per nanocrystal | 116.5 | 85.0 |
| $Cd(O_2CR)_2$ per nanocrystal after isolation | 64.5 | 50.7 |
| Carboxylate ligand density ($nm^{-2}$) | 3.3 | 3.1 |
| Percent of surface chalcogen sites occupied | 55.4% | 59.6% |

*1.4.3. Structural Insights*

A variety of factors can influence the affinity of cadmium carboxylate for the nanocrystal surface. At high coverage, cadmium carboxylate dissociates on binding to minimize interchain steric interactions and to neutralize the basicity and acidity of the metal and chalcogen surface sites respectively.[42,43] On descending the group from CdS to CdTe the covalency and dielectric constant both increase (Table 1.4.3), thereby reducing the driving force for neutralization. Reconstruction of the unpassivated facet also minimizes the acidity and basicity of the exposed Cd and chalcogen ions by concentrating chalcogen *s*-orbital character in the exposed lone-pair.[44,45] This effect is greatest in the case of Te

because of its large effective nuclear charge and the large splitting between the Te(*6s*) and Te(*5p*) levels; a property that leads to the so-called "inert pair effect". These effects weaken the driving force to neutralize the polarity of CdTe surfaces, and thereby weakens the affinity of cadmium carboxylate for CdTe compared to CdSe or CdS (Scheme 1.4.2). Geometric factors including the importance of chelation of the carboxylate ion and ligand packing effects are sensitive to the underlying surface atom density and facet geometry that will further modify the relative affinities.[46,47] Computational investigations of these effects would provide valuable guidance to the design of passivation layers that maximize adsorption affinity and minimize nonradiative recombination.

Scheme 1.4.2. Binding and dissociation of cadmium carboxylate at a reconstructed cadmium telluride surface neutralizes surface charge polarity.

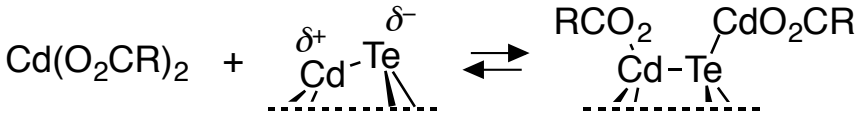


Table 1.4.3. Electronic properties of cadmium chalcogenide semiconductors relevant to ionic/covalent character.[48] In addition to large differences in electronegativity, strong ionic character manifests in small static and optical dielectric constants ($\varepsilon_0$, $\varepsilon_\infty$, respectively; relative to the dielectric constant of vacuum).[49]

| Material | CdS | CdSe | CdTe |
|---|---|---|---|

| | | | |
|---|---|---|---|
| Pauling electronegativity difference | 0.89 | 0.86 | 0.41 |
| Dielectric constant ($\varepsilon_0/\varepsilon_\infty$) | 8.28/5.23 | 9.3/6.2 | 10.4/7.1 |

## 1.5. Summary

In this chapter, we have discussed the importance of CdTe crystal surfaces in the context of photovoltaic efficiency and the history of $M(EAr)_2$ complexes as efficient ME precursors, and used this knowledge to design the first CdTe nanocrystal synthesis demonstrated only a single ligand type. We have then used $(CdTe)_m(Cd(O_2CR)_2)_n$ as a synthon for quantitative chemistry, showing a substantially lower affinity for $Cd(O_2CR)_2$ Z-type ligands than analogous CdSe samples. Since the complete absence of non-conductive aliphatic impurities is paramount to photovoltaic device efficiency, this weak interaction suggests that it should be possible to fabricate efficient solar cells from CdTe nanocrystal solutions and begin to compete with industrial vapor-deposited processes.

## 1.6. Experimental Details

### *1.6.1. Materials and Methods*

Unless otherwise indicated, all manipulations were performed under air-free conditions using standard Schlenk techniques and/or in a nitrogen-filled glovebox. Cadmium nitrate tetrahydrate (99%), sodium hydroxide, and phenyllithium (1.8 M in dibutyl ether), tetradecanoic acid (myristic acid, Sigma

grade, ≥ 99%), octadecylamine (≥ 99.0%), and diphenyl ditelluride (98%) were purchased from Sigma Aldrich and used without further purification. Oleic acid (99%) was obtained from either Sigma Aldrich or Alfa Aesar and used without further purification. Tellurium (ingot, 99.999% or shot, 99.999%) was obtained from either Sigma Aldrich or Alfa Aesar. 1-Octadecene (tech. 90%), tetraethylene glycol dimethyl ether ("tetraglyme," ≥ 99%), hexadecane (99%), dioctyl ether (99%), n-octylamine (99%), and chlorotrimethylsilane (> 97%), and were obtained from Aldrich; *N*,*N*,*N'*,*N'*-tetramethylethylenediamine ("TMEDA," 99%) and tri-*n*-butylphosphine (99%) were obtained from Strem Chemicals; all were distilled from calcium hydride and stored under nitrogen or argon prior to use. Solvents were stored over activated 3Å molecular sieves for at least 24 h before use. *tert*-Butyldimethylchlorosilane (97%) was obtained from Aldrich and sublimed prior to use. Anhydrous tetrahydrofuran (≥ 99.9%, inhibitor-free) and anhydrous methyl acetate (99.5%) were purchased from Sigma Aldrich, shaken with activated alumina, filtered, and stored over activated 3Å molecular sieves for at least 24 h before use. Toluene (> 99.5%) was dried over alumina columns and stored over 3Å molecular sieves for at least 24 h prior to use. Anhydrous benzene-$d_6$ ("$C_6D_6$", D, 99.5%) and toluene-$d_8$ (D, 99.5%) were obtained from Cambridge Isotope Laboratories and stored over activated 3Å molecular sieves for at least 24 h before use. ACS grade toluene (> 99.5%) used for optical

spectroscopy was purchased from Sigma Aldrich and used without further purification.

Cadmium oleate was prepared on an 88.5 mmol scale according to Chen *et al*.[50] and dried overnight under vacuum (60 mtorr) at 50°C.

NMR spectra were recorded on Bruker Avance III 400 and 500 MHz instruments. $^{1}$H NMR spectra are reported in ppm relative to $SiMe_4$ and were referenced internally with respect to the protio solvent impurity. $^{13}$C NMR spectra are reported in ppm relative to $SiMe_4$ and were referenced internally with respect to the solvent. $^{1}$H NMR spectra of nanocrystal samples were collected using acquisition times sufficient to obtain reliable integrals (5 s, T1 = 1.37 s) and relaxation delay times sufficient to allow complete relaxation between pulses (30 s), consistent with previous studies.[41,51,52] $^{125}$Te spectra are reported in ppm relative to $Me_2Te$ ($\delta$ = 0 ppm) and were referenced internally with respect to a diphenyl ditelluride standard in benzene-$d_6$ ($\delta$ = 420 ppm[53]) sealed in a glass capillary tube. UV-visible absorption data were obtained using a Perkin-Elmer Lambda 950 spectrophotometer equipped with deuterium and tungsten halogen lamps. Photoluminescence measurements were performed using a FluoroMax 4 from Horiba Scientific. Photoluminescence quantum yields were measured using an integrating sphere; samples were diluted to concentrations below 0.1 absorbance units at the lowest energy electronic transition to minimize

reabsorption. Powder XRD analysis was performed on a Scintag X-ray diffractometer equipped with a wide-angle detector.

*1.6.2. Synthesis of $PhTeSi(CH_3)_3$*

CAUTION*: Organotellurium compounds are toxic and possess foul odors. Exposure to small quantities (μg - mg) is reported to cause prolonged vile smelling breath, body odors, and urine; these compounds should only be handled by a highly trained and skilled scientist*. Adapting a procedure from Yamago and Yoshida,[36] finely ground tellurium (12.76 g; 100.0 mmol) and tetrahydrofuran (55 mL) are loaded into a Teflon-sealable Schlenk tube in a glove box. Phenyllithium solution (55 mL, 1.8 M in dibutyl ether, 0.99 equiv.) is slowly added to the mixture with stirring. The reaction mixture is allowed to stir for 60 minutes and then is transferred to a Schlenk line. Chlorotrimethylsilane (10.86 g, 12.7 mL, 1 equiv.) is then added slowly to the reaction mixture, giving a yellow suspension. This mixture is stirred for 60 minutes, during which time the color of the suspension gradually becomes red-orange. The reaction mixture is transferred via cannula to a vacuum distillation apparatus, and volatiles are removed under vacuum at room temperature. The temperature is then increased until a colorless fraction distills (55-70 °C, 60 mtorr) that is collected in a Teflon-sealable receiving flask cooled to -78 °C. A red-orange slurry remains in the still pot. The pale yellow distillate is then placed under argon, protected from light and stored in a glove

box at -40 °C. In the event that accidental contamination with oxygen occurs, a yellow to orange color develops. This material should be purified by redistillation prior to long-term storage. Yield: 15.75 g (56.7%). $^{1}$H NMR ($C_6D_6$, 400 MHz): $\delta$ = 7.80 (m, 2H, *m*-CH), 7.01 (m, 1H, *p*-CH), 6.86 (m, 2H, *o*-CH), 0.36 (s, 9H, $CH_3$). $^{13}C\{^{1}H\}$ NMR: ($C_6D_6$, 100 MHz) $\delta$ = 141.30 (*m*-C), 128.83 (*o*-C), 127.16 (*p*-C), 105.32 (*ipso*-C, $J_{C\text{-}Te}$ = 261.2 Hz), 2.50 ($CH_3$, $J_{C\text{-}Si}$ = 51 Hz, $J_{C\text{-}Te}$ = 12 Hz). $^{125}$Te NMR ($C_6D_6$, 126 MHz): $\delta$ = -6.01 ($J_{C\text{-}Te}$ = 272.1 Hz).

*1.6.3. Synthesis of PhTeSi$^{t}$Bu(CH$_3$)$_2$*

PhTeSi$^{t}$Bu($CH_3$)$_2$ is prepared analogously to PhTeSi($CH_3$)$_3$ on a 47 mmol scale, using a solution of tert-butyldimethylchlorosilane (1.4 M in THF) in place of chlorotrimethylsilane. Yield: 4.54 g (30.2%). $^{1}$H NMR ($C_6D_6$, 400 MHz): $\delta$ = 7.80 (m, 2H, *m*-CH), 7.02 (m, 1H, *p*-CH), 6.86 (m, 2H, *o*-CH), 0.91 (s, 9H, C($CH_3$)$_3$), 0.33 (s, 6H, Si($CH_3$)$_2$). $^{13}C\{^{1}H\}$ NMR ($C_6D_6$, 100 MHz): $\delta$ = 142.14 (*m*-C), 129.13 (*o*-C), 127.61 (*p*-C), 105.07 (*ipso*-C), 26.92 (Si-C($\underline{C}H_3$)$_3$), 19.35 (Si-$\underline{C}$($CH_3$)$_3$), -1.14 (Si($CH_3$)$_2$). $^{125}$Te NMR ($C_6D_6$, 126 MHz): $\delta$ = -74.23.

*1.6.4. Synthesis of Cd(TePh)$_2$*

In a glove box, cadmium oleate (1.215 g, 1.80 mmol) is dissolved in toluene (35 mL) with > 30 minutes of stirring. Phenyl(trimethylsilyl)telluride (1.00 g, 2 equiv.) is diluted with toluene (5 mL) in a separate vessel and then

added dropwise to the cadmium oleate solution. A yellow precipitate gradually forms during the addition, and the resulting suspension is allowed to stir for 2 hours. The reaction mixture is then poured into a centrifuge tube and centrifuged (7000 rpm, 10 min). The supernatant is carefully decanted and the pellet resuspended in toluene (20 mL), thoroughly breaking up any chunks. The process of centrifugation and resuspension is repeated twice more, and the resulting yellow solid is thoroughly dried under vacuum. Yield: 934.3 mg (99.5%). Several drops of *n*-octylamine are added to $Cd(TePh)_2$ (< 20 mg) in benzene-$d_6$ until a homogeneous solution is obtained, that is then analyzed with NMR spectroscopy (resonances for *n*-octylamine not reported below). Prior to use in nanocrystal reactions, $Cd(TePh)_2$ is ground in a mortar and pestle until a fine, homogenous powder is obtained. $^1$H NMR ($C_6D_6$, 400 MHz): $\delta$ = 8.06 (d, $J$ = 7.0 Hz, 2H, m-CH), 6.96 (t, $J$ = 7.3 Hz, 1H, p-CH), 6.86 (t, $J$ = 7.5 Hz, 2H, o-CH). $^{13}C\{^1H\}$ NMR ($C_6D_6$, 100 MHz): $\delta$ = 143.15 (m-C), 129.18 (o-C), 126.20 (p-C), 107.92 (ipso-C). $^{125}$Te NMR ($C_6D_6$, 126 MHz): $\delta$ = -250.70. Anal. Calcd for $C_{12}H_{10}CdTe_2$: C, 27.62; H, 1.93; N, 0.00. Found: C, 27.44; H, 1.80; N, < 0.02. The reaction scale may be doubled with no significant changes.

*1.6.5. Synthesis of ($\kappa^2$-TMEDA)Cd(TePh)$_2$*

Excess N,N,N′,N′-tetramethylethylenediamine (TMEDA) is added to a suspension of $Cd(TePh)_2$ in toluene, resulting in a colorless solution. Vapor

diffusion of pentane into the toluene solution at -40 °C yields single crystals of ($\kappa^2$-TMEDA)Cd(TePh)$_2$ suitable for X-ray crystallography.

*1.6.6. Synthesis of CdTe Nanocrystals*

In a glovebox, finely ground Cd(TePh)$_2$ (52.2 mg; 0.100 mmol), cadmium oleate (202.6 mg; 0.300 mmol, 3 equiv.), and hexadecane (5.00 mL) are added to a three-neck round-bottom flask fitted with a septum, an argon inlet, and a glass thermocouple adapter. The reaction vessel is transferred to a Schlenk line and heated to 220 °C at an average rate of 20 °C/min with efficient stirring. The timing discussed in the main text begins when the mantle is turned on. The reaction is allowed to run for 60 minutes. Once a homogenous solution forms (typically near 170 °C), 100 μL aliquots are removed and dissolved in 6.0 mL of toluene for UV-vis and fluorescence measurements. This reaction may be scaled by > 25 times without observable changes.

*1.6.7. Isolation of CdTe Nanocrystals*

At completion of a nanocrystal reaction at a 0.261 mmol scale the reaction mixture is cooled to room temperature, dry THF (15 mL) is added, and the dark solution is cannula transferred to a Teflon-sealable Schlenk tube and taken into a glovebox. Methyl acetate (170 mL) is added and the suspension is centrifuged (7000 rpm in 10 min). The dark residue is redissolved in THF (20 mL),

precipitated with methyl acetate (80 mL), and centrifuged. This process is repeated twice more with THF (10 mL) and methyl acetate (60 mL), and then once more with toluene (10 mL) in place of THF. The nanocrystals are then passed through a syringe filter (PTFE, 0.2 μm), dried thoroughly under vacuum, and dissolved in benzene-$d_6$ or toluene-$d_8$ for analysis by $^1$H NMR and UV-visible spectroscopies.

*1.6.8. Synthesis of Larger CdTe Nanocrystals*

In a glovebox, $Cd(TePh)_2$ (287.0 mg, 0.550 mmol), cadmium oleate (1.114 g, 1.65 mmol, 3 equiv.), and hexadecane (27.5 mL) added to a flask that is then sealed with a rubber septum. The vessel is transferred to a Schlenk line and heated to 60 °C in an oil bath with efficient stirring. Using a syringe equipped with a wide-bore needle, 5 mL of this precursor mixture is added dropwise over 6-8 minutes to a crude nanocrystal synthesis mixture prepared as described above and held at 220 °C. The reaction mixture is allowed to react for 30 minutes before further dropwise additions. This cycle is repeated until the desired nanocrystal size has been reached.

*1.6.9. Isolation of CdTe Nanocrystals with Low $Cd(O_2CR)_2$ Coverage*

A solution of TMEDA in toluene (82.5 mM, 9.3 or 50.0 μL) is added to a stock solution of CdTe nanocrystals (500 μL, $[Cd(O_2CR)_2]$ = 14.4 mM) and stirred

for 1 h. Nanocrystals are isolated by precipitation using methyl acetate and centrifugation. The dark precipitate is dissolved in 1 mL of toluene and isolated by precipitation and centrifugation two additional times. The nanocrystals are then dissolved in toluene, dried under vacuum, and characterized by $^{1}$H NMR, UV-visible, and photoluminescence spectroscopies.

*1.6.10. NMR and UV-Vis Kinetics*

The procedure for CdTe nanocrystal synthesis is carried out at twice the concentration described above. Aliquots (250 μL) are taken with a glass microliter syringe at 4, 10, 15, 20, 30, 60, and 150 minutes after turning on the heating mantle. A portion of this aliquot (200 μL) is added to an NMR tube containing benzene-$d_6$ (300 μL) and *n*-octylamine (100 μL) and used to monitor the concentration of diphenyl telluride co-product. The remainder of the aliquot (50 μL) is added to 2.45 mL of toluene for analysis with UV-visible absorbance spectroscopy and determination of [CdTe] and [nanocrystal] (see below).

*1.6.11. Disproportionation of $Cd(TePh)_2$ to CdTe and $Ph_2Te$ in Hexadecane*

In a glovebox, $Cd(TePh)_2$ (50 mg, 0.096 mmol) and hexadecane (10 mL) are added to a scintillation vial and capped with a rubber septum. The vessel is pierced with an argon inlet needle and the suspension heated to 220 °C under nitrogen for 150 minutes, at which point an aliquot (200 μL) is removed and

added to an NMR tube containing the final aliquot from a Kinetics reaction (see above). This aliquot is used as a $Ph_2Te$ standard;[29,30,53] the absence of any new resonances in the $^1H$ NMR spectrum of this tube is taken as evidence that $Ph_2Te$ is the aromatic co-product of the nanocrystal reaction. The reaction mixture is allowed to cool to room temperature and then centrifuged (7000 rpm, 5 minutes). The black pellet is resuspended in hexanes (5 mL) with sonication, re-centrifuged, and then collected for powder X-ray diffraction analysis.

*1.6.12. Measurement of the Ligand and Nanocrystal Concentration*

The concentrations of nanocrystals and cadmium carboxylate ligands in toluene-$d_8$ stock solutions are determined using a combination of NMR and UV−visible absorption spectroscopies. Ferrocene dissolved in toluene-$d_8$ (100 μL, 0.051 M) is added to a known volume of the nanocrystal stock solution and used as an internal standard. The concentration of ligands is determined relative to the internal standard by integrating the ligand vinyl and ferrocene resonances and normalizing the integrals by the appropriate number of hydrogens, respectively (2:10). In cases where the vinyl resonance has two overlapping components, the integrals of each are approximated by a two-Gaussian fit. The broader, more downfield resonance is considered "bound" and the sharper, more upfield resonance is considered "free." An example is shown in Figure 1.4.3. The molar concentration of CdTe nanocrystals in these stock solutions is determined by

diluting 10–30 μL to a known volume with toluene and measuring the absorbance at $\lambda$ = 410 nm.[39]

In some cases, these measurements were confirmed by dissolving a known mass of purified and dried nanocrystals in a known volume of benzene-$d_6$ or toluene-$d_8$ together with a ferrocene standard. The ratio of the vinyl and ferrocene resonances in the NMR spectrum was then used to determine the molar concentration of oleyl ligands and the mass fraction of cadmium oleate and cadmium telluride assuming that CdTe is the only other species contributing to the mass. These measurements are consistent with the ratios determined using the extinction coefficient within 10%.

*1.6.13. Energy-Dispersive X-Ray Spectroscopy*

Energy-dispersive X-ray spectroscopy was performed using a JEOL JEM-2100 TEM equipped with an Oxford X-Max$^N$ 80 mm$^2$ silicon drift detector. Dilute nanocrystal solutions were drop cast onto carbon-coated copper TEM grids (Ted Pella Product No. 01824) and allowed to dry. An accelerating voltage of 200 kV was used, and data were collected over 0.3 - 1 μm$^2$ areas. The L-series lines of Cd and Te were analyzed using Oxford AZtec software that relates intensity to concentration using element-specific "k factors" accounting for atomic weight, X-ray fluorescence, ionization cross-section, type of X-ray line, and detector efficiency. This allows for elemental ratio determination.

*1.6.14. Surface Site Density Calculations*

Values are reported in Table 1.4.2. Nanocrystal surface site density is estimated under the assumptions of 1) spherical nanocrystal shape, 2) equal distribution of {100} and {111} facets, 3) negligible surface reconstruction, 4) charge neutrality in the nanocrystal, and 5) each surface chalcogen site being bound at most by one cadmium carboxylate.

Because the {100} and {111} facets are polar, containing only cadmium or chalcogen atoms, but the overall nanocrystal is charge-neutral, we assume a 1:1 ratio of cadmium-rich facets to chalcogen-rich facets. Therefore, their surface atom densities per $nm^2$ are halved to give the chalcogen site density. The surface atom densities are then multiplied by the nanocrystal surface area to arrive at the number of surface chalcogen sites per nanocrystal. The percent of surface chalcogen sites occupied is the number of cadmium carboxylates per nanocrystal (measured by $^1H$ NMR and UV-vis spectroscopies) divided by the number of surface chalcogen sites per nanocrystal.

*1.6.15. Crystal, intensity collection, and refinement data for (TMEDA)Cd(TePh)$_2$.*

| Crystal size | 0.480 x 0.200 x 0.80 mm |
|---|---|
| Lattice | Monoclinic |
| Formula | $C_{18}H_{26}CdN_2Te_2$ |
| Formula weight | 638.01 |
| Space group | P2(1)/c |
| a (Å) | 13.0754(8) |
| b (Å) | 11.4619(7) |
| c (Å) | 15.1442(10) |
| $\alpha$ (deg.) | 90 |
| $\beta$ (deg.) | 112.3765(8) |
| $\gamma$ (deg.) | 90 |
| V (Å$^3$) | 2098.7(2) |
| Z | 4 |
| Temperature (K) | 130(2) |
| Radiation ($\lambda$, Å) | 0.71073 |
| $\varrho$ (calcd.) (g/cm$^3$) | 2.019 |
| $\mu$ (Mo K$\alpha$) (mm$^{-1}$) | 3.767 |
| $\Theta$ max (deg.) | 33.004 |
| No. of data collected | 36600 |
| No. of data | 7586 |
| No. of parameters | 212 |
| $R_1$ [$I > 2\sigma(I)$] | 0.0184 |
| $\omega R_2$ [$I > 2\sigma(I)$] | 0.0424 |
| $R_1$ [all data] | 0.0206 |
| $\omega R_2$ [all data] | 0.0432 |
| GOF | 1.105 |

## 1.7. References


(1) Martin, R. *MIT Technology Review*. March 3, 2016,.
(2) Wolden, C. A.; Kurtin, J.; Baxter, J. B.; Repins, I.; Shaheen, S. E.; Torvik, J. T.; Rockett, A. A.; Fthenakis, V. M.; Aydil, E. S. *J. Vac. Sci. Technol. Vac. Surf. Films* **2011**, *29* (3), 30801.
(3) Panthani, M. G.; Kurley, J. M.; Crisp, R. W.; Dietz, T. C.; Ezzyat, T.; Luther, J. M.; Talapin, D. V. *Nano Lett.* **2014**, *14* (2), 670.
(4) Crisp, R. W.; Panthani, M. G.; Rance, W. L.; Duenow, J. N.; Parilla, P. A.; Callahan, R.; Dabney, M. S.; Berry, J. J.; Talapin, D. V.; Luther, J. M. *ACS Nano* **2014**, *8* (9), 9063.
(5) Grecu, D.; Compaan, A. D. *Appl. Phys. Lett.* **1999**, *75* (3), 361.
(6) Li, C.; Wu, Y.; Poplawsky, J.; Pennycook, T. J.; Paudel, N.; Yin, W.; Haigh, S. J.; Oxley, M. P.; Lupini, A. R.; Al-Jassim, M.; Pennycook, S. J.; Yan, Y. *Phys. Rev. Lett.* **2014**, *112* (15).
(7) Wei, S.-H.; Zhang, S. B.; Zunger, A. *J. Appl. Phys.* **2000**, *87* (3), 1304.
(8) Yan, Y.; Albin, D.; Al-Jassim, M. M. *Appl. Phys. Lett.* **2001**, *78* (2), 171.
(9) Hendricks, M. P.; Cossairt, B. M.; Owen, J. S. *ACS Nano* **2012**, *6* (11), 10054.
(10) Hendricks, M. P.; Campos, M. P.; Cleveland, G. T.; Plante, I. J.-L.; Owen, J. S. *Science* **2015**, *348* (6240), 1226.
(11) Abe, S.; Čapek, R. K.; De Geyter, B.; Hens, Z. *ACS Nano* **2012**, *6* (1), 42.
(12) Abe, S.; Capek, R. K.; De Geyter, B.; Hens, Z. *ACS Nano* **2013**, *7* (2), 943.
(13) Guo, Y.; Alvarado, S. R.; Barclay, J. D.; Vela, J. *ACS Nano* **2013**, *7* (4), 3616.
(14) García-Rodríguez, R.; Hendricks, M. P.; Cossairt, B. M.; Liu, H.; Owen, J. S. *Chem. Mater.* **2013**, *25* (8), 1233.
(15) Zingaro, R. A. In *Organic Selenium and Tellurium Compounds (1986)*; Patai, S., Rappoport, Z., Eds.; John Wiley & Sons, Inc., 1986; pp 343–367.
(16) Lobana, T. S. In *Progress in Inorganic Chemistry*; Lippard, S. J., Ed.; John Wiley & Sons, Inc., 1989; pp 495–588.
(17) Zingaro, R. A.; Steeves, B. H.; Irgolic, K. *J. Organomet. Chem.* **1965**, *4* (4), 320.
(18) Zingaro, R. A. *J. Organomet. Chem.* **1963**, *1* (2), 200.
(19) Dean, P. A. W. *Can. J. Chem.* **1979**, *57* (7), 754.
(20) Zingaro, R. A.; McGlothin, R. E. *J. Chem. Eng. Data* **1963**, *8* (2), 226.
(21) Yu, W. W.; Wang, Y. A.; Peng, X. *Chem. Mater.* **2003**, *15* (22), 4300.
(22) Yang, Y. A.; Wu, H.; Williams, K. R.; Cao, Y. C. *Angew. Chem. Int. Ed.* **2005**, *44* (41), 6712.
(23) Kloper, V.; Osovsky, R.; Kolny-Olesiak, J.; Sashchiuk, A.; Lifshitz, E. *J. Phys. Chem. C* **2007**, *111* (28), 10336.
(24) Dorfs, D.; Franzl, T.; Osovsky, R.; Brumer, M.; Lifshitz, E.; Klar, T. A.; Eychmüller, A. *Small* **2008**, *4* (8), 1148.

(25) Murray, C. B.; Norris, D. J.; Bawendi, M. G. *J. Am. Chem. Soc.* **1993**, *115* (19), 8706.
(26) Stuczynski, S. M.; Brennan, J. G.; Steigerwald, M. L. *Inorg. Chem.* **1989**, *28* (25), 4431.
(27) Steigerwald, M. L.; Sprinkle, C. R. *Organometallics* **1988**, *7* (1), 245.
(28) Shen, H.; Wang, H.; Chen, X.; Niu, J. Z.; Xu, W.; Li, X. M.; Jiang, X.-D.; Du, Z.; Li, L. S. *Chem. Mater.* **2010**, *22* (16), 4756.
(29) Steigerwald, M. L.; Sprinkle, C. R. *J. Am. Chem. Soc.* **1987**, *109* (23), 7200.
(30) Brennan, J. G.; Siegrist, T.; Carroll, P. J.; Stuczynski, S. M.; Reynders, P.; Brus, L. E.; Steigerwald, M. L. *Chem. Mater.* **1990**, *2* (4), 403.
(31) Brennan, J. G.; Siegrist, T.; Carroll, P. J.; Stuczynski, S. M.; Brus, L. E.; Steigerwald, M. L. *J. Am. Chem. Soc.* **1989**, *111* (11), 4141.
(32) Craig, D.; Dance, I. G.; Garbutt, R. *Angew. Chem. Int. Ed. Engl.* **1986**, *25* (2), 165.
(33) Dance, I. G. *J. Am. Chem. Soc.* **1980**, *102* (10), 3445.
(34) Yosef, M.; Schaper, A. K.; Fröba, M.; Schlecht, S. *Inorg. Chem.* **2005**, *44* (16), 5890.
(35) Eichhöfer, A.; Jiang, J.-J.; Sommer, H.; Weigend, F.; Fuhr, O.; Fenske, D.; Su, C.-Y.; Buth, G. *Eur. J. Inorg. Chem.* **2010**, *2010* (3), 410.
(36) Yamago, S.; Yoshida, J. Organic tellurium compound, process for producing the same, living radical polymerization initiator, process for producing polymer with the same, and polymer. KR100708959B1, April 18, 2007.
(37) García-Rodríguez, R.; Liu, H. *J. Am. Chem. Soc.* **2014**, *136* (5), 1968.
(38) Dakternieks, D. *Aust. J. Chem.* **1982**, *35* (3), 469.
(39) Kamal, J. S.; Omari, A.; Van Hoecke, K.; Zhao, Q.; Vantomme, A.; Vanhaecke, F.; Capek, R. K.; Hens, Z. *J. Phys. Chem. C* **2012**, *116* (8), 5049.
(40) Yu, W. W.; Qu, L.; Guo, W.; Peng, X. *Chem. Mater.* **2003**, *15* (14), 2854.
(41) Anderson, N. C.; Hendricks, M. P.; Choi, J. J.; Owen, J. S. *J. Am. Chem. Soc.* **2013**, *135* (49), 18536.
(42) Bealing, C. R.; Baumgardner, W. J.; Choi, J. J.; Hanrath, T.; Hennig, R. G. *ACS Nano* **2012**, *6* (3), 2118.
(43) Zherebetskyy, D.; Scheele, M.; Zhang, Y.; Bronstein, N.; Thompson, C.; Britt, D.; Salmeron, M.; Alivisatos, P.; Wang, L.-W. *Science* **2014**, *344* (6190), 1380.
(44) Duke, C. B. *Chem. Rev.* **1996**, *96* (4), 1237.
(45) Manna, L.; Wang; Cingolani, R.; Alivisatos, A. P. *J. Phys. Chem. B* **2005**, *109* (13), 6183.
(46) Beecher, A. N.; Yang, X.; Palmer, J. H.; LaGrassa, A. L.; Juhas, P.; Billinge, S. J. L.; Owen, J. S. *J. Am. Chem. Soc.* **2014**, *136* (30), 10645.
(47) Morris-Cohen, A. J.; Frederick, M. T.; Lilly, G. D.; McArthur, E. A.; Weiss, E. A. *J. Phys. Chem. Lett.* **2010**, *1* (7), 1078.

(48) He, B.; Zhang, W. In *Handbook of Chalcogen Chemistry*; 2013; pp 180–231.
(49) Heath, J. R. *Chem. Soc. Rev.* **1998**, *27* (1), 65.
(50) Chen, O.; Chen, X.; Yang, Y.; Lynch, J.; Wu, H.; Zhuang, J.; Cao, Y. C. *Angew. Chem. Int. Ed.* **2008**, *47* (45), 8638.
(51) Anderson, N. C.; Owen, J. S. *Chem. Mater.* **2013**, *25* (1), 69.
(52) Tavasoli, E.; Guo, Y.; Kunal, P.; Grajeda, J.; Gerber, A.; Vela, J. *Chem. Mater.* **2012**, *24* (21), 4231.
(53) *The Chemistry of organic selenium and tellurium compounds*; Patai, S., Rappoport, Z., Eds.; The Chemistry of functional groups; Wiley: Chichester [Sussex] ; New York, 1986.

## CHAPTER 2. A Tunable Library of Substituted Thiourea Precursors to Metal Sulfide Nanocrystals

### Table of Contents

Reproduced in part from:

Hendricks, M. P.; Campos, M. P.; Cleveland, G. T.; Jen-La Plante, I.; Owen, J. S. *Science* **2015**, *348*, 1226.

Some of the experiments described herein were performed by M. P. Hendricks, G. T. Cleveland, and I. Jen-La Plante. Their collaboration in this endeavor is greatly acknowledged.

## 2.1. Abstract

### *2.1.1. Technical Abstract*

Controlling the number and size of crystallites formed in colloidal nanocrystal synthesis is essential to realizing their potential as extraordinary opto-electronic materials. The prevailing method of size control in the nanocrystal community achieves size control by terminating growth early or tuning surfactant concentrations. In this section, we demonstrate the use of substituted thioureas as a class of sulfur precursors to colloidal metal sulfide nanocrystals. The number of substituents and the electronic/steric character of each substituent is used to finely tune the solute supply rate, which in turn tunes the number of crystallites formed during nucleation. Since thioureas convert quantitatively to metal sulfide, this allows for exquisite size control at full yield without significantly altering the composition of the reaction mixture. Using PbS as a model system, we study this relationship quantitatively using *in situ* spectroscopic methods, optimize a multigram synthesis, and demonstrate the general utility of thiourea precursors for several other classes of nanocrystals.

### *2.1.2. Plain English Abstract*

Controlling the size of nanocrystals is crucial to their adoption as optical and electronic materials. Most methods stop nanocrystal synthesis reactions early

in order to achieve a certain size, which sacrifices yield. In this chapter, we demonstrate and exploit a relationship between the rate of precursor reaction and the number of crystals formed in order to control their size by changing only the reaction rate. We achieve this though a library of thiourea compounds whose organic fragments influence the reaction rate with a variety of metal precursors to form metal sulfide nanocrystals. From this concept we develop methods to prepare nanocrystals of many compositions, sizes, and shapes in 100% yields. This advance should accelerate the adoption of nanocrystals on industrial scales.

**2.2. Context**

Colloidal nanocrystals are inherently kinetic products; inorganic crystals have a strong thermodynamic driving force to form bulk crystal lattices. Thus, nanocrystal synthesis is a balancing act between rates. As it turns out, precursor conversion, nucleation, crystal growth, ripening/aggregation, and other side reactions are all critically important in determining the outcome of a given synthesis. Complicating matters further, these rates are almost always interrelated and have different dependences on factors like concentration, temperature, and solvent. In the following section, we will discuss several theoretical frameworks that describe experimental results reasonably well. In Chapter 4, however, we will discuss their limitations and inadequacies in greater depth.

*2.2.1. Theories of Nanocrystal Synthesis*

There have been several attempts to use theoretical models to describe nanocrystal synthesis by homogeneous nucleation, which can broadly be grouped into three approaches: 1) classical nucleation theory, the "physical" approach, 2) mass balance of solute in solution and in crystals, the "engineering" approach, and 3) a series of reversible polymerization reactions, the "chemical" approach.

Classical nucleation theory, based on the work of Gibbs,[1] Volmer,[2] and Becker and Döring,[3,4] and others, focuses on the change in free energy ($\Delta G$) of a system undergoing a phase change such as precipitation. The $\Delta G$ between solute and a solid particle can be broken down into contributions from the interior and the surface. Assuming a spherical particle, this relationship takes the form written in Equation 2.2.1 and depicted in Figure 2.2.1:

$$\Delta G = \frac{4}{3}\pi r^3 \phi + 4\pi r^2 \gamma$$

Equation 2.2.1

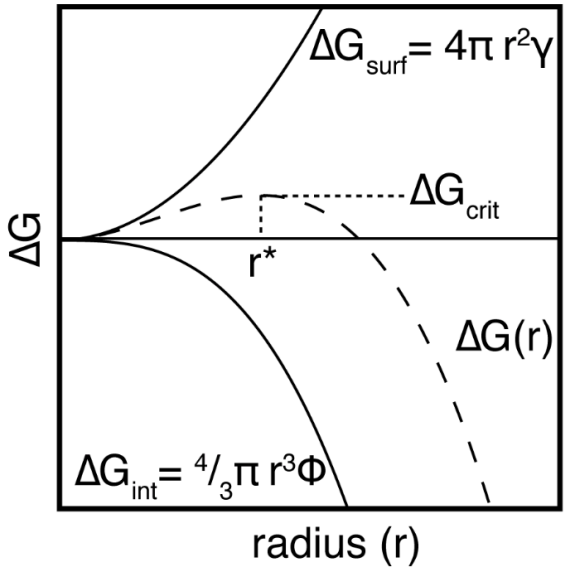


Figure 2.2.1. $\Delta G_{interior}$, $\Delta G_{surface}$, and $\Delta G$ as a function of particle radius.

The energy associated with the interior comprises the particle volume ($\frac{4}{3}\pi r^3$) times the energy change per unit volume ($\phi$), a negative quantity since crystallization is exothermic, and the energy associated with the surface comprises the particle surface ($4\pi r^2$) times the surface tension per unit area ($\gamma$), a positive quantity since surface formation is endothermic. Since the two terms oppose each other with volume dominating at large sizes, ΔG takes its maximum at:

$$\frac{d\Delta G}{dr} = 4\pi {r_{crit}}^2 \phi + 8\pi r_{crit} \gamma = 0$$

Equation 2.2.2

This critical radius, $r_{crit}$, is the minimum size of a stable nucleus. Below $r_{crit}$ crystallites tend to dissolve and above $r_{crit}$ crystallites tend to grow. The energy of the critical nucleus can be simplified as:

$$\Delta G_{crit} = \frac{4}{3}\pi\gamma r_{crit}^2$$

Equation 2.2.3

Given a statistical distribution of molecular velocities and local energies, the rate of nucleation $J$ can be expressed in terms of an Arrhenius rate equation commonly used to describe thermally activated processes:

$$J = Aexp\left(\frac{-\Delta G}{kT}\right)$$

Equation 2.2.4

where $A$ is an exponential pre-factor, $k$ is Boltzmann's constant and T is the temperature in Kelvin. In concert with the Gibbs-Thomson relationship between particle size and solubility,[5] the nucleation rate can be expressed as:

$$J = Aexp\left(-\frac{16\pi\gamma^3 V_M^3}{3k^3T^3(\ln(S))^2}\right)$$

Equation 2.2.5

where $V_M$ is the molar volume of crystalline material and $S$ is the supersaturation of solute. From this equation we can see that nucleation is sensitive to surface

tension, temperature, and supersaturation. Classical nucleation theory is a useful paradigm to understand nanocrystal synthesis, but it presently suffers from three key limitations. First is the fact that the sizes of critical nuclei predicted by this theory are often on the order of those observed in semiconductor nanocrystal synthesis,[6] casting doubt on the validity of the method. Second is the fact that this theory fails to provide insight into the distribution of particle sizes. Third is the difficulty in measuring and manipulating quantities such as $S$ and $\gamma$; in IV-VI and IV-VI nanocrystal syntheses, solute is highly reactive, its structure and solubility in surfactant media are not known, and the surface tension of few-nanometer crystallites is limited to speculation.

The mass balance approach addresses some of the issues of classical nucleation theory. First proposed by La Mer and Dinegar in 1950,[7] it envisions a three-phase process in which the solute concentration supersaturates (I) until it reaches a critical concentration at which nucleation takes place at a nearly infinite rate (II). The time spent in this phase defines the polydispersity of the ensemble, since the first nucleus formed spends more time growing than the last nucleus formed. The formation and growth of nuclei relieves the supersaturation until nucleation ceases and the existing nuclei continue to consume solute until its concentration reaches equilibrium (III).

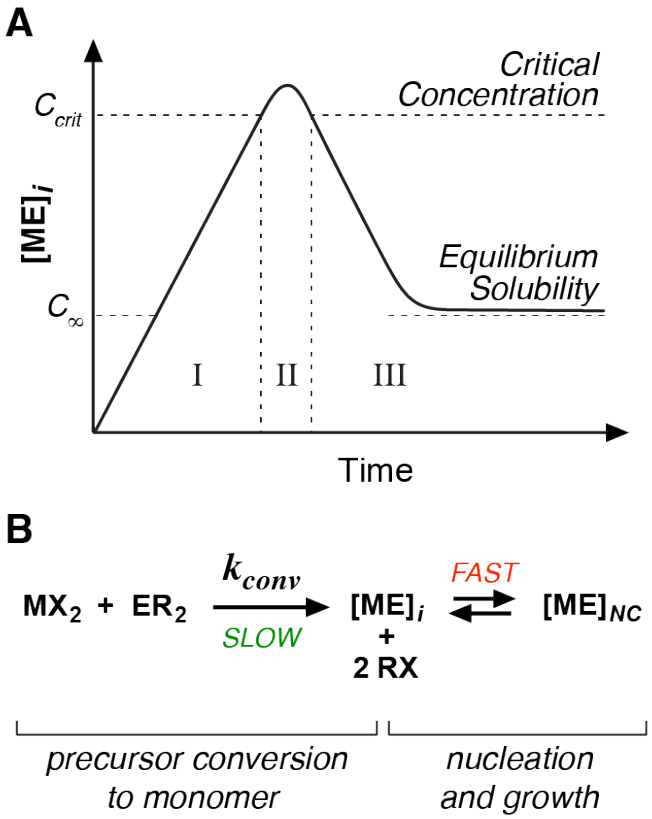


Figure 2.2.2. A) The Lamer modeling with its three stages; I = build-up of monomer concentration, II = burst nucleation, III = nanocrystal growth. B) Typical conversion of precursors in semiconductor nanocrystals. In a first step, the precursors convert slowly into monomers and in a second step, the monomers crystallize fast to form nanocrystals.

In the 1990s, Sugimoto added to this model by assuming that the solute concentration was constant during nucleation; any incremental solute produced during this step must be consumed by either nucleation or growth.[8–10]

$$Production = Consumption_{nucleation} + Consumption_{growth}$$

Equation 2.2.6

$$Q_0 V_M = v_0 \frac{dn}{dt} + \dot{v} n$$

Equation 2.2.7

Treating the growth rate per particle during nucleation ($\dot{v}$, $nm^3$ $sec^{-1}$) as a constant, Equation 2.2.6 can be rewritten as Equation 2.2.7, where $Q_0$ is the rate of solute production (mol $sec^{-1}$), $V_M$ is the molar volume of the solid ($nm^3$ $mol^{-1}$), $v_0$ is the volume of the initial stable nucleus, or critical nucleus ($nm^3$), $\frac{dn}{dt}$ is the rate of nucleus production ($sec^{-1}$), and $n$ is the number of stable particles (unitless). During nucleation, the nucleation rate ($J$ or $\frac{dn}{dt}$) rapidly increases and then decreases to zero, after which Equation 2.2.7 simplifies to:

$$Q_0 V_M = \dot{v} n$$

Equation 2.2.8

from which it is clear that greater numbers of crystals produced during nucleation lead to greater rates of consumption. It is this relationship that results in termination of nucleation. Rewriting Equation 2.2.8 as:

$$n = \frac{V_M}{\dot{v}} Q_o$$

Equation 2.2.9

It becomes clear that the number of crystals is dependent only upon material constants and the solute production rate, and surprisingly, not on the rate of nucleation, the size of the critical nucleus, or the duration of the nucleation phase. It also predicts a linear relationship between the solute production rate and the number of crystals, which Sugimoto first demonstrated through cleverly designed AgCl and AgBr nanocrystal syntheses, and which Owen and others have shown for CdSe.[11–13] Interestingly, in several of these cases, the number of crystals appears to plateau with increasing solute production rate; in Chapter 4 we will explore that relationship in depth.

The third, "chemical" approach is inspired by polymerization mechanisms. Following precursor conversion to solute, the solute undergoes nucleation and growth as proposed by La Mer, but these two steps comprise many discrete, reversible reactions, each with its own rate constant:

Scheme 2.2.1. A series of simplified reactions leading to nucleation.

$$[ME]_i + [ME]_i \underset{k_{-2}}{\overset{k_2}{\rightleftharpoons}} [ME]_2$$

$$[ME]_2 + [ME]_i \underset{k_{-3}}{\overset{k_3}{\rightleftharpoons}} [ME]_3$$

$$[ME]_{n-1} + [ME]_i \underset{k_{-n}}{\overset{k_n}{\rightleftharpoons}} [ME]_n \quad \text{(stable nucleus)}$$

This already complicated model omits many possible complications underlying nanocrystal synthesis, such as concentration dependence of the solute structure proposed in classical nucleation theory, solute-ligand interactions, and fusion of two nuclei, making it clear that a precise kinetic treatment of the underlying chemical reactions is effectively impossible. However, given that the vast majority of possible reactions are very similar and many of the reaction variables can be assumed constant, a model inspired by this approach is quite reasonable.

While these three models cover a wide range of possibilities, there are several factors they completely omit. These are 1) the existence of metastable cluster intermediates (covered in great depth elsewhere[14]), 2) precursor structure evolution during synthesis (e.g. cadmium oleate coordination polymer transitions from lamellar to micellular with increasing temperature[15]), and 3) the possibility of heterogeneous nucleation due to insoluble components or foreign particles in solution.

*2.2.2. Survey of Current Sulfide Precursors*

In order to realize any of these theoretical descriptions in metal sulfide nanocrystal synthesis, practical synthetic methods must be developed. To this end, several sulfide precursors have emerged:[16] 1) *bis*(trimethylsilyl)sulfide ($TMS_2S$), 2) tri-*n*-octylphosphine sulfide ($Oct_3PS$), 3) sulfur dissolved in 1-octadecene or oleylamine, 4) alkylthiols, 5) radical initiators, and 6) single-source precursors.

We will begin with $TMS_2S$. TMS groups are widely in organic synthesis in order to protect alcohols toward various reactions. Since the Si-O bond is quite strong, TMS groups are only cleaved by reaction with $F^-$ sources (since the Si-F bond is even stronger) or by acidic hydrolysis. However, since the Si-S bond is not particularly strong, $TMS_2S$ is an extremely reactive source of $S^{2-}$,[17] behaving essentially as a liquid version of $H_2S$ gas.

Upon exposure to metal complexes, $TMS_2S$ reacts rapidly and fully to form metal sulfide and silylated co-product (Scheme 2.2.2),[18] in many cases even below room temperature. While this reaction is highly efficient, its extreme reactivity presents problems in nanocrystal synthesis, which is almost always conducted at temperatures above 80 °C. When precursor reactivity is competitive with the rate of precursor injection, the solute concentration is continuously held at the critical concentration for nucleation, resulting in a long nucleation process,

a lack of distinction between nucleation and growth, and highly polydisperse nanocrystal samples.

Scheme 2.2.2. Nominal reaction of $TMS_2S$ with metal complexes.

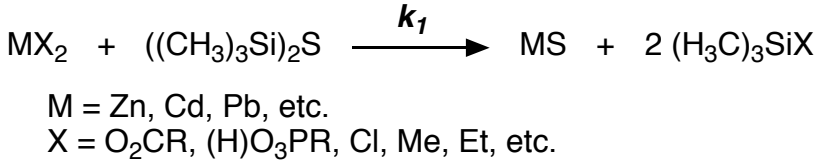


$TMS_2S$ is also highly sensitive to water and other protic impurities that may be present in the metal precursor or solvent. This leads to side reactions that produce $H_2S$, complicating the overall metal sulfide formation kinetics and synthetic results (Scheme 2.2.3). We will discuss these complications in greater detail in Section 2.4.

Scheme 2.2.3. Side reactions between $TMS_2S$ and protic impurities in PbS nanocrystal synthesis.

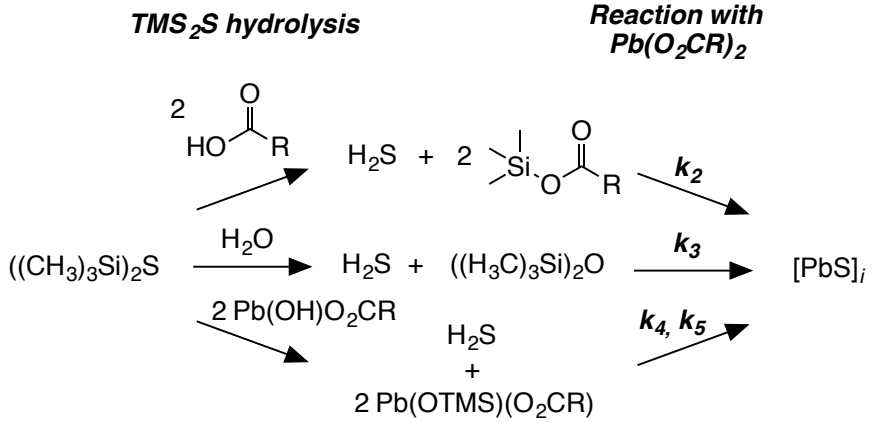


Given this extreme reactivity, and the wealth of knowledge that organic chemists have developed on myriad protecting groups and their rates of deprotection,[19] it

is somewhat surprising that the nanocrystal community has not developed alternative protecting groups to modulate reactivity while taking advantage of the quantitative reactivity of $TMS_2S$. The most likely reason for this is the lack of commercial availability of alternatives and difficult and hazardous synthesis. As a volatile source of sulfide that hydrolyzes to $H_2S$ in air and smells identical to a natural gas leak, $TMS_2S$ is extremely dangerous and prone to evacuating areas of several city blocks. This seems fairly forgivable.

The second major precursor is $Oct_3PS$, which is prepared by simply oxidizing trioctylphosphine with sulfur powder either neat or in solution (Scheme 2.2.4). Although trioctylphosphine is used almost exclusively in the nanocrystal community, this reaction is quite general to many phosphines and phosphites.[20]

Scheme 2.2.4. Synthesis of phosphine sulfides.

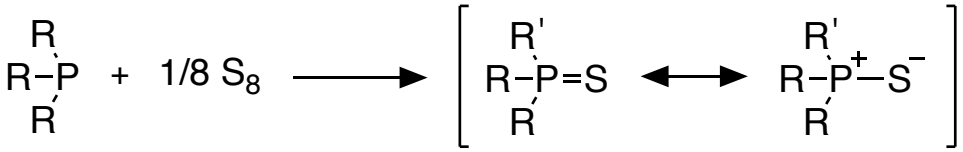


R = alkyl, aryl, alkoxy, aryloxy, dialkylamino, H, etc.

When it comes to nanocrystal synthesis, $Oct_3PS$ turns out to be orders of magnitude less reactive than $TMS_2S$, reacting sluggishly with metal complexes until relatively high temperatures and giving low yields. Careful studies on the reactivity of phosphine chalcogenides have established likely mechanisms for

conversion, based on observed co-products (Scheme 2.2.5). Moreover, these studies show that the presence of secondary phosphine impurities and adventitious water tend to accelerate conversion rates, explaining long-standing synthetic irreproducibilities.[16,21–23] Notably, $Oct_3PSe$ approaches 70-80% conversion under anhydrous conditions but reaches ~100% conversion in the presence of added water.[21] Thus, while phosphine sulfides have been instrumental to advancing nanocrystal science, they will remain unfortunately impractical at larger scales.

Scheme 2.2.5. Reaction between phosphine chalcogenide and metal carboxylate (top) or metal hydrogen phosphonate (bottom).

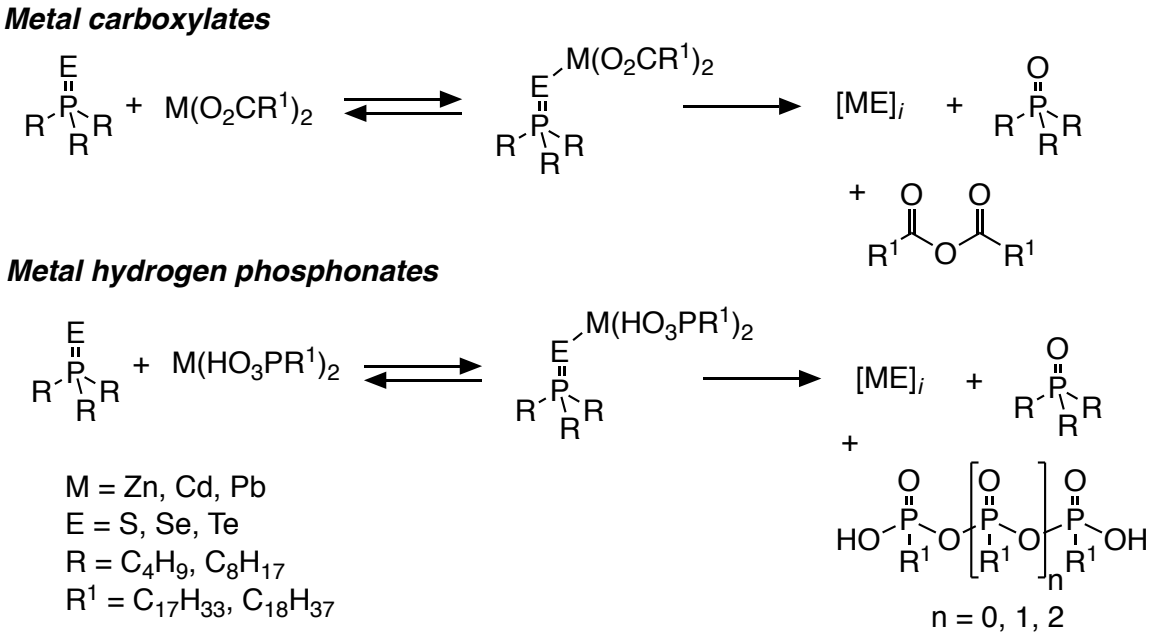

Sulfur dissolved in 1-octadecene and/or oleylamine has emerged as another popular precursor system because of its intermediate, somewhat tunable reactivity in the synthesis of PbS and CdS nanocrystals.[24–33] Because it employs elemental sulfur, it is sometimes referred to as a green, atom-economical precursor. However, this perspective is overly simplistic. Elemental sulfur is only slightly soluble in organic solvents,[34] but it is known to carry out unselective radical oxidations on a wide range of organic molecules, liberating ill-defined and time-dependent mixtures of $H_2S$, hydrosulfides, polysulfides, thiophenes, and other products (Scheme 2.2.6, Table 2.2.1).[16,35,36] One published synthesis was even conducted in commercial olive oil, which is primarily oleic acid and its glycerides.[37,38]

Scheme 2.2.6. Reaction of sulfur with alkenes.

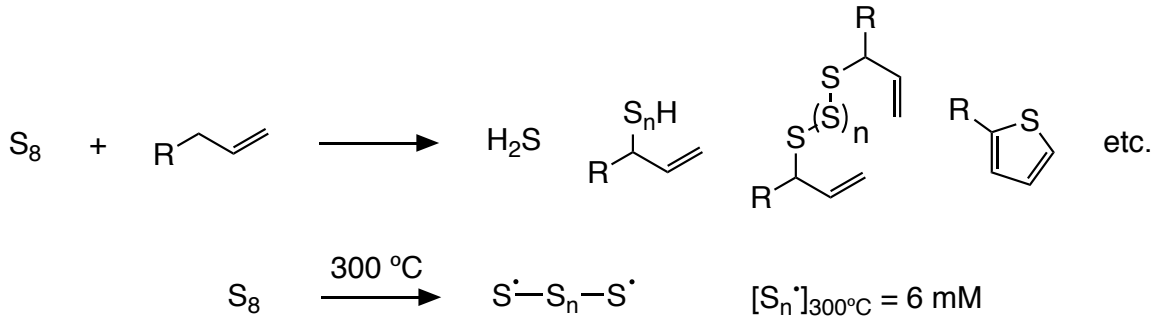


Table 2.2.1. Yield of $H_2S$ from reaction between sulfur and various solvents at 250 °C.[35]

| Compound | Yield (%) |
|---|---|
| Liquid paraffin | 79 |

| | |
|---|---|
| Hexadecylamine | 73 |
| Stearic acid | 64 |
| Trioctylphosphine oxide | 54 |
| Oleic acid | 10 |
| Sunflower-seed oil | 9 |
| 1-Octadecene | 6 |

This process is known to the rubber industry as vulcanization, and while there have been some efforts to quantify $H_2S$ formation in various solvents,[35] the complex underlying chemistry and kinetics lead to complicated nanocrystal reactions. Thus we must come to a similar conclusion as in the case of phosphine sulfides – sulfur dissolution is an interesting method, but after many studies still poorly understood.

Alkylthiols have also been used as sulfide precursors, although primarily for the purpose of CdS shell growth.[39,40] These are intriguing compounds since there are many commercial derivatives available in high purity and in their deprotonated thiolate form they are known to bind nanocrystal surfaces.[41–46] Their primary mode of reaction is most likely a two-step process involving proton-mediated displacement of carboxylic acid from a metal carboxylate followed by a unimolecular disproportionation to metal sulfide and dialkyl sulfide (Scheme 2.2.7). This process is likely sensitive to hard-soft matches between metal, thiolate, and carboxylate, as well as acidities ($pK_{a,DMSO}(CH_3CO_2H)$

= 12.6; $pK_{a,DMSO}(C_4H_9SH)$ = 17.0), but $pK_a$s measured in polar solvents like water, DMSO, and acetonitrile are likely poor representations of their behavior in nanocrystal reaction mixtures. In this kind of nonpolar solution, carboxylic acid dimerization, ion-pairing, and anion complexation can take place, complicating the relevant acidities.

Scheme 2.2.7. Reaction between cadmium carboxylates and alkylthiols.

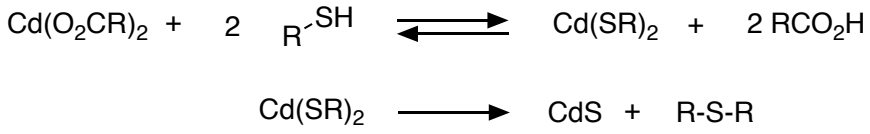


However, their extent of conversion has not been carefully measured and their presence as surface ligands is known to lead to photochemical instability in final nanocrystals.[42,45]

Lastly, there are several "single-source precursors" containing both metal and sulfur that have found use as nanocrystal precursors. Like many good ideas in nanocrystal synthesis, single-source precursors began with Steigerwald and coworkers, who showed that zinc, cadmium, and mercury arylthiolate complexes converted to metal sulfides at mild temperatures.[47] O'Brien and coworkers greatly expanded the range of single-source precursors to metal sulfide-based nanocrystals through his work on cadmium dialkyldithiocarbamates.[48–51]

*2.2.3. Motivation for a Precursor Library*

While these precursors have led to the synthesis of a variety of monodisperse nanocrystal samples, it has been mostly through trial and error that nanocrystal synthesis has advanced. This is because, as mentioned above, nanocrystal synthesis is a delicate balance between rates with different dependences on concentration, temperature, solute, etc., such that traditional points of control in chemical reactions lead to complex changes.

One way to reduce this complexity is to identify levers changing one variable completely independently of all others. We and others identified that if there were a way to tune the rate of precursor conversion through organic substituent modification, it would be minimally disruptive to the crystallization medium and perhaps reduce the study of nanocrystal synthesis to a single variable at a time. This would lead to a conceptual departure from the tradition of blind attempts at reaction optimization across many variables.

*2.2.4. Previous Efforts Toward Precursor Libraries*

There have been notable efforts to build tunable libraries of 1) phosphine chalcogenide and 2) dichalcogenide precursors. Vela and coworkers have published several studies on various phosphine chalcogenides in CdS synthesis, demonstrating an ability to influence nanorod shape and S/Se composition with phosphine sulfides and selenides of different reactivities.[52] This class is

particularly interesting since phosphine synthesis and coordination chemistry is well understood and easily studied by $^{31}P$ NMR and crystallography. In a recent study, they further quantified properties of phosphine, phosphite, and aminophosphine chalcogenides using DFT and NMR.[20] While they measure values such as P-S/P-Se bond lengths, $^{31}P$-$^{77}Se$ NMR coupling constants and Tolman cone angles, the major value they quantify is P-S/P-Se bond dissociation energy (BDE). Qualitatively, BDE seems to track with reactivity, but it is not clear what insight BDE provides into the mechanism of reaction. BDE describes homolytic P-E dissociation, which does not take place in the mechanisms established in Scheme 2.2.5. Perhaps most importantly, their system of choice fails demonstrate a general, high-quality application of the precursor tuning approach.

Scheme 2.2.8. Homolytic dissociation of phosphine sulfide assuming a P-S bond order of 2.

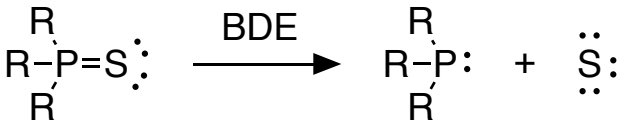


Teams led by Brutchey and Vela have also explored tunable dichalcogenide (RE-ER) precursors to metal chalcogenide nanocrystals, demonstrating syntheses of CdSe, CdS, ZnSe, $Cu_{2-x}S_ySe_{1-y}$, $CuInS_2$, $CuInSe_2$, $Cu_2ZnSn(S_{1-x}Se_x)_4$, $Cu_2SnSe_3$, $In_2S_3$, $Sn_xGe_{1-x}Se$, SnTe, $MoSe_2$, $WSe_2$, BiSe, $CuFeS_2$,

$In_2O_3$, and somewhat shape-tunable CdS nanocrystals.[53,54] A range of dialkyl and diaryl disulfides are commercially available and many more can be synthesized by oxidative dimerization of thiols, making them readily tunable and somewhat practical if you're willing to work with thiols. However, the mechanism of action and effects of substituent tuning remain unclear despite computational and experimental approaches.

**2.3. Thioureas**

In 2013, Mark Hendricks in our group set out to design a new class of sulfide precursors that would combine tunability, full conversion, safety, and easy synthetic accessibility. He arrived at substituted thioureas as an intriguing option – they had been used to precipitate bulk and nanocrystalline metal sulfides (primarily in polar/aqueous solution),[55,56] they are easily synthesized in one step (Scheme 2.3.1), and there are many well-studied derivatives, including a host of prominent Brønsted acid organocatalysts and ligands for metals.[57–59] In this section I will discuss their synthesis, structural characteristics, reactivity, and industrial uses.

*2.3.1. Synthesis of a Library*

There are seven major methods for thiourea synthesis, as shown in Scheme 2.3.1. Given the structural diversity possible among up to four R groups

with possible ring closure, each method may be preferable given certain synthetic requirements.

Scheme 2.3.1. Synthetic routes to thioureas.[55]

***1) Isothiocyanates + amines***

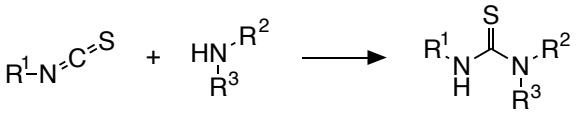

***2) Anilines + $CS_2$***

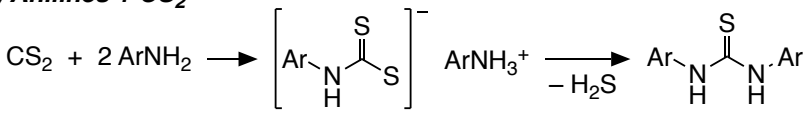

***3) Amines + thiophosgene***

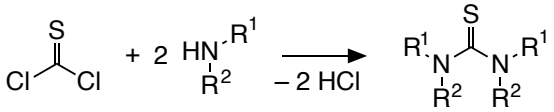

***4) Ammonium thiocyanate decomposition***

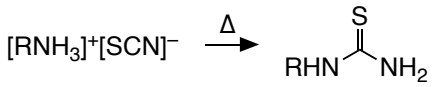

***5) Cyanamides + $H_2S$ equivalent***

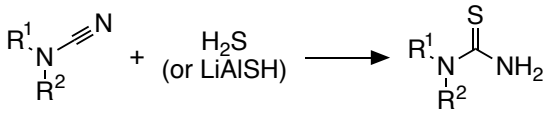

***6) Sulfurization of ureas***

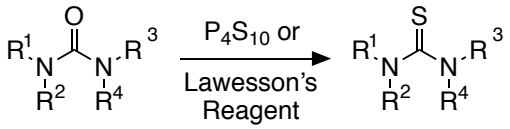

***7) Diamines + thiourea***

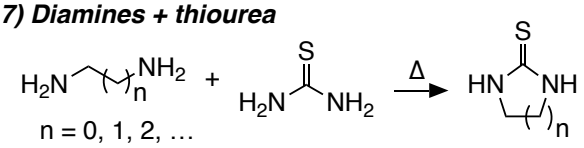

In this chapter we rely heavily upon the reaction between amines and isothiocyanates, since 1) it is an atom-economical "click" reaction, 2) we estimate $10^3$-$10^4$ di- and trisubstituted derivatives are accessible in a single step from

commercial amines and isothiocyanates, 3) it goes to quantitative yield, 4) it is easily scalable to > 30 g quantities using standard laboratory glassware, and 5) the resultant thiourea doesn't require purification. In most permutations of this reaction, the electrophilicity of the isothiocyanate *sp* carbon makes this reaction rapid at room temperature in solvents as polar as methanol and as non polar as hexane. Notably, however, there is a threshold of amine nucleophilicity and isothiocyanate electrophilicity to be met. For example, **4** can be prepared from hexylamine and phenyl isothiocyanate, but aniline and hexyl isothiocyanate react too slowly to be practical. Nonetheless, after minimal optimization, we arrived at the following library of thioureas **1**-**11** for metal sulfide nanocrystal synthesis (

Table 2.3.1), which includes *N*,*N*′-diarylthioureas (**1**, **2**), *N*,*N*′-dialkylthioureas (**5**-**8**), mixed *N*-alkyl-*N*′-arylthioureas (**3a**-**3f**), *N*,*N*,*N*′-trialkylthioureas (**9**, **10**), and *N*′-alkyl-*N*,*N*-diarylthioureas (**11**).

Table 2.3.1. Table of di- and trisubstituted thiourea precursor structures.

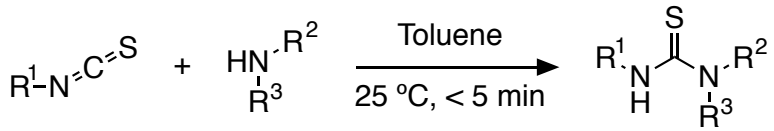


***> 95% yield***

| Compound | $R^1$ | $R^2$ | $R^3$ |
|---|---|---|---|
| **1** | 3,5-$(CF_3)_2$-Ph | Ph | H |
| **2** | Ph | Ph | " |
| **3a** | 4-CN-Ph | $C_{12}H_{25}$ | " |
| **3b** | 4-$CF_3$-Ph | " | " |
| **3c** | 4-Cl-Ph | " | " |
| **3d** | Ph | " | " |
| **3e** | 4-Me-Ph | " | " |
| **3f** | 4-MeO-Ph | " | " |
| **4** | Ph | $C_6H_{13}$ | " |
| **5** | $^t$Bu | $C_{12}H_{25}$ | " |
| **6** | $^i$Pr | " | " |
| **7** | Cyclohexyl | " | " |
| **8** | $C_6H_{13}$ | " | " |
| **9** | " | $C_4H_9$ | $C_4H_9$ |
| **10** | " | $C_8H_{17}$ | $C_8H_{17}$ |
| **11** | Ph | $C_4H_9$ | $C_4H_9$ |

*2.3.2. Characteristics and Reactivity*

Thiourea is a colorless, crystalline, odorless solid that is soluble in protic and polar aprotic solvents but insoluble in nonpolar solvents. Because of conjugation throughout the molecule's $sp^2$ core, thioureas have several important resonance structures and tautomers that inform their reactivity.[55]

Scheme 2.3.2. Thione-thiol tautomerism (left) and resonance (right) in thiourea.

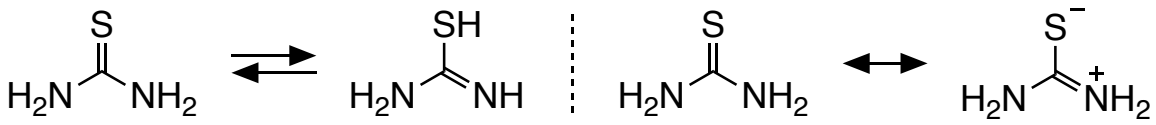

Thus, thioureas combine elements of reactivity commonly observed among amines, imines, thiones, and thiols, and can be activated at either amino group or the thione. This multifunctionality makes them amenable to multi-step reactions and cyclizations. Thioureas are also mildly acidic ($pK_{a,DMSO}$(thiourea) = 21.0; $pK_{a,DMSO}$(**2**) = 13.5),[60] and under basic conditions thiourea is hydrolyzed to cyanamide.[61] In Section ,2.5, we will show in greater detail that careful tuning of thiourea acidity via substituent modification has large impacts on nanocrystal synthesis. Various organic methodologies have taken advantage of this acidity and thioureas' wide R-group tunability to carry out enantioselective hydrogen bond catalysis.[58,59]

Thiourea is on the safer end of the spectrum of organosulfur compounds, with reported $LD_{50}$ levels between 1,000 and 10,000 mg/kg and limited toxicity, and mutagenicity, although it is a suspected carcinogen. In humans, most thiourea is excreted unchanged in the urine. However, N-phenyl derivatives and imidazolidine-2-thiones are known toxins with $LD_{50}$ values in the range of 0.5-5 mg/kg.[55]

*2.3.3. Industrial Uses*

Substituted thioureas have found industrial use as vulcanization accelerators, pharmaceuticals, and pesticides. Vulcanization accelerators are typically simple N,N'-dialkylthioureas, **2**, or imidazolidine-2-thiones and apply to Neoprene and ethylene-propylene-diene terpolymers.[62] Thiourea-based pharmaceuticals have much greater structural variety, but tend to be useful as thyrotheraputic, antiseptic, anti-infective, and narcotic agents.[55] Thiourea pesticides all have one highly substituted N-phenyl substituent, finding use as insecticides and fungicides.[55] Given these varied uses at scale, it is encouraging to the present study on nanocrystal precursors to know that there is already industrial knowledge and infrastructure devoted to thiourea production.

**2.4. Synthesis of Lead(II) Oleate**

Throughout the metal chalcogenide nanocrystal literature, much less attention has been paid to the metal size of the equation because of its perceived simplicity. However, simplicity could not be further from the truth. In this section, we will several under-appreciated pitfalls in metal carboxylate synthesis through the lens of our efforts to update the synthesis of lead(II) oleate. While the focus of this section is on lead, these problems likely apply to other metals including cadmium, zinc, and indium, as well as other surfactant systems including phosphonates and straight-chain carboxylates.

*2.4.1. Importance and Problems with Traditional Methods*

Long-chain lead(II) carboxylates ($Pb(O_2CR)_2$) are coordination polymers with low solubility at room temperature. This arises from their lamellar structure directed by alkyl chain packing that gives way to form micellular structures in solution at elevated temperature (see Chapter 4). Interestingly, the stereochemically active $6s^2$ lone pair in lead(II) complexes leads to voids in the coordination sphere of short-chain $Pb(O_2CR)_2$, while longer-chain analogues show isotropic coordination.[63] The longest-chain example that has been studied crystallographically, lead(II) nonanoate, is shown in Figure 2.4.1.

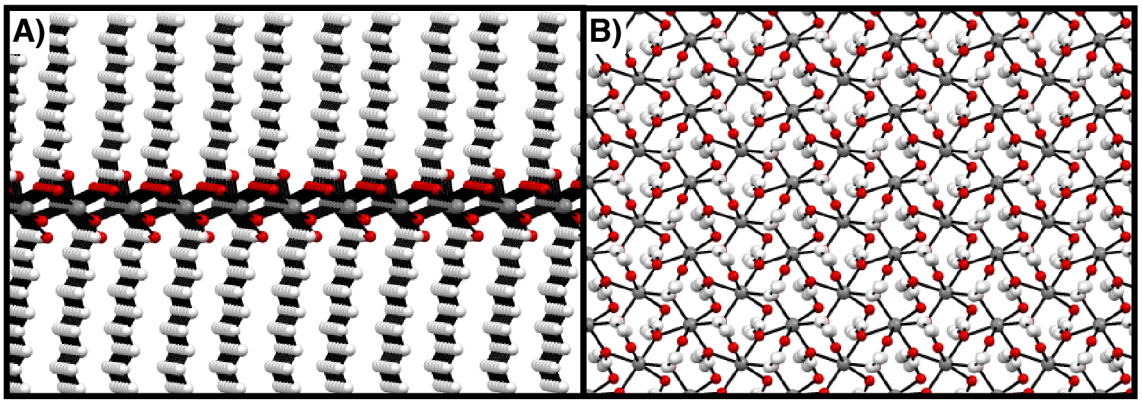


Figure 2.4.1. Lamellar structure of lead(II) nonanoate viewed down the A) b-axis and B) a-axis. Atoms are plotted at the 50% probability level. Pb atoms are gray, O atoms are red, and C atoms are white. Hydrogens are omitted for clarity.[63]

In nanocrystal synthesis, $Pb(O_2CR)_2$ ($R = C_{17}H_{33}$) is typically prepared by the reaction of PbO or $Pb(OAc)_2 \bullet 3H_2O$ with excess oleic acid in 1-octadecene at approximately 100 °C under vacuum. PbO and $Pb(OAc)_2 \bullet 3H_2O$ are insoluble, so

the reaction is considered complete upon dissolution of the solids, and the solution is considered anhydrous because of the reduced pressure. Since this reaction is conducted in situ immediately before injection of the chalcogen precursor, the resulting $Pb(O_2CR)_2$ is only rarely characterized by infrared spectroscopy, and almost never isolated and characterized by NMR spectroscopy and elemental analysis.

Scheme 2.4.1. In situ synthesis and hydroxylation of $Pb(O_2CR)_2$ from A) PbO and B) $Pb(OAc)_2 \bullet 3H_2O$.

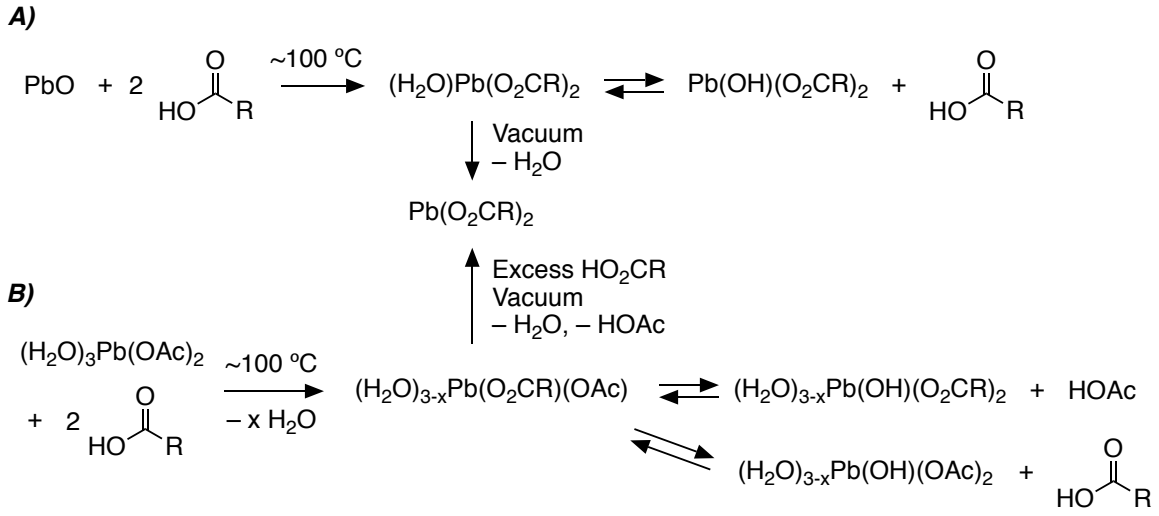


Two notable studies have shown that this approach is incomplete. Zherebetskyy et al. used density functional theory to argue that residual water from PbO coordinates to lead(II) even at high temperature under reduced pressure, and correlated state of hydration with more spherical PbS nanocrystal shapes.[64] Houtepen et al. showed that residual acetate from $Pb(OAc)_2$ leads to irregular star-shaped PbSe nanocrystals.[65] Given the small (if any) difference in

acidity between oleic and acetic acid, residual acetate is highly likely to persist in the absence of a large excess of oleic acid. These data paint a complicated picture of in situ $Pb(O_2CR)_2$ synthesis (Scheme 2.4.1) that is dependent upon non-standard reaction times, temperatures, concentrations, vacuum strengths, and reagent purities. These complications, in addition to difficulties with chalcogen precursors detailed in Section 2.2.2, have led PbE nanocrystal synthesis to be notoriously difficult to reproduce. In this section we will focus on PbS, but as we will discuss in Chapter 3, this is even more problematic for PbSe.

*2.4.2. Generation I: Synthesis from $Pb(NO_3)_2$*

We decided to approach $Pb(O_2CR)_2$ synthesis by synthesizing and isolating pure material before use in nanocrystal synthesis. Our first strategy was a salt-exchange between lead(II) nitrate and sodium oleate (Scheme 2.4.2) modeled after the standard $Cd(O_2CR)_2$ synthesis described by Chen et al.[66] and used in Chapter 1 as well as much of our group's other work.[67–72]

Scheme 2.4.2. Synthesis of lead(II) oleate from $Pb(NO_3)_2$.

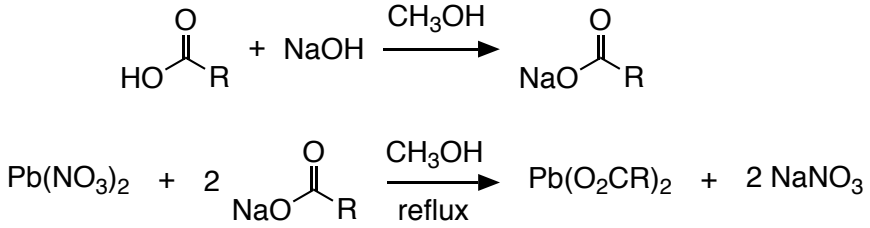

This approach afforded analytically pure lead(II) oleate as characterized by $^{1}H$ NMR spectroscopy, FTIR spectroscopy, CHN analysis, and mass analysis following cleavage by trimethylsilyl chloride. However, three major issues remained. First was the formation of an unknown yellow oil upon addition of $Pb(NO_3)_2$ from which the solution must be decanted. Second was the low solubility of $Pb(NO_3)_2$ in methanol, leading to large reaction volumes and the potential for incomplete removal of $Pb(NO_3)_2$ by filtration and methanol washes. Third was the low yield (25 – 50%) of lead(II) oleate, affording 7.8 – 15.6 g from reaction volumes of ~2.5 L and necessitating frequent synthesis.

*2.4.3. Generation II: Synthesis from PbO via $Pb(BF_4)_2$*

In order to intensify this process, we sought to identify lead(II) salts that would be more soluble in organic solvents. $Pb(BF_4)_2$ was a promising candidate given reports of its use in solvents like methanol and dimethylformamide[73] and its solubility in water of up to 50% by mass.[74,75]

Scheme 2.4.3. Synthesis of lead(II) oleate from PbO via $Pb(BF_4)_2$.

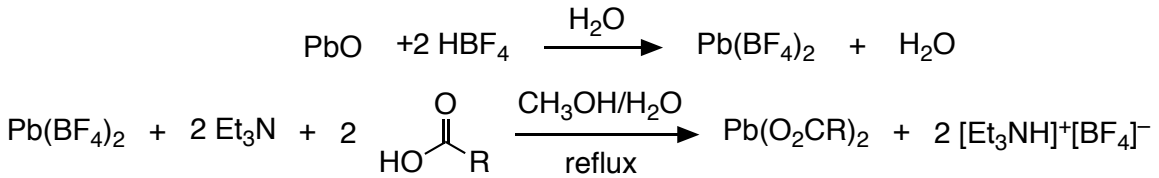


However, the isolated material produced by this reaction did not fully dissolve in hot toluene, indicating the presence of polar impurities. Upon further

investigation, it became clear that while $Pb(BF_4)_2$ had remained soluble in 1:1 $H_2O$/methanol solutions, it precipitated from $H_2O$/methanol solutions containing high concentrations of nonpolar compounds such as oleic acid. Thus, it became clear that this was an unsuitable synthesis.

*2.4.4. Generation III: Synthesis from PbO via $Pb(O_2CCF_3)_2$*

After going back to the drawing board, we hypothesized that lead(II) trifluoroacetate ($Pb(O_2CCF_3)_2$) could be an ideal source of lead(II). First, the analogous $Pb(OAc)_2$ is known to be soluble in methanol, ethanol, glycerol, and formic acid,[76,77] so it seemed reasonable that $Pb(O_2CCF_3)_2$ might be as well. Second, it should be possible to prepare $Pb(O_2CCF_3)_2$ cleanly from PbO since trifluoroacetic acid is much stronger than alkylcarboxylic acids ($pK_{a,DMSO}(CF_3CO_2H)$ = 0.31; $pK_{a,DMSO}(CH_3CO_2H)$ = 12.6),[78,79] and trifluoroacetic anhydride is an even more powerful Lewis acid. Third, both trifluoroacetic acid and anhydride are inexpensive commodity chemicals available in high purity from many suppliers. Fourth, it should be convenient to quantify purity using $^{19}F$ NMR spectroscopy to identify any residual trifluoroacetate anion.

Scheme 2.4.4. Synthesis of lead(II) oleate from PbO via $Pb(O_2CCF)_2$.

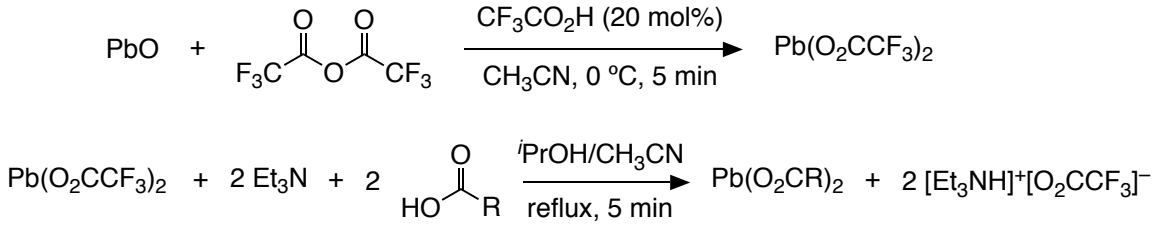


These hypotheses were all confirmed, and after optimization we were able to synthesize lead(II) oleate from $Pb(O_2CCF_3)_2$ in 90-95% yields, with < 0.1% $^-O_2CCF_3$ impurity (measured vs. $C_6F_6$ internal standard), and at up to 96 g scale in a volume of ~750 mL, according to the reactions shown in Scheme 2.4.4. The inclusion of a catalytic amount of trifluoroacetic acid increased the rate of reaction relative to the anhydride-only reaction, though the amount of acid was not carefully isolated. We also attempted this reaction in neat acid/anhydride, but encountered mixing and solidification issues as $Pb(O_2CCF_3)_2$ accumulated. By $^1H$, $^{13}C$, and $^{19}F$ NMR spectroscopies, FTIR spectroscopy, CHN analysis, and tests in nanocrystal syntheses, it is indistinguishable from lead(II) oleate prepared from $Pb(NO_3)_2$. In particular, an FTIR spectrum shows the absence of water/hydroxide impurities (3100-3700 $cm^{-1}$) or residual solvents (Figure 2.4.2). This is the first large-scale synthesis of lead(II) oleate ever reported and the first quantification of its purity.

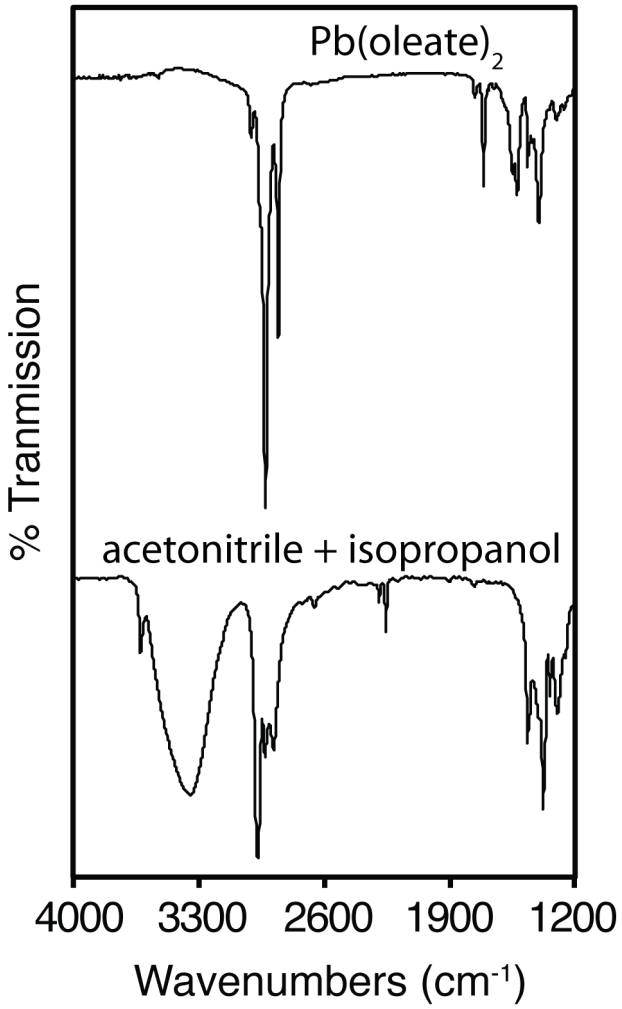


Figure 2.4.2. FTIR spectrum of lead(II) oleate (top) and synthesis reaction solvents (bottom) acquired in a liquid cell by dissolving the compounds in tetrachloroethylene.

There are several notes worth mentioning regarding this synthesis. First, the order of reagent addition during synthesis is important. In particular, it is important to neutralize oleic acid with a slight excess of triethylamine prior to its addition to the $Pb(O_2CCF_3)_2$-containing reaction mixture. If oleic acid is added in the absence of a base, a rapid reaction takes place and a deep red color develops.

This is likely because the $Pb(O_2CCF_3)_2$ solution retains the 20 mol% trifluoroacetic acid used as a catalyst. Trifluoroacetic acid is known to react with Z-alkenes,[80] although the specific source of the color in our case is unknown.

Second, the purity of PbO is important. While 99.9995% purity PbO from Alfa Aesar is a bright canary yellow color and dissolves cleanly in trifluoroacetic anhydride solution, ≥ 99.0% PbO from Sigma Aldrich is orange and leaves a colored residue in trifluoroacetic anhydride solution. This may arise from three sources. The first possibility is that the orange material is a mixture of the massicot (yellow) and litharge (red) phases of PbO, the latter of which is more stable at room temperature,[81] presenting a kinetic barrier to dissolution. The second possibility is that the orange material is contaminated by Pb(IV), since higher oxides of lead are known to take on deeper colors ranging from red to dark brown.[81] The third possibility is that the ppm-level contamination of metals like Ag, Cu, Fe, Ca listed on the product page for ≥ 99.0% PbO[82] impart deeper color.

Table 2.4.1. Grades and colors of various oxides of lead.

| Compound | Pb oxidation state | Supplier, purity | Color |
|---|---|---|---|
| PbO | 2+ | Strem, 99.999+% | Yellow |
| PbO | 2+ | Alfa Aesar, 99.9995% | Yellow |
| PbO | 2+ | Sigma Aldrich, ≥99.0% | Orange |
| PbO (massicot) | 2+ | Single crystal[81] | Yellow |

| | | | |
|---|---|---|---|
| PbO (litharge) | 2+ | Single crystal[81] | Red |
| $Pb_{12}O_{19}$ | 2+, 4+ | Single crystal[81] | Dark brown/black |
| $Pb_2O_3$ | 2+, 4+ | Single crystal[81] | Black |
| $Pb_3O_4$ | 2+, 4+ | Sigma Aldrich, 99.99% | Red |
| $PbO_2$ | 4+ | Strem, 97+% | Dark red-brown |

Any of these possibilities is alarming not only because of the visibly different reactivity of this starting material, but especially because most in situ syntheses of lead(II) oleate for nanocrystal synthesis begin with ≥ 99.0% PbO. At best, this means that numerous inert metal ion or particulate contaminants are left in solution during nanocrystal synthesis. At worst, this could mean that all reported PbS nanocrystal samples are heterogeneous reactions whose products are doped with Pb(IV) and transition metal ions. This would with downstream impacts on solar cells and other PbS nanocrystal devices where dopants levels are critically important.

## 2.5. Synthesis of PbS Nanocrystals

### *2.5.1. Synthesis and Basic Characterization*

Upon reacting lead(II) oleate (synthesized from $Pb(O_2CCF_3)_2$) with substituted thioureas it became clear that 1) thioureas are efficient precursors to monodisperse PbS nanocrystals and 2) the thiourea substituents influence the rate of reaction and final nanocrystal size. Upon injection of a substituted

thiourea into a solution of a slight excess of lead(II) oleate (1.2 – 1.5 equiv), the solution turns a deep brown color following a short induction period during which the solution is colorless. This induction period represents the buildup of $[PbS]_i$ solute prior to nucleation (discussed in greater detail in Chapter 4), and the onset of color represents PbS crystallite nucleation. At completion of the reaction, UV-vis-NIR absorbance spectroscopy of an aliquot removed from the reaction shows a quantitative yield of PbS nanocrystals according to published extinction coefficients at $\lambda$ = 400 nm, where absorbance is proportional to the concentration of crystalline PbS formula units.[83] This quantitative yield is consistent across all thioureas studied. This leads us to assign the conversion and crystallization chemistry shown in Scheme 2.5.1, consistent with prior studies by Sugimoto and Owen.

Scheme 2.5.1. Reaction between lead(II) oleate and substituted thioureas to form monodisperse lead sulfide nanocrystals (top) and influence of number of substituents on thiourea conversion rates (bottom).

***Precursor conversion***

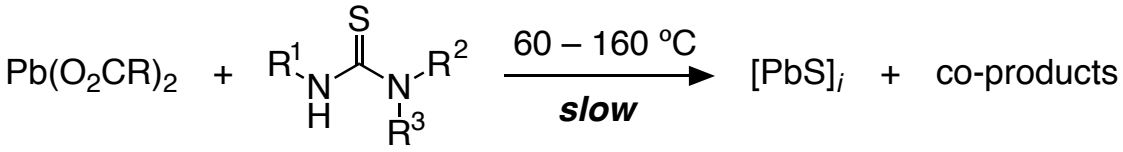


***Crystallization***

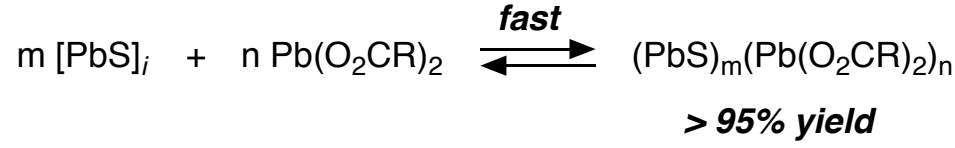

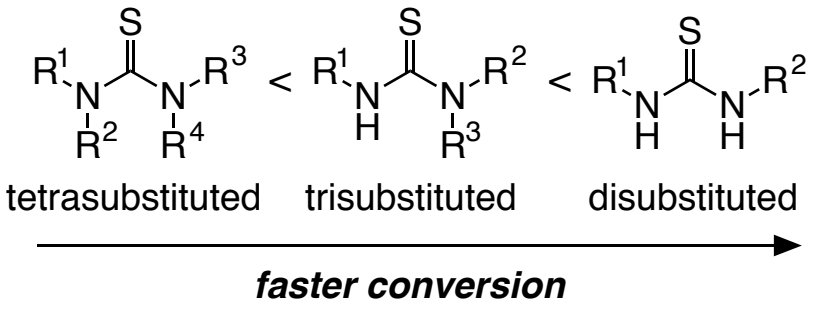


The thiourea conversion reactivity depends on the number of substituents and their electronic and steric properties. The rate decreases as the number of substituents increases: Tetrasubstituted thioureas convert most slowly, followed by trisubstituted and then disubstituted derivatives (Scheme 2.5.1). Thus, the substitution pattern can be used to optimize monomer supply kinetics at the desired crystallization temperature. For example, monodisperse lead sulfide nanocrystals can be synthesized from lead oleate and reactive disubstituted thioureas at temperatures from 60 °C to 150 °C. However, monodisperse CdS nanocrystals require higher temperature conditions (150 ° to 250 °C, Section 2.7.1), where disubstituted thioureas convert at a rate that is limited by mixing during the injection. Instead, less-reactive *N*,*N*,*N*′-trialkylthioureas (**9** to **11**) or *N*,*N*,*N*′,*N*-tetramethylthiourea (**12**) were found to have the appropriate conversion reactivity (see Section 2.7.1). Monodisperse zinc sulfide nanocrystals could also be obtained, but the lower reactivity of zinc oleate compared with cadmium oleate allows more-reactive disubstituted thioureas to be used at high temperatures (≥ 240°C) (see Section 2.7.2). In each case, the conversion reactivity

could be optimized to induce nucleation shortly after injection at the temperature needed to obtain narrow size distributions. Beyond temperature, the specific reaction conditions (solvents, concentrations, volumes, etc.) also have predictable impacts and will be discussed further in Section 2.6.

The resultant nanocrystals have been characterized by a variety of techniques. UV-vis-NIR absorbance spectroscopy shows the sharp electronic transitions expected from monodisperse quantum-confined PbS, with larger nanocrystals exhibiting redder absorption features (Figure 2.5.1). Slower converting precursors systematically lead to larger final nanocrystal diameters. Photoluminescence spectroscopy shows narrow, Stokes-shifted, size-dependent emission across the NIR (Figure 2.5.2). Photoluminescence quantum yields (PLQYs) were measured relative to LDS925 (Styryl 13) dye (assumed PLQY = 0.018), resulting in PLQYs of 3.3% to 16.1%, with most samples close to 10%. Although infrared quantum yields are notoriously difficult to measure accurately, these values are consistent with prior reports on carboxylate-terminated PbS nanocrystals.[84] Powder X-ray diffraction (XRD) of isolated material shows the expected rock salt PbS crystal structure with broadened reflections indicative of small crystallite size (Figure 2.5.3). Transmission electron microscopy (TEM) shows nearly monodisperse, quasi-spherical PbS nanocrystals whose sizes closely match those indicated by UV-vis-NIR spectroscopy (Figure

2.5.4). The observed hexagonal lattices of nanocrystals are evidence of very low polydispersity and flexible ligand coordination spheres.[85,86]

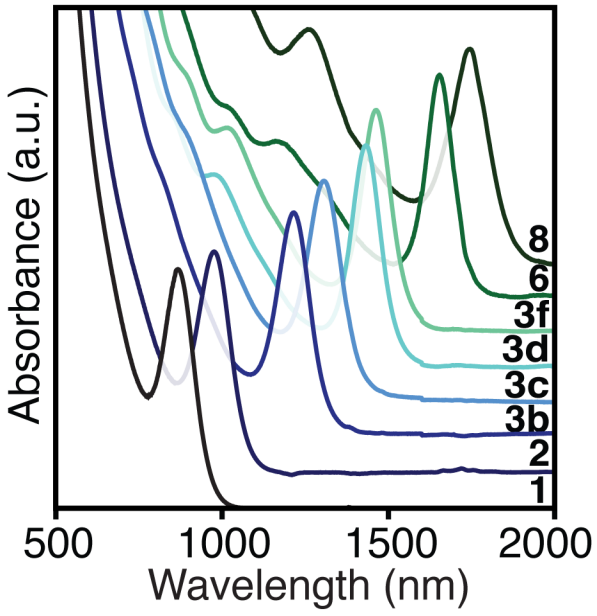


Figure 2.5.1. UV-Vis-NIR absorption spectra of PbS nanocrystals synthesized under identical reaction conditions using substituted thioureas: **1**, **2** (95 °C); **3b, c, d, f** (120 °C); **6**, **8** (150 °C).

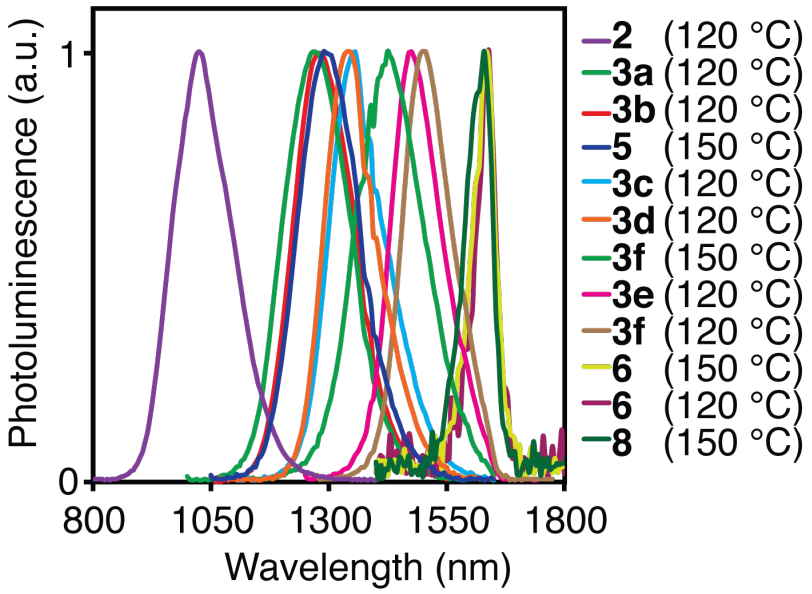


Figure 2.5.2. Photoluminescence spectra of PbS nanocrystals, measured using excitation from a 6-picosecond supercontinuum laser. After spectral filtering, the excitation light (590 ± 10 nm, <25 nJ $cm^{-2}$ per pulse) was focused onto a dilute solution of nanocrystals. The emission was collected using reflective optics, dispersed by a 1/3-meter spectrometer, and detected with an InGaAs photodiode and lock-in amplifier. The grating angle was scanned to acquire spectra. All yields and spectra were corrected for grating and detector efficiency, and the measurements were conducted under inert atmosphere with weak excitation and stirring to prevent experimental artifacts due to oxidation, multiple excitation, and photocharging.

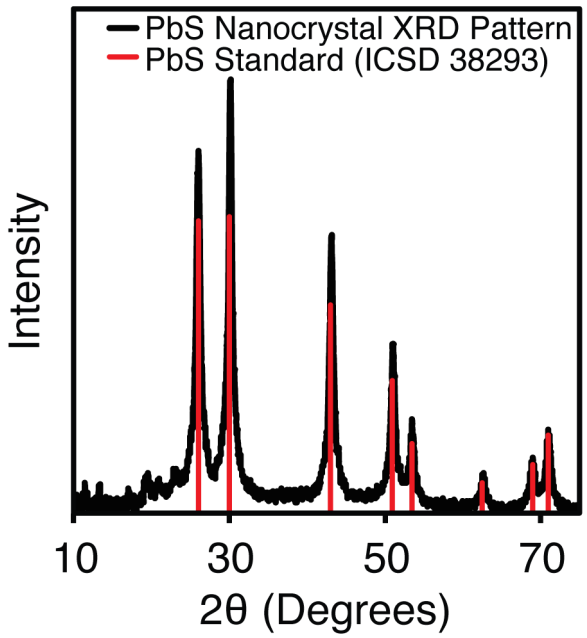


Figure 2.5.3. Powder X-ray diffraction pattern of PbS nanocrystals. The black curve was obtained from PbS nanocrystals isolated from a reaction under conditions similar to those described for the large-scale synthesis of 6.5 nm PbS nanocrystals, but the scale was doubled and diphenyl ether was used as the injection solvent rather than diglyme. An exponential baseline correction was applied to the data to remove signal from scattering. The red PbS standard was obtained from the International Crystallographic Structure Database (ICSD) as coll. code 38293.

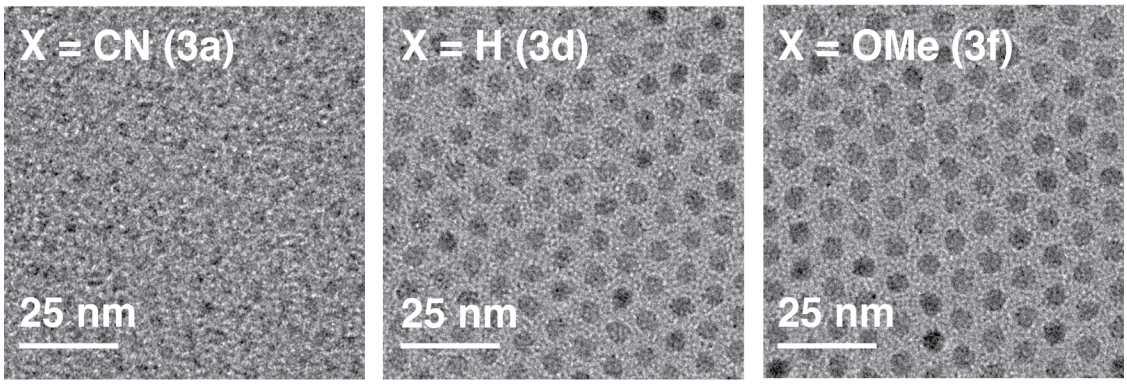


Figure 2.5.4. Transmission electron micrographs of PbS nanocrystals synthesized from precursors **3a**, **3d**, and **3f** under otherwise identical reaction conditions (see experimental for kinetics experiments).

We also investigated whether or not Ostwald ripening took place during this synthesis. Ostwald ripening is a process in which smaller crystals with higher surface energies dissolve in favor of further growth of larger, more bulk-like crystals.[87] In quantum dot synthesis, this results in broadening and red-shifting of the absorption spectrum if reaction conditions are maintained following complete precursor conversion. In order to test this, we ran a PbS nanocrystal synthesis overnight, periodically measuring the absorption spectra of removed aliquots. As shown in Figure 2.5.5, the aliquots show little to no change over time, demonstrating that Ostwald ripening is slow under our standard reaction conditions. However, the PbS nanocrystals synthesized in this experiment are fairly large ($d$ = 5.2 nm) and it is possible that smaller nanocrystals with higher surface energy would ripen more quickly.

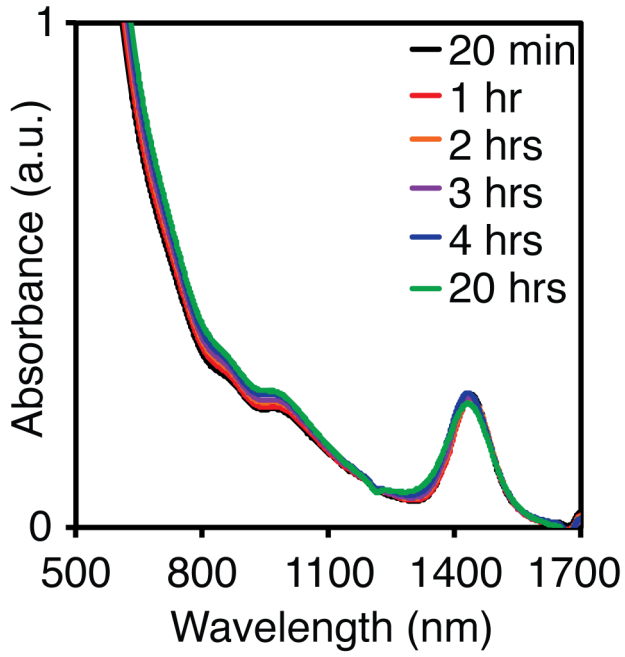


Figure 2.5.5. Following the same procedure described for the synthesis of PbS nanocrystals for absorbance and photoluminescence spectroscopies, *N*-phenyl-*N'*-*n*-dodecylthiourea (**3d**) was injected into the lead oleate solution at 120 °C. Aliquots (125 μL) were removed at 20 minutes, 1 hour, 2 hours, 3 hours, 4 hours, and 20 hours after injection and dissolved in tetrachloroethylene (2.35 mL) for absorption spectroscopy.

*2.5.2. Kinetics*

As described in Section 2.2.1, tuning the solute supply rate can be used to control the number of nanocrystals formed during nucleation. Given the systematic trend observed in nanocrystal size at full precursor conversion shown in Figure 2.5.1, Figure 2.5.2, and Figure 2.5.4, we sought to quantify the relationship between thiourea structure and conversion rate. In order to do this, we monitored the formation kinetics of PbS in situ by measuring the absorbance

at $\lambda$ = 400 nm during nanocrystal synthesis and computing percent yield using the proportionality between absorbance and crystalline PbS formula units discussed earlier.[83] In order to carry out these studies, we built an airfree adapter onto a fiber optic dip probe connected to a UV-vis absorbance spectrometer and immersed it into the reaction mixture.

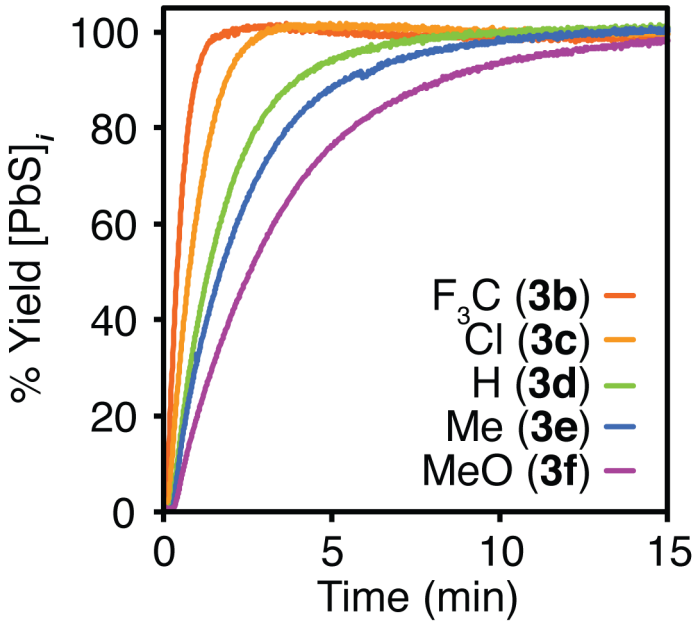


Figure 2.5.6. Kinetics of lead sulfide formation measured in situ by following the absorbance at $\lambda$ = 400 nm.

Over may reactions, PbS formation approaches 100% yield within a few minutes and can be approximated by a single exponential process (Figure 2.5.7), from which rate constants ($k_{obs}$(**1**) to $k_{obs}$(**8**) ($s^{-1}$)) are extracted. By normalizing $k_{obs}$(**1**) through $k_{obs}$(**8**) to the rate constant of the slowest precursor ($k_{obs}$(**8**)), we determined relative single exponential rate constants ($k_{rel}$(**1**) to $k_{rel}$(**8**)) across a range of temperatures (

Table 2.5.1), allowing the reactivity to be quantitatively compared over more than three orders of magnitude. These measurements show a well-defined dependence of the conversion reactivity on the thiourea structure that is defined by the substituents.

Table 2.5.1. Effect of thiourea substitution pattern on the relative thiourea conversion rate constants [$k_{rel}$(**1**) to $k_{rel}$(**8**), e.g., $k_{rel}$(**7**) = $k$(**7**)/$k$(**8**)]. The wide range of reactivity requires that kinetics are measured at multiple temperatures. To account for the temperature dependence of the conversion rate constant, **3b** and **3f** were measured at two temperatures, and the change in rate constant was used to normalize the relative rate constants of the respective temperatures {e.g., $k_{rel}$(**3b**) = [$k$(**3b**)$^{120°C}$/$k$(**8**)$^{150°C}$] × [$k$(**3f**)$^{150°C}$/$k$(**3f**)$^{120°C}$]}.

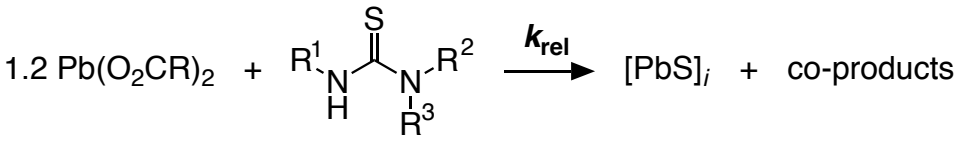


| Compound | $R^1$ | $R^2$ | T (°C) | $k_{rel}$ |
|---|---|---|---|---|
| **1** | 3,5-$(CF_3)_2$-Ph | Ph | 90 | 4000 |
| **2** | Ph | Ph | 90 | 1100 |
| **3a** | 4-CN-Ph | $C_{12}H_{25}$ | 120 | 200 |
| **3b** | 4-$CF_3$-Ph | " | 90, 120 | 91 |
| **3c** | 4-Cl-Ph | " | 120 | 45 |
| **3d** | Ph | " | 120 | 21 |
| **3e** | 4-Me-Ph | " | 120 | 16 |
| **3f** | 4-MeO-Ph | " | 120, 150 | 11 |
| **5** | $^t$Bu | " | 150 | 19 |
| **6** | $^i$Pr | " | 150 | 2.6 |
| **7** | Cyclohexyl | " | 150 | 2.3 |
| **8** | $C_6H_{13}$ | " | 150 | 1 |

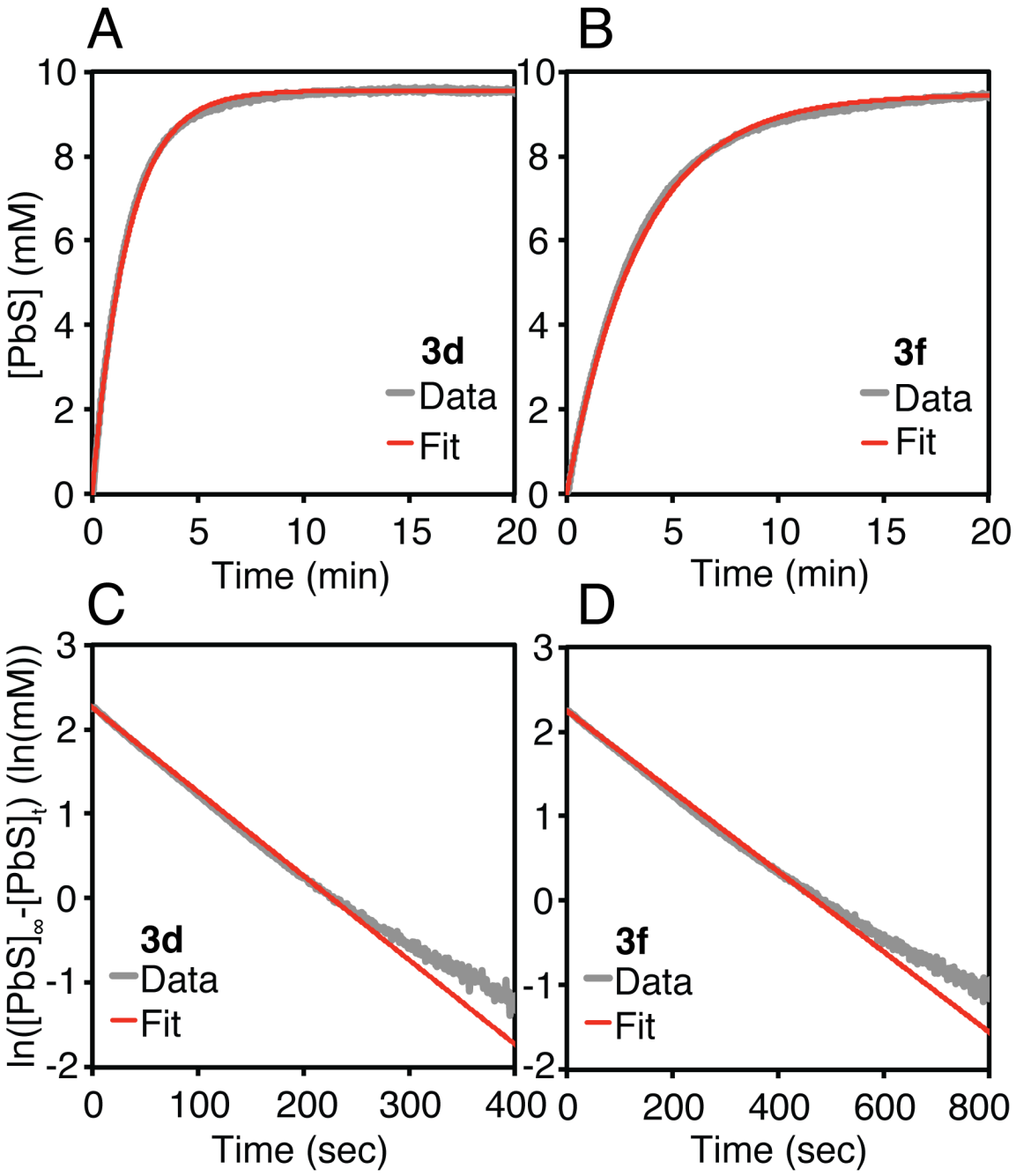


Figure 2.5.7. Example single-exponential fits to kinetics data. A,B) The evolution of [PbS] (gray) fit to a single exponential function (red). C,D) First order plots of data shown in A) and B). The linearity of the data over several orders of magnitude supports the use of a single exponential to

model the data. The reactions were run as described for kinetics experiments with **3d** (A, C) and **3f** (B, D).

Within the disubstituted thiourea derivatives, the conversion rate constants decrease over three orders of magnitude upon replacing electron-withdrawing aryl substituents with alkyl substituents. Thus, *N*,*N*′-diarylthioureas such as *N*-(3,5-*bis*-(trifluoromethyl)phenyl)-*N*′-phenylthiourea (**1**) convert most rapidly, whereas *N*,*N*′-di-*n*-alkylthioureas (**8**) react 4000 times more slowly. Similar results were obtained for cadmium oleate (see section 2.7.1). Mixed *N*-alkyl-*N*′-aryl variants showed intermediate reactivity toward lead(II) oleate that can be finely adjusted by appending electron withdrawing or donating substituents on the aromatic ring. The conversion rate constants of 4-substituted *N*-4-X-phenyl-*N*′-*n*-dodecylthioureas (**3a** to **3f**, where X = CN, $CF_3$, Cl, H, Me, MeO) increase by a factor of 20 as the 4-substituent becomes increasingly electron withdrawing. The logarithms of the observed rate constants are plotted versus the Hammett sigma parameter of the 4-substituent (

Table 2.5.2, Figure 2.5.8).[88–90] A linear relationship is observed, demonstrating a well-behaved dependence of conversion kinetics on the thiourea acidity.

Table 2.5.2. Selected Hammett σ parameters.

| Substituent | Hammett σ |
|---|---|
| 4-MeO | –0.27 |
| 4-Me | -0.14 |
| 4-H | 0 |
| 4-Cl | 0.24 |
| 4-$CF_3$ | 0.53 |
| 4-CN | 0.70 |

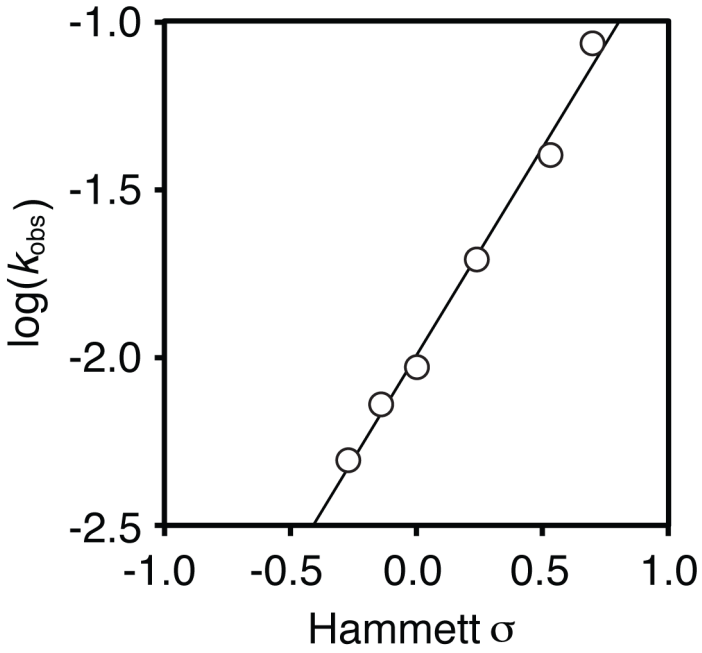


Figure 2.5.8. Hammett plot illustrating the well-defined relationship between the electronic structure of the thiourea and the rate of lead sulfide formation. Slope of linear fit = 1.3.

The large positive slope ($\rho$ = 1.3) indicates a buildup of negative charge during the rate-limiting step, which is overcome faster with the help of electron-withdrawing substituents. This could be explained by rate-limiting

deprotonation of the thiourea to give a thioureate or by nucleophilic attack on the thiocarbonyl carbon to give a quaternary central carbon. Conversion of **3d** is faster in the presence of tri-*n*-butylamine and slower when oleic acid is present, both of which suggest that deprotonation of the thiourea precedes the formation of lead sulfide. Deprotonation of thiourea in water is known to speed its hydrolysis to cyanamide.[61] Increasing steric bulk of the thiourea substituents also speeds the rate of conversion (**5**-**8**); the increased bulk may accelerate elimination of lead sulfide from an intermediate lead thioureate complex formed by deprotonation of a lead-bound thiourea. Although detailed work is required to determine the precise conversion mechanism, these observations highlight the importance of the microscopic steps leading to the rate determining precursor conversion step, which vary depending on the surfactants used as well as the nature of the metal co-reactant.

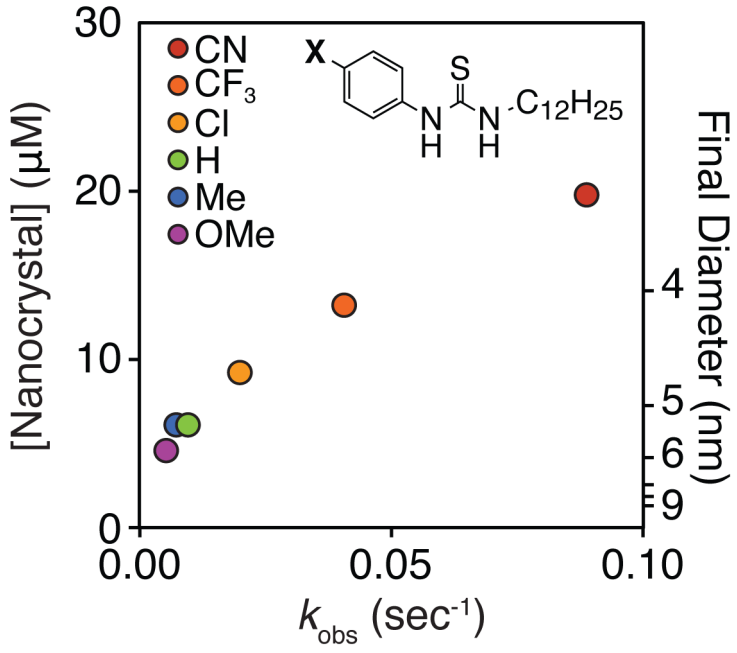


Figure 2.5.9. Relationship between $k_{obs}$, [nanocrystal], and final nanocrystal diameter ([nanocrystal] ∝ [PbS]/r$^3$) under conditions detailed in kinetics experiments.

The nanocrystal concentrations obtained from **3a** to **3f** are plotted versus $k_{obs}$ in Figure 2.5.9, where an eightfold increase in the conversion rate leads to a fourfold increase in the nanocrystal concentration. The finely tuned monomer supply kinetics controls the extent of nucleation, because the rate of Ostwald ripening is negligibly slow under these conditions (Figure 2.5.5). A similar dependence is observed in studies of ZnS, $Cu_{2-x}S$, NiS, CdS quantum dots, and CdS nanorods (see Section 2.7).

As discussed in Section 2.2.1, previous theoretical and experimental work on AgCl,[9] AgBr,[10] and CdSe[11] describes a linear relationship between the solute supply rate ($Q_0$) and the nanocrystal concentration formed during nucleation ($n$):

$$n = \frac{V_m}{\dot{v}} Q_0$$

Equation 2.5.1

However, in the present study we observe a systematic deviation from this relationship, in which fewer nanocrystals are formed than predicted. This indicates that updated models are necessary to understand quantum dot nucleation and growth. This will discussed in greater detail in Chapter 4. Even so, this relationship is a powerful tool for developing practical syntheses of colloidal nanocrystals, allowing for predictive control over diameter at full conversion.

*2.5.3. Mechanistic Insights*

In order to understand the remarkable tunability of thiourea-based nanocrystal synthesis, we set out to learn about the reaction mechanism. By analyzing the trends laid out in Scheme 2.5.1,

Table 2.5.1, Figure 2.5.8, and Figure 2.5.9, we can make three broad conclusions and begin to outline likely mechanisms.

First, greater Brønsted acidity of the NH protons and/or Lewis acidity of the thiocarbonyl group leads to higher reactivity. Within disubstituted thioureas, appending electron-withdrawing groups to substituents increases acidity and leads to systematically faster rates. As mentioned previously, adjusting the acidity of the reaction mixture with oleic acid or tri-*n*-butylamine decreases and increases PbS formation rates, respectively.

Replacing NH protons with alkyl/aryl substituents decreases the acidity of the thiourea and leads to dramatically slower rates. These results are consistent with rate-limiting 1) deprotonation of a lead-bound thioureate complex and 2) nucleophilic attack at the thiocarbonyl carbon by an intra- or intermolecular carboxylate. The fact that all observed rate constants fit to single exponential functions points toward a unimolecular process, although more detailed studies are under way to investigate this.

Second, steric bulk leads to higher reactivity among disubstituted thioureas. This is clear from the observed trend across compounds **5** – **8**. This is consistent with a unimolecular process in which steric crowding following coordination and deprotonation accelerates elimination of PbS. However, there is

necessarily a limit to this trend; a thiourea so bulky that the lead(II) oleate cannot access it should not be reactive.

Scheme 2.5.2. Proposed mechanism of reaction between disubstituted thioureas and lead(II) carboxylate.

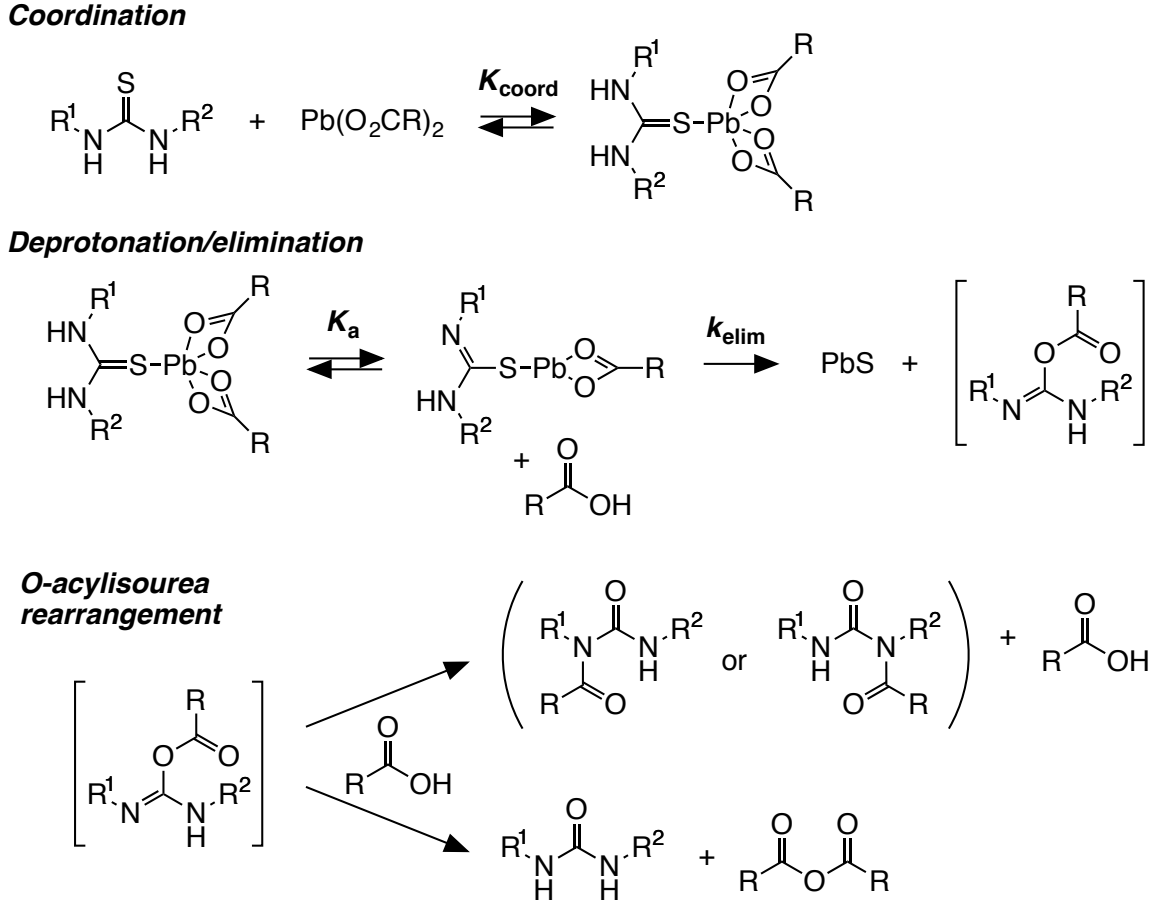


Third, the mechanism of reaction changes with different numbers of substituents, an idea best exemplified by the following two examples. First, among trisubstituted thioureas, the acidity trend observed among disubstituted thioureas is reversed; aryl groups lead to *slower* rates than alkyl groups. As will be discussed in Chapter 3, this is true for trisubstituted selenoureas as well.

Second, tetrasubstituted thioureas cannot convert through a deprotonation pathway since they have no NH protons, instead likely proceeding through nucleophilic attack. These differences are reflected in the reaction co-products; tetrasubstituted thioureas (and selenoureas) lead to urea and anhydride co-products, while disubstituted thioureas lead to mixtures of the urea and anhydride *as well as N*-acylurea and carboxylic acid. Interestingly, the character of the thiourea substituents and lead(II) carboxylate R group dictate the distribution of *N*-acylurea vs. urea.[56] The only co-products of trisubstituted selenoureas are the *N*-acylurea and oleic acid set, which will be discussed in Chapter 3 since it was studied for selenoureas in the most detail.

Scheme 2.5.3. Co-products identified from the reaction between disubstituted (top) and tetrasubstituted (bottom) thioureas and lead(II) carboxylate.

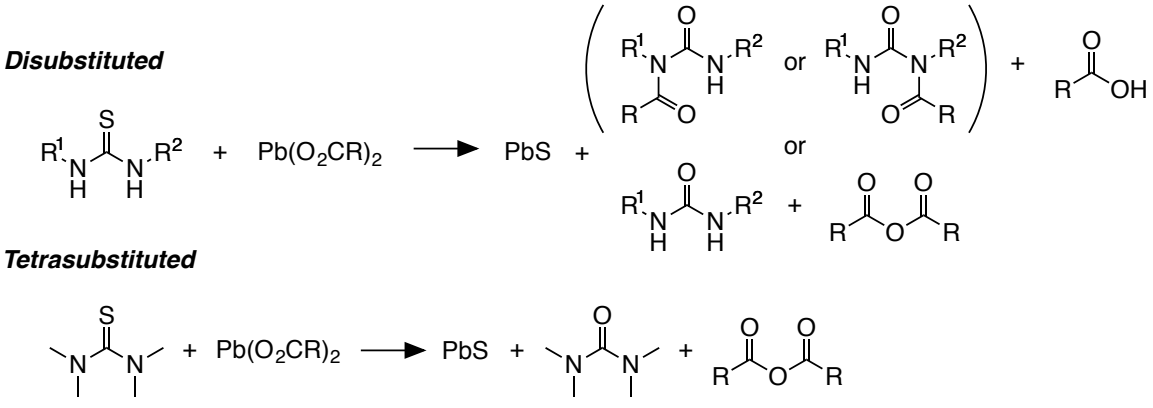


These mechanistic insights have helped accelerate the development of structures that are likely to meet specific rate targets. This has been particularly

useful in the realm of trisubstituted selenourea sterics, which will be discussed in Chapter 3 as well.

### 2.6. PbS Nanocrystal Scale-Up and Reaction Optimization

There are many published methods to synthesize PbS nanocrystals, but without fail they suffer from trade-offs between scalability, tunability, and monodispersity. In order to demonstrate the practicality and flexibility of PbS nanocrystal synthesis from thioureas, we set out to 1) explore the widest range of synthesis conditions possible and 2) optimize large-scale (multigram) syntheses without sacrificing the core principles of tunability and monodispersity. In particular, we were interested in solvent, concentration, volume, temperature, and thiourea substituent design. The major trends we observed are summarized in Table 2.6.1 and detailed in the rest of this section.

Table 2.6.1. Summary of parameters affecting the outcome of PbS nanocrystal synthesis.

| Parameter | Effects on final $d_{NC}$, $\lambda_{max}$ | Magnitude |
|---|---|---|
| Precursor choice | Faster conversion rate leads to greater numbers of smaller nanocrystals | Large |
| Alkane/1-alkene solvent | Lower viscosity leads to smaller nanocrystals at constant reaction rate | Medium ($\Delta\lambda_{max} \leq 100$ nm) |
| Injection solvent | Higher polarity leads to larger nanocrystals | Medium ($\Delta\lambda_{max} \leq 100$ nm) |
| Concentration | Higher concentration leads to larger nanocrystals | Medium ($\Delta\lambda_{max} \leq 100$ nm) |

| | | |
|---|---|---|
| Volume | Larger reaction volumes lead to larger nanocrystals | Medium ($\Delta\lambda_{max} \leq 100$ nm) |
| Temperature | Higher temperature leads to faster precursor conversion with little change in size | Small ($\Delta\lambda_{max} \leq 50$ nm) |
| Precursor solubility | More soluble precursors lead to narrower size distributions at small nanocrystal sizes and low temperatures | Medium |
| Lead-to-sulfur ratio | Higher lead-to-sulfur ratios lead to narrower size distributions at small nanocrystal sizes | Small |

*2.6.1. Solvent Choice and Viscosity*

Solvent choice is ingrained in the history of nanocrystal synthesis. As discussed in Section 2.4.1, lead(II) oleate is traditionally prepared in situ under vacuum at 100 °C, which requires the use of high-boiling solvents.[18] Most researchers choose 1-octadecene (b.p. = 315 °C) for its low cost. Other syntheses based on $PbCl_2$ use oleylamine (b.p. = 364 °C) as the solvent for its high boiling point and ability to coordinate $PbCl_2$ as an L-type ligand.[24,26] In some syntheses, trioctylphosphine (b.p. = 400-406 °C) or trioctylphosphine oxide (b.p. = 411 °C) are used as co-solvent. As a side note, PbS and PbSe syntheses do not have a monopoly on high-boiling solvents; for the sake of degassing reaction mixtures immediately prior to precursor injection, almost every metal chalcogenide nanocrystal synthesis is conducted in one of these four solvents or a few analogues. Suffice it to say that lower-boiling solvents has not been an active area of research.

Our development of a synthesis of lead(II) oleate allowed us to independently choose appropriate reaction solvents. In particular, we were interested in enabling solvent removal at room temperature under vacuum following completion of the reaction. After a broad survey, it became clear that a wide variety of solvents were viable within a framework of 95% alkane/1-alkene and 5% ether/nitrile injection solvent (Table 2.6.2). For the purpose of reaction scalability at 90 – 120 °C, combinations of 1-octene/dibutyl ether and 1-octene/diglyme emerged as particularly appealing solvent mixtures.

While this range is quite broad, there are several important limitations. First, the main solvent must be completely nonpolar. Second, chlorinated injection solvents like tetrachloroethylene cause rapid nanocrystal aggregation. In the case of tetrachloroethylene, this is likely because of its one- and two-electron oxidation capabilities. Third, aromatic injection solvents like toluene, *p*-xylene, *m*-xylene, and *o*-xylene also cause aggregation (Table 2.6.3). The reason for this is less clear, given that 1) diphenyl ether and anisole are perfectly viable injection solvents, 2) benzene and toluene are viable solvents for isolation and storage (see Section 2.6.6), and 3) a prior study synthesized PbSe nanocrystals in toluene.[23]

Table 2.6.2. Solvents successfully used in PbS nanocrystal synthesis from thioureas.

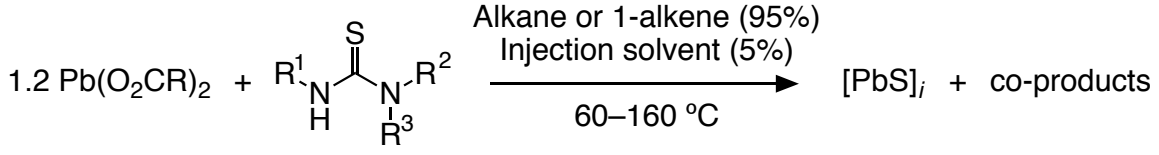


| Alkane | b.p. (°C) | 1-Alkene | b.p. (°C) | Injection solvent | b.p. (°C) |
|---|---|---|---|---|---|
| Hexane | 68 | 1-Hexene | 63 | Dibutyl ether | 142 |
| Heptane | 98 | 1-Heptene | 94 | Diphenyl ether | 258 |
| Octane | 125 | 1-Octene | 121 | Dioctyl ether | 286-287 |
| Decane | 174 | 1-Decene | 167-174 | Anisole | 154 |
| Dodecane | 216 | 1-Dodecene | 214 | Glyme | 85 |
| Tetradecane | 254 | 1-Tetradecene | 251 | Diglyme | 162 |
| Hexadecane | 287 | 1-Hexadecene | 274 | Triglyme | 216 |
| Octadecane | 317 | 1-Octadecene | 315 | Tetraglyme | 275-276 |
| Eicosane | 343 | | | Benzonitrile | 188-191 |
| Tetracosane | 391 | | | γ-Butyrolactone | 204 |

Table 2.6.3. Compatibilities of injection solvents surveyed in this study.

| Compatible | Incompatible |
|---|---|
| 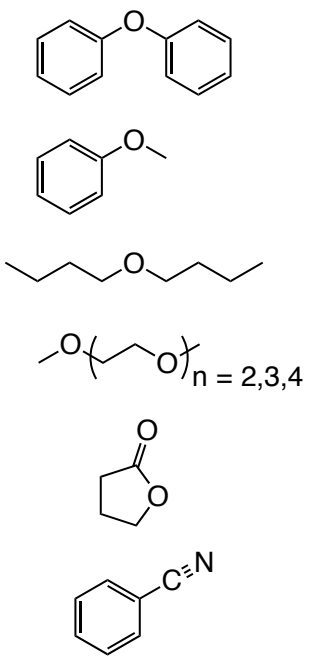 | 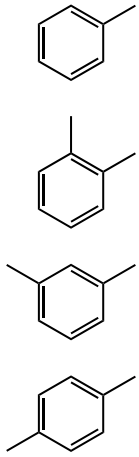 |

Solvent choice has implications for reaction mixture viscosity. For example, at room temperature, hexane is free-flowing liquid, hexadecane is an oil, and tetracosane is a crystalline solid. More quantitative viscosity-temperature relationships are known across wide ranges in temperature (Figure 2.6.1).[91] Since we can tune this parameter independently, we started to pose new questions about nanocrystal synthesis. Does increasing viscosity cause microscopic mass transport limitations during extremely rapid nucleation processes? Is there any dependence on viscosity at all?

To answer these questions, we surveyed a range of alkane solvents ($C_8$–$C_{20}$) under identical conditions. Figure 2.6.2A shows that viscosity has a small,

relatively insignificant effect upon the rate of precursor conversion, while Figure 2.6.2B shows a systematic decrease in [nanocrystal] and concomitant increase in final nanocrystal diameter with increasing viscosity. From this study, it is clear that viscosity has a small but measurable impact on the process of nucleation and growth, suggesting that nucleation has some degree of mass transport dependence. This will be discussed in greater detail in Chapter 4. For the present optimization study, this knowledge is practically useful as another knob to tune final nanocrystal size. Given the traditional difficulties of synthesizing small PbS nanocrystals in high yield for solar cells, less viscous and lower-boiling solvents provide two practical benefits simultaneously. In our own scale-up work moving forward we use 1-octene because of its low cost relative to octane (at the time of this writing, 1-octene is $32.20/L from Alfa Aesar while octane is $92/L from Sigma-Aldrich. These prices may change with economies of scale; it is hard to imagine, for example, that 1-octene is cheaper than *n*-octane industrially since the former is primarily produced by ethylene tetramerization while the latter is a major component of oil that is not particularly valuable to gasoline production, with an octane rating of –10. The cost difference may also be explained by difficulty of isolation.).

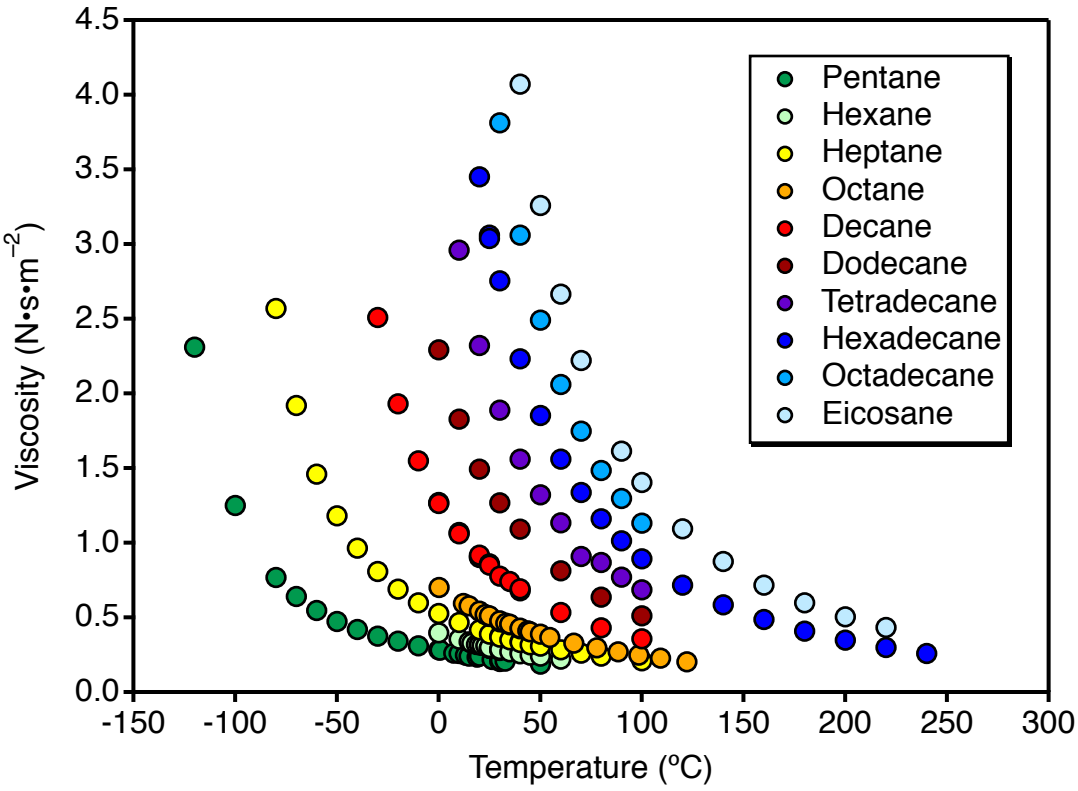


Figure 2.6.1. Temperature dependence of alkane ($C_5$–$C_{20}$) viscosity, re-plotted from literature data.[91]

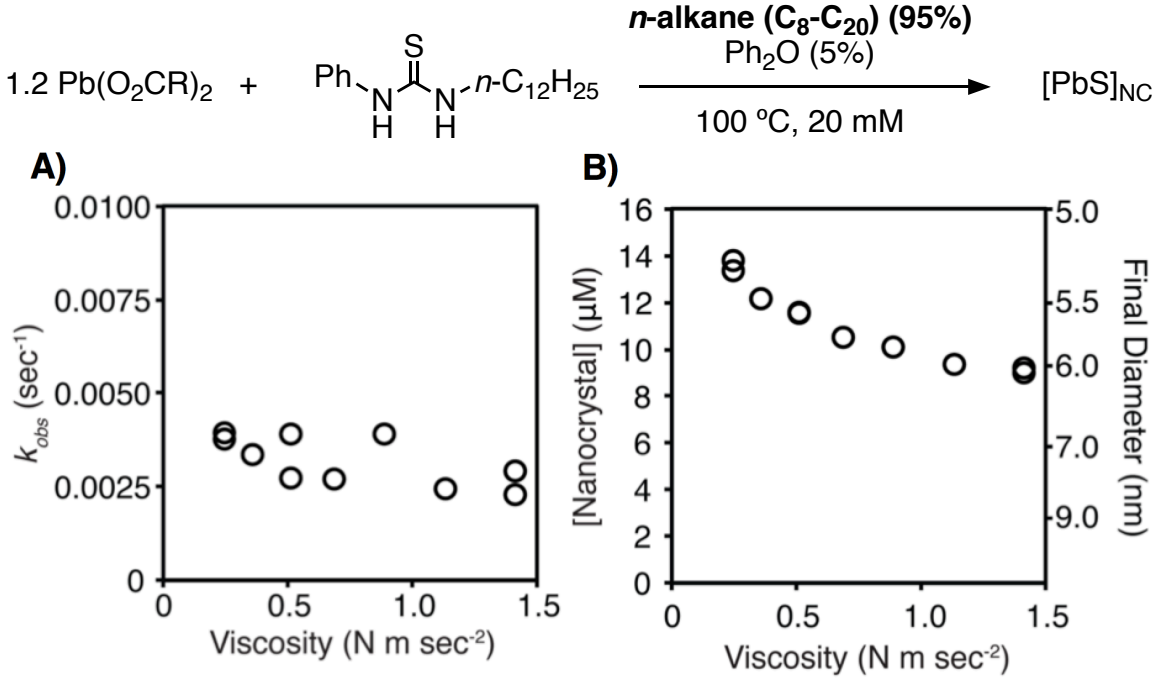

Figure 2.6.2. A) Plot showing minimal effect of *n*-alkane viscosity on PbS formation rate. B) Relationship between [nanocrystal] and *n*-alkane viscosity. Contributions to viscosity from *N*-dodecyl-*N'*-phenylthiourea (**3d**), lead(II) oleate, and diphenyl ether injection solvent are ignored.

*2.6.2. Concentration*

Our next consideration was reaction concentration, since a scaled-up reaction should be as concentrated as possible in order to limit size and expense. Most syntheses of PbS nanocrystals are carried out in the range of 10-100 mM [PbS],[24–26,92] and all thiourea-based reactions shown prior to this point were carried out at 9-20 mM.

Although we did not design a careful concentration study, data collected from several comparable reactions are shown in Figure 2.6.3. From these data we can conclude that this reaction can be run at 100 mM with little difference from small scale. However, across other datasets we observe slight, systematic red shifts with higher concentration. This will be shown explicitly for an analogous PbSe synthesis in Chapter 3. It is worth noting that *N*-(2-ethylhexyl)-*N'*-phenylthiourea was chosen in this case for the excellent solubility imparted by the branched 2-ethylhexyl group without significantly altering the thiourea electronics. While the improved solubility of branched alkyl chains is a concept that has been used in the organic electronics community for years,[93] the

nanocrystal community is just beginning to embrace it in designing nanocrystal ligands for optimal solubility.[94–96]

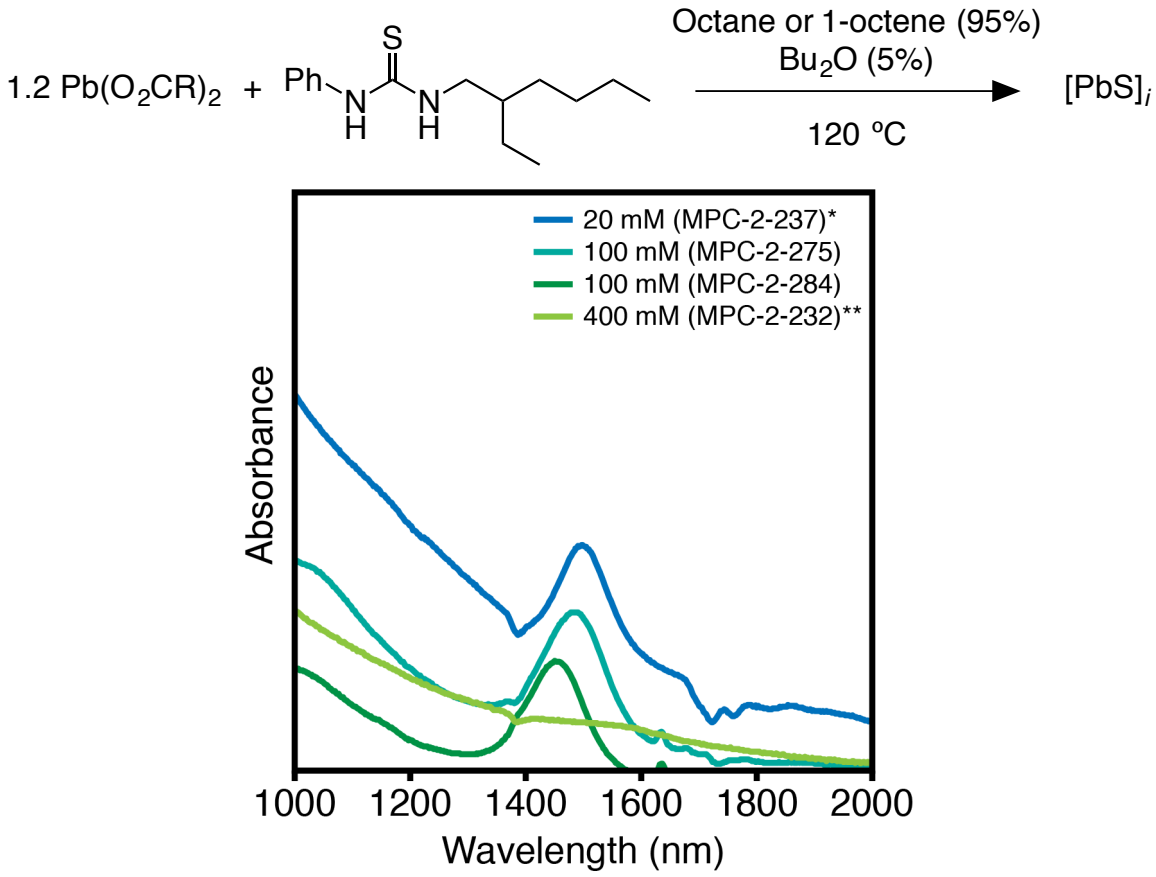


Figure 2.6.3. Concentration dependence of PbS nanocrystal synthesis. (*) Performed using lead(II) tetradecanoate as the lead precursor, which is much less soluble than lead(II) oleate and responsible for the observed scattering background. (**) No $Bu_2O$ co-solvent was present.

It is unusual that the size distribution is relatively unchanged at high precursor (up to 100 mM) and nanocrystal concentrations (up to 0.12 mM). This illustrates the reliability and homogeneity provided by well-defined and characterized lead and sulfur precursors.

*2.6.3. Temperature*

Reaction temperature is important in any chemical reaction, but particularly so in kinetically controlled scenarios with multiple steps. While it is straightforward to measure the temperature dependence of precursor conversion/metal sulfide formation by NMR and/or UV-vis, the subsequent nucleation and growth steps are likely to have different temperature dependences that influence the final products. Across many precursor-temperature combinations, we assembled the plot shown in Figure 2.6.4 and obtain similar [nanocrystal] vs. $k_{obs}$ dependences to that observed in Figure 2.5.9, albeit with steeper relationships at lower temperatures and shallower relationships at higher temperatures.

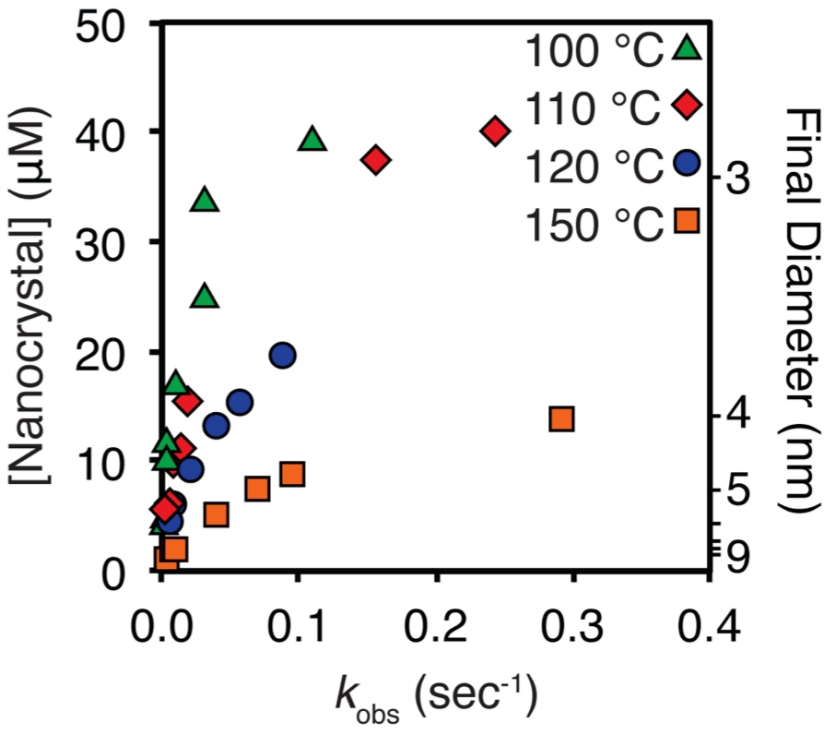


Figure 2.6.4. Temperature dependence of [nanocrystal] vs. solute supply rate.

From these data, it is clear that [nanocrystal] and final diameter are more sensitive to rate at lower temperatures. Further, more reactive precursors are necessary to obtain the same rate at lower temperatures. There is much more that can be said about this plot, but we will reserve that discussion for Chapter 4. For the present discussion, suffice it to say that it is preferable to synthesize small nanocrystals at lower temperatures where reaction rates are slow enough to avoid mixing-limited kinetics (> ~0.1 $s^{-1}$), but it is preferable to synthesize large nanocrystals at higher temperatures where reaction rates are fast enough to finish practically reasonable times (up to ~2 h). To visualize these statements

using Figure 2.6.4, imagine a horizontal line drawn across the plot at the desired final diameter, then interpolate the rate constants necessary to obtain that size at various temperatures.

The final caveat in this discussion is the temperature window for PbS nanocrystal synthesis. While Figure 2.6.4 shows a range from 100 – 150 °C, we have prepared high-quality samples at temperatures from 60 – 160 °C with potential to expand even more widely. The low end is likely limited by a threshold temperature of crystallization that is material dependent. The high end is limited by lead(II) oleate thermal decomposition and may begin as high as >220 °C, based on literature methods.[97]

*2.6.4. Lead-to-Sulfur Ratio*

Given the dramatic role that surfactant concentrations play in determining nanocrystal growth rate, facet selectivity, and surface tension, as well as the impact that post-synthesis ligand coverage has on quantum dot optical properties, we sought to determine the most appropriate feed ratios of lead(II) oleate to thiourea in nanocrystal synthesis. Lead(II) oleate is consumed stoichiometrically by thioureas and none of the co-products are particularly effective nanocrystal ligands, so the only ligand source following conversion is any excess lead(II) oleate. This stoichiometry is approximated in Scheme 2.6.1.

Thiourea conversion to PbS highlighting the fate of excess lead(II) carboxylate and its equilibrium with bare PbS surfaces.

Scheme 2.6.1. Thiourea conversion to PbS highlighting the fate of excess lead(II) carboxylate and its equilibrium with bare PbS surfaces.

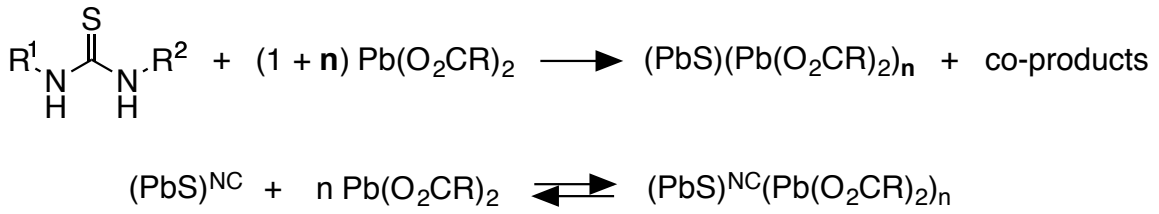


By Le Chatelier's principle, a greater excess of lead(II) carboxylate should lead to better-passivated nanocrystal surfaces. Since nanocrystals are inherently kinetic products whose thermodynamic tendency is the formation of bulk material, good ligand passivation is important to a controlled synthesis. Especially in the cases of PbS and PbSe, low surface lead(II) oleate ligand densities on certain facets have been shown to lead to dimerization, precipitation, and in carefully controlled settings, "supercrystal" formation, through oriented attachment at room temperature.[98–100]

Moreover, since sizes are tunable and thioureas convert fully to metal sulfide, the same amount of excess lead(II) carboxylate has to passivate different surface areas depending on the resulting final diameter. Therefore, the "demand" for ligands should be greater in syntheses that produce small nanocrystals. In optimizing PbS synthesis from thioureas, we found evidence this

may be the case: absorption linewidths of small PbS nanocrystals synthesized from thioureas **1** and **2** are narrower when the synthesis is conducted with lead-to-sulfur ratios (1.5:1 – 3:1) (Figure 2.6.5), while larger nanocrystals synthesized from slower precursors like **3d** and **3e**, exhibit virtually no effect provided the lead-to-sulfur ratio is at least 1:1. Lastly, there is a small blue shift of the peak position and decrease of final nanocrystal size at higher lead-to-sulfur ratios. By Sugimoto's nucleation mass balance equation (Equation 2.6.1), this effect consistent with: A) faster solute supply rates ($Q_0$) leading to greater numbers of nanocrystals ($n$); B) slower per-particle growth rates during nucleation ($\dot{v}$) leading to greater numbers of nanocrystals needed to match the solute supply rate and pull the solute concentration below the critical concentration; and C) increased viscosity at higher lead(II) oleate concentration leading to the nucleation of more nanocrystals (as discussed in Section 2.6.1 in the context of *n*-alkane chain length).

$$n = \frac{Q_0 V_m}{\dot{v}}$$

Equation 2.6.1

In weighing these trade-offs for our own multigram scale-up work, we decided to use lead-to-sulfur ratios of 1.5 for **2** and 1.2 for **3d**.

*2.6.5. Volume*

In order to be practical at industrial scales, it is crucial to understand how a process scales with volume as well. In order to show this for PbS nanocrystal synthesis from thioureas, we set out develop standard conditions for multigram batches of "large" and "small" nanocrystals, the latter having an absorption profile appropriate for solar cells. Using insights from the previous sections, we conducted five sets of experiments in triplicate, varying volume and other variables systematically (Figure 2.6.5).

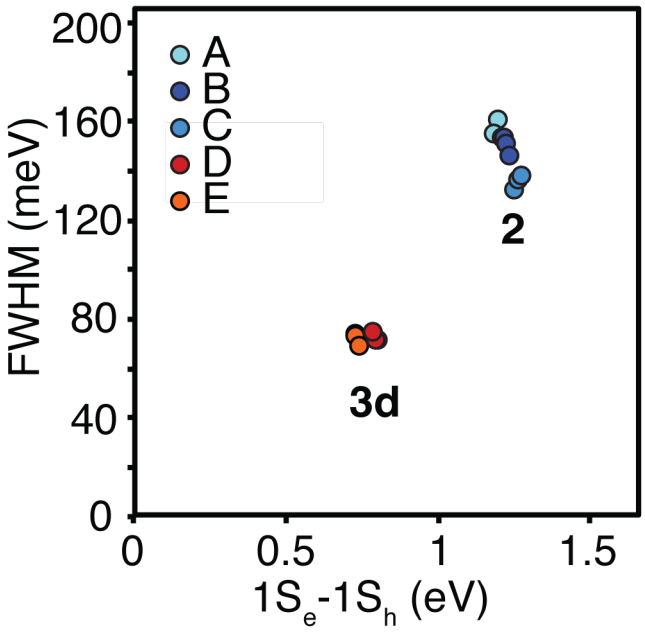


Figure 2.6.5. Detailed reaction conditions in PbS reproducibility study. Each dot represents data from an absorbance spectrum obtained from an independent reaction. Reactions were run as described for large-scale synthesis of 3.4 nm PbS nanocrystals with *N*,*N*′-diphenylthiourea (**2**) and for large-scale synthesis of 6.5 nm PbS nanocrystals with *N*-*n*-dodecyl-*N*′-

phenylthiourea (**3d**), with the following adjustments: A) ran as described for 3.4 nm PbS nanocrystals; B) 1/15 scale; C) 1/15 scale and thiourea concentration reduced by half resulting in 75 mM $Pb(oleate)_2$ and 25 mM **3d**; D) 1/15 scale; E) ran as described for 6.5 nm PbS nanocrystals.

The most direct comparisons between volumes are A/B and D/E. By examining the peak positions, we can see small, but significant red shifting with scale increases. When converted to the wavelength domain, this shift is up to 100 nm in some cases. By examining the linewidths, we can see that there is virtually no effect of scale for the relatively slow-reacting thiourea **3d**, but that there is a small, systematic linewidth broadening for the fast-reacting thiourea **2** as the reaction is scaled up from 10 mL to 150+ mL (Figure 2.6.5). This is likely a result of mixing limitations, which are increasingly difficult to overcome with conventional laboratory-scale equipment as scale increases. By eye, the onset of deep brown color starts 5-10 seconds following injection for **2**, making this conclusion reasonable given the limitations of academic laboratory equipment.

*2.6.6. Purification and Isolation*

In order to complete a practical scaled-up process, we set out to design a reproducible purification and isolation procedure taking advantage of 1) the well-defined solution composition following complete thiourea conversion and

2) the volatility of 1-octene, diglyme, and dibutyl ether reaction solvents (see Table 2.6.2). We decided to pursue the traditional purification route, which involves repeated precipitation of nanocrystals from polar solution, centrifugation to remove soluble species, and dissolution of the nanocrystal residue in a nonpolar solvent. Detailed procedures are available in Sections 2.9.6 and 2.9.7. The concept of nanocrystal "purity" is surprisingly complex, being dependent upon ligand packing densities on curved surfaces,[101] adventitious acid contaminants, metal ion excess, and intended downstream use,[69,70,72] but for the purposes of this work we will simply try to achieve reasonable $Pb(O_2CR)_2$ ligand densities of ≤ ~4 $nm^{-2}$.

From developing this method, several salient trends have emerged. First, the volumes of toluene/pentane solvent and methyl acetate antisolvent are greatly reduced because the reaction solvents are removed under vacuum following conversion, leaving a concentrated residue to begin the purification process. This helps reduce cost, footprint, and makes the process easier to carry out within a nitrogen-filled glovebox.

Second, reactions with higher lead-to-sulfur ratios require more precipitation/redissolution steps to achieve similar ligand coverages. This is a reasonable result since PbS nanocrystals and lead(II) oleate can have similar

solubility, especially in the limit of small nanocrystal size and high degree of lead(II) oleate polymerization.

Third, it can be difficult to visually determine whether or not a PbS nanocrystal sample is completely dissolved, since the concentrated solutions used during work-up are extremely dark brown. Incomplete dissolution, followed by precipitation, renders the purification process less effective and inhomogeneous throughout the sample. Because of this, we recommend carefully inspecting solutions for precipitate after sitting undisturbed for > 1 minute.

Fourth, nanocrystal solubility appears to decrease with increasing size, unsurprisingly, but it also appears to change in an unexpected way. Smaller nanocrystals are more soluble in toluene than pentane, while larger nanocrystals are more soluble in pentane than toluene (Figure 2.6.6). This is perplexing because toluene is typically a better solvent than pentane even for nonpolar molecules, and if there were indeed some feature making pentane a more favorable solvent (e.g. improved ligand shell penetration, lower viscosity, etc.), it is difficult to imagine why it would only start to dominate at large nanocrystal size. For reference, lead(II) oleate is qualitatively more soluble in toluene than pentane at room temperature.

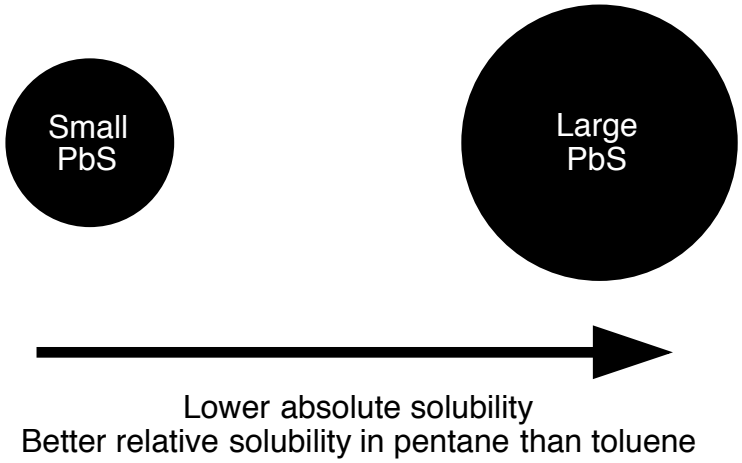


Figure 2.6.6. Trends in PbS nanocrystal solubility.

Following an appropriate number of purification cycles (typically 4 – 6, depending on starting lead-to-sulfur ratio), the nanocrystals are dried under vacuum and stored as a concentrated stock solution ([NC] = 1 – 3 mM) in benzene-$d_6$, toluene-$d_8$, or tetrachloroethylene. Small amounts of this solution are removed for $^1$H NMR and absorbance spectroscopies. $^1$H NMR spectroscopy *versus* an internal standard gives the $Pb(O_2CR)_2$ concentration while absorbance spectroscopy gives [NC], *d*, and [PbS]. These data are used to compute numbers of ligands per particle and ligand density per square nanometer of nanocrystal surface area (See Section 2.9.9 for details). An example spectrum is shown in Figure 2.6.7.

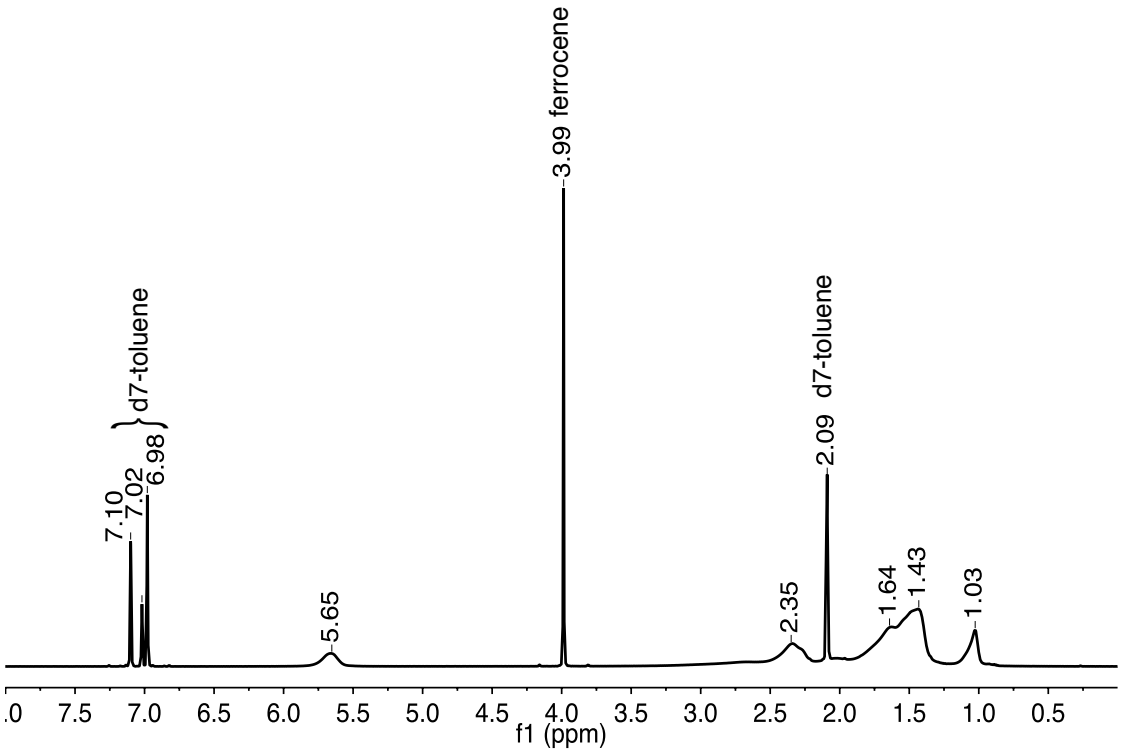


Figure 2.6.7. $^{1}$H NMR spectrum of PbS nanocrystals isolated from a large-scale reaction. The broad resonance at 5.65 ppm is characteristic of lead(II) oleate complexes bound to slowly tumbling nanocrystals and is integrated relative to a ferrocene internal standard (See Section 2.9.9 for details).

*2.6.7. Areas for Further Optimization*

There are several other areas for further optimization of this synthesis that may be relevant for further scale-up (e.g. in an industrial context). These include 1) lowering the reaction temperature for fast precursors, which would allow less expensive, lower-boiling solvents (hexane, 1-hexene, cyclohexane, glyme, THF, etc.) to be used, 2) pinpointing the upper concentration limit of this reaction as functions of temperature, excess lead, solvent, etc., which is likely greater than

the 50 mM and 100 mM numbers we have used thus far; 3) carefully optimizing the lead-to-sulfur feed ratio to minimize both size distribution and waste products, 4) quantifying the qualitative trends in peak position and linewidth discussed here, as functions of temperature, solvent mixture, concentration, volume, feed ratio, etc.; and 5) developing more scalable purification procedures such as column chromatography, differential flow, and membrane separations.

**2.7. Synthesis of Other Metal Sulfide Nanocrystals**

Thus far our discussion has focused on PbS nanocrystals, but thiourea precursors are by no means limited to PbS. In this section we will discuss our efforts to rapidly develop modern syntheses of a representative sample of technologically interesting metal sulfide nanocrystals. For PbS and CdS, we have developed new synthetic methods from the ground up, but in the interest of making an initial broad demonstration, in other cases we have substituted thiourea precursors into existing literature methods written with other sulfur precursors (e.g. sulfur in octadecene, trioctylphosphine sulfide, dodecanethiol). The larger goal of this study was to create a paradigm shift in the philosophy of nanocrystal synthesis; control over particle size is inherently a kinetic problem (except in cases of metastable clusters, which deviate from the Gibbs-Thomson relationship and create local minima), so a tunable precursor class offering

control over kinetics should rapidly advance many other types of nanocrystal synthesis.

*2.7.1. CdS*

The first example we pursued was CdS, given its utility as a photocatalyst[102] and quantum dot shell material,[103] and its well-understood optical properties.[104] We used chemistry directly analogous to our PbS synthesis; $Cd(O_2CR)_2$ is simply substituted for $Pb(O_2CR)_2$ and the reaction temperature adjusted accordingly. The scheme and results of a representative reaction are shown in Figure 2.7.1. The absorbance and band-edge fluorescence linewidths are unusually narrow, again demonstrating the ability of well-defined precursors to make improvements to even well-established syntheses.

We performed a study of [nanocrystal] vs. rate, again finding that faster conversion rates lead to greater numbers of nanocrystals (Figure 2.7.2), although this relationship appears to be superlinear rather than sublinear as in the case of PbS (Figure 2.5.9). This could be the result of a change in mechanism from di- to trisubstituted thioureas as discussed in Section 2.5.3.

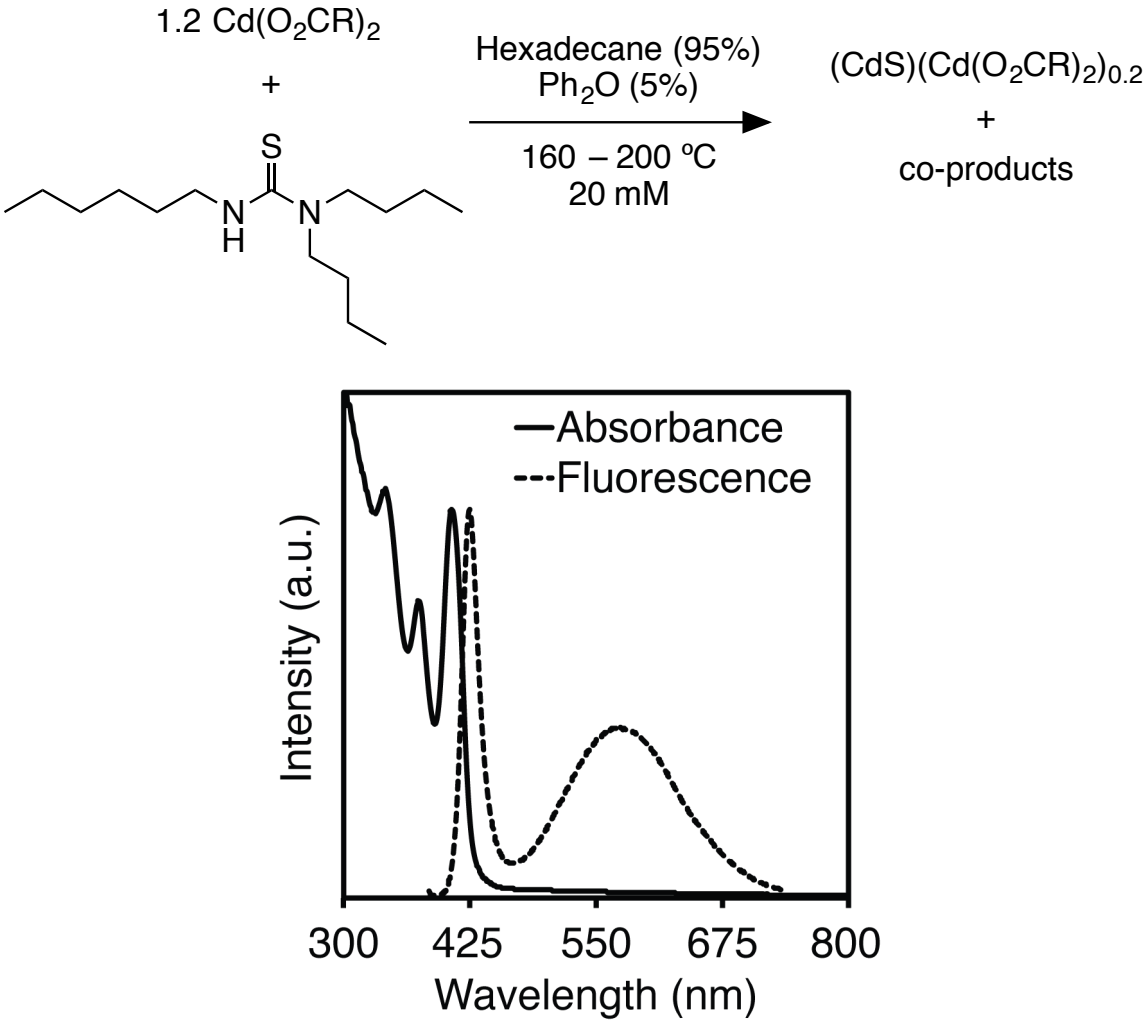


Figure 2.7.1. UV-visible absorption and photoluminescence spectra of CdS nanocrystals synthesized from **9**.

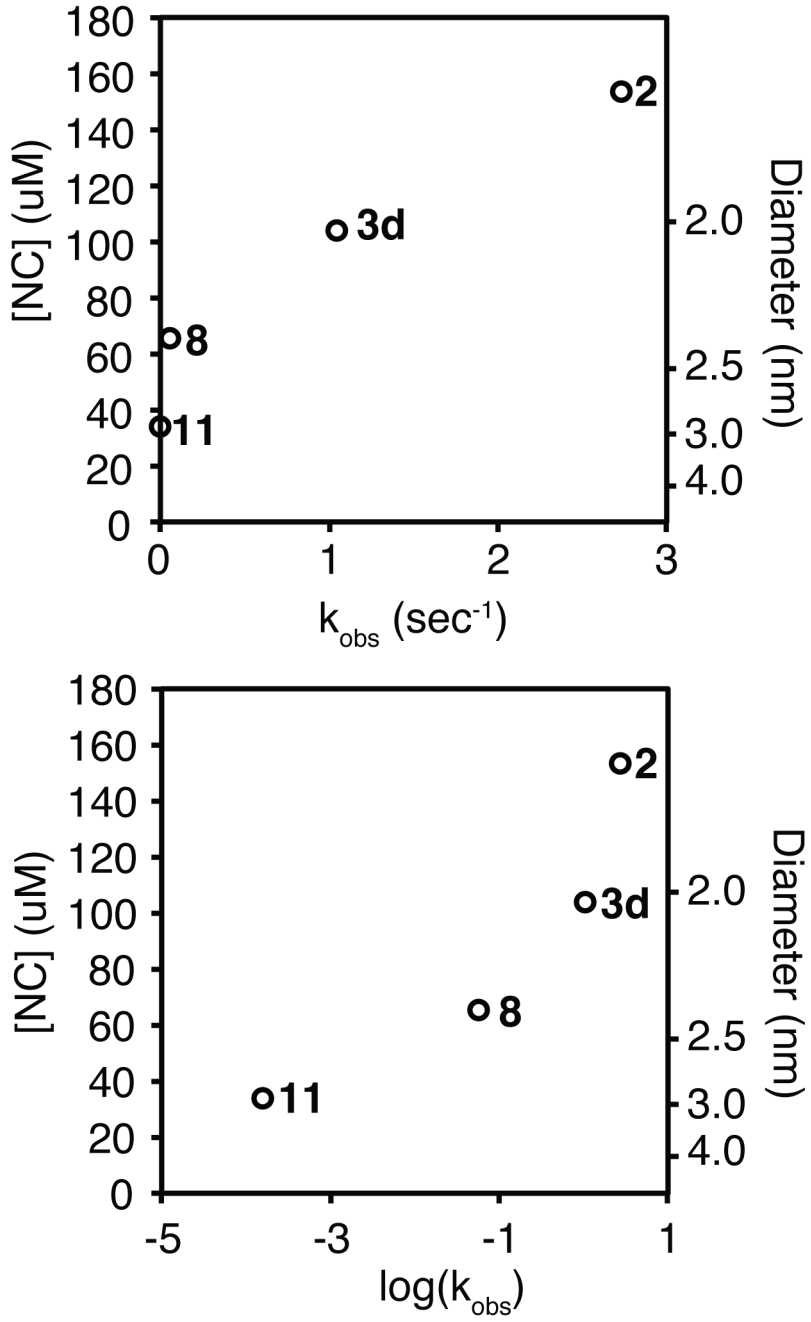


Figure 2.7.2. CdS nanocrystal number and size as a function of rate constant. Final nanocrystal concentration and diameter are plotted versus $k_{obs}$ (top) and log($k_{obs}$) (bottom) for a variety of substituted thiourea precursors: *N*,*N*′-diphenylthiourea (**2**), *N*-phenyl-*N*′-*n*-dodecylthiourea (**3d**), *N*-*n*-hexyl-*N*′-*n*-dodecylthiourea (**8**), and *N*-phenyl-*N*′-di-*n*-

butylthiourea (**11**). The reactivity trend is the same as was observed for reaction of these compounds with lead oleate: the conversion rate slows as the substituents change from aryl to alkyl and as the number of substituents increases from disubstituted thioureas to trisubstituted thioureas. However, the nanocrystal number and size have a weaker dependence on conversion rate for CdS, therefore requiring larger changes in rate to span similar ranges of size. **2** converts at a rate that is near the limit of mixing kinetics under these conditions, so the measured rate is likely an underestimate. *N*,*N*,*N*′,*N*′-tetramethylthiourea (**12**) was also tested and found to react most slowly. As expected, the nanocrystals were larger, however, the conversion rate required extremely long reaction times at 150 °C and eventually produced an insoluble precipitate. As a result it was omitted from the plot above.

*2.7.2. ZnS*

We next turned our attention to ZnS, a wide bandgap material studied primarily as a host for luminescent ion dopants[105,106] and as a shell material for CdSe quantum dots.[103] Surprisingly, we noticed a dearth of methods for ZnS synthesis given how widely studied it is, so we developed our own using chemistry analogous to our CdS and PbS syntheses.

The results are shown in Figure 2.7.3. ZnS nanocrystals from **8** show a remarkably narrow lowest energy electronic transition compared to the best in the literature;[107,108] however, nanocrystals made from slower-converting **11** show few features despite showing low polydispersity by TEM. This change in optical

properties derives from zinc sulfide's small Bohr exciton radius (2.5 nm); nanocrystals close to this size and above are expected to show only weak quantum confinement effects. By powder X-ray diffraction, it is clear that ZnS is in the zinc blende phase, but a distinct peak at smaller angles persists even after purification procedures. We tentatively assign this to residual $Zn(O_2CR)_2$ bound to nanocrystals on the basis of 1) the relatively high excess (1.5 equiv.) of starting $Zn(O_2CR)_2$ in the reaction mixture, 2) the relative difficulty of removing polymeric metal carboxylate from small nanocrystal samples as discussed in Section 2.6.6 and 2.9.15, 3) the broadened scattering pattern relative to pure zinc oleate, which suggests that there is poorer ordering between alkyl chains, as would be expected from ligands bound to spherical nanocrystals, and 4) the relatively weak X-ray scattering properties of Zn and S relative to C (as compared to heavier metals like Cd and Pb). Alternatively, this small-angle intensity may have to do with the regular packing observed in samples like that shown in Figure 2.7.3C. Lastly, $^1$H NMR spectroscopy of an isolated sample shows a single broad alkene resonance, consistent with bound oleate chains.

This synthesis is a solid launching point for further development. Standalone ZnS nanocrystals are less technologically useful than epitaxial ZnS shells on luminescent nanocrystals, but nonetheless we can use this platform to study conversion rates, size tunability, nucleation thresholds, and ZnS surface

chemistry. Further study should focus on developing quantitative methods to track precursor conversion and ZnS formation; unlike PbS and CdS, sizing formulas and extinction coefficients have not been published for ZnS nanocrystals, making rapid study by absorbance spectroscopy more difficult in the short term. However, it should be possible to study precursor disappearance by $^{1}H$, $^{13}C$, or $^{19}F$ NMR, if substituents and/or isotopic labels are chosen judiciously.

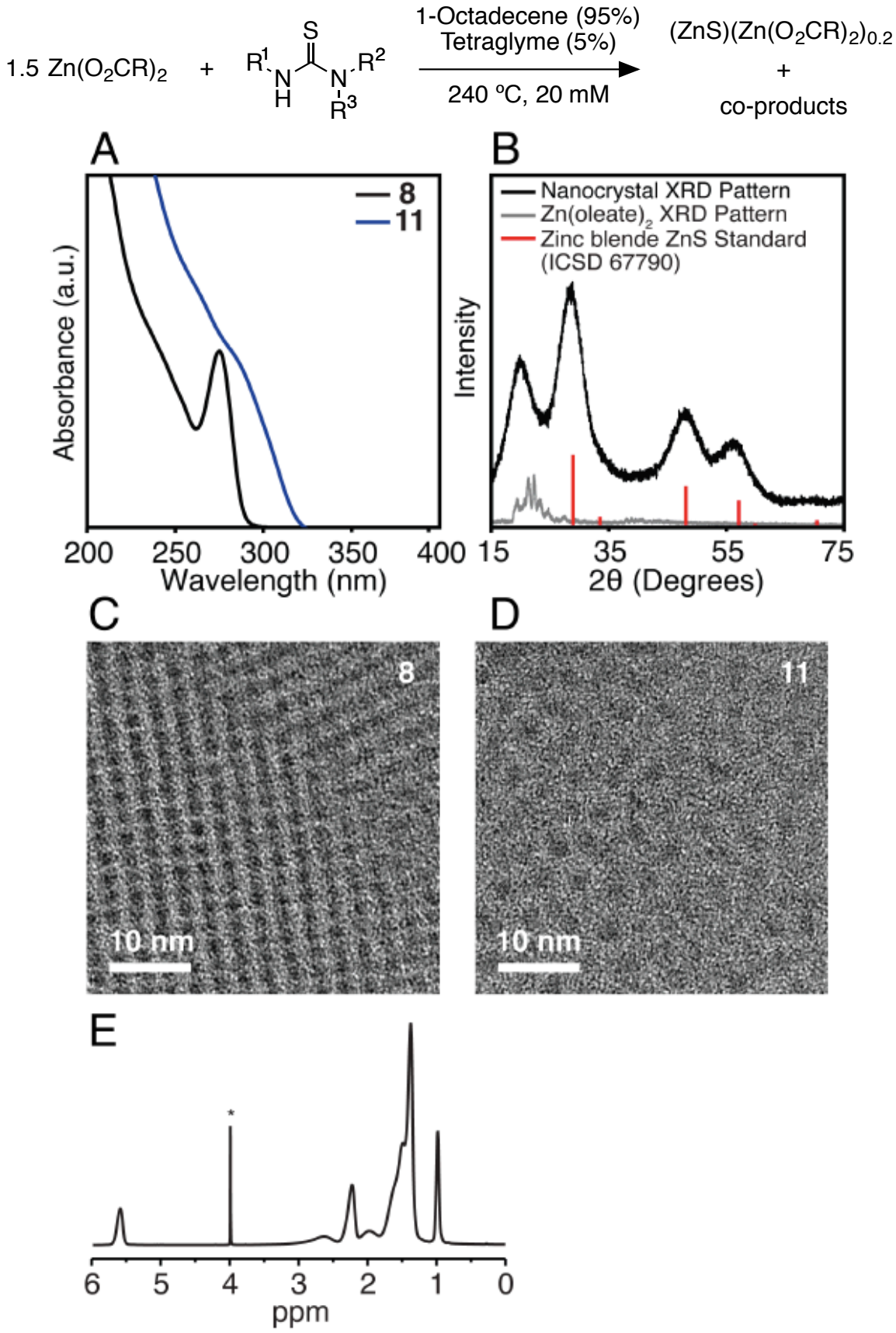
1.5 Zn(O2CR)2
+
S
R1
N
H
N
R2
R3
1-Octadecene (95%)
Tetraglyme (5%)
240 °C, 20 mM
(ZnS)(Zn(O2CR)2)0.2
+
co-products
A
8
11
Absorbance (a.u.)
200
250
300
350
400
Wavelength (nm)
B
Nanocrystal XRD Pattern
Zn(oleate)2 XRD Pattern
Zinc blende ZnS Standard
(ICSD 67790)
Intensity
15
35
55
75
2θ (Degrees)
C
8
10 nm
D
11
10 nm
E
*
6
5
4
3
2
1
0
ppm

Figure 2.7.3. A) UV-vis absorption spectrum of ZnS nanocrystals synthesized from *N*-hexyl-*N'*-dodecylthiourea (**8**) and *N*-phenyl-*N'*,*N'*-di-*n*-butylthiourea (**11**). B) Powder X-ray diffraction pattern of ZnS nanocrystals after isolation as described below. An exponential baseline correction was applied to the data to remove signal from scattering. The peak at 20° is attributed to zinc oleate associated with nanocrystals. The ZnS standard was obtained from International Crystallographic Structure Database (ICSD) as coll. code 67790. C) Transmission electron micrograph of ZnS nanocrystals synthesized from *N*-hexyl-*N'*-dodecylthiourea (**8**) with a measured diameter of 1.8 ± 0.2 nm D) Transmission electron micrograph of ZnS nanocrystals synthesized from *N*-phenyl-*N'*,*N'*-di-*n*-butylthiourea (**11**) with a measured diameter of 2.5 ± 0.4 nm (E) $^{1}$H NMR spectrum of isolated ZnS nanocrystals. (*) Sharp signal at $\delta$ = 4.0 is a ferrocene internal standard.

*2.7.3. CdS Nanorods*

The general applicability of thioureas to spherical quantum dots made us wonder if similar size tunability would be possible in anisotropic nanocrystal synthesis. To test this idea, we used several substituted thioureas in place of trioctylphosphine sulfide in a slightly modified literature CdS nanorod synthesis.[109] As is clear from Figure 2.7.4, Figure 2.7.5, and Figure 2.7.6, slower converting thioureas lead to longer nanorod aspect ratios. This is consistent with the idea that fewer nanocrystals nucleate under slower solute supply rates, and allows us to deconvolute the effects of precursor conversion rate versus

surfactant mixture in studying anisotropic nanomaterials. In the present case, nanorod formation is favored by intentionally spiking wurtzite CdS synthesis with low concentrations of short-chain phosphonic acids that favor elongated faceting. More broadly speaking, from this dataset we have learned that conversion rate tunes the nanocrystal number while surfactant composition tunes the nanocrystal morphology.

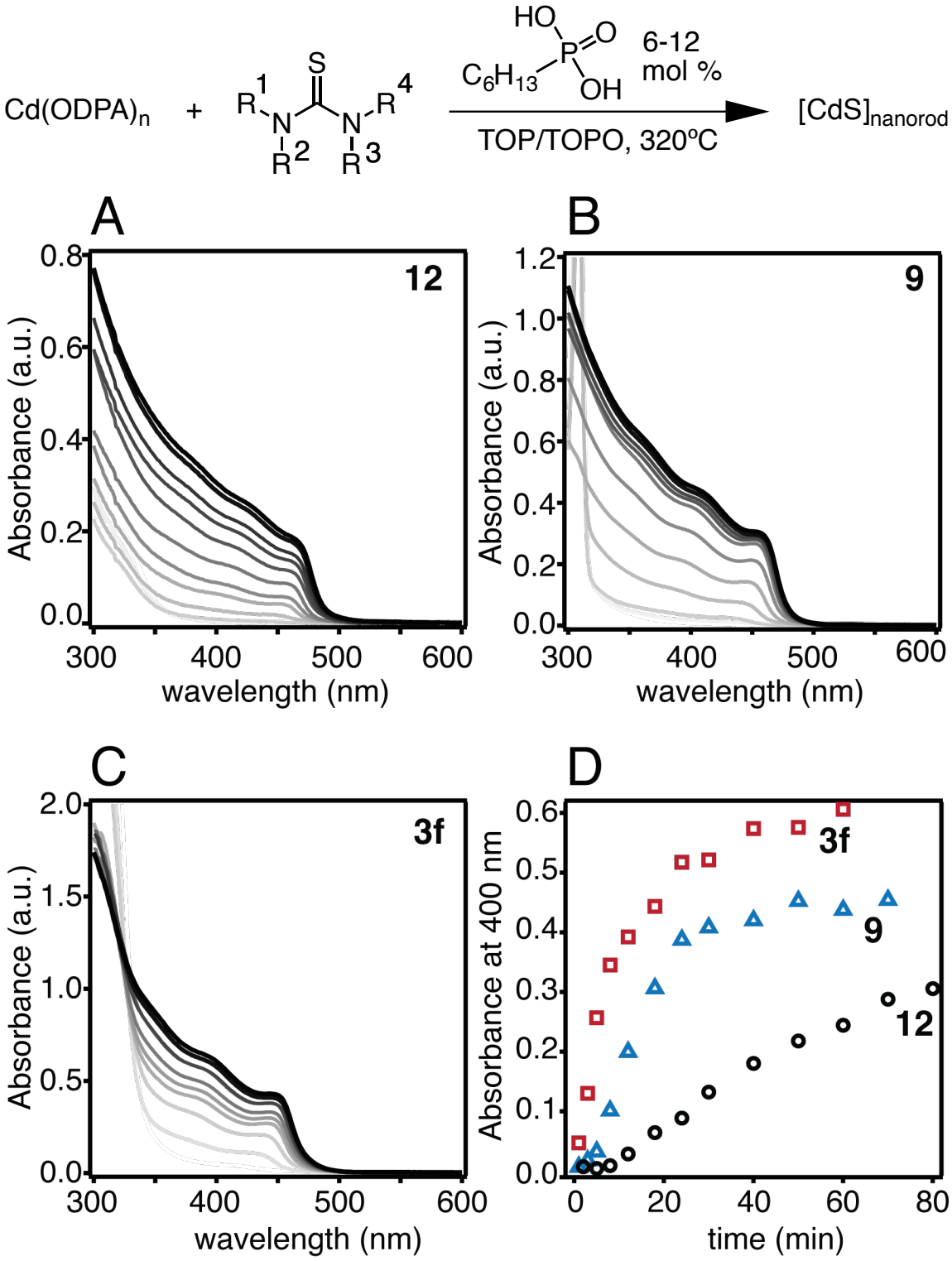


Figure 2.7.4. Synthesis and optical characterization of CdS nanorods. UV-Vis absorbance spectra of reaction aliquots taken from the syntheses of

CdS nanorods synthesized with 12 mol% hexylphosphonic acid and A) **12**, B) **9**, and C) **3f**. D) Absorbance measured at 400 nm from each aliquot versus time gives a rough estimate of reaction kinetics for each synthesis.

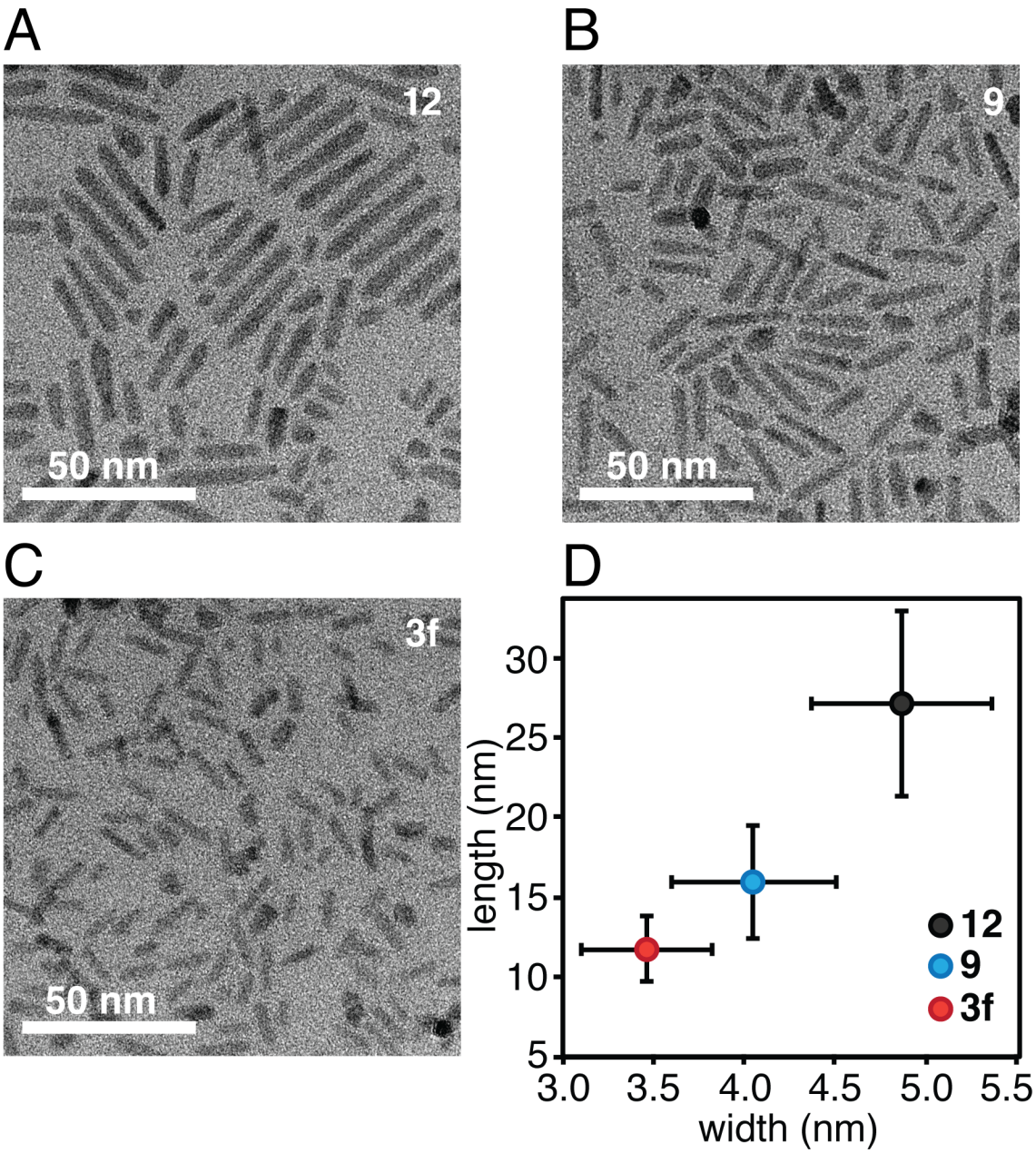


Figure 2.7.5. Transmission electron microscope images of CdS nanorods synthesized with 12 mol% hexylphosphonic acid and thiourea (A) **12**, (B) **9**, and (C) **3f**; samples were prepared without any intentional size selective

precipitation. D) Average nanorod dimensions for the three samples measured from the images of at least 200 nanorods in each sample. Error bars represent one standard deviation.

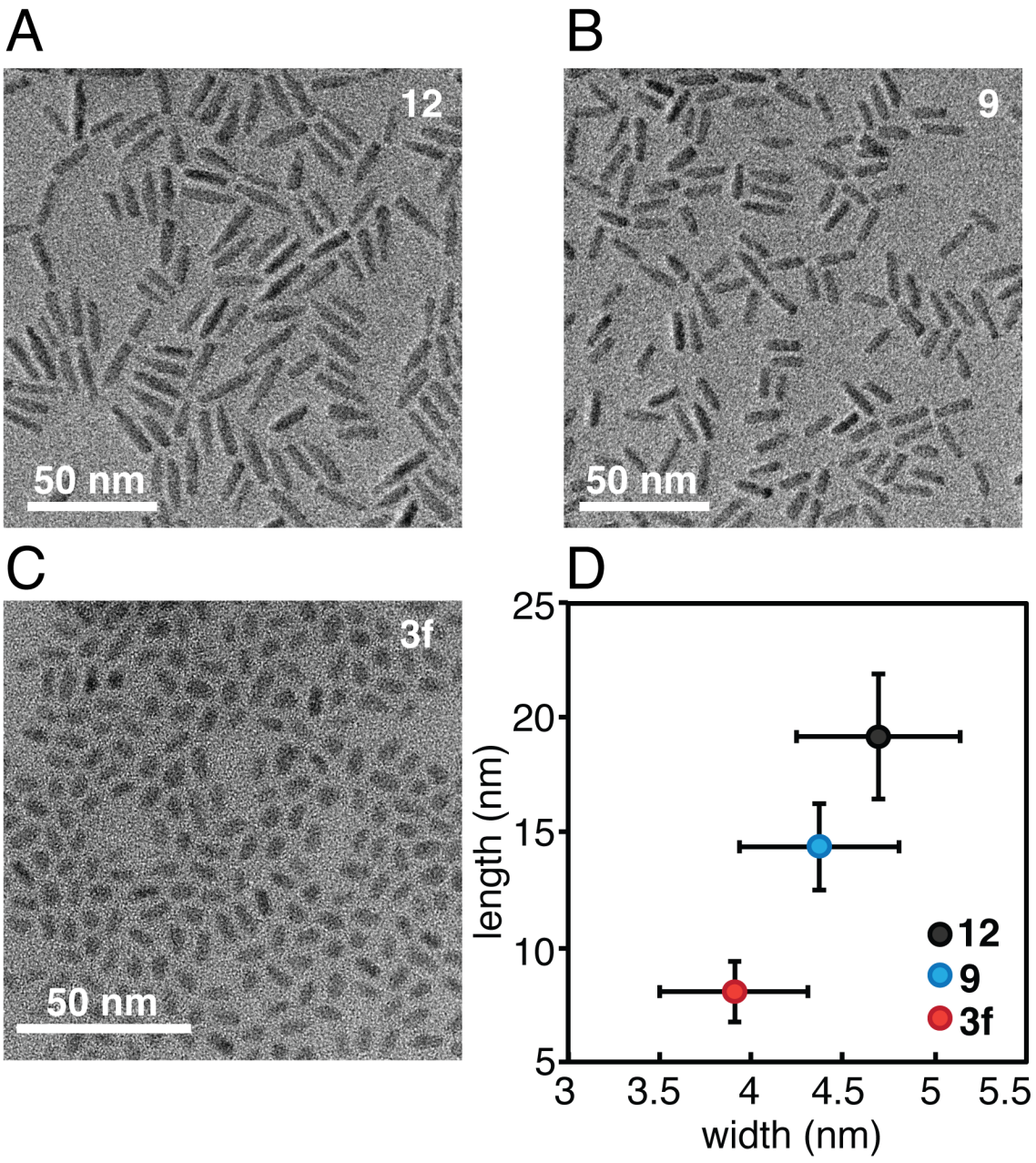


Figure 2.7.6. Transmission electron micrographs of CdS nanorods synthesized with 6 mol% hexylphosphonic acid and thiourea A) **12**, B) **9**,

and C) **3f**; samples were prepared without any intentional size selective precipitation. The lower concentration of short-chain phosphonic acids results in an overall decrease in the aspect ratio with an increase in the monodispersity of the nanorod lengths. D) Average nanorod dimensions for the three samples measured from the images of at least 200 nanorods in each sample. Error bars represent one standard deviation.

*2.7.4. $Cu_{2-x}S$ Nanoplatelets, SnS Nanosheets, and NiS Nanocrystals*

By adapting several literature methods,[110,111] we developed syntheses of $Cu_{1.8}S$ nanoplatelets (Figure 2.7.7), SnS nanosheets (Figure 2.7.8), and irregular NiS nanocrystals (Figure 2.7.9). We were able to demonstrate size tunability in $Cu_{1.8}S$ and NiS, again extending the concept of kinetic size control to unexplored venues. All three materials display high degrees of anisotropy as well, particularly in the case of few-layer-thick, 100+ nm-wide SnS nanosheets. $Cu_{2-x}S$ nanocrystals are known to have composition-dependent plasmonic properties, making kinetic control over synthesis important.[112–115]

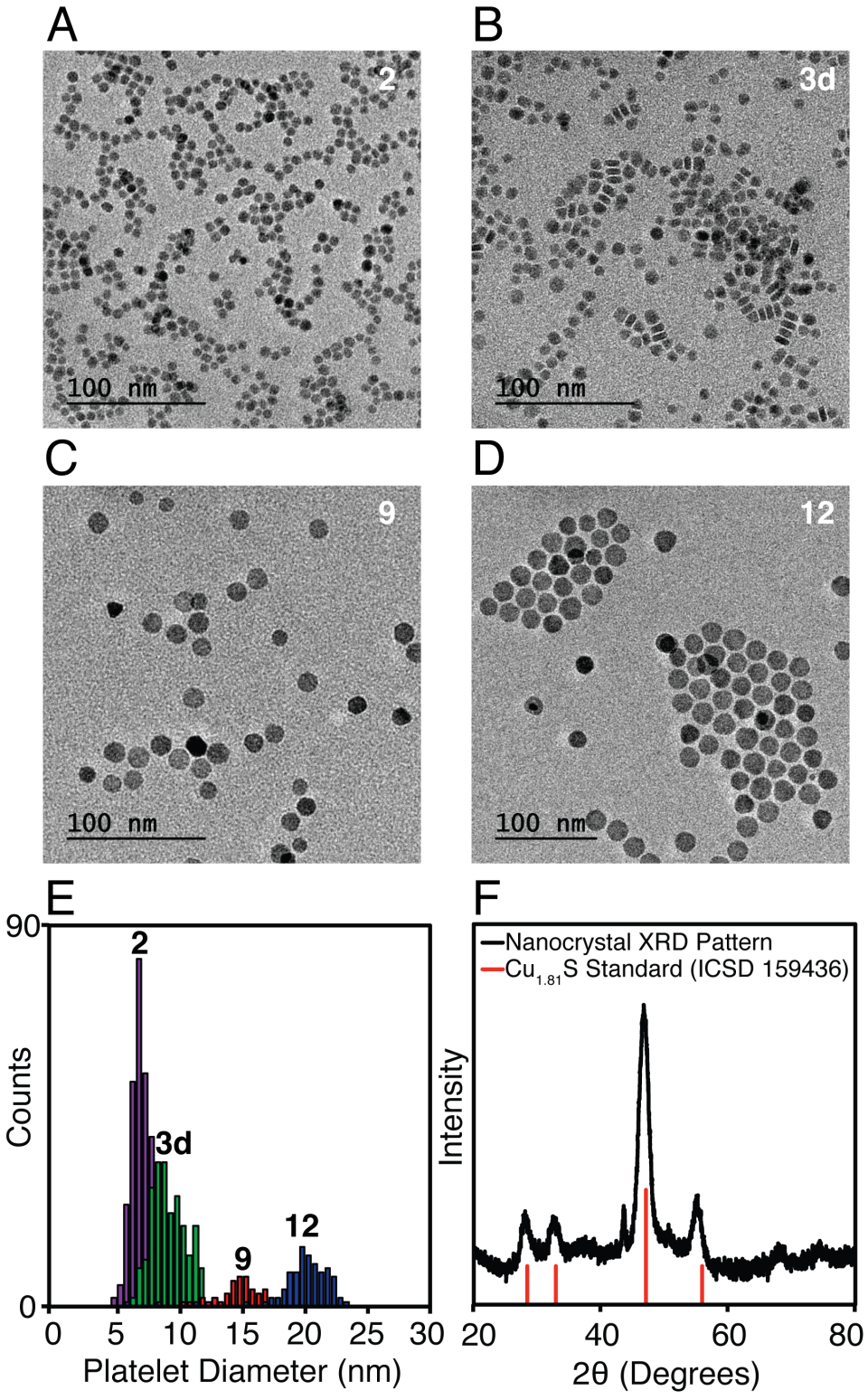


Figure 2.7.7. Synthesis and characterization of copper sulfide nanoplatelets. Transmission electron micrographs of $Cu_{2-x}S$ nanocrystals

synthesized with A) *N*,*N*′-diphenylthiourea (**2**), B) *N*-phenyl-*N*′-*n*-dodecylthiourea (**3d**), C) *N*-*n*-hexyl-*N*′,*N*′-di-*n*-butylthiourea (**9**), and D) *N*,*N*,*N*′,*N*′-tetramethylthiourea (**12**). A histogram of the platelet diameters (ignoring the platelet depth, e.g. the short lengths in B)) is shown in E), clearly demonstrating a systematic variation in size. F) X-ray powder diffraction data from $Cu_{2-x}S$ nanocrystals synthesized from **2**. The $Cu_{1.8}S$ standard was obtained from the International Crystallographic Structure Database (ICSD) as coll. code 159436. An exponential baseline correction was applied to the data to remove signal from scattering.

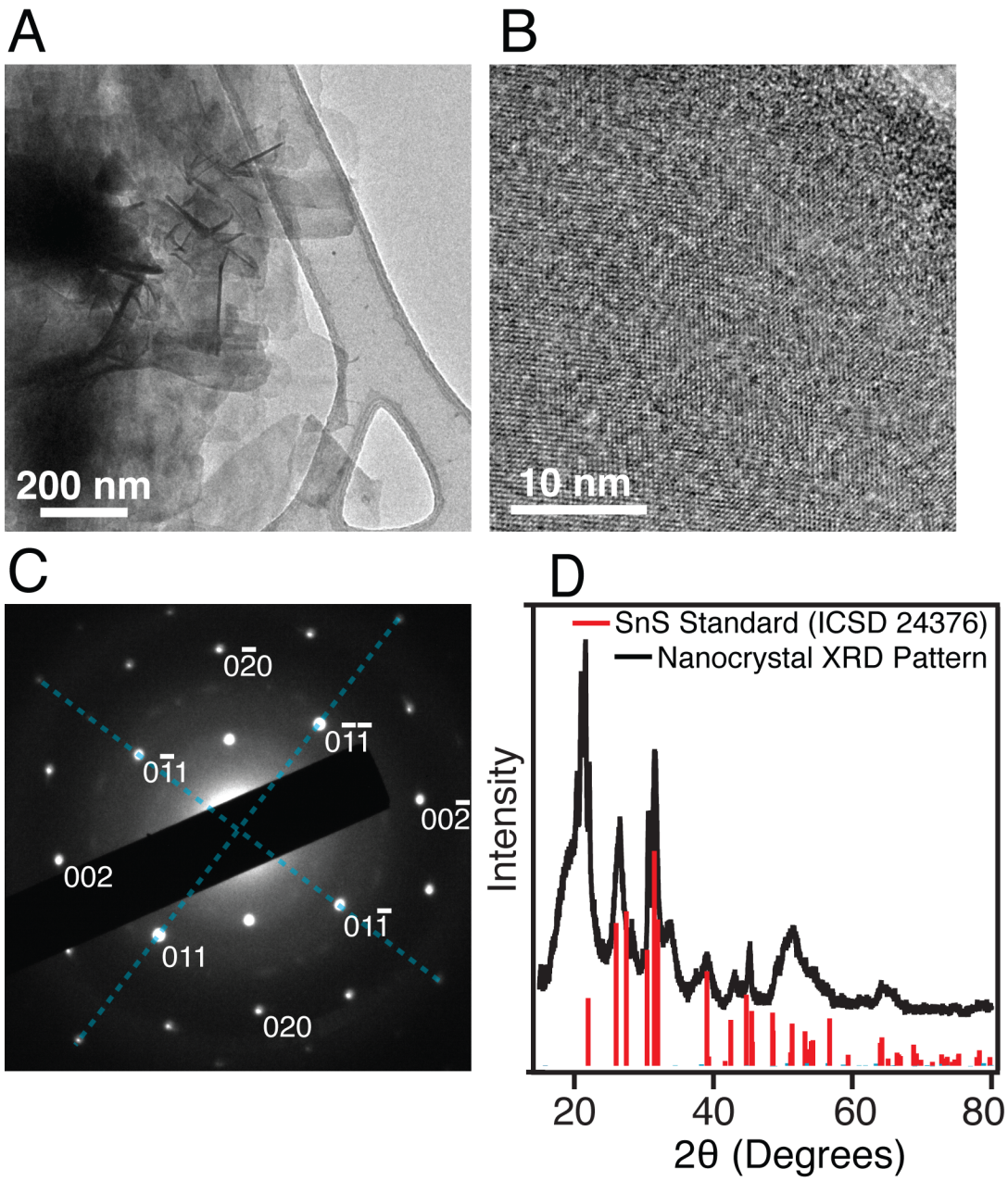


Figure 2.7.8. Synthesis and characterization of SnS nanosheets. A) Transmission electron micrograph of SnS nanosheets; B) High resolution transmission electron micrograph showing the crystallinity of the nanosheet product. C) Electron diffraction of a single SnS nanosheet, indexed according to a known modification.[111] The diffraction shows a slight distortion from the bulk orthorhombic phase as seen previously. D)

Powder X-ray diffraction pattern of SnS nanocrystals. An exponential baseline correction was applied to the XRD data to remove signal from scattering. The $\alpha$-SnS standard was obtained from the International Crystallographic Structure Database (ICSD) as coll. code 24376.

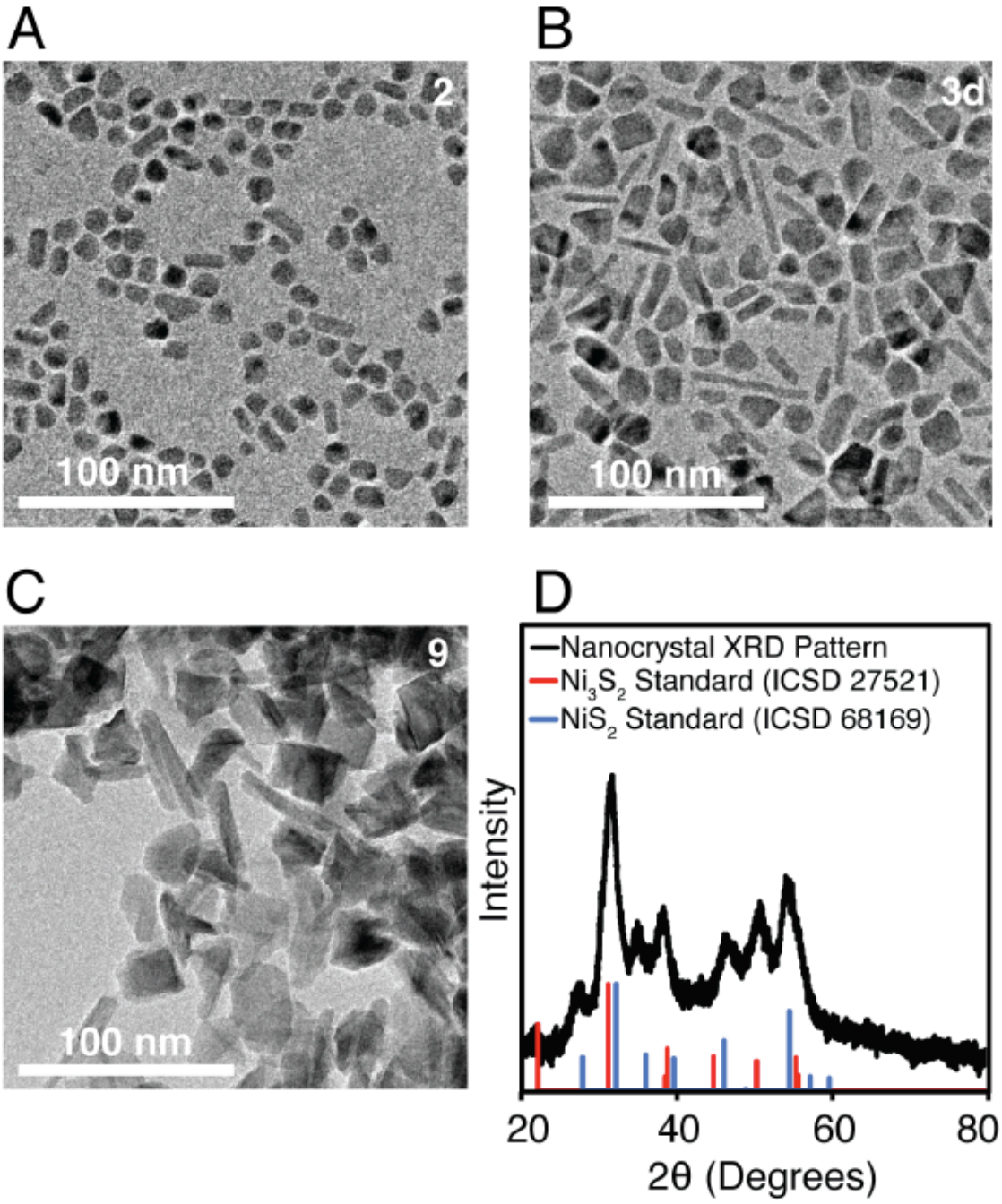

Figure 2.7.9. Synthesis and characterization of NiS nanocrystals. Transmission electron micrographs of NiS nanocrystals synthesized from A) *N*,*N*′-diphenylthiourea (**2**), B) *N*-phenyl-*N*′-*n*-dodecylthiourea (**3d**), and C) *N*-*n*-hexyl-*N*′,*N*′-di-*n*-butylthiourea (**9**). D) X-ray powder diffraction data nickel sulfide nanocrystals synthesized from **2**. The standard were obtained from the International Crystallographic Structure Database (ICSD) as coll. codes 27521 and 68169. An exponential baseline correction was applied to the data to remove signal from scattering.

*2.7.5. $Cu_2ZnSnS_4$*

We next sought to extend thiourea-based synthesis to copper zinc tin sulfide ($Cu_2ZnSnS_4$, "CZTS") nanocrystals. This material system served two purposes: 1) a demonstration of thioureas' applicability to complex quaternary materials, and 2) a low-cost synthesis of a solution-processible solar photovoltaic material. We adapted a recent synthesis that utilized two sulfur sources: carbon disulfide to react at low temperature and nucleate particles, and dodecanethiol to react more slowly and promote growth after a temperature increase.[116] We replaced these with *N*,*N*′-diphenylthiourea (**2**) and *N*,*N*,*N*′,*N*′-tetramethylthiourea (**12**), respectively, and arrived at a synthesis that produced the desired kesterite phase of CZTS (Figure 2.7.10). Importantly, while the size distributions shown in Figure 2.7.10D are comparable to those in the literature, it is clear that thioureas alone do not lead to narrow size distributions.

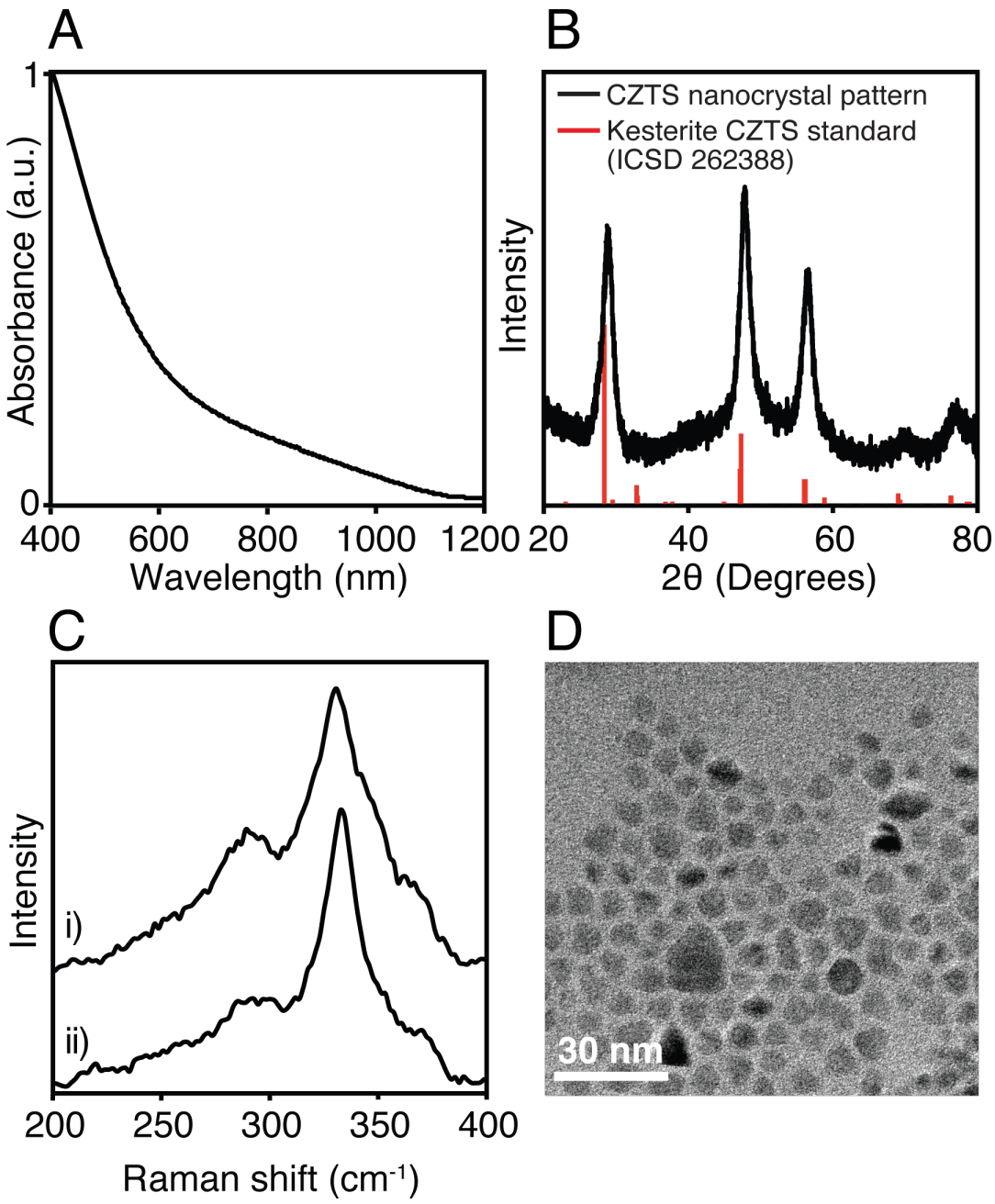


Figure 2.7.10. Synthesis and characterization of kesterite CZTS nanocrystals. A) UV-Vis-NIR absorbance spectrum of CZTS nanocrystals dissolved in chloroform. B) Powder X-ray diffraction pattern of CZTS nanocrystals (CZTS standard was obtained from International Crystallographic Structure Database (ICSD) as coll. code 262388). C)

Raman spectra of CZTS nanocrystals i) as synthesized and ii) after annealing at 400 °C under vacuum for 5 minutes. The lineshape is similar to those reported by Chesman et al.[116] and can be used to rule out the presence of impurity phases. (D) Transmission electron micrograph of CZTS nanocrystals.

*2.7.6. CdSe/CdS/ZnS*

Lastly, we adapted thioureas to the synthesis of luminescent core/shell nanocrystals by a traditional method known as successive ion layer adsorption and reaction (SILAR).[117] This strategy involves sequential additions of metal and nonmetal precursor each aimed at growing half of a monolayer onto the existing nanocrystals. Once the desired size/brightness is achieved, the reaction is halted. Since its introduction in 2003, it has become one of the most widely used quantum dot shelling methods.

We replaced the traditional S-ODE precursor with *N*-*n*-hexyl-*N*′,*N*′-di-*n*-octylthiourea (**10**) and achieved similar results to commonly reported CdSe/CdS/ZnS core/shell/shell nanocrystals synthesized by SILAR. Importantly, we found it necessary to cut the amount of thiourea by 1/3 in order to achieve the same results; this is because thioureas convert completely to metal sulfide while S-ODE does not (see Section 2.2.2).

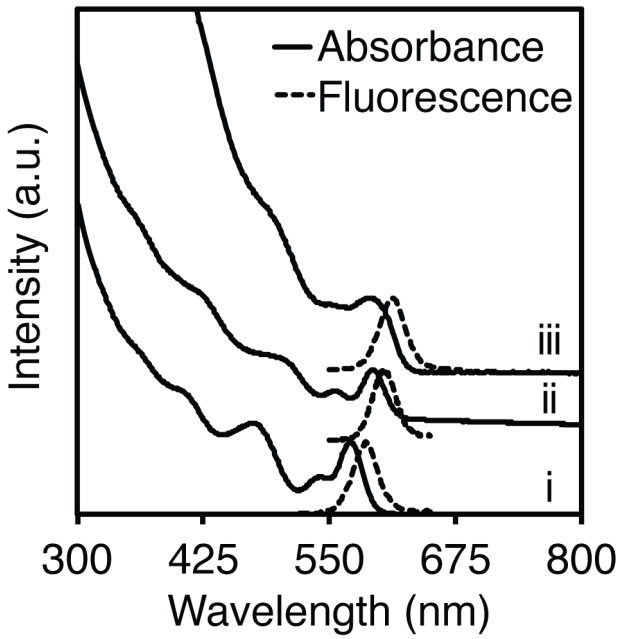


Figure 2.7.11. Synthesis and characterization of CdSe/CdS/ZnS core/shell/shell nanocrystals. UV-Vis absorbance and photoluminescence spectra of (i) CdSe cores, (ii) CdSe/CdS core/shell heterostructures, and (iii) CdSe/CdS/ZnS core/shell/shell heterostructures synthesized as described below. The photoluminescence quantum yield of the nanocrystals increased from 30% for the unshelled cores to 55% when shelled with CdS and ZnS. This is comparable to the results of the published synthesis that was adapted.[117]

This being said, SILAR is not an optimal strategy for large-scale nanocrystal production because of its time-consuming, multistep nature and its sensitivity to slight perturbations. In Chapter 4, we will discuss our subsequent efforts to develop syntheses of $CdSe_{1-x}S_x$ core/shell and graded alloy nanocrystals by injection mixtures of thio- and selenoureas simultaneously.

## 2.8. Summary

In this chapter, we have explored the theory and history of colloidal nanocrystal synthesis and leveraged an easily synthesized library of thiourea derivatives toward size-tunable nanocrystal synthesis in quantitative yields. We have accomplished this by taking advantage of the "critical" relationship between the rate of solute supply to the crystallization medium and the extent of nucleation. Using PbS as a model system, we have demonstrated relationships between substituent character, reaction rate, nanocrystal concentration, and nanocrystal size. We then used these observations to optimize large-scale syntheses of PbS and demonstrate broad applicability of thioureas across an extremely wide parameter space. These advances are substantial, but the concept of rate tunability is the truly important feature of this work. The thiourea "platform" should increase access to high-quality nanocrystalline materials and accelerate the pace of progress in nanocrystal science, which is becoming increasingly important as nanocrystal-based materials make their way into industrial and consumer products. Moreover, thioureas are not the only library of compounds imaginable. In Chapter 3, we will discuss our subsequent work on selenoureas, and in Chapter 4, we will show the use of thiocarbonate precursors developed in parallel.

## 2.9. Experimental Details

### *2.9.1. General Considerations*

All manipulations were performed in air unless otherwise indicated. Toluene (99.5%), tetrachloroethylene (99%), methyl acetate (99%), hexanes (98.5%), methanol (99.8%), ethanol (≥99.8%), dichloromethane (≥99.5%), chloroform (≥99.8%), acetone (≥99.8%), acetonitrile (99.5%), diphenyl ether (99%), 1-octadecene (90%), tetraethylene glycol dimethyl ether ("tetraglyme" ≥99%), isopropanol (≥99.7%), triethylamine (≥99%), tri-*n*-butylamine (≥99.5%), trifluoroacetic acid (99%), trifluoroacetic anhydride (≥99%), cadmium nitrate tetrahydrate (98%), zinc acetate dihydrate (≥99.0%), zinc nitrate hexahydrate (98%), copper(I) iodide (99.999%), tin(IV) chloride pentahydrate (98%), tin(II) chloride (98%) zinc chloride (99.99%), nickel(II) chloride (98%), hexylphosphonic acid (95%), *N*,*N*,*N'*,*N'*-tetramethylthiourea (98%) (**12**), hexamethyldisilazane (99.9%), myristic acid (≥99%), sodium hydroxide (97%, 98%), selenium (pellets, < 4 mm, ≥99.99%), phenyl isothiocyanate (98%), 4-chlorophenyl isothiocyanate (99%), hexyl isothiocyanate (95%), cyclohexyl isothiocyanate (98%), 4-methoxyphenyl isothiocyanate (98%), isopropyl isothiocyanate (97%), 4-(trifluoromethyl)phenyl isothiocyanate (97%), 4-cyanophenyl isothiocyanate (98%), hexylamine (99%), octylamine (99%), dodecylamine (98%), octadecylamine (99%), oleylamine (technical grade, 70%), oleylamine (98%,

primary amine), aniline (99%), *o*-toluidine (≥99%), di-*n*-octylamine (98%), and di-*n*-butylamine (99.5%) were obtained from Sigma Aldrich and used without further purification. Oleic acid (99%) was obtained from either Sigma Aldrich or Alfa Aesar and used without further purification. Cadmium oxide (99.99%), copper(II) acetylacetonate (98+%), nickel(II) stearate, tri-*n*-octylphosphine (min. 97%), and tri-*n*-butylphosphine (99%) were purchased from Strem Chemicals and used as received. Lead(II) oxide was obtained from either Strem (99.999+%) or Alfa Aesar (99.9995%) and used without further purification. 3,5-bis(trifluoromethyl)phenyl isothiocyanate (97+%) was obtained from Maybridge and used as received. Hexadecane (99%) and 2-isopropylaniline (97%) were obtained from Sigma Aldrich, stirred with calcium hydride overnight, and distilled prior to use. 1-Octene (99%) was obtained from Acros Organics, stirred with calcium hydride overnight, and distilled prior to use. Diethylene glycol dimethyl ether ("diglyme", anhydrous, 99.5%) was obtained from Sigma Aldrich and shaken with activated alumina prior to use. *N*,*N*'-diphenylthiourea (98%) (**2**) was obtained from Aldrich or synthesized according to the procedure below. Tri-*n*-octylphosphine oxide (99%) was obtained from Aldrich and recrystallized from hot acetonitrile.

Kinetics experiments were monitored at 400 nm using an Ocean Optics TP300 dip probe (2 mm path length) attached to a Perkin-Elmer Lambda 650

spectrophotometer equipped with deuterium and halogen lamps. UV-Vis-NIR spectra were obtained using a Perkin-Elmer Lambda 950 spectrophotometer equipped with deuterium and halogen lamps and either a PbS or InGaAs detector. UV-Vis-NIR spectra were corrected with a linear baseline correction and an offset at the detector change (860 nm). Samples for UV-Vis-NIR and photoluminescence spectroscopies were dissolved in tetrachloroethylene for PbS, toluene for CdS, and hexanes for ZnS, and a blank with the same solvents at the concentrations of the corresponding sample was used. Photoluminescence measurements in the range 300-800 nm were performed using a Fluoromax 4 from Horiba Scientific, and quantum yields were determined using a quanta-phi integrating sphere accessory. Transmission electron microscopy (TEM) was performed on either a JEOL JEM-100CX or a JEOL 2100 TEM. Powder X-ray diffraction (XRD) was measured on a PANalytical X'Pert Powder X-ray diffractometer. Raman spectra were obtained using a Renishaw inVia Raman Microscope with a 532 nm laser operating at 27 mW and 1% power, in the range of 200-400 $cm^{-1}$ with a resolution of 2 $cm^{-1}$. Acquisition times were 10 s per scan with the final spectrum from the co-addition of 185 scans.

*2.9.2. Synthesis of Substituted Thioureas*

A solution of alkylamine (3.0 mmol) in toluene (2.5 mL) was added to a solution of alkyl or aryl isothiocyanate (3.0 mmol) in toluene (2.5 mL). The

solution became warm upon the addition and was allowed to stir for a few minutes before the volatiles were removed under vacuum. The product is thoroughly dried under vacuum to remove trace toluene, the duration of which depends on the reaction scale (3 – 24 hours), resulting in quantitative yield in all cases. These reactions can be run at 30x the scale and 3x the concentration described with no observable changes. A wide variety of *N*-alkyl-*N'*-arylthioureas (**3a-3f**) are best obtained from aryl isothiocyanates and alkylamines rather than the corresponding alkyl isothiocyanate, which react sluggishly with anilines.

*2.9.3. Example Thiourea Synthesis:* N-*dodecyl*-N*'-phenylthiourea (**3d**)*

*N*-dodecyl-*N'*-phenylthiourea was prepared according to the general procedure from solutions of dodecylamine (11.56 g, 62.4 mmol) in toluene (20 mL) and phenyl isothiocyanate (8.44 g, 62.4 mmol) in toluene (20 mL), producing a white powder. Yield: 19.56 g (98%).

*2.9.4. Synthesis of Lead(II) Oleate from Lead(II) Trifluoroacetate*

Lead(II) oxide (10.00 g, 44.8 mmol) and acetonitrile (20 mL) are added to a 100 mL round bottom flask. The suspension is stirred while being cooled in an ice bath for ten minutes, after which trifluoroacetic acid (0.7 mL, 8.96 mmol, 0.2 equiv.) and trifluoroacetic anhydride (6.2 mL, 44.8 mmol, 1 equiv.) are added.

After fifteen minutes the yellow lead oxide has dissolved, resulting in a clear and colorless solution that is allowed to warm to room temperature. To a 500 mL Erlenmeyer flask, oleic acid (25.437 g, 90.05 mmol, 2.01 equiv.), isopropanol (180 mL), and triethylamine (10.246 g, 101.25 mmol, 2.26 equiv.) are added. The lead trifluoroacetate solution is then added to the oleic acid solution with stirring, resulting in the formation of a white precipitate. The mixture is heated to reflux in order to dissolve the precipitate whereupon a clear and colorless solution is obtained. The heat is then turned off and the flask allowed to slowly cool to room temperature over > 2 hours, followed by further cooling in a –20 °C freezer for > 2 hours. The resulting white powder is isolated by suction filtration using a glass fritted funnel, the filtrate thoroughly washed with methanol (3 x 300 mL) being careful to thoroughly stir the slurry to break up any large pieces, and then dried under vacuum for > 6 hours. The free flowing white powder is stored in a nitrogen-filled glovebox. Typical yields are 31.1 g – 32.8 g (90 – 95%). This reaction can be run at three times the scale described with no observable changes.

*2.9.5. Synthesis of Lead(II) Oleate from Lead(II) Nitrate*

Select experiments were conduced with lead oleate prepared from lead nitrate prepared as described below. No noticeable difference in reactivity was observed. However, the procedure using lead trifluoroacetate described above is

strongly preferred because of the availability of higher purity PbO, as well as the smaller required reaction volumes and greater yields obtained.

The following method was adapted from a preparation of cadmium tetradecanoate.[66] Sodium hydroxide (1.800 g, 45 mmol, 2.25 equiv.) is dissolved in methanol (1 L). To this solution oleic acid (12.710 g, 45 mmol, 2.25 equiv.) is slowly added. A solution of lead (II) nitrate (6.624 g, 20 mmol, 1.0 equiv.) in methanol (250 mL) is then added, the mixture heated until a clear solution is obtained, and the heat and stirring are turned off. After cooling to room temperature, the solution is decanted to remove any insoluble residue, and stored in a 5 °C refrigerator overnight during which time a white powder precipitates. The resulting white powder is isolated by suction filtration using a fine glass fritted funnel, the filtrate thoroughly washed with methanol (3 x 300 mL) being careful to thoroughly stir the slurry to break up any large pieces, and then dried under vacuum for > 6 hours. The white powder is stored in a nitrogen-filled glovebox. Typical yields are 3.9 g – 7.8 g (25 – 50%). This reaction can be run at double the scale described with no observable changes.

*2.9.6. Example Large-Scale Synthesis of 3.4 nm PbS Nanocrystals*

In a nitrogen-filled glove box, lead(II) oleate (8.812 g, 11.44 mmol, 1.5 equiv) and 1-octene (105.5 g, 147.5 mL) are added to a 250 mL 3-neck round bottom flask equipped with a stir bar and the flask is sealed with two rubber

septa and an air-free vacuum adapter. In a 20 mL scintillation vial, *N*,*N*′-diphenylthiourea (1.742 g, 7.63 mmol) and diglyme (5 mL) are mixed and the vial sealed with a rubber septum. Both vessels are transferred to a Schlenk line where they are attached to an argon inlet and brought to 95 °C in an oil bath. After the temperature of the reaction vessel is stable (15 minutes), the solution of thiourea is quickly injected into the clear colorless solution. The stirring should be vigorous and the injection should ideally be completed prior to the darkening of the mixture (< 1 second). Simultaneous injection using two syringes may be helpful. The reaction is allowed to run for 60 seconds before the flask is removed from the hot oil bath. Once cooled to room temperature, the septa are replaced with glass stoppers under positive argon flow and the volatiles removed under vacuum. The flask is sealed under vacuum and brought into a glove box whereupon toluene (40 mL) is added. The resulting slurry is split between four 50 mL centrifuge tubes and centrifuged (7000 rpm, 10 minutes). The dark nanocrystal solution is decanted and any remaining solids discarded. Methyl acetate (120 mL) is then added to the toluene solution to precipitate the nanocrystals. After centrifugation (7000 rpm, 10 minutes), the clear, pale brown solution is discarded and the remaining nanocrystal residue redissolved in toluene (40 mL). The cycle of precipitation from toluene with methyl acetate is performed six times in total to reach a ligand coverage of 5.7 oleate ligands per

square nanometer as measured by UV-Visible-NIR absorption and $^{1}$H NMR spectroscopy. Yield of (PbS)(Pb(oleate)$_2$)$_{0.26}$: 2.67 g (79.5%). *Commercially available anhydrous octane (b.p. = 125-126°C) may also be used in place of 1-octene*.

*2.9.7. Example Large-Scale Synthesis of 6.5 nm PbS Nanocrystals*

In a nitrogen-filled glove box, lead(II) oleate (14.099 g, 22.88 mmol, 1.2 equiv) and 1-octene (105.5 g, 147.5 mL) are added to a 250 mL 3-neck round bottom flask equipped with a stir bar, that is then sealed with two rubber septa and an air-free vacuum adapter. In a 20 mL scintillation vial, *N*-dodecyl-*N*'-phenylthiourea (4.890 g, 15.26 mmol) and diglyme (5 mL) are mixed and the vial sealed with a rubber septum. Both vessels are transferred to a Schlenk line where they are attached to an Argon inlet and brought to 120 °C in an oil bath. Once the temperature is stable (15 minutes), the solution of thiourea is quickly injected into the clear colorless solution. Simultaneous injection using two syringes may be helpful. The reaction is allowed to run for 10 minutes before the flask is removed from the oil bath. Once cooled to room temperature, the septa are replaced with glass stoppers under positive argon flow and the volatiles removed under vacuum. The flask is then sealed under vacuum and brought into a nitrogen glovebox. Toluene (60 mL) is added and the resulting slurry split between six 50 mL centrifuge tubes and centrifuged (7000 rpm, 10 minutes). The dark nanocrystal solution is decanted and any remaining solids discarded.

Methyl acetate (180 mL) is then added to the toluene solution to precipitate the nanocrystals. After centrifugation (7000 rpm, 10 minutes), the clear, pale brown solution is discarded and the remaining nanocrystal residue redissolved in toluene. The cycle of precipitation from toluene with methyl acetate is performed six times in total to reach a ligand coverage of 2.9 oleate ligands per square nanometer as measured by UV-Visible-NIR absorption and $^{1}$H NMR spectroscopy. *Commercially available anhydrous octane (b.p. = 125-126°C) may also be used in place of 1-octene*.

*2.9.8. Synthesis of PbS Nanocrystals for Absorbance and Photoluminescence Spectroscopies*

In a nitrogen-filled glovebox, lead(II) oleate (**1**-**2**: 231.0 mg, 0.30 mmol, 1.5 equiv.; **3a**-**3f**, **5**-**8**: 184.8 mg, 0.24 mmol, 1.2 equiv.) and hexadecane (7.344 g, 9.5 mL) were added to a 40 mL vial equipped with a stir bar and sealed with a rubber septum. The vial is removed from the glovebox, and the septum pierced with an argon inlet needle and submerged in an oil bath at the desired temperature (**1**-**2**: 95 °C; **3a**-**3f**, **5**: 120 °C; **3f**, **5**-**8:** 150 °C). Separately, the thiourea (0.30 mmol) is dissolved in diphenyl ether (0.805 g, 0.75 mL) by heating the mixture in the same oil bath. After reaching thermal equilibrium (10 minutes) the thiourea solution (500 μL, 0.20 mmol, 1.0 equiv.) is injected into the lead oleate solution. An aliquot (125 μL) is removed after 5 minutes from reactions at 95 °C

and after 20 minutes from reactions at 120 or 150 °C. The aliquot is dissolved in tetrachloroethylene (2.35 mL) for absorption and photoluminescence spectroscopies.

*2.9.9. Quantification of Nanocrystal Surface Ligand Density*

The concentrations of oleate, PbS, and nanocrystals were determined by a combination of $^1$H NMR and UV-Vis-NIR absorption spectroscopies. A toluene solution of purified nanocrystals is dried under vacuum and dissolved in $d_8$-toluene. Ferrocene dissolved in $d_8$-toluene (100 μL, 51 mM) was added to a known volume of the nanocrystal stock solution and used as an internal standard for $^1$H NMR. The concentration of ligands was determined relative to the ferrocene internal standard by integrating the ligand vinyl and ferrocene resonances and normalizing for the number of hydrogens, respectively (2:10). $^1$H NMR spectra were acquired with sufficient relaxation delay to allow complete relaxation between pulses (30 s). The molar concentration of PbS in these stock solutions was determined by diluting 10 – 50 μL to a known volume with tetrachloroethylene and measuring the absorbance at λ = 400 nm. At this wavelength, the extinction coefficient is independent of size and proportional to the concentration of PbS formula units.[83]

The wavelength of the lowest energy absorption maximum was used to determine the average nanocrystal diameter.[83] From this diameter, the number of

PbS units per nanocrystal were calculated by assuming a spherical shape and the molar volume of the bulk. The concentration of nanocrystals, the ratio of ligands per nanocrystal, and the ligand surface density were calculated from the number of PbS units per nanocrystal, the molar concentration of PbS, and ligands in the stock solution.

*2.9.10. PbS Kinetics Experiments*

In a nitrogen-filled glovebox, lead(II) oleate (0.166 g, 0.216 mmol) and hexadecane (19 mL) are added to a three neck round bottom flask equipped with a stir bar and the flask sealed with two rubber septa and an air-free vacuum adapter. The vessel is attached to a Schlenk line via an argon inlet and one of the septa replaced with a homemade air-free adapter for an in situ optical absorption dip-probe. The flask is covered in foil to eliminate ambient light and immersed in a silicon oil bath of the desired temperate. A stock solution of the desired thiourea (0.216 mmol) in diphenyl ether (1.25 g, 1.2 mL) is prepared in a 2 mL scintillation vial. After allowing the flask to reach thermal equilibrium with the oil bath (10 minutes), the vial containing the thiourea stock solution is immersed in the oil bath for 30 seconds. Continuous recording of the absorbance at 400 nm is initiated and the thiourea stock solution (1 mL, 0.18 mmol thiourea) quickly injected into the flask with vigorous stirring. This results in 20 mL of total solution, and an initial lead oleate concentration of 10.8 mM and thiourea

concentration of 9 mM. The reaction is run for 20 minutes after the injection, at which time a 250 μL aliquot was removed to measure the full UV-Vis-NIR spectrum and a 150 μL aliquot was removed for TEM analysis. The UV-Vis-NIR aliquot was dissolved in tetrachloroethylene (2.25 mL), and the TEM aliquot was dissolved in hexane (3 mL). The kinetics data was corrected by setting t = 0 as the initial appearance of absorbance at 400 nm. The baseline was also zeroed at λ = 400 nm prior to injection. The data were fit to single exponential functions, allowing single exponential rate constants to be extracted. Relative rate constants are computed versus the rate of *N*-*n*-hexyl-*N*′-dodecyl-thiourea (**8**) at 150 °C. Relative rates were determined over a range of temperatures by running some precursors at two temperatures (**3b**: 90, 120 °C and **3f**: 120, 150 °C).

*2.9.11. Synthesis and Characterization of CdS Nanocrystals*

Cadmium tetradecanoate is synthesized according to literature methods.[66] In a nitrogen-filled glovebox, cadmium tetradecanoate (136 mg, 0.24 mmol, 1.2 equiv.) and hexadecane (7.344 g, 9.5 mL) are added to a vial, which is loaded with a stir bar and sealed with a rubber septum. The vial is removed from the glovebox, the septum pierced with an argon inlet needle and submerged in an oil bath heated to 160 °C. Separately, *N*′-*n*-hexyl-*N*,*N*-di-*n*-butylthiourea (**9**) (54.5 mg, 0.2 mmol, 1.0 equiv.) is dissolved in diphenyl ether (0.537 g, 0.5 mL) by heating the mixture in the same oil bath. After both solutions reach thermal

equilibrium (10 minutes), the thiourea solution is injected into the cadmium tetradecanoate solution and a timer started. After one hour the temperature is increased to 200 °C at an average rate of 2 °C $min^{-1}$. The reaction is held at 200 °C for another 3.67 hours (for a full reaction time of 5 hours) and an aliquot is removed and dissolved in toluene for absorption and photoluminescence analysis, shown above.

*2.9.12. CdS Kinetics Experiments*

Cadmium sulfide kinetics experiments were run similarly to those described for lead sulfide kinetics, with the following changes. Cadmium oleate was used in the place of lead oleate and was prepared by the method reported for cadmium tetradecanoate.[66] The reactions were monitored at 300 nm rather than 400 nm (except for precursor **11** in which the formation of CdS was monitored using the extinction coefficient reported by Peng et al. due to an observable intermediate absorbing at high energy at early times).[104] All reactions were run at 150 °C. For slower precursors (**11**, **12**), the absorbance was monitored by removing aliquots from the reaction and diluting in toluene rather than using the in-situ dip probe. The precursor conversion reaction was considered complete when the absorbance at 300 nm stopped increasing, at which time a final aliquot was removed and used to determine the final nanocrystal volume

using the Peng sizing formula. Final nanocrystal concentration was calculated by dividing the theoretical CdS yield by the nanocrystal volume.

*2.9.13. Synthesis of CdS Nanorods*

Cadmium sulfide nanorods were synthesized by mixing cadmium oxide (56 mg, 0.44 mmol) with a mixture of hexylphosphonic acid (10-20 mg, 0.06-0.12 mmol) and octadecylphosphonic acid (274-294 mg, 0.82-0.88 mmol) where the total amount of phosphonic acids was held at 0.94 mmol in 1.75 g recrystallized trioctylphosphine oxide. This solution was first degassed under vacuum (50 mTorr) for 30 min at 100 °C, followed by heating to 320 °C under Ar for 20 min resulting in a clear solution. After lowering the temperature to 120 °C, the solution was degassed a second time under vacuum for 60 min to remove water and then heated back to 320 °C under Ar. Trioctylphosphine (2.0 g) was added and the temperature was allowed to stabilize at 320 °C. Separately, a solution of the respective thiourea (0.36 mmol) was dissolved in 0.5 g trioctylphosphine with gentle heating and then injected to the cadmium phosphonate solution. Aliquots were periodically removed and monitored using UV-Vis spectroscopy and the reaction allowed to proceed for 60-120 min. After cooling to < 100 °C, acetone (30 mL) was added to precipitate the sample, which was then centrifuged at 8000 rpm for 5 min. The precipitate was resuspended in dichloromethane (5 mL) and octylamine (5 mL), then acetone was added (20-30 mL) until the solution became

turbid. The solution was then centrifuged again at 8000 rpm for 10 min and resuspended in hexane. Any solids that precipitated were removed.

*2.9.14. Synthesis of ZnS Nanocrystals*

Zinc oleate was synthesized by adapting the method reported for cadmium tetradecanoate.[66] In a nitrogen-filled glovebox, zinc oleate (188.5 mg, 0.30 mmol, 1.5 equiv) and octadecene (9.5 mL) were loaded into a 3-neck round bottom flask equipped with a rubber septum, Schlenk adapter, and thermocouple adapter. The desired thiourea (0.20 mmol) and tetraglyme (0.5 mL) were loaded into a vial and sealed with a septum. Both vessels were transferred to a Schlenk line. The zinc oleate solution was heated to 240 °C and the thiourea solution was heated to 100 °C. Once both temperatures stabilized, the thiourea solution was rapidly injected into the zinc oleate solution. After 5 minutes of stirring at 240 °C, the flask was allowed to cool to room temperature. Acetone (30 mL) was added to the reaction mixture to induce precipitation. This mixture was centrifuged (7000 rpm, 15 minutes) and the clear supernatant was discarded. The remaining residue was dissolved in hexane (1 mL), precipitated with acetone (14 mL), and centrifuged (7000 rpm, 15 minutes). This procedure was repeated twice more, and the resulting white solid was dissolved in hexane for analysis. This reaction may be run at 2.5 times the concentration and twice the scale written above with little noticeable difference.

*2.9.15. Quantification of $Zn(O_2CR)_2$ in ZnS Samples*

The ratio of zinc oleate and ZnS in the product can estimated by dissolving a known mass of purified and dried nanocrystals in $d_6$-benzene (500 μL) with a ferrocene standard and measuring the ratio of the vinyl and ferrocene resonances. (For related procedure, see Section 2.9.9) $^1$H NMR spectra were acquired with sufficient relaxation delay to allow complete relaxation between pulses (30 s). From the measured zinc oleate concentration, a mass fraction of the sample due to zinc oleate may be calculated and subtracted from the total sample mass. Assuming ZnS is the only other chemical species present in the sample, a molar ratio of zinc oleate to zinc sulfide, and therefore zinc to sulfur, may be estimated: Zn:S = 1.6 ± 0.2. This near starting Zn:S ratio of the precursors of 1.5 to 1.

*2.9.16. Synthesis of Copper Sulfide Nanoplatelets*

Copper sulfide nanocrystals were synthesized by adapting a procedure previously reported by Korgel et al.[110] In a nitrogen-filled glovebox, copper(II) acetylacetonate (0.2616 g, 1 mmol), 1-octadecene (7.89 g, 10 mL), and distilled oleylamine (1.605 g, 6.0 mmol) are combined in a septum-sealed vial. The vial is removed from the glovebox, pierced with an argon inlet needle, and submerged in an oil bath heated to 160 °C. After five minutes in the oil bath, a solution of the desired thiourea (0.5 mmol) in diphenyl ether (0.5 mL) was injected. The reaction

was allowed to proceed for 30 minutes, after which the vial was removed from the oil bath and cooled to room temperature. The nanocrystals were isolated by precipitation with 20 mL methyl acetate, centrifugation (5 minutes, 7000 rpm), decanting the liquor, and re-dissolving the remaining nanocrystal residue in 5 mL hexane. This was repeated twice more using 10 mL methyl acetate to precipitate the nanocrystals.

*2.9.17. Synthesis of SnS Nanosheets*

SnS nanosheets were prepared by adapting a procedure previously published by Schaak et al.[111] Tin(II) acetate (24 mg, 0.10 mmol) and oleylamine (20 mL) were sonicated for 10 minutes, forming an opalescent mixture. The mixture was then degassed under vacuum at 120 °C for 10 min. After cooling to 90 °C under Ar, hexamethyldisilazane (1.0 mL, 4.77 mmol) was added. In a separate vessel, *N*-*n*-hexyl-*N'*-dodecylthiourea (**8**) (36 mg, 0.11 mmol) was mixed with diphenyl ether (0.5 mL) and briefly heated to form a homogenous solution. The thiourea solution was added to the metal solution at 90 °C, and the temperature was then increased to 180 °C over 10 minutes, turning brown after approximately 4 min at 180 °C. After 30 minutes at 180 °C, the reaction mixture was allowed to cool to room temperature. The reaction mixture was then opened to air, washed with an acetone/toluene/hexane mixture (30 mL, 3:1:1 ratio), and

centrifuged. The precipitate was washed twice more with a toluene/methanol mixture (20 mL, 1:1 ratio) prior to characterization.

*2.9.18. Synthesis of NiS Nanocrystals*

Nickel sulfide nanocrystals were prepared in a similar fashion to $Cu_{2-x}S$.[110] In a nitrogen-filled glovebox, nickel(II) stearate (62.6 mg, 0.1 mmol) and distilled oleylamine (10 mL, 8.13 g) were combined in a septum-sealed vial. The vial is removed from the glovebox, pierced with an argon inlet needle, and submerged in an oil bath heated to 200 °C. After five minutes in the oil bath, a solution of substituted thiourea (0.1 mmol) in oleylamine (0.5 mL) was injected. The reaction was allowed to proceed for 30 minutes, after which the vial was removed from the oil bath and cooled to room temperature. The nanocrystals were isolated by precipitation with 20 mL methyl acetate, centrifugation (5 minutes, 7000 rpm), decanting the liquor, and redissolving the remaining nanocrystal residue in 5 mL hexane. This was repeated twice more using 10 mL methyl acetate to precipitate the nanocrystals.

*2.9.19. Synthesis of CZTS Nanocrystals*

Kesterite CZTS nanocrystals were synthesized by adapting a procedure reported by Chesman and coworkers.[116] *N*,*N*′-diphenylthiourea (**2**) was substituted for carbon disulfide and *N*,*N*,*N*′,*N*′-tetramethylthiourea (**12**) was

substituted for dodecanethiol. Briefly, copper(I) iodide (667 mg, 3.5 mmol, 0.4375 equiv.), tin(IV) chloride hexahydrate (701 mg, 2.0 mmol, 0.250 equiv), and zinc chloride (340 mg, 2.5 mmol, 0.3125 equiv.) are added to oleylamine (16 mL) and degassed under vacuum for 60 minutes at 100 °C, giving a blue-green solution, and then placed under argon. During this time, **2** (571 mg, 2.5 mmol, 0.3125 equiv.), **12** (727 mg, 5.5 mmol, 0.6875 equiv.), and tetraglyme (2 mL) were added to a scintillation vial and heated to 100 °C, giving a pale yellow solution. The thiourea solution was rapidly injected into the metal solution, giving a dark reaction mixture. The mixture was stirred at 100 °C for 60 minutes, then heated to 250 °C and held there for 60 minutes, then heated to 290 °C and held there for 10 minutes, and finally allowed to cool to 60 °C. The reaction mixture was then opened to air, diluted with chloroform (7.5 mL), precipitated with acetone (12.5 mL) and methanol (12.5 mL), and centrifuged (4000 rpm, 5 minutes), giving a clear pale yellow supernatant. The dark residue was dissolved in chloroform (5 mL) and centrifuged (4000 rpm, 5 minutes) to remove a small amount of aggregated material (< 20% of product). The dark brown solution was decanted, precipitated with ethanol (5 mL), and centrifuged (4000 rpm, 5 minutes), giving a clear colorless supernatant. The dark residue is dissolved in chloroform (5 mL) and dried under vacuum, giving a brown-black nanocrystal solid.

*2.9.20. Synthesis of CdSe/CdS/ZnS Core/Shell/Shell Nanocrystals*

**Synthesis of CdSe cores:** Wurtzite CdSe nanocrystals were synthesized according to a published procedure with slight modifications.[118] Briefly, cadmium oxide (77 mg, 0.6 mmol) and oleic acid (0.68 g, 2.4 mmol) are added to 1-octadecene (6.0 g), degassed under Ar flow for 30 minutes at room temperature, and then heated to 240 °C until clear (15 minutes). This solution was then cooled to < 70 °C and trioctylphosphine (1.5 g) and octadecylamine (4.5) are added under an overpressure of Ar. The reaction solution is degassed under Ar flow for 15 minutes and then heated to 270 °C. Once stable at this temperature, 3.0 g of tributylphosphine selenide diluted in 1-octadecene (Se, 1.4 g, 17.6 mmol; tributylphosphine, 3.84 g, 18.8 mmol; 1-octadecene, 12.3 g) was injected rapidly and the temperature reduced to 250 °C. The reaction is allowed to proceed until the desired nanocrystal size is reached (3 minutes), at which point the heating source is removed and the solution cooled with an oil bath. Once the temperature reaches < 80 °C, hexane is added (10 mL). The hexane solution is washed twice with methanol and stored in the dark.

**Shelling procedure:** CdS and ZnS shells are grown on the preformed CdSe cores using an alternating addition strategy.[117] CdSe cores dissolved in hexane (100 nmol in QDs as determined by absorbance at the first excitonic transition)[104,119] are added to octadecylamine (1.5 g) and 1-octadecene (5.0 g) and

degassed under vacuum at 100 °C to remove all of the hexane (30 minutes). The reaction solution is then heated to 240 °C under Ar and the temperature allowed to stabilize for 30 minutes. Next, alternating additions of cadmium oleate (0.04 M in 1-octadecene; CdO, 62 mg, 0.48 mmol; oleic acid, 1.08 g, 3.83 mmol; 1-octadecene, 8.5 g) and *N*-*n*-hexyl-*N'*,*N'*-di-*n*-octylthiourea (**10**) (0.04 M in 1-octadecene; **10**, 154 mg, 0.4 mmol; 1-octadecene, 7.9 g) are added dropwise to the reaction for the formation of CdS layers. Following the growth of CdS, alternating additions of zinc oleate (0.04 M in 1-octadecene; zinc acetate dihydrate, 44 mg, 0.20 mmol; oleic acid, 0.24 g, 0.85 mmol; 1-octadecene, 6.0 g) and **10** (0.04 M in 1-octadecene) are added dropwise for the formation of the ZnS layers. The molar amount for each metal cation addition is calculated to produce one half-monolayer based on a diameter change of 0.35 nm for one full monolayer assuming the bulk density of CdSe. The molar amount for each S addition is 2:3 compared to the metal-cation addition due to the complete conversion of the thiourea precursors. Following each addition, the mixture is allowed to react for 10 minutes. After the last addition, the solution is allowed to cool to < 80 °C before the addition of toluene (10 mL). After centrifugation (5000 rpm, 5 min), the clear nanocrystal solution is decanted and the solid precipitates discarded. Sufficient methyl acetate is added to form a cloudy suspension (approximately 10 mL), which is then centrifuged (7000 rpm, 10 min.) The solid

nanocrystal residue is suspended in toluene and stored in the dark. Any residual organic solids could be removed at this stage either by centrifugation or filtration.

*2.9.21. Precursor Characterization*

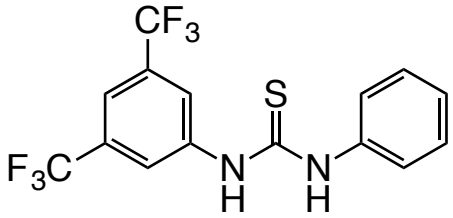

***N*-(3,5-*bis*(trifluoromethylphenyl))-*N′*-phenylthiourea (1).** White powder. $^{1}$H NMR ($CD_2Cl_2$, 500 MHz): $\delta$ = 7.33-7.40 (m, 3H, *o*-CH and *p*-CH (unsub.)), 7.48 (m, 2H, *m*-CH (unsub.)), 7.71 (s, 1H, *p*-CH (sub.)), 8.01 (s, 2H, *o*-CH (sub.)), 8.04 (b, 1H, NH (unsub.)), 8.92 (b, 1H, NH (sub.)); $^{13}$C {$^{1}$H} (125 MHz, $CD_2Cl_2$): $\delta$ = 119.68 (*p*-C (sub.), p), 123.50 (-$CF_3$, q, $J_{C-F}$ = 271 Hz), 125.21 (*m*-C (sub.), q, $J_{C-F}$ = 4 Hz), 125.85 (*o*-C (unsub.)), 128.33 (*p*-C (unsub.)), 130.66 (m-C (unsub.)), 132.12 (m-C (sub.), q, $J_{C-F}$ = 34 Hz), 136.39 (*i*-C), 140.25 (*i*-C), 180.19 (C(S)); Anal. Calcd for $C_{15}H_{10}F_6N_2S$: C, 49.32, H, 3.04, N, 7.67. Found: C, 49.53; H, 2.89; N, 7.68. MS (FAB) *m*/*z* Calcd for $C_{15}H_{11}F_6N_2S^+$: 365.05. Found: 365.07.

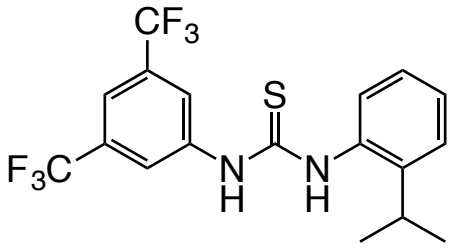

***N*-(3,5-bis(trifluoromethyl)phenyl)-*N*′-(2-isopropylphenyl)thiourea**.

White powder. Recrystallized by addition of hexanes to a saturated solution in dichloromethane. Isolated by suction filtration and dried under vacuum >3 hours. $^{1}$H NMR ($C_6D_6$, 500 MHz): $\delta$ = 0.97 (d, $J_{H\text{-}H}$ = 6.9 Hz, 6H, $CH_3$), 3.00 (sept., $J_{H\text{-}H}$ = 6.9 Hz, 1H, isopropyl CH), 6.84 (m, 3H, aryl CH), 7.00 (m, 2H, aryl CH), 7.47 (s, 1H, NH), 7.64 (s, 2H, aryl CH), 8.09 (br s, 1H, NH). $^{13}$C{$^{1}$H} (125 MHz, $C_6D_6$): $\delta$ = 22.9 ($CH_3$), 28.2 (isopropyl CH), 118.9 (aryl CH or $CF_2\underline{C}HCF_3$), 123.2 ($CF_3$, q, $J_{C\text{-}F}$ = 272.8 Hz), 124.8 (aryl CH or $CF_2\underline{C}HCF_3$), 127.1 (aryl CH), 127.2 (aryl CH), 129.2 (CH), 131.5 ($\underline{C}CF_3$, q, $J_{C\text{-}F}$ = 33 Hz), 133.0 (*i*-C), 140.0 (*i*-C), 146.2 ($\underline{C}CH(CH_3)_2$), 180.7 (C(S)). Anal. Calcd for $C_{18}H_{16}F_6N_2S$: C, 53.20; H, 3.97; N, 6.89. Found: C, 53.05; H, 3.74; N, 6.78. MS (ASAP) *m*/*z* Calcd for [$C_{18}H_{16}F_6N_2{}^{32}S$ + $H^+$]: 407.1017. Found: 407.1016.

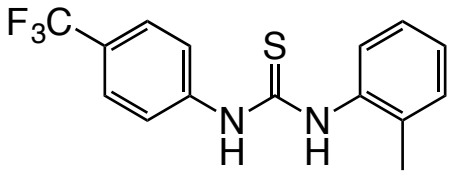


***N*-(*o*-tolyl)-*N*′-(4-(trifluoromethyl)phenyl)thiourea.** White powder. $^{1}$H NMR ($C_6D_6$, 500 MHz): $\delta$ = 3.01 (s, 3H, $CH_3$), 6.87-6.95 (m, 4H, aryl CH), 7.09 (m, 2H, aryl CH), 7.17 (m, 2H, aryl CH), 7.52 (br, 1H, NH), 8.29 (br, 1H, NH). $^{13}$C{$^{1}$H} (125 MHz, $C_6D_6$): $\delta$ = 17.80 ($CH_3$), 123.68 (aryl CH), 124.76 (q, $J_{C\text{-}F}$ = 271.6 Hz, $CF_3$), 126.08 (q, $J_{C\text{-}F}$ = 3.8 Hz, $\underline{C}HCCF_3$), 127.29 (q, $J_{C\text{-}F}$ = 32.5 Hz, $\underline{C}CF_3$), 127.46 (aryl CH),

128.51 (aryl CH), 131.69 (aryl CH), 135.52 (*i*-C), 135.81 (*i*-C), 141.66 (*i*-C), 180.15 (C(S)). Anal. Calcd for $C_{15}H_{13}F_3N_2S$: C, 58.05; H, 4.22; N, 9.03. Found: C, 58.06; H, 4.11; N, 9.01. MS (ASAP) *m*/*z* Calcd for [$C_{15}H_{13}F_3N_2{}^{32}S + H^+$]: 311.0830. Found: 311.0831.

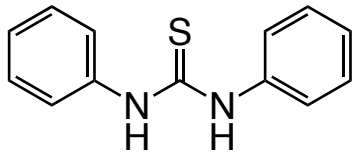

***N,N′*-diphenylthiourea (2).** The synthesis was run at half the concentration reported above. White powder. $^1$H NMR ($C_6D_6$, 500 MHz): $\delta$ = 7.00 (m, 10H, -$C_6H_5$), 7.59 (s, 2H, NH); $^{13}$C {$^1$H} (125 MHz, $C_6D_6$): $\delta$ = 124.32 (*o*-C), 125.94 (*p*-C), 129.18 (*m*-C), 137.91 (*i*-C), 179.56 (C(S)); Anal. Calcd for $C_{13}N_2SH_{12}$: C, 68.39; H, 5.30; N, 12.27. Found: C, 68.49; H, 5.46; N, 12.28. MS (FAB) *m*/*z* Calcd for $C_{13}H_{13}N_2S^+$: 229.08. Found: 229.32.

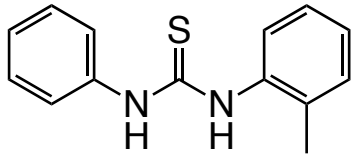

***N*-phenyl-*N′*-(*o*-tolyl)thiourea.** White powder. $^1$H NMR ($CDCl_3$, 500 MHz): $\delta$ = 2.34 (s, 3H, $CH_3$), 7.25-7.32 (m, 4H, aryl CH), 7.36-7.42 (m, 5H, aryl CH), 7.93 (br s, 2H, NH). $^{13}$C{$^1$H} ($CDCl_3$, $C_6D_6$): $\delta$ = 18.07 ($CH_3$), 125.46 (aryl CH), 127.02 (aryl CH), 127.29 (aryl CH), 127.86 (aryl CH), 128.44 (aryl CH), 129.47 (aryl CH), 131.47 (aryl CH), 135.45 (*i*-C), 135.52 (*i*-C), 137.47 (*i*-C), 180.47 (C(S)). Anal.

Calcd for $C_{14}H_{14}N_2S$: C, 69.39; H, 5.82; N, 11.56. Found: C, 69.34; H, 5.61; N, 11.52. MS (ASAP) *m*/*z* Calcd for [$C_{14}H_{14}N_2{}^{32}S + H^+$]: 243.0956. Found: 243.0958.

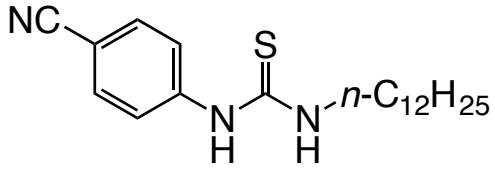


***N*-(4-cyanophenyl)-*N′*-dodecylthiourea (3a).** White powder. $^1$H NMR ($C_6D_6$, 500 MHz): $\delta$ = 0.45 (s, 1H, -CN), 0.93 (t, 3H, -$CH_3$), 1.07-1.36 (b, 20H, $(CH_2)_{10}$), 3.40 (b, 2H, -$CH_2$), 5.32 (s, 1H, NH), 6.49 (d, 2H, *o*-CH), 6.83 (d, 2H, *m*-CH), 7.39 (s, 1H, NH); $^{13}$C{$^1$H} (125 MHz, $C_6D_6$): $\delta$ = 14.39 (-$CH_3$), 23.15 ($CH_2$), 27.23 ($CH_2$), 29.03 ($CH_2$), 29.67 ($CH_2$), 29.84 ($CH_2$), 29.98 ($CH_2$), 30.04 ($CH_2$), 30.13 ($CH_2$), 30.14 ($CH_2$), 32.36 ($CH_2$), 45.53 ($NCH_2$), 108.70 (*p*-C), 118.38 (-CN), 122.45 (*o*-C), 133.44 (*m*-C), 141.29 (*i*-C), 180.57 (C(S)); Anal. Calcd for $C_{20}H_{31}N_3S$: C, 71.80; H, 10.24; N, 8.37. Found: C, 71.57; H, 10.52; N, 8.37. MS (FAB) *m*/*z* Calcd for $C_{20}H_{32}N_3S^+$: 346.23. Found: 346.36.

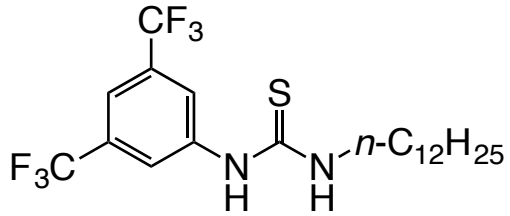


***N*-(3,5-*bis*(trifluoromethyl)phenyl)-*N′*-dodecylthiourea.** White powder. $^1$H NMR ($C_6D_6$, 500 MHz): $\delta$ = 0.92 (t, $J_{H\text{-}H}$ = 7.1 Hz, 3H, $CH_3$), 1.09-1.35 (m, 20H, $CH_2$), 3.37 (br, 2H, $\alpha$-$CH_2$), 5.41 (br, 1H, NH), 7.40 (s, 2H, aryl CH), 7.44 (s, 1H,

aryl CH), 7.56 (br, 1H, NH). $^{13}C\{^{1}H\}$ (125 MHz, $C_6D_6$): $\delta$ = 14.38 ($CH_3$), 23.15 ($CH_2$), 27.33 ($CH_2$), 28.95 ($CH_2$), 29.70 ($CH_2$), 29.85 ($CH_2$), 29.98 ($CH_2$), 30.05 ($CH_2$), 30.13 ($CH_2$), 30.15 ($CH_2$), 32.37 ($CH_2$), 45.43 ($\alpha$-$CH_2$), 118.38 (m, aryl CH), 132.20 (m, aryl CH), 123.46 (q, $J_{C-F}$ = 273.0 Hz, $CF_3$), 132.77 (q, $J_{C-F}$ = 33.5 Hz, $\underline{C}CF_3$), 139.83 (*i*-C), 180.77 (C(S)). Anal. Calcd for $C_{21}H_{30}F_6N_2S$: C, 55.25; H, 6.62; N, 6.14. Found: C, 55.24; H, 6.89; N, 6.11. MS (ASAP) *m*/*z* Calcd for [$C_{21}H_{30}F_6N_2{}^{32}S + H^+$]: 457.2112. Found: 457.2110.

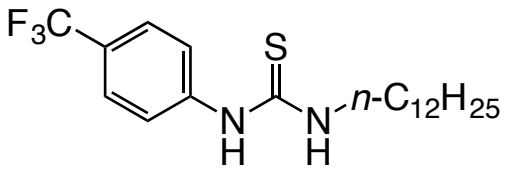


***N*-(4-(trifluoromethyl)phenyl)-*N'*-dodecylthiourea (3b).** White powder. $^{1}H$ NMR ($C_6D_6$, 500 MHz): $\delta$ = 0.93 (t, 3H, -$CH_3$), 1.08-1.32 (m, 20H, $(CH_2)_{10}$), 3.47 (b, 2H, -$CH_2$), 5.57 (b, 1H, NH), 6.79 (d, 2H, *o*-CH), 7.17 (d, 2H, *m*-CH), 8.53 (b, 1H, NH); $^{13}C\{^{1}H\}$ (125 MHz, $C_6D_6$): $\delta$ = 14.40 (-$CH_3$), 23.15 ($CH_2$), 27.26 ($CH_2$), 29.14 ($CH_2$), 29.70 ($CH_2$), 29.85 ($CH_2$), 30.00 ($CH_2$), 30.06 ($CH_2$), 30.14 ($CH_2$), 30.16 ($CH_2$), 32.37 ($CH_2$), 45.55 ($NCH_2$), 123.57 (*o*-C), 124.61 (-$CF_3$, d, $J_{C-F}$ = 271 Hz), 127.06 (*m*-C), 127.40 (*p*-C, d, $J_{C-F}$ = 33 Hz), 140.92 (*i*-C), 180.68 (C(S)); Anal. Calcd for $C_{20}H_{31}F_3N_2S$: C, 61.83; H, 8.04; N, 7.21. Found: C, 61.73; H, 8.08; N, 7.13. MS (FAB) *m*/*z* Calcd for $C_{20}H_{32}F_3N_2S^+$: 389.22. Found: 389.26.

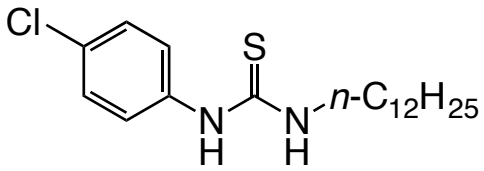


***N*-(4-chlorophenyl)-*N*′-dodecylthiourea (3c).** White powder. $^{1}$H NMR ($C_6D_6$, 500 MHz): $\delta$ = 0.92 (t, 3H, -$CH_3$), 1.06-1.36 (m, 20H, $(CH_2)_{10}$), 3.47 (b, 2H, -$CH_2$), 5.47 (b, 1H, NH), 6.58 (d, 2H, *o*-CH), 6.88 (d, 2H, *m*-CH), 8.17 (b, 1H, NH); $^{13}$C{$^{1}$H} (125 MHz, $C_6D_6$): $\delta$ = 14.40 (-$CH_3$), 23.15 ($CH_2$), 27.21 ($CH_2$), 29.24 ($CH_2$), 29.68 ($CH_2$), 29.85 ($CH_2$), 29.98 ($CH_2$), 30.04 ($CH_2$), 30.14 ($CH_2$), 30.15 ($CH_2$), 32.37 ($CH_2$), 45.50 ($NCH_2$), 126.16 (*o*-C), 130.01 (*m*-C), 131.86 (*p*-C), 135.92 (*i*-C), 181.23 (C(S)); Anal. Calcd for $C_{19}H_{31}ClN_2S$: C, 64.29; H, 8.80; N, 7.89. Found: C, 63.97; H, 8.62; N, 7.73. MS (FAB) *m*/*z* Calcd for $C_{19}H_{32}ClN_2S^{+}$: 355.20. Found: 355.27.

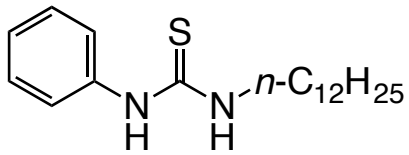


***N*-phenyl-*N*′-dodecylthiourea (3d).** White powder. $^{1}$H NMR ($C_6D_6$, 500 MHz): $\delta$ = 0.92 (t, 3H, -CH3), 1.05-1.35 (m, 20H, $(CH_2)_{10}$), 3.48 (b, 2H, $NCH_2$), 5.67 (b, 1H, NH), 6.83 (t, 1H, *p*-CH), 6.87 (d, 2H, *o*-CH), 6.96 (t, 2H, *m*-CH), 8.51 (b, 1H, NH); 13C{1H} (125 MHz, $C_6D_6$): $\delta$ = 14.40 (-$CH_3$), 23.15 ($CH_2$), 27.22 ($CH_2$), 29.26 ($CH_2$), 29.67 ($CH_2$), 29.85 ($CH_2$), 29.99 ($CH_2$), 30.04 ($CH_2$), 30.14 ($CH_2$), 30.15 ($CH_2$), 32.37 ($CH_2$), 45.49 ($NCH_2$), 125.00 (*o*-C), 126.34 (*p*-C), 129.96 (*m*-C), 137.55 (*i*-C), 181.35 (C(S)); Anal. Calcd for $C_{19}H_{32}N_2S$: C, 71.19; H, 10.06; N, 8.74. Found:

C, 71.05; H, 9.74; N, 8.62. MS (FAB) *m*/*z* Calcd for $C_{19}H_{33}N_2S^+$: 321.24. Found: 321.35.

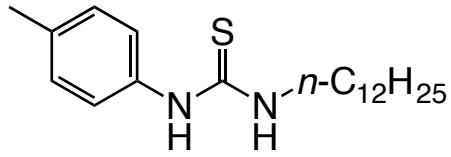


***N*-(4-methylphenyl)-*N′*-dodecylthiourea (3e).** White powder. $^1$H NMR ($C_6D_6$, 500 MHz): $\delta$ = 0.92 (t, 3H, -$CH_3$), 1.05-1.35 (m, 20H, $(CH_2)_{10}$), 1.97 (s, 3H, -$CH_3$), 3.53 (m, 2H, $CH_2$), 5.74 (s, 1H, NH), 6.80 (d, 2H, *o*-CH), 6.85 (d, 2H, *m*-CH), 8.78 (s, 1H, NH); $^{13}$C{$^1$H} (125 MHz, $C_6D_6$): $\delta$ = 14.40 (-$CH_3$), 20.81 (*o*-$CH_3$), 23.15 ($CH_2$), 27.24 ($CH_2$), 29.36 ($CH_2$), 29.70 ($CH_2$), 29.85 ($CH_2$), 30.00 ($CH_2$), 30.05 ($CH_2$), 30.14 ($CH_2$), 30.16 ($CH_2$), 32.38 ($CH_2$), 45.44 ($NCH_2$), 125.44 (*o*-C), 130.60 (*m*-C), 134.95 (*p*-C), 136.32 (*i*-C), 181.49 (C(S)); Anal. Calcd for $C_{20}H_{34}N_2S$: C, 69.52; H, 9.04; N, 12.16. Found: C, 69.65; H, 9.31; N, 12.22. MS (FAB) *m*/*z* Calcd for $C_{20}H_{35}N_2S^+$: 335.25. Found: 335.38.

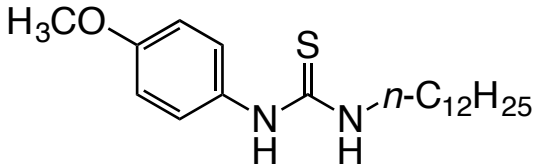


***N*-(4-methoxyphenyl)-*N′*-dodecylthiourea (3f).** White powder. $^1$H NMR ($C_6D_6$, 500 MHz): $\delta$ = 0.92 (t, 3H, -$CH_3$), 1.06-1.33 (m, 20H, $(CH_2)_{10}$), 3.19 (s, 3H, -$OCH_3$), 3.55 (m, 2H, -$CH_2$), 5.56 (b, 1H, NH), 6.55 (d, 2H, *o*-CH), 6.79 (d, 2H, *m*-CH), 8.24 (b, 1H, NH); $^{13}$C{$^1$H} (125 MHz, $C_6D_6$): $\delta$ = 14.40 (-$CH_3$), 23.15 ($CH_2$),

27.21 ($CH_2$), 29.44 ($CH_2$), 29.70 ($CH_2$), 29.85 ($CH_2$), 30.00 ($CH_2$), 30.05 ($CH_2$), 30.14 ($CH_2$), 30.15 ($CH_2$), 32.37 ($CH_2$), 45.46 ($NCH_2$), 54.98 (-$OCH_3$), 100.37 (*i*-C), 115.21 (*m*-C), 127.69 (*o*-C), 158.82 (*p*-C), 182.04 (C(S)); Anal. Calcd for $C_{20}H_{34}N_2OS$: C, 68.52; H, 9.78; N, 7.99. Found: C, 69.44; H, 10.03; N, 8.00. MS (FAB) *m*/*z* Calcd for $C_{20}H_{35}N_2OS^+$: 351.25. Found: 351.31.

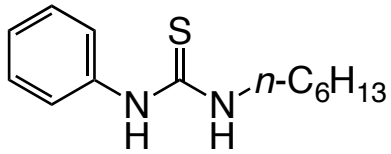


***N*-phenyl-*N*′-hexylthiourea (4).** White powder. $^1$H NMR ($C_6D_6$, 500 MHz): $\delta$ = 0.82 (t, 3H, -CH3), 0.98-1.25 (m, 8H, $(CH_2)_4$), 3.46 (b, 2H, $NCH_2$), 5.74 (b, 1H, NH), 6.83 (t, 1H, *p*-CH), 6.94-6.98 (m, 4H, *o*-CH & *m*-CH), 8.97 (b, 1H, NH); 13C{1H} (125 MHz, $C_6D_6$): $\delta$ = 14.20 (-$CH_3$), 22.89 ($CH_2$), 26.82 ($CH_2$), 29.16 ($CH_2$), 31.72 ($CH_2$), 45.42 ($NCH_2$), 125.02 (*o*-C), 126.34 (*p*-C), 129.97 (*m*-C), 137.62 (*i*-C), 181.22 (C(S)); Anal. Calcd for $C_{13}H_{20}N_2S$: C, 66.06; H, 8.53; N, 11.85. Found: C, 66.31; H, 8.80; N, 11.73. MS (FAB) *m*/*z* Calcd for $C_{13}H_{21}N_2S^+$: 237.14. Found: 237.27.

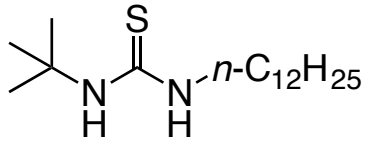


***N*-*tert*-butyl-*N*′-dodecylthiourea (5).** White powder. $^1$H NMR ($C_6D_6$, 500 MHz): $\delta$ = 0.92 (t, 3H, -$CH_3$), 1.16-1.44 (m, 29H, $(CH_2)_{10}$ & $(CH_3)_3$), 3.43 (b, 2H, -

$CH_2$), 5.54 (b, 1H, NH), 5.76 (s, 1H, NH); $^{13}C\{^1H\}$ (125 MHz, $C_6D_6$): $\delta$ = 14.40 (-$CH_3$), 23.16 ($CH_2$), 27.42 ($CH_2$), 29.44 (-$CH_3$), 29.63 ($CH_2$), 29.82 ($CH_2$), 29.86 ($CH_2$), 30.06 ($CH_2$), 30.10 ($CH_2$), 30.16 ($CH_2$), 30.18 ($CH_2$), 32.38 ($CH_2$), 44.98 ($NCH_2$), 52.70 (NC), 182.47 (C(S)); Anal. Calcd for $C_{17}H_{36}N_2S$: C, 67.94; H, 12.07; N, 9.32. Found: C, 68.21; H, 11.87; N, 9.25. MS (FAB) *m*/*z* Calcd for $C_{17}H_{37}N_2S^+$: 301.27. Found: 301.42.

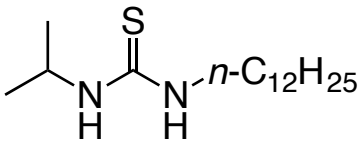


***N*-isopropyl-*N'*-dodecylthiourea (6).** White powder. $^1H$ NMR ($C_6D_6$, 500 MHz): $\delta$ = 0.90-0.96 (m, 9H, -$CH_3$), 1.13-1.40 (m, 20H, $(CH_2)_{10}$), 3.26 (b, 2H, -$CH_2$), 4.33 (b, 1H, -CH), 5.20 (b, 1H, NH), 5.38 (b, 1H, NH); $^{13}C\{^1H\}$ (125 MHz, $C_6D_6$): $\delta$ = 14.40 (-$CH_3$), 22.64 (-$CH_3$), 23.16 ($CH_2$), 27.36 ($CH_2$), 29.59 ($CH_2$), 29.82 ($CH_2$), 29.86 ($CH_2$), 30.06 ($CH_2$), 30.11 ($CH_2$), 30.16 ($CH_2$), 30.19 ($CH_2$), 32.38 ($CH_2$), 44.36 (NCH), 45.92 ($NCH_2$), 182.14 (C(S)); Anal. Calcd for $C_{16}H_{34}N_2S$: C, 67.07; H, 11.96; N, 9.78. Found: C, 67.31; H, 11.69; N, 9.82. MS (FAB) *m*/*z* Calcd for $C_{16}H_{35}N_2S^+$: 287.53. Found: 287.39.

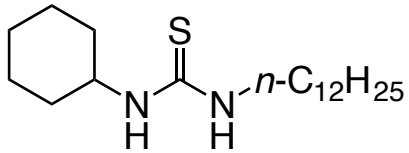

***N*-cyclohexyl-*N′*-dodecylthiourea (7).** Pale yellow powder. $^{1}$H NMR ($C_6D_6$, 500 MHz): $\delta$ = 0.93 (t, 3H, -$CH_3$), 1.01-1.63 (m, 28H, $(CH_2)_{10}$ & 2,3,5,6-$CH_2$), 2.09 (d, 2H, 4-$CH_2$), 3.48 (b, 2H, -$CH_2$), 4.30 (b, 1H, NH), 6.22 (b, 1H, NH ), 6.43 (s, 1H, 1-CH); $^{13}$C{$^{1}$H} (125 MHz, $C_6D_6$): $\delta$ = 14.41 (-$CH_3$), 23.16 ($CH_2$), 27.41 ($CH_2$), 29.43 ($CH_2$), 29.63 ($CH_2$), 29.82 ($CH_2$), 29.86 ($CH_2$), 30.06 ($CH_2$), 30.10 ($CH_2$), 30.16 ($CH_2$), 30.18 ($CH_2$), 32.38 ($CH_2$), 44.98 ($NCH_2$), 52.69 (NCH), 182.48 (C(S)); Anal. Calcd for $C_{19}H_{38}N_2S$: C, 69.88; H, 11.73; N, 8.58. Found: C, 69.78; H, 11.46; N, 8.33. MS (FAB) *m*/*z* Calcd for $C_{19}H_{39}N_2S^+$: 327.28. Found: 327.43.

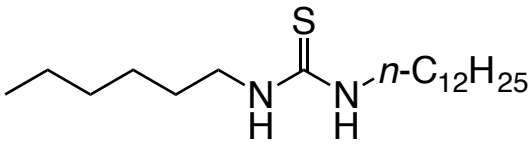


***N*-*n*-hexyl-*N′*-dodecylthiourea (8).** White powder. $^{1}$H NMR ($C_6D_6$, 500 MHz): $\delta$ = 0.88 (t, 3H, -$CH_3$), 0.93 (t, 3H, -$CH_3$), 1.11-1.40 (m, 28H, $(CH_2)_{10}$ & $(CH_2)_4$), 3.26 (b, 4H, -$CH_2$), 5.43 (b, 2H, NH); $^{13}$C{$^{1}$H} (125 MHz, $C_6D_6$): $\delta$ = 14.27 (-$CH_3$), 14.40 (-$CH_3$), 22.99 ($CH_2$), 23.16 ($CH_2$), 26.97 ($CH_2$), 27.36 ($CH_2$), 29.51 ($CH_2$), 29.60 ($CH_2$), 29.84 ($CH_2$), 29.87 ($CH_2$), 30.08 ($CH_2$), 30.13 ($CH_2$), 30.17 ($CH_2$), 30.20 ($CH_2$), 31.90 ($CH_2$), 32.38 ($CH_2$), 44.46 ($NCH_2$), 44.50 ($NCH_2$), 183.02 (C(S)); Anal. Calcd for $C_{19}H_{40}N_2S$: C, 69.45; H, 12.27; N, 8.53. Found: C, 69.65; H, 12.09; N, 8.49. MS (FAB) *m*/*z* Calcd for $C_{19}H_{41}N_2S^+$: 329.30. Found: 329.44.

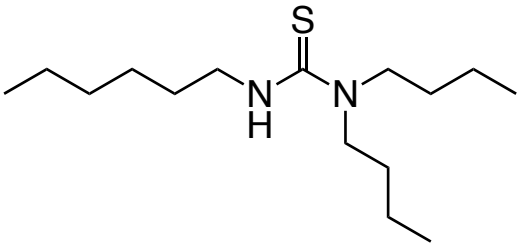


***N*-*n*-hexyl-*N*′,*N*′-di-*n*-butylthiourea (9).** Pale yellow oil. $^{1}$H NMR ($C_6D_6$, 500 MHz): $\delta$ = 0.82 (t, 6H, -$CH_3$), 0.86 (t, 3H, -$CH_3$), 1.08-1.26 (m, 10H, $(CH_2)_5$), 1.40-1.52 (m, 6H, $CH_2$), 3.34 (t, 4H, N$(CH_2)_2$), 3.73 (q, 2H, N$CH_2$), 4.97 (b, 1H, NH); $^{13}$C{$^{1}$H} (125 MHz, $C_6D_6$): $\delta$ = 14.13 (-$CH_3$), 14.26 (-$CH_3$), 20.52 ($CH_2$), 23.06 ($CH_2$), 27.14 ($CH_2$), 29.89 ($CH_2$), 30.09 ($CH_2$), 31.98 ($CH_2$), 46.28 (N$CH_2$), 50.89 (N$(CH_2)_2$), 182.12 (C(S)); Anal. Calcd for $C_{15}H_{32}N_2S$: C, 66.12; H, 11.84; N, 10.28. Found: C, 66.07; H, 11.57; N, 10.34. MS (FAB) *m*/*z* Calcd for $C_{15}H_{33}N_2S^+$: 273.24. Found: 273.30.

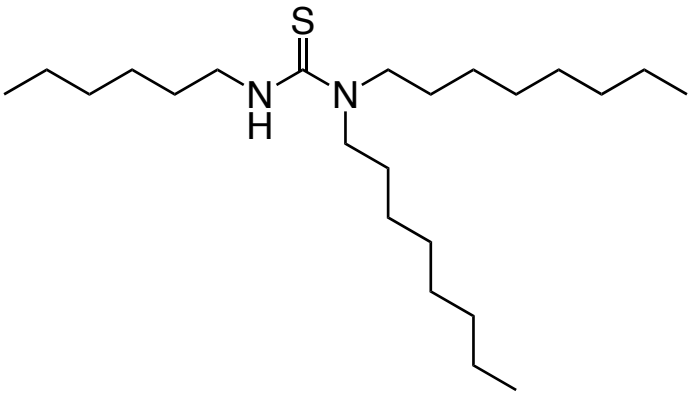


***N*-*n*-hexyl-N′,*N*′-di-*n*-octylthiourea (10).** Pale yellow oil. $^{1}$H NMR ($C_6D_6$, 500 MHz): $\delta$ = 0.87 (t, 3H, -$CH_3$), 0.91 (t, 6H, -$CH_3$), 1.15-1.33 (m, 26H, $(CH_2)_5$ & $(CH_2)_3$), 1.49-1.59 (m, 6H, $CH_2$), 3.44 (t, 4H, N$(CH_2)_2$), 3.75 (q, 2H, N$CH_2$), 5.13 (b,

1H, NH); $^{13}C\{^{1}H\}$ (125 MHz, $C_6D_6$): $\delta$ = 14.26 (-$CH_3$), 14.38 (-$CH_3$), 23.05 ($CH_2$), 23.10 ($CH_2$), 27.16 ($CH_2$), 27.40 ($CH_2$), 28.05 ($CH_2$), 29.70 ($CH_2$), 29.84 ($CH_2$), 29.90 ($CH_2$), 31.99 ($CH_2$), 32.25 ($CH_2$), 46.29 ($NCH_2$), 51.22 ($N(CH_2)_2$), 182.26 (C(S)); Anal. Calcd for $C_{23}H_{48}N_2S$: C, 71.81; H, 12.58; N, 7.28. Found: C, 72.06; H, 12.44; N, 7.33. MS (FAB) *m*/*z* Calcd for $C_{23}H_{49}N_2S^+$: 385.36. Found: 385.30.

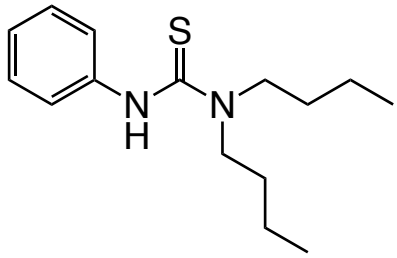


***N*-phenyl-*N'*,*N'*-di-*n*-butylthiourea (11).** White powder. $^{1}H$ NMR ($C_6D_6$, 500 MHz): $\delta$ = 0.67 (t, 6H, -$CH_3$), 0.96 (m, 4H, $CH_2$), 1.31 (m, 4H, $CH_2$), 3.21 (t, 4H, $N(CH_2)_2$), 6.54 (b, 1H, NH), 6.82 (t, 1H, *p*-CH), 7.01 (t, 2H, *m*-CH), 7.21 (d, 2H, *o*-CH); $^{13}C\{^{1}H\}$ (125 MHz, $C_6D_6$): $\delta$ = 13.62 (-$CH_3$), 20.05 ($CH_2$), 29.50 ($CH_2$), 51.03 ($NCH_2$), 124.46 (*o*-CH), 124.65 (*p*-CH), 128.42 (*m*-CH), 140.68 (*i*-C), 182.03 (C(S)); Anal. Calcd for $C_{15}H_{24}N_2S$: C, 68.13; H, 9.15; N, 10.59. Found: C, 67.95; H, 8.85; N, 10.55. MS (FAB) *m*/*z* Calcd for $C_{15}H_{25}N_2S^+$: 265.17. Found: 265.24.

**Lead(II) oleate from lead(II) trifluoroacetate.** Fluffy white solid. $^{1}H$ NMR ($C_6D_6$, 500 MHz) $\delta$ = 0.95 (t, $^{3}J_{H-H}$ = 6.8 Hz, 6H), 1.27-1.58 (m, 40H, $(CH_2)_6$ and $(CH_2)_4$), 1.89 (m, 4H, $COCH_2C\underline{H}_2$), 2.19 (m, 8H, $=CHC\underline{H}_2$), 2.53 (t, $^{3}J_{H-H}$ = 7.7 Hz, 4H, $COCH_2$), 5.56 (m, 4H, =CH-); $^{13}C$ NMR ($C_6D_6$, 125 MHz) $\delta$ = 14.43 ($CH_3$), 23.20

($\underline{C}H_2CH_3$), 26.31 ($COCH_2\underline{C}H_2$), 27.86 (=$CH\underline{C}H_2$-), 27.95 (=$CH\underline{C}H_2$-), 29.89 ($CH_2$), 29.91 ($CH_2$), 30.14 ($CH_2$), 30.36 ($CH_2$), 30.38 ($CH_2$), 30.58 ($CH_2$), 32.43 ($CH_2$), 40.04 ($CO\underline{C}H_2$), 130.17 (=CH-),130.36 (=CH-),184.22 (OOC); IR (liquid cell in tetrachloroethylene): 1304.79, 1401.77, 1466.38, 1524.19, 1549.93, 1710.59, 1761.22, 2854.97, 2927.3, 3006.15 $cm^{-1}$; Anal. Calcd. For $PbO_4C_{36}H_{66}$: C, 56.15; H, 8.64; N, 0.0. Found: C, 56.07; H, 8.44; N, <0.02. Residual trifluoroacetate content may be measured by $^{19}F$ NMR relative to a $C_6F_6$ internal standard (10 μL); typical residual trifluoroacetate content is ≤0.1% by mass and may be further reduced by recrystallization from hot isopropanol.

**Lead(II) oleate from lead(II) nitrate.** Fluffy white solid. $^1H$ NMR ($C_6D_6$, 500 MHz) $\delta$ = 0.93 (t, $^3J_{H\text{-}H}$ = 7 Hz, 6H), 1.25-1.46 (m, 40H, $(CH_2)_6$ and $(CH_2)_4$), 1.74 (m, 4H, $COCH_2C\underline{H}_2$), 2.14 (m, 8H, =$CHC\underline{H}_2$), 2.34 (t, $^3J_{H\text{-}H}$ = 8 Hz, 4H, $COCH_2$), 5.53 (m, 4H, =CH-); $^{13}C$ NMR ($C_6D_6$, 125 MHz) $\delta$ = 14.40 ($CH_3$), 23.15 ($\underline{C}H_2CH_3$), 25.99 ($COCH_2\underline{C}H_2$), 27.79 (=$CH\underline{C}H_2$-), 27.80 (=$CH\underline{C}H_2$-), 29.81 ($CH_2$), 29.82 ($CH_2$), 29.99 ($CH_2$), 30.05 ($CH_2$), 30.31 ($CH_2$), 30.35 ($CH_2$), 32.36 ($CH_2$), 38.62 ($CO\underline{C}H_2$), 130.19 (=CH-),130.33 (=CH-),182.77 (OOC); IR (DRIFTS): 1311.74, 1345.74, 1404.69, 1425.94, 1468.73, 1486.83, 1657.51, 2826.85, 2850.8, 2871.97, 2918.77, 2952.2, 3003.73 $cm^{-1}$; Anal. Calcd. For $PbO_4C_{36}H_{66}$: C, 56.15; H, 8.64; N, 0.0. Found: C, 55.96; H, 8.87; N, <0.02.

## 2.10. References


(1) Gibbs, W. J. Yale University Press: New Haven, CT, 1948.
(2) Volmer, M. *Kinetik der Phasenbildung*; T. Steinkopf: Leipzig, 1939.
(3) Becker, R.; Döring, W. *Ann. Phys.* **1935**, *416* (8), 719.
(4) Becker, R.; Doring, W. **1954**.
(5) Mullin, J. W. In *Crystallization (Fourth Edition)*; Butterworth-Heinemann: Oxford, 2001; pp 181–215.
(6) Rempel, J. Y.; Bawendi, M. G.; Jensen, K. F. *J. Am. Chem. Soc.* **2009**, *131* (12), 4479.
(7) LaMer, V. K.; Dinegar, R. H. *J. Am. Chem. Soc.* **1950**, *72* (11), 4847.
(8) Sugimoto, T. *J. Colloid Interface Sci.* **1992**, *150* (1), 208.
(9) Sugimoto, T.; Shiba, F.; Sekiguchi, T.; Itoh, H. *Colloids Surf. Physicochem. Eng. Asp.* **2000**, *164* (2), 183.
(10) Sugimoto, T.; Shiba, F. *Colloids Surf. Physicochem. Eng. Asp.* **2000**, *164* (2), 205.
(11) Owen, J. S.; Chan, E. M.; Liu, H.; Alivisatos, A. P. *J. Am. Chem. Soc.* **2010**, *132* (51), 18206.
(12) Abe, S.; Čapek, R. K.; De Geyter, B.; Hens, Z. *ACS Nano* **2012**, *6* (1), 42.
(13) Abe, S.; Capek, R. K.; De Geyter, B.; Hens, Z. *ACS Nano* **2013**, *7* (2), 943.
(14) Beecher, A. N. Using atomically precise clusters to model materials, Columbia University: New York, NY, 2016.
(15) Abécassis, B.; Bouet, C.; Garnero, C.; Constantin, D.; Lequeux, N.; Ithurria, S.; Dubertret, B.; Pauw, B. R.; Pontoni, D. *Nano Lett.* **2015**, *15* (4), 2620.
(16) García-Rodríguez, R.; Hendricks, M. P.; Cossairt, B. M.; Liu, H.; Owen, J. S. *Chem. Mater.* **2013**, *25* (8), 1233.
(17) Matulenko, M. A.; Degl'Innocenti, A.; Capperucci, A. In *Encyclopedia of Reagents for Organic Synthesis*; John Wiley & Sons, Ltd, 2001.
(18) Hines, M. a.; Scholes, G. d. *Adv. Mater.* **2003**, *15* (21), 1844.
(19) Hanson, J. R. *Protecting groups in organic synthesis*; Sheffield Academic: Sheffield, 1999.
(20) Alvarado, S. R.; Shortt, I. A.; Fan, H.-J.; Vela, J. *Organometallics* **2015**, *34* (16), 4023.
(21) Liu, H.; Owen, J. S.; Alivisatos, A. P. *J. Am. Chem. Soc.* **2007**, *129* (2), 305.
(22) Steckel, J. S.; Yen, B. K. H.; Oertel, D. C.; Bawendi, M. G. *J. Am. Chem. Soc.* **2006**, *128* (40), 13032.
(23) Evans, C. M.; Evans, M. E.; Krauss, T. D. *J. Am. Chem. Soc.* **2010**, *132* (32), 10973.
(24) Cademartiri, L.; Bertolotti, J.; Sapienza, R.; Wiersma, D. S.; von Freymann, G.; Ozin, G. A. *J. Phys. Chem. B* **2006**, *110* (2), 671.

(25) Moreels, I.; Justo, Y.; De Geyter, B.; Haustraete, K.; Martins, J. C.; Hens, Z. *ACS Nano* **2011**, *5* (3), 2004.
(26) Weidman, M. C.; Beck, M. E.; Hoffman, R. S.; Prins, F.; Tisdale, W. A. *ACS Nano* **2014**, *8* (6), 6363.
(27) Liu, T.-Y.; Li, M.; Ouyang, J.; Zaman, M. B.; Wang, R.; Wu, X.; Yeh, C.-S.; Lin, Q.; Yang, B.; Yu, K. *J. Phys. Chem. C* **2009**, *113* (6), 2301.
(28) Yu, W. W.; Peng, X. *Angew. Chem. Int. Ed.* **2002**, *41* (13), 2368.
(29) Protière, M.; Reiss, P. *Nanoscale Res. Lett.* **2006**, *1* (1), 62.
(30) Swafford, L. A.; Weigand, L. A.; Bowers, M. J.; McBride, J. R.; Rapaport, J. L.; Watt, T. L.; Dixit, S. K.; Feldman, L. C.; Rosenthal, S. J. *J. Am. Chem. Soc.* **2006**, *128* (37), 12299.
(31) Li, Z.; Ji, Y.; Xie, R.; Grisham, S. Y.; Peng, X. *J. Am. Chem. Soc.* **2011**, *133* (43), 17248.
(32) Thomson, J. W.; Nagashima, K.; Macdonald, P. M.; Ozin, G. A. *J. Am. Chem. Soc.* **2011**, *133* (13), 5036.
(33) van Embden, J.; Jasieniak, J.; Mulvaney, P. *J. Am. Chem. Soc.* **2009**, *131* (40), 14299.
(34) *CRC Handbook of Chemistry and Physics*; Haynes, W. M., Ed.; CRC Press/Taylor & Francis: Boca Raton, FL, 2017.
(35) Yordanov, G. G.; Yoshimura, H.; Dushkin, C. D. *Colloid Polym. Sci.* **2008**, *286* (6–7), 813.
(36) McPhail, M. R.; Weiss, E. A. *Chem. Mater.* **2014**, *26* (11), 3377.
(37) Sapra, S.; Rogach, A. L.; Feldmann, J. *J. Mater. Chem.* **2006**, *16* (33), 3391.
(38) Blekas, G.; Tsimidou, M. In *Olive oil: Chemistry and technology*; Boskou, D., Ed.; Elsevier Science, 2006; Vol. 4.
(39) Chen, O.; Zhao, J.; Chauhan, V. P.; Cui, J.; Wong, C.; Harris, D. K.; Wei, H.; Han, H.-S.; Fukumura, D.; Jain, R. K.; Bawendi, M. G. *Nat. Mater.* **2013**, *12* (5), 445.
(40) Jeong, B. G.; Park, Y.-S.; Chang, J. H.; Cho, I.; Kim, J. K.; Kim, H.; Char, K.; Cho, J.; Klimov, V. I.; Park, P.; Lee, D. C.; Bae, W. K. *ACS Nano* **2016**, *10* (10), 9297.
(41) Owen, J. *Science* **2015**, *347* (6222), 615.
(42) Aldana, J.; Wang, Y. A.; Peng, X. *J. Am. Chem. Soc.* **2001**, *123* (36), 8844.
(43) Luther, J. M.; Law, M.; Song, Q.; Perkins, C. L.; Beard, M. C.; Nozik, A. J. *ACS Nano* **2008**, *2* (2), 271.
(44) Barkhouse, D. A. R.; Pattantyus-Abraham, A. G.; Levina, L.; Sargent, E. H. *ACS Nano* **2008**, *2* (11), 2356.
(45) Zhang, A.; Dong, C.; Liu, H.; Ren, J. *J. Phys. Chem. C* **2013**, *117* (46), 24592.
(46) Weinberg, D. J.; He, C.; Weiss, E. A. *J. Am. Chem. Soc.* **2016**, *138* (7), 2319.

(47) Brennan, J. G.; Siegrist, T.; Carroll, P. J.; Stuczynski, S. M.; Reynders, P.; Brus, L. E.; Steigerwald, M. L. *Chem. Mater.* **1990**, *2* (4), 403.
(48) Trindade, T.; O'Brien, P. *Adv. Mater.* **1996**, *8* (2), 161.
(49) Trindade, T.; O'Brien, P. *J. Mater. Chem.* **1996**, *6* (3), 343.
(50) Trindade, T.; O'Brien, P.; Zhang, X. *Chem. Mater.* **1997**, *9* (2), 523.
(51) Malik, M. A.; O'Brien, P.; Revaprasadu, N. *Chem. Mater.* **2002**, *14* (5), 2004.
(52) Ruberu, T. P. A.; Albright, H. R.; Callis, B.; Ward, B.; Cisneros, J.; Fan, H.-J.; Vela, J. *ACS Nano* **2012**, *6* (6), 5348.
(53) Brutchey, R. L. *Acc. Chem. Res.* **2015**, *48* (11), 2918.
(54) Guo, Y.; Alvarado, S. R.; Barclay, J. D.; Vela, J. *ACS Nano* **2013**, *7* (4), 3616.
(55) Mertschenk, B.; Beck, F.; Bauer, W. In *Ullmann's Encyclopedia of Industrial Chemistry*; Wiley-VCH Verlag GmbH & Co. KGaA, 2000.
(56) Ghosh, H.; Sarkar, S.; Ali, A. R.; Patel, B. K. *J. Sulfur Chem.* **2010**, *31* (1), 1.
(57) Koketsu, M.; Ishihara, H. In *Handbook of Chalcogen Chemistry*; Royal Society of Chemistry: Cambridge, 2007; pp 145–194.
(58) Takemoto, Y. *Org. Biomol. Chem.* **2005**, *3* (24), 4299.
(59) Takemoto, Y. *Chem. Pharm. Bull. (Tokyo)* **2010**, *58* (5), 593.
(60) Bordwell, F. G.; Algrim, D. J.; Harrelson, J. A. *J. Am. Chem. Soc.* **1988**, *110* (17), 5903.
(61) Marcotrigiano, G.; Peyronel, G.; Battistuzzi, R. *J. Chem. Soc. Perkin Trans. 2* **1972**, No. 11, 1539.
(62) Glenn, F. E. In *Kirk-Othmer Encyclopedia of Chemical Technology*; John Wiley & Sons, Inc., 2000.
(63) Catalano, J.; Murphy, A.; Yao, Y.; Yap, G. P. A.; Zumbulyadis, N.; Centeno, S. A.; Dybowski, C. *Dalton Trans* **2015**, *44* (5), 2340.
(64) Zherebetskyy, D.; Scheele, M.; Zhang, Y.; Bronstein, N.; Thompson, C.; Britt, D.; Salmeron, M.; Alivisatos, P.; Wang, L.-W. *Science* **2014**, *344* (6190), 1380.
(65) Houtepen, A. J.; Koole, R.; Vanmaekelbergh, D.; Meeldijk, J.; Hickey, S. G. *J. Am. Chem. Soc.* **2006**, *128* (21), 6792.
(66) Chen, O.; Chen, X.; Yang, Y.; Lynch, J.; Wu, H.; Zhuang, J.; Cao, Y. C. *Angew. Chem. Int. Ed.* **2008**, *47* (45), 8638.
(67) Hendricks, M. P.; Cossairt, B. M.; Owen, J. S. *ACS Nano* **2012**, *6* (11), 10054.
(68) Anderson, N. C.; Owen, J. S. *Chem. Mater.* **2013**, *25* (1), 69.
(69) Anderson, N. C.; Hendricks, M. P.; Choi, J. J.; Owen, J. S. *J. Am. Chem. Soc.* **2013**, *135* (49), 18536.
(70) Norman, Z. M.; Anderson, N. C.; Owen, J. S. *ACS Nano* **2014**, *8* (7), 7513.
(71) Campos, M. P.; Owen, J. S. *Chem. Mater.* **2016**, *28* (1), 227.
(72) Chen, P. E.; Anderson, N. C.; Norman, Z. M.; Owen, J. S. *J. Am. Chem. Soc.* **2017**, *139* (8), 3227.
(73) Farina, P.; Latter, T.; Levason, W.; Reid, G. *Dalton Trans.* **2013**, *42* (13), 4714.

(74) Lead(II) tetrafluoroborate solution 401579 http://www.sigmaaldrich.com/catalog/product/aldrich/401579 (accessed Jul 17, 2017).
(75) 13814-96-5 - Lead(II) tetrafluoroborate, 50% w/w aq. soln. - 41956 - Alfa Aesar https://www.alfa.com/en/catalog/041956/ (accessed Jul 17, 2017).
(76) Oida, T.; Uemura, S. In *Encyclopedia of Reagents for Organic Synthesis*; John Wiley & Sons, Ltd, 2001.
(77) Kiper, R. Lead(II) Acetate http://chemister.ru/Database/properties-en.php?dbid=1&id=1990 (accessed Jul 17, 2017).
(78) McCallum, C.; Pethybridge, A. D. *Electrochimica Acta* **1975**, *20* (11), 815.
(79) Kolthoff, I. M.; Chantooni, M. K.; Bhowmik, S. *J. Am. Chem. Soc.* **1968**, *90* (1), 23.
(80) Allen, A. D.; Tidwell, T. T. *J. Am. Chem. Soc.* **1982**, *104* (11), 3145.
(81) In *Chemistry of the Elements (Second Edition)*; Butterworth-Heinemann: Oxford, 1997; pp 367–405.
(82) Lead(II) oxide 402982 http://www.sigmaaldrich.com/catalog/product/sigald/402982 (accessed Jul 17, 2017).
(83) Moreels, I.; Lambert, K.; Smeets, D.; De Muynck, D.; Nollet, T.; Martins, J. C.; Vanhaecke, F.; Vantomme, A.; Delerue, C.; Allan, G.; Hens, Z. *ACS Nano* **2009**, *3* (10), 3023.
(84) Semonin, O. E.; Johnson, J. C.; Luther, J. M.; Midgett, A. G.; Nozik, A. J.; Beard, M. C. *J. Phys. Chem. Lett.* **2010**, *1* (16), 2445.
(85) Murray, C. B.; Kagan, and C. R.; Bawendi, M. G. *Annu. Rev. Mater. Sci.* **2000**, *30* (1), 545.
(86) Boles, M. A.; Engel, M.; Talapin, D. V. *Chem. Rev.* **2016**, *116* (18), 11220.
(87) Ratke, L. *Growth and coarsening : Ostwald ripening in material processing*; Springer: New York, 2002.
(88) Hammett, L. P. *J. Am. Chem. Soc.* **1937**, *59* (1), 96.
(89) Ritchie, C. D.; Sager, W. F. In *Progress in Physical Organic Chemistry*; Cohen, S. G., Jr, A. S., Taft, R. W., Eds.; John Wiley & Sons, Inc., 1964; pp 323–400.
(90) Hansch, C.; Leo, A.; Taft, R. W. *Chem. Rev.* **1991**, *91* (2), 165.
(91) *Viscosity of liquids: theory, estimation, experiment, and data*; Viswanath, D. S., Ed.; Springer: Dordrecht, 2007.
(92) Zhang, J.; Gao, J.; Miller, E. M.; Luther, J. M.; Beard, M. C. *ACS Nano* **2014**, *8* (1), 614.
(93) Zhang, F.; Hu, Y.; Schuettfort, T.; Di, C.; Gao, X.; McNeill, C. R.; Thomsen, L.; Mannsfeld, S. C. B.; Yuan, W.; Sirringhaus, H.; Zhu, D. *J. Am. Chem. Soc.* **2013**, *135* (6), 2338.
(94) Yang, Y.; Qin, H.; Peng, X. *Nano Lett.* **2016**, *16* (4), 2127.

(95) Yang, Y.; Qin, H.; Jiang, M.; Lin, L.; Fu, T.; Dai, X.; Zhang, Z.; Niu, Y.; Cao, H.; Jin, Y.; Zhao, F.; Peng, X. *Nano Lett.* **2016**, *16* (4), 2133.
(96) De Nolf, K.; Cosseddu, S. M.; Jasieniak, J. J.; Drijvers, E.; Martins, J. C.; Infante, I.; Hens, Z. *J. Am. Chem. Soc.* **2017**, *139* (9), 3456.
(97) Murray, C. B.; Sun, S.; Gaschler, W.; Doyle, H.; Betley, T. A.; Kagan, C. R. *IBM J. Res. Dev.* **2001**, *45* (1), 47.
(98) Boneschanscher, M. P.; Evers, W. H.; Geuchies, J. J.; Altantzis, T.; Goris, B.; Rabouw, F. T.; Rossum, S. A. P. van; Zant, H. S. J. van der; Siebbeles, L. D. A.; Tendeloo, G. V.; Swart, I.; Hilhorst, J.; Petukhov, A. V.; Bals, S.; Vanmaekelbergh, D. *Science* **2014**, *344* (6190), 1377.
(99) Evers, W. H.; Schins, J. M.; Aerts, M.; Kulkarni, A.; Capiod, P.; Berthe, M.; Grandidier, B.; Delerue, C.; van der Zant, H. S. J.; van Overbeek, C.; Peters, J. L.; Vanmaekelbergh, D.; Siebbeles, L. D. A. *Nat. Commun.* **2015**, *6*, 8195.
(100) Walravens, W.; De Roo, J.; Drijvers, E.; ten Brinck, S.; Solano, E.; Dendooven, J.; Detavernier, C.; Infante, I.; Hens, Z. *ACS Nano* **2016**, *10* (7), 6861.
(101) Beecher, A. N.; Yang, X.; Palmer, J. H.; LaGrassa, A. L.; Juhas, P.; Billinge, S. J. L.; Owen, J. S. *J. Am. Chem. Soc.* **2014**, *136* (30), 10645.
(102) Weiss, E. A. *ACS Energy Lett.* **2017**, *2* (5), 1005.
(103) Reiss, P.; Protière, M.; Li, L. *Small* **2009**, *5* (2), 154.
(104) Yu, W. W.; Qu, L.; Guo, W.; Peng, X. *Chem. Mater.* **2003**, *15* (14), 2854.
(105) Buonsanti, R.; Milliron, D. J. *Chem. Mater.* **2013**, *25* (8), 1305.
(106) Norris, D. J.; Efros, A. L.; Erwin, S. C. *Science* **2008**, *319* (5871), 1776.
(107) Li, L. S.; Pradhan, N.; Wang, Y.; Peng, X. *Nano Lett.* **2004**, *4* (11), 2261.
(108) Dawood, F.; Schaak, R. E. *J. Am. Chem. Soc.* **2009**, *131* (2), 424.
(109) Peng, P.; Sadtler, B.; Alivisatos, A. P.; Saykally, R. J. *J. Phys. Chem. C* **2010**, *114* (13), 5879.
(110) Ghezelbash, A.; Korgel, B. A. *Langmuir* **2005**, *21* (21), 9451.
(111) Biacchi, A. J.; Vaughn, D. D.; Schaak, R. E. *J. Am. Chem. Soc.* **2013**, *135* (31), 11634.
(112) Liu, M.; Xue, X.; Ghosh, C.; Liu, X.; Liu, Y.; Furlani, E. P.; Swihart, M. T.; Prasad, P. N. *Chem. Mater.* **2015**, *27* (7), 2584.
(113) Wang, X.; Swihart, M. T. *Chem. Mater.* **2015**, *27* (5), 1786.
(114) Liu, X.; Wang, X.; Swihart, M. T. *Chem. Mater.* **2013**, *25* (21), 4402.
(115) Liu, X.; Wang, X.; Zhou, B.; Law, W.-C.; Cartwright, A. N.; Swihart, M. T. *Adv. Funct. Mater.* **2013**, *23* (10), 1256.
(116) Chesman, A. S. R.; van Embden, J.; Duffy, N. W.; Webster, N. A. S.; Jasieniak, J. J. *Cryst. Growth Des.* **2013**, *13* (4), 1712.
(117) Li, J. J.; Wang, Y. A.; Guo, W.; Keay, J. C.; Mishima, T. D.; Johnson, M. B.; Peng, X. *J. Am. Chem. Soc.* **2003**, *125* (41), 12567.

(118) Peng, Z. A.; Peng, X. *J. Am. Chem. Soc.* **2001**, *123* (1), 183.
(119) Jasieniak, J.; Smith, L.; van Embden, J.; Mulvaney, P.; Califano, M. *J. Phys. Chem. C* **2009**, *113* (45), 19468.

## CHAPTER 3. A Library of Selenourea Precursors to PbSe Nanocrystals with Size Distributions Near the Homogeneous Limit

### Table of Contents

Reproduced in part from:

Campos, M. P.; Hendricks, M. P.; Beecher, A. N.; Walravens, W.; Swain, R. A.; Cleveland, G. T.; Hens, Z.; Sfeir, M. Y.; Owen, J. S. *J. Am. Chem. Soc.* **2017**, *139* (6), 2296.

Some of the experiments described herein were performed by A. N. Beecher, W. Walravens, and M. Y. Sfeir. Their collaboration in this endeavor is gratefully acknowledged.

## 3.1. Abstract

### *3.1.1. Technical Abstract*

We report a tunable library of *N*,*N*,*N'*-trisubstituted selenourea precursors and their reaction with lead oleate at 60–150 °C to form carboxylate-terminated PbSe nanocrystals in quantitative yields. Single exponential conversion kinetics can be tailored over four orders of magnitude by adjusting the selenourea structure. The wide range of conversion reactivity allows the extent of nucleation ([nanocrystal] = 4.6 – 56.7 μM) and the size following complete precursor conversion ($d$ = 1.7 – 6.6 nm) to be controlled. Narrow size distributions ( $\sigma$ = 0.5 – 2%) are obtained whose spectral linewidths are dominated (73 – 83%) by the intrinsic single particle spectral broadening, as observed using spectral hole burning measurements. The intrinsic broadening decreases with increasing size (FWHM = 320 – 65 meV, $d$ = 1.6 – 4.4 nm) that derives from exciton fine structure and exciton-phonon coupling rather than broadening caused by the size distribution.

### *3.1.2. Plain English Abstract*

Lead selenide (PbSe) nanocrystals are a notoriously difficult material to synthesize. In this section, we build and leverage a library of selenourea compounds as precursors for PbSe nanocrystal synthesis. Each selenourea's

specific substitution pattern influences the rate of PbSe formation, which in turn influences the number and size of the nanocrystals produced. We have used this fine tunability to 1) develop practical syntheses of PbSe and 2) carefully study the size distribution of our samples, which in many cases turn out to be the most uniform ever measured.

### 3.2. Context

Lead selenide (PbSe) nanocrystals have shown several highly desirable optoelectronic properties including efficient multiple exciton generation in photovoltaic devices[1–3] and the assembly of square and honeycomb lattices with topological states and Dirac cones in their band structure.[4–6] These lattices have potential to display unprecedented electrical transport behavior provided that disorder from the nanocrystal size distribution can be reduced.[7] However, it has proven challenging to synthesize PbSe nanocrystals from conventional nanocrystal precursors such as tri-*n*-alkylphosphine selenides, which are relatively unreactive toward lead carboxylate. Low yields of PbSe (< 3%) are typically formed from more reactive secondary phosphine impurities in the tri-*n*-alkylphosphine starting material.[8,9] More recently, diphenylphosphine selenide,[9,10] *bis*(trimethylsilyl)selenide,[11] and other additives such as hexadecanediol[12] have been used to boost the conversion reactivity and improve

the yield, but size control, and, in particular, a high-yielding synthesis of PbSe nanocrystals relevant for photovoltaic cells ($d < 3.9$ nm, $E_g > 1.0$ eV), is needed.

In order to address the lack of selenium reagents with reactivity appropriate for the synthesis of PbSe, we developed a library of N,N,N'-trisubstituted selenoureas. The conversion reactivity of these precursors can be tailored by adjusting their substitution pattern, as we recently demonstrated using a library of analogous thioureas.[13] This tunable reactivity allows the rate of solute supply and the concentration of nanocrystals formed during nucleation to be adjusted[14–18] and the final size following complete precursor conversion to be controlled. Herein we report optimized precursors and conditions for the synthesis of PbSe nanocrystals across a broad range of sizes and at large scale. Narrow size distributions are obtained whose absorption spectral linewidths are dominated by the intrinsic single-particle line broadening rather than heterogeneous broadening caused by the size distribution. These narrow distributions reveal a decreasing single particle spectral linewidth as the size of the nanocrystal increases.

## 3.3. Selenoureas

### *3.3.1. Synthesis of a Library*

Di- and trisubstituted selenoureas can be synthesized from isoselenocyanates, LiAlSeH, NaHSe, $(Me_2Al)_2Se$, N-heterocyclic carbenes, carbon diselenide, and Woollins' Reagent ($[PhP(Se)(\mu\text{-}Se)]_2$),[19] but these approaches can be complicated because key reagents or intermediates are unstable or must be prepared in multiple steps. However, a few disubstituted selenoureas have been prepared in a single step from alkyl isocyanides, elemental selenium, and primary amines.[20–23] We have greatly expanded this approach to prepare a library of di- and trisubstituted selenoureas **1–31** in 60–98% yields (Table 3.3.1). Unlike thioureas, tri- and di- substituted selenoureas are air-sensitive,[24] and in some cases slightly light-sensitive, eventually depositing elemental selenium over several months if stored under ambient conditions. Selenoureas are therefore best handled in the absence of air and stored in the dark, where they are indefinitely stable.

Table 3.3.1. Synthesis of a library of *N,N′*-disubstituted and *N,N,N′*-trisubstituted selenoureas. Reactions performed on 3 mmol scale for 1 hour unless otherwise noted. [a] Performed on 6.6 mmol scale. [b] Performed on 10 mmol scale. [c] 1.5 hour reaction time. [d] 2 hour reaction time. [e] 3 hour reaction time.

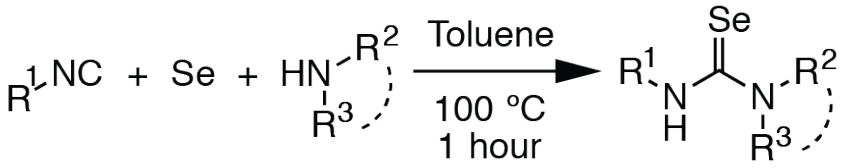


| Compound | $R^1$ | $R^2$ | $R^3$ | Yield (%) |
|---|---|---|---|---|
| **1** | *n*-$C_4H_9$ | $^i$Pr | $^i$Pr | 94 |
| **2** | *n*-$C_4H_9$ | –$(CH_2)_5$– | | 95 |
| **3** | *n*-$C_4H_9$ | *n*-$C_4H_9$ | *n*-$C_4H_9$ | 97 |
| **4** | *n*-$C_4H_9$ | Et | Et | 94 |
| **5** | *n*-$C_4H_9$ | *n*-$C_4H_9$ | Me | 98 |
| **6** | *n*-$C_4H_9$ | Allyl | Allyl | 97 |
| **7** | *n*-$C_4H_9$ | Me | Me | 88 |
| **8** | *n*-$C_4H_9$ | –$(CH_2)_4$– | | 68[a] |
| **9** | *n*-$C_4H_9$ | 4-MeO-Ph | Me | 72[c] |
| **10** | Cy | *n*-$C_{12}H_{25}$ | H | 90[b] |
| **11** | Cy | Cy | Cy | 65 |
| **12** | Cy | $^i$Pr | $^i$Pr | 57 |
| **13** | Cy | $^i$Pr | Et | 79 |
| **14** | Cy | $^i$Pr | Me | 90 |
| **15** | Cy | –$(CH_2)_5$– | | 82 |
| **16** | Cy | *n*-$C_4H_9$ | *n*-$C_4H_9$ | 76 |
| **17** | Cy | Et | Et | 84 |
| **18** | Cy | Et | Me | 69 |
| **19** | Cy | 2-Me-$(CH_2)_4$– | | 88 |

| | | | | |
|---|---|---|---|---|
| **20** | Cy | tetrahydroisoquinolyl | | 95 |
| **21** | Cy | Allyl | Allyl | 98 |
| **22** | Cy | Me | Me | 76[a] |
| **23** | Cy | –$(CH_2)_4$– | | 89 |
| **24** | Cy | 4-MeO-Ph | Me | 71 |
| **25** | Cy | Ph | Me | 64[d] |
| **26** | Cy | 4-Cl-Ph | Me | 27[e] |
| **27** | *n*-$C_{16}H_{33}$ | $^{i}$Pr | Me | 76 |
| **28** | *n*-$C_{16}H_{33}$ | Allyl | Allyl | 63 |
| **29** | *n*-$C_{16}H_{33}$ | Ph | Me | 73 |
| **30** | $^{t}$Bu | Me | Me | 72 |
| **31** | $^{t}$Bu | –$(CH_2)_4$– | | 68 |

Isocyanides react with elemental selenium at 100 °C in toluene to produce isoselenocyanates that are trapped by a variety of nucleophilic amines to form di- and trisubstituted selenoureas. Formation of the selenourea is conveniently monitored by $^{77}$Se nuclear magnetic resonance (NMR) spectroscopy, where the chemical shifts of alkyl isoselenocyanates ($\delta$ = -345 to -358 ppm)[25] and selenoureas ($\delta$ = 175 to 290 ppm) are distinct (Figure 3.3.1). In most cases, the isoselenocyanate does not accumulate and the rate of selenourea formation is limited by the dissolution of elemental selenium, which typically reaches completion over the course of one hour if 100 mesh selenium powder is used. However, less nucleophilic amines are slower to react and an isoselenocyanate intermediate can be observed. For example, while *n*-butylisoselenocyanate reacts

quantitatively with electron-rich 4-methoxy-N-methylaniline to form **9** within 35 minutes, the analogous reaction with N-methylaniline proved more sluggish, requiring more than 2 hours to reach completion. Even more electron deficient 4-cyano-N-methylaniline proved unreactive toward *n*-butylisoselenocyanate over 8 hours (Table 3.3.2). Sterically bulky derivatives such as *N,N,N'*-tricyclohexylselenourea (**2**) can also be prepared in good yields provided that the amine trapping agent is sufficiently nucleophilic.

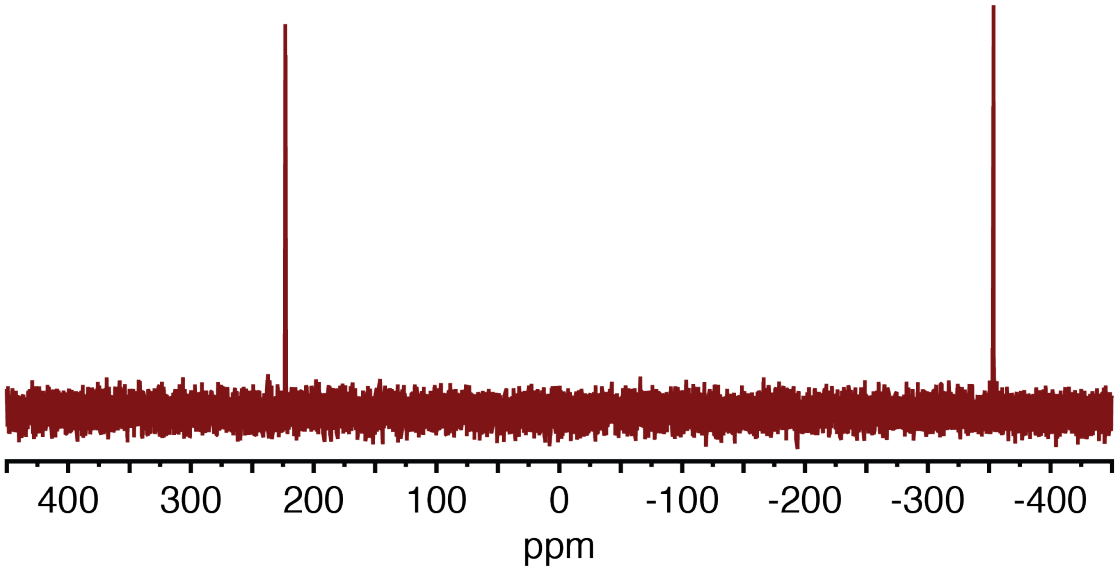


Figure 3.3.1. Example $^{77}$Se NMR spectrum in benzene-$d_6$ containing *N,N,N'*-tricyclohexylselenourea (**11**, 223.09 ppm) and cyclohexyl isoselenocyanate (-353.55 ppm). The chemical shift of **11** differs from that reported in the experimental section (190.99 ppm); solvent and concentration effects are known to influence $^{77}$Se NMR chemical shifts of organoselenium compounds by up to 50 ppm.[26]

Table 3.3.2. Conversion of alkyl isoselenocyanates in the presence of *N*-methylanilines (entries 1–4) and dialkylamines (entries 5-6) determined by $^{77}$Se NMR spectroscopy.

| Entry | $R^1$ | $R^2$ | $R^3$ | Time (h) | Conv. (%) |
|---|---|---|---|---|---|
| 1 | *n*-$C_4H_9$ | 4-MeO-Ph | Me | 1.5 | >99 |
| 2 | *n*-$C_4H_9$ | Ph | Me | 2 | 85 |
| 3 | *n*-$C_4H_9$ | 4-Cl-Ph | Me | 3 | 80 |
| 4 | *n*-$C_4H_9$ | 4-CN-Ph | Me | 8 | < 1 |
| 5 | *n*-$C_4H_9$ | *n*-$C_4H_9$ | *n*-$C_4H_9$ | 0.5 | >99 |
| 6 | Cy | Cy | Cy | 0.5 | 87 |

*3.3.2. Characteristics, Reactivity, and Differences from Thioureas*

Most selenoureas in Table 3.3.1 are readily purified by recrystallization and have been structurally characterized using single crystal X-ray diffraction analysis (Sections 3.7.17, 3.7.18). These structures reveal planar nitrogen atoms, an average C–Se bond length of 1.873 Å, and an average ∠NCN bond angle of 117.2° (Table 3.7.1). In all cases, a hydrogen atom was identified on the nitrogen atom and the C–Se bond length fell within the range typical of double bonds. Both features support the selone tautomer, as has been observed in other selenoureas.[27]

## 3.4. Synthesis of PbSe Nanocrystals

### *3.4.1. Synthesis and Basic Characterization*

PbSe nanocrystals are synthesized by injection of *N*,*N*,*N*′-trisubstituted selenoureas dissolved in diphenyl ether, diglyme, or dibutyl ether into a solution of lead oleate in alkane or 1-alkene solvent at 60–150 °C (Figure 3.4.1A, Figure 3.4.2). The formation of a deep red/brown color occurs 1–50 seconds following the injection, the timing of which depends on the selenourea structure. Monitoring the UV-Vis-NIR spectra of aliquots taken from the reaction mixture shows an increase in the concentration of PbSe and an increase in the average nanocrystal size (Figure 3.4.3). Depending on the selenourea structure and temperature, the reaction reaches completion and the nanocrystals approach their final size between 30 seconds (**12**) and 3 hours (**9**) following the injection.

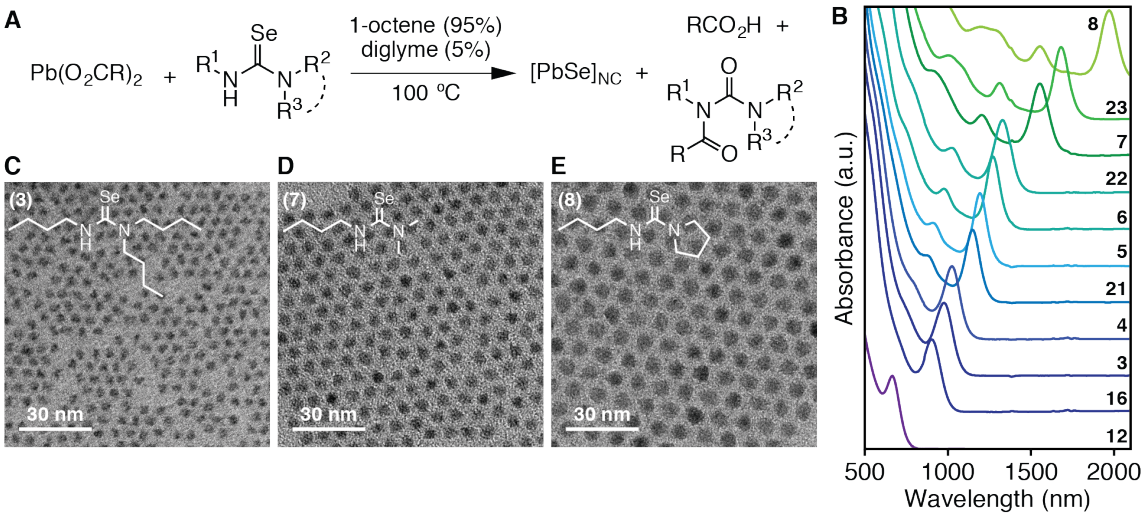


Figure 3.4.1. A) Reaction scheme for the synthesis of PbSe nanocrystals. B) UV-vis-NIR absorption spectra of aliquots removed from PbSe nanocrystal synthesis reactions at completion using the indicated precursors. C-E) Transmission electron micrographs of PbSe nanocrystals synthesized from **3**, **7**, and **8**. R = $C_{17}H_{33}$; $R^1$, $R^2$, $R^3$ = alkyl, aryl.

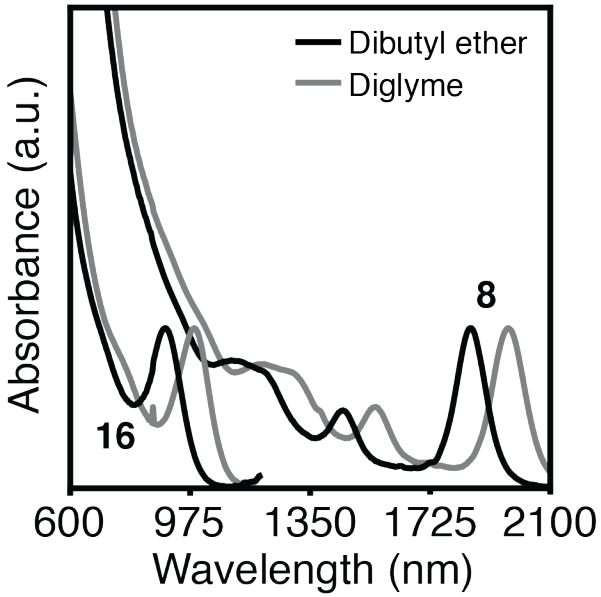


Figure 3.4.2. Effect of changing selenourea injection solvent on final nanocrystal size. Spectra were obtained by removing aliquots from nanocrystal synthesis reactions at completion, according to the procedure reported in Section 3.7.9 from **16** and **8**.

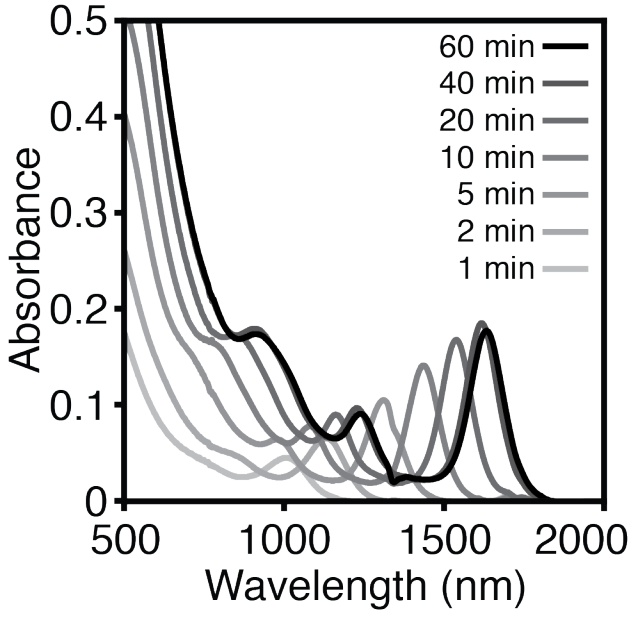


Figure 3.4.3. UV-vis-NIR spectra of aliquots removed from a synthesis of PbSe nanocrystals from **23**. Conditions given in Section 3.7.9.

The flexibility of this synthesis platform has allowed us to optimize the crystallization conditions to achieve unusually low polydispersity. By doing so we have arrived at 1), selenourea concentrations of 5–75 mM, 2) lead-to-selenium ratios of 1.2–1.5, where the 20–50% excess lead oleate passivates the surface,[28] and 3) an ideal reaction temperature of 100 °C, where the conversion reactivity is controlled and does not suffer from mixing-limited kinetics, but below which broader spectral linewidths can result. To put this temperature in context, 100 °C is considerably lower than those typically used to prepare PbSe from trioctylphosphine selenide (150–180 °C)[29,30] and within the range of temperatures used to synthesize PbSe from secondary phosphine selenide precursors (80–135°C).[9,10]

The structure of the selenourea reliably dictates the precursor reactivity and the nanocrystal size following complete conversion. The library of structures allows a wide range of nanocrystal sizes to be synthesized ($d$ = 1.7–6.6 nm, $\lambda_{max}(1S_e\text{-}1S_h)$ = 615–2000 nm) with linewidths indicative of a narrow distribution of sizes (Figure 3.4.1, Figure 3.4.4). High-resolution electron microscopies reveal a quasi-spherical shape (Figure 3.4.1C-E, Figure 3.4.5). The full-width at half-maximum (FWHM) of the $1S_e$–$1S_h$ transition ranges from 35–350 meV and decreases with increasing nanocrystal size (see Figure 3.5.3). At larger sizes ($d$ >

3.9 nm, $E_g$ < 1.0 eV), these spectral linewidths are comparable to the best reported literature spectra,[31,32] but the smaller nanocrystals synthesized using selenoureas ($d$ < 3.9 nm, $E_g$ > 1.0 eV), including those that have band gaps relevant for solar cells ($E_g$ > 1.2 eV), have much narrower linewidths than previous reports. In the case of more reactive precursors **1** and **11–15,** unusually small nanocrystals were obtained ($d$ = 1.6–2.9 nm, $E_g$ = 1.3–2.1 eV) with spectral linewidths narrower than any previous example.[33–35]

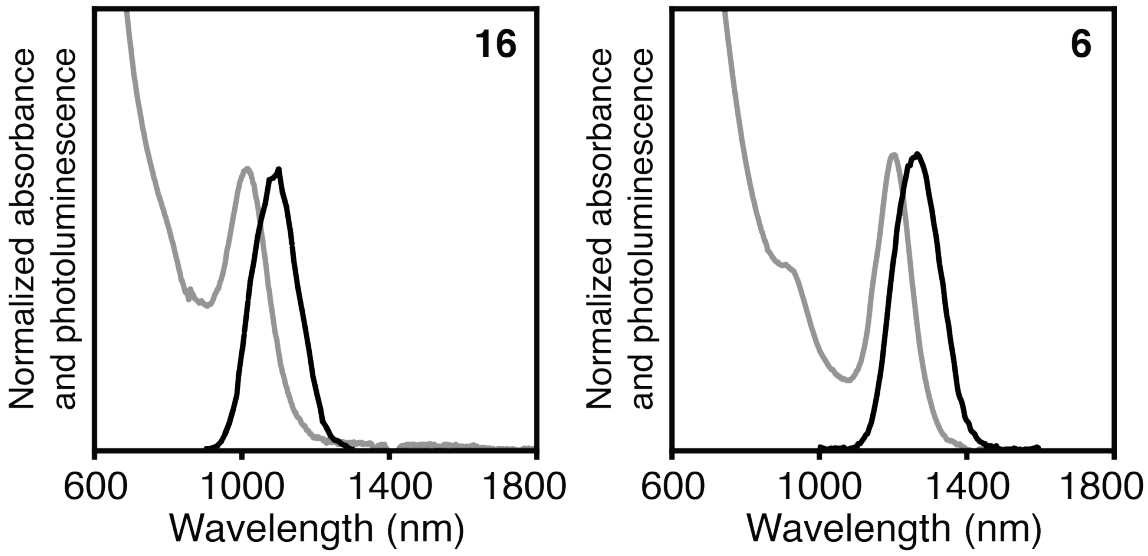


Figure 3.4.4. Example photoluminescence spectra of PbSe nanocrystals (black) overlaid with corresponding absorbance spectra (gray). The spectra were obtained by removing aliquots from completed nanocrystal synthesis reactions performed at half the concentration reported in Section 3.7.9 from **16** and **6**. Samples were diluted so that the absorbance $1S_e$-$1S_h$ peak maximum was between 0.1 and 0.3.

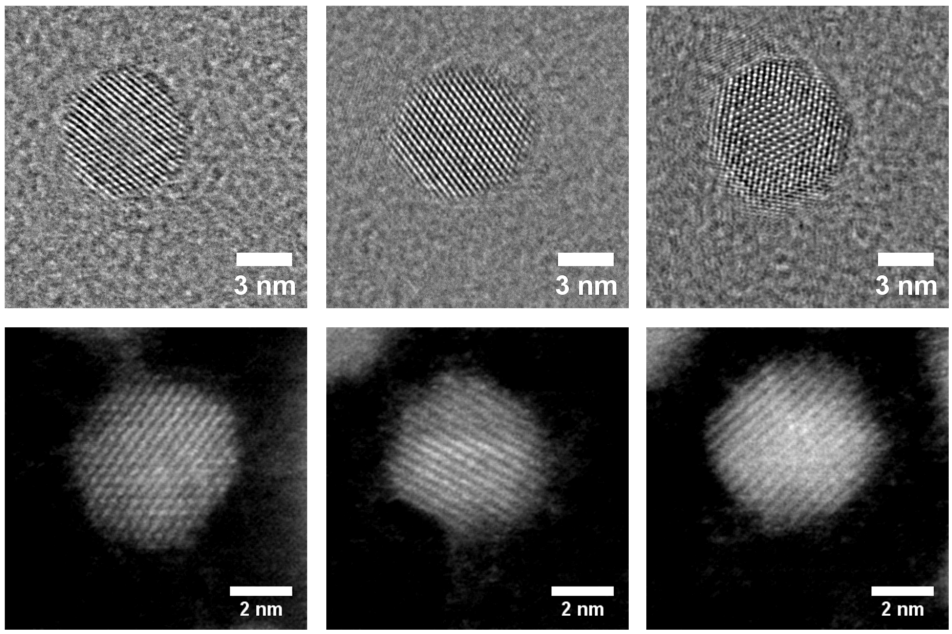


Figure 3.4.5. High-resolution TEM (top row) and STEM (bottom row) images of 6.6 nm and 5.4 nm nanocrystals, respectively, illustrating a uniform faceted, quasi-spherical shape.

*3.4.2. Kinetics, Mechanistic Insights, and Scale-Up*

The kinetics of PbSe formation were monitored *in situ* using a dip probe to measure the absorbance at $\lambda$ = 400 nm.[13] At this wavelength the absorbance does not depend on the nanocrystal size and is proportional to the concentration of crystalline PbSe units.[8] Using $^{1}$H NMR spectroscopy, clean conversion of the selenourea to the corresponding *N*-acylurea and oleic acid co-products is observed (Figure 3.4.1A, Figure 3.4.7). The kinetics of the conversion reaction match the formation of PbSe measured using absorption spectroscopy (Figure 3.4.8). Thus, as was concluded in previous studies of PbS,[13] CdSe,[17] CdS,[36] and

CdTe,[37] the precursor conversion kinetics can be indirectly monitored by the appearance of the nanocrystal absorption. Example UV-Vis absorption kinetics are shown in Figure 3.4.6B where the formation of PbSe approaches completion over the course of several minutes to an hour. Following a short induction period preceding crystal nucleation (1–50 sec), the evolution of the absorbance at 400 nm is well-described by a single exponential function (Figure 3.4.6C, Figure 3.4.9) from which we extract a rate constant ($k_{obs}$, $sec^{-1}$).

A

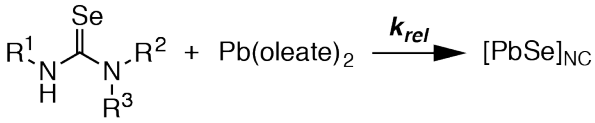


C

| | R¹ | R² | R³ | T (°C) | $k_{rel}$ |
|---|---|---|---|---|---|
| **12** | Cy | $^i$Pr | $^i$Pr | 60 | **12000** |
| **13** | Cy | $^i$Pr | Et | 60 | **960** |
| **14** | Cy | $^i$Pr | Me | 60 | **350** |
| **15** | Cy | –$(CH_2)_5$– | | 80 | **260** |
| **16** | Cy | *n*-$C_4H_9$ | *n*-$C_4H_9$ | 60, 80 | **110** |
| **17** | Cy | Et | Et | 80 | **110** |
| **3** | *n*-$C_4H_9$ | *n*-$C_4H_9$ | *n*-$C_4H_9$ | 80 | **71** |
| **18** | Cy | Et | Me | 80 | **36** |
| **5** | *n*-$C_4H_9$ | *n*-$C_4H_9$ | Me | 80 | **21** |
| **19** | Cy | 2-Me-$(CH_2)_4$- | | 80 | **20** |
| **21** | Cy | Allyl | Allyl | 80 | **14** |
| **22** | Cy | Me | Me | 80, 90 | **13** |
| **23** | Cy | –$(CH_2)_4$– | | 90, 110 | **2.7** |
| **24** | Cy | 4-MeO-Ph | Me | 110, 120 | **1.9** |
| **25** | Cy | Ph | Me | 120 | **1.0** |
| **26** | Cy | 4-Cl-Ph | Me | 120 | **1.0** |
| **8** | *n*-$C_4H_9$ | –$(CH_2)_4$– | | 110 | **1.8** |
| **9** | *n*-$C_4H_9$ | 4-MeO-Ph | Me | 110 | **1.2** |

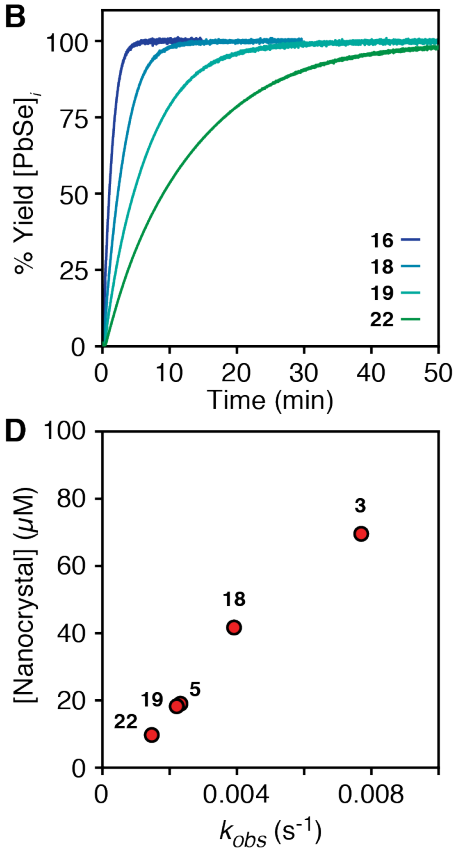


Figure 3.4.6. A) Kinetic studies of PbSe formation from the reaction of lead oleate and selenoureas at 60 – 120 °C. B) Kinetics of PbSe formation as measured *in situ* by the absorbance at $\lambda$ = 400 nm. C) Effect of structural

changes on the relative single exponential rate constants ($k_{rel}$(**12**) to $k_{rel}$(**8**), e.g., $k_{rel}$(**24**) = $k$(**24**)/$k$(**26**)) of selenourea conversion. The wide range of reactivity requires that kinetics are measured at multiple temperatures. To account for the temperature dependence of the conversion rate constant, **16** and **22**–**24** were measured at two temperatures, and the change in rate constant was used to normalize the relative rate constants of the respective temperatures (e.g. $k_{rel}$(**8**) = [$k$(**8**)$^{110°C}$/$k$(**24**)$^{110°C}$] x [$k$(**24**)$^{120°C}$/$k$(**26**)$^{120°C}$]. D) Nanocrystal concentration versus rate constant ($k_{obs}$) of PbSe formation at 80 ° for **3**, **5**, **18**, **19**, and **22**. Reported $k$ values are averages of three trials.

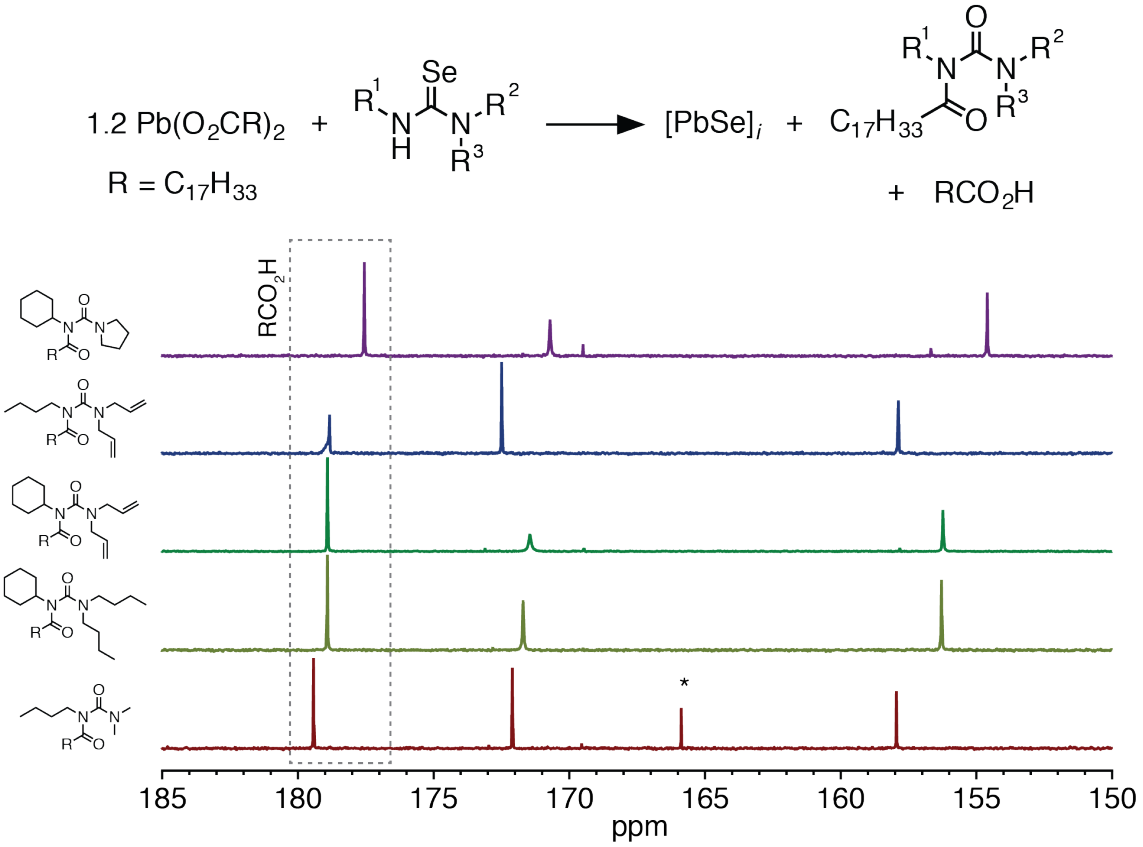


Figure 3.4.7. $^{13}$C NMR spectra of PbSe synthesis co-products identified as oleic acid and N-acylureas. Reactions were carried out as described in

Section 3.7.9 with selenourea **7** and as described in Section 3.7.10 with selenoureas **6**, **16**, **21**, and **23**. For the bottom spectrum, the co-product assignment was confirmed by separately synthesizing *N*-butyl-*N'*-(dimethylcarbamoyl)oleylamide from *N'*-butyl-*N*,*N*-dimethylurea and oleoyl chloride analogously to Rodrigues *et al*.[38] This set of co-products is consistent with a previous report on the reaction between lead(II) acetate trihydrate and disubstituted thioureas.[39] Another possible set of co-products, *N*,*N*-dimethyl-*N'*-butylurea and oleic anhydride, was ruled out by the appearance of new resonances upon addition of these compounds to the sample from which the bottom spectrum was obtained. (*) denotes dimethyl terephthalate standard.

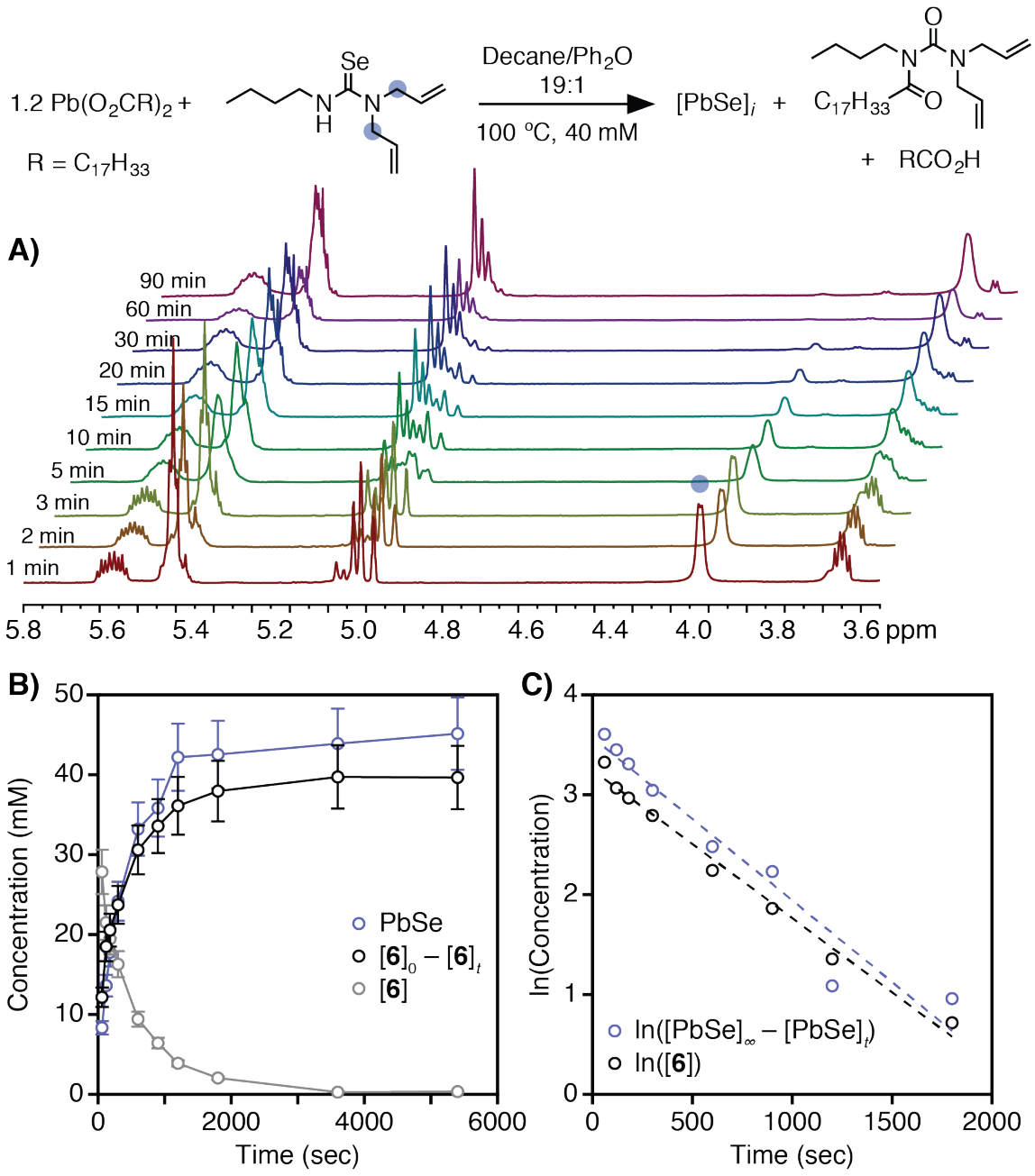


Figure 3.4.8. Comparison of PbSe formation kinetics by UV-vis-NIR spectroscopy and conversion kinetics of **6** by $^1$H NMR spectroscopy. 500 μL aliquots were removed at the indicated times and split between UV-vis-NIR (100 μL into 8 mL tetrachloroethylene) and NMR (400 μL into 400 μL benzene-$d_6$. Dimethyl terephthalate (11.2 mM) was included in the reaction mixture as an internal standard. A) NMR spectra of aliquots. B)

Conversion of **6** and formation of PbSe over time. C) First order plots of **6** conversion and PbSe formation.

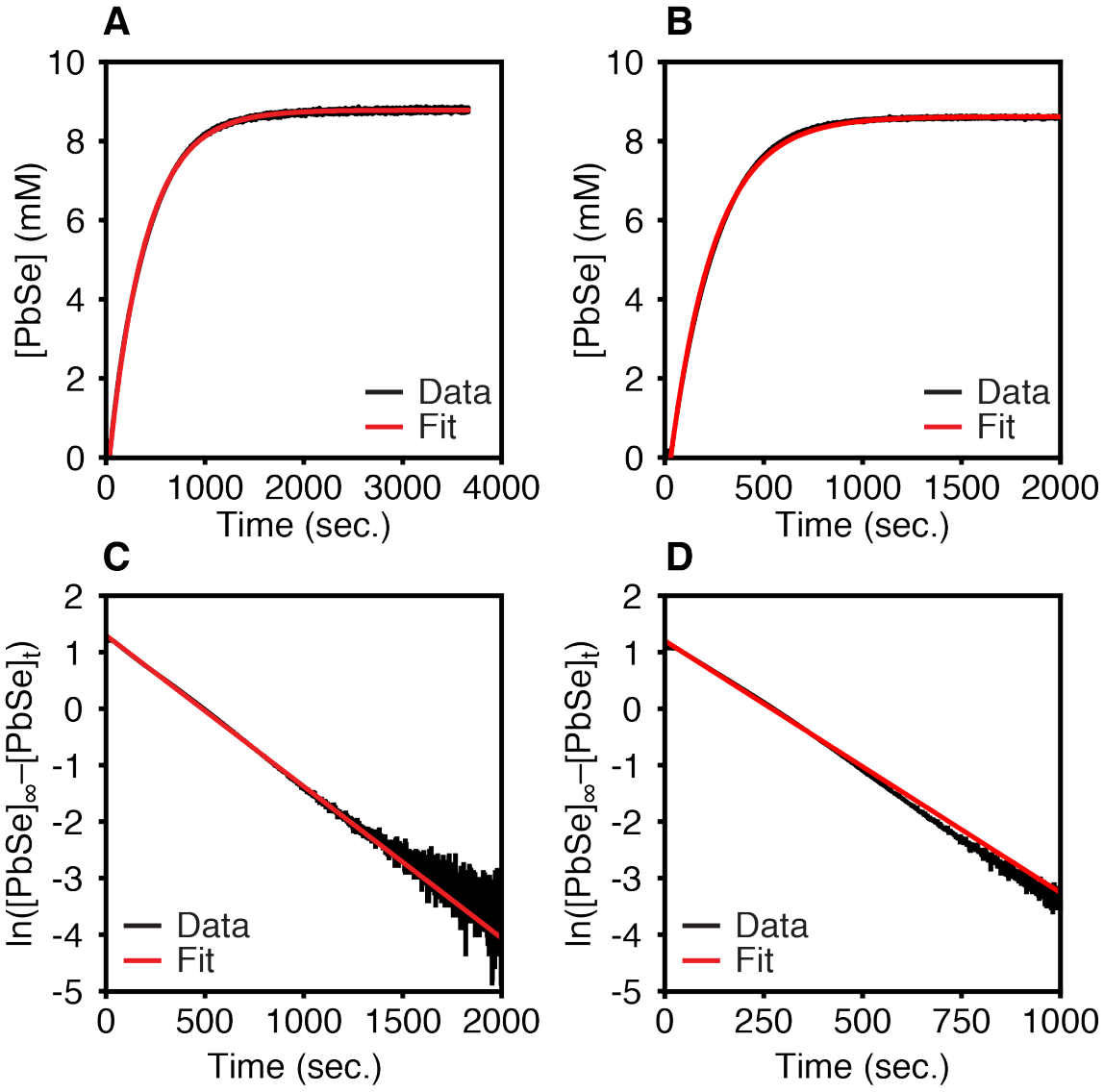


Figure 3.4.9. Example single exponential fits to kinetics data. The reactions were run as described for kinetics experiments with **19** (left) at 80 °C and **22** (right) at 90 °C. The upper plots (A, B) show the formation of PbSe as a function of time, fit with a single exponential trace in red. The lower plots (C, D) show the same data plotted against ln([PbSe]). $t$ = 0 was defined as the onset of absorption at $\lambda$ = 400 nm.

By normalizing the $k_{obs}$ to the slowest precursor (**26**), a series of relative conversion rate constants ($k_{rel}$) are obtained that can be used to assess the effect of the selenourea structure on the conversion reactivity (see Section 3.7). For example, increasing the steric bulk of the substituents increases the $k_{rel}$ over more than three orders of magnitude (Figure 3.4.6C). A similar increase in reactivity of thioureas with steric bulk suggests that elimination of lead sulfide and lead selenide from a chalcogenoureate complex may be involved in the rate determining step.[13] It is interesting to note that pyrrolidine-derived selenoureas are relatively unreactive compared to di-*n*-alkyl derivatives. We attribute the decreased reactivity to the more acute C–N–C substituent bond angle of the five-membered pyrrolidine ring (**23**, Figure 3.7.15), which lowers its steric encumbrance. Consistent with this hypothesis, the analogous selenourea derived from piperidine (**15**, Figure 3.7.7) has a wider C–N–C angle within the ring and converts at a faster rate. Aryl-substituted selenoureas (**24**–**26**, **9**) react an order of magnitude more slowly than their alkyl analogues (**18**, **22**). Similarly, *N*,*N*,*N*′-trisubstituted *thioureas* with aryl substituents are less reactive toward cadmium oleate than the aliphatic analogues.[13] However, aryl substituents *increase* the reactivity of *N*,*N*′-disubstituted thioureas toward lead oleate, where deprotonation or nucleophilic attack at the central carbon are thought to limit the rate of conversion. On the other hand, the greater reactivity of electron-rich and

bulky *N,N,N′*-trisubstituted selenoureas with lead oleate suggests that the conversion may be limited by unimolecular elimination of the metal chalcogenide.

Following the nucleation mass balance described by Sugimoto,[14] the number of nanocrystals produced by nucleation ($n_f$ ,$L^{-1}$) is determined by the solute supply ($Q_0$, mol $L^{-1}$ $s^{-1}$) and the nucleus growth rate ($v_n$, $nm^3$ $L^{-1}$ $s^{-1}$), where $V_m$ is the molar volume ($nm^3$ $mol^{-1}$) of a PbSe crystal monomer (Equation 3.4.1)

$$n_f = \frac{Q_o V_m}{v_n}$$

Equation 3.4.1.

Consistent with this theory and previous studies of AgCl,[15] AgBr,[16] CdSe,[17] CdS,[13] and PbS,[13] we find that faster selenourea conversion kinetic result in larger $n_f$ and smaller final nanocrystal sizes. This correlation is caused by changes to the extent of nucleation and is not affected by Ostwald ripening (Figure 3.4.10). The $k_{obs}$ values extracted from PbSe formation kinetics are plotted versus the resultant nanocrystal concentrations in Figure 3.4.6D, where a linear correlation between the conversion reactivity and the nanocrystal concentration can be observed. From the slope of the plot we extract a nucleus growth rate $v_n$ of 0.94 PbSe units/sec according to Equation 3.4.1. Using this growth rate and the size distributions extracted below, we estimate the length of the nucleation period to be on the order of 3–16 seconds.

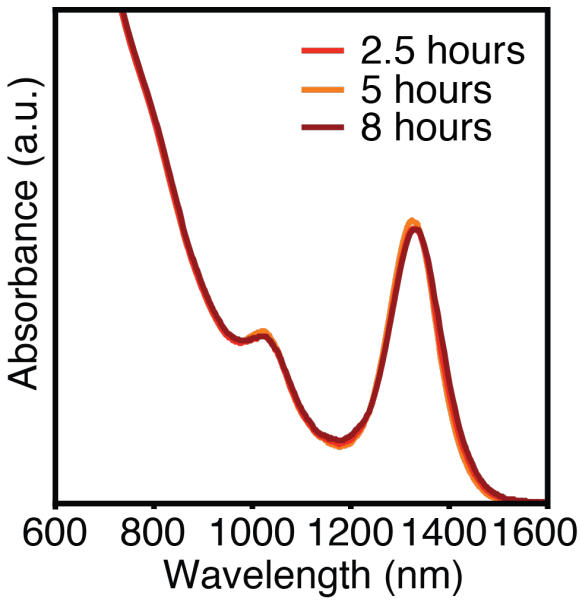


Figure 3.4.10. Absorbance spectra of aliquots showing slow Ostwald ripening. The spectra were obtained by removing aliquots from nanocrystal synthesis reactions performed at half the concentration reported in Section 3.7.9 from *N*,*N*-diallyl-*N'*-butylselenourea (**6**), with hexadecane as the reaction solvent and diphenyl ether as the injection solvent.

The library of conversion reactivity also allows the reaction temperature and precursor to be independently optimized to obtain a desired result. For example, by choosing the appropriate precursor, mixing-limited kinetics during the injection are avoided at large reaction scales (1 – 5 grams) (Figure 3.5.3, Figure 3.4.11, Figure 3.4.12). This allowed us to develop a large scale synthesis of nanocrystals with a band gap appropriate for the fabrication of photovoltaic devices ($l_{max}(1S_e–1S_h)$ = 985 – 1015 nm). Moreover, low-boiling solvents (b.p.(1-octene) = 122 °C; b.p.($Bu_2O$) = 142 °C; b.p.(diglyme) = 162 °C, respectively) can be

chosen that are then easily distilled from the crude nanocrystal product, facilitating the isolation process on large scale. Complete conversion of the starting materials leaves a final reaction mixture whose composition is defined by the starting ratios of reactants, thereby allowing a standard purification procedure to be developed that reproducibly produces nanocrystals with a known ligand coverage (Table 3.4.1, Figure 3.4.13). Optimized isolation procedures that provide reproducible chemical compositions are especially important in light of the reversible surface passivation provided by metal carboxylates, which bind the nanocrystal and influence the photoexcited carrier recombination.[28,40]

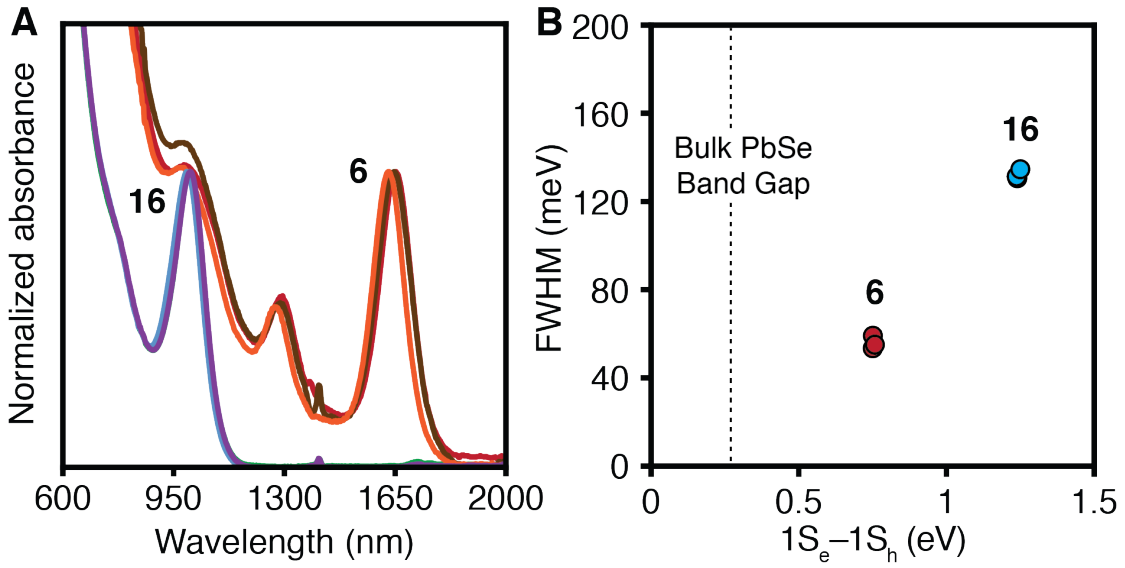


Figure 3.4.11. A) UV-vis-NIR absorbance spectra of six large-scale PbSe nanocrystal syntheses (reproducibility study). B) FWHM vs. lowest energy electronic transition extracted from the six spectra. Reactions were run according to Section 3.7.9.

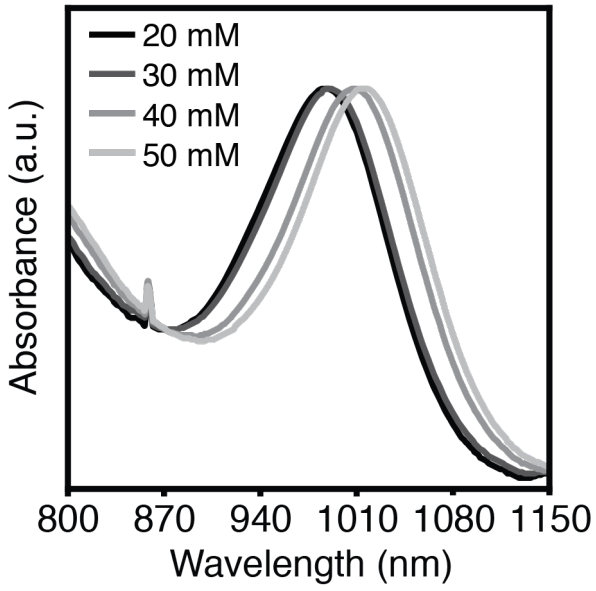


Figure 3.4.12. Effect of reaction concentration on final nanocrystal size. Spectra were obtained by removing aliquots from nanocrystal synthesis reactions at completion, according to the procedure reported in Section

3.7.9 from **16**. Listed concentrations refer to **16**; the $Pb(oleate)_2$-to-**16** ratio was held constant at 1.5.

Table 3.4.1. Sizes, yields, and ligand coverages of nanocrystals produced from **16** after isolation using standard purification procedure described in Section 3.7.10.

| **Sample** | **1** | **2** | **3** |
|---|---|---|---|
| Peak position (nm) | 986 | 995 | 1014 |
| Peak position (eV) | 1.26 | 1.25 | 1.22 |
| Average nanocrystal diameter (nm) | 3.0 | 3.0 | 3.1 |
| Oleate ligand density ($nm^{-2}$) | 5.4 | 6.0 | 5.3 |
| Estimated Pb:Se ratio | 1.32 | 1.35 | 1.30 |
| Nanocrystal empirical formula mass (g/mol) | 529 | 554 | 516 |
| Millimoles **16** used | 2.30 | 2.30 | 2.30 |
| Theoretical yield (g) | 1.2168 | 1.2571 | 1.1871 |
| Actual yield (g) | 1.1278 | 1.0640 | 1.1486 |
| Percent yield (%) | 92.7% | 83.4% | 96.8% |

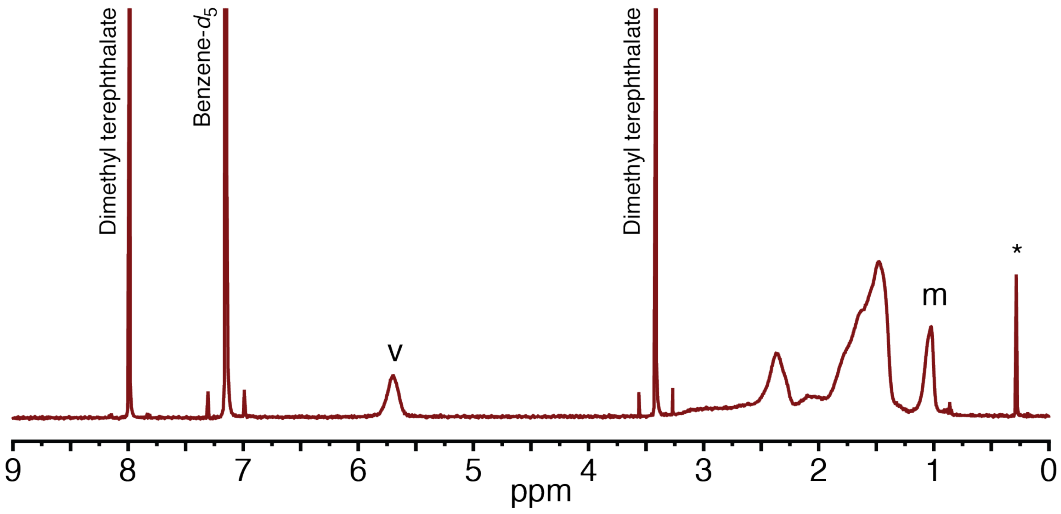


Figure 3.4.13. $^1$H nuclear magnetic resonance spectrum of 5.2 nm PbSe nanocrystals isolated with a surface coverage of 3.1 oleates/nm$^2$. The broad peak at 5.7 ppm corresponds to the vinyl protons of surface-bound lead oleate complexes. Dimethyl terephthalate is included as an internal standard. (*) denotes a small silicone impurity leached from the liner of the vial caps.

## 3.5. PbSe Nanocrystal Size Distributions

### *3.5.1. Relationship Between Linewidth and Size Distribution*

The size distribution of colloidal nanocrystals is often estimated by analyzing the spectral linewidth of the first optical transition. However, this analysis typically assumes the intrinsic linewidth of a single size is much lower than broadening caused by the size distribution.[36,41,42] Recent measurements suggest that exciton-phonon coupling, spectral diffusion, and exciton fine structure can account for more than 50% of the room temperature ensemble

linewidth in highly monodisperse samples, which is at odds with the aforementioned assumption.[43–45] Moreover, several methods, including photoluminescence correlation measurements,[44] photon-echo techniques,[46] single-dot spectroscopy,[47,48] and acquiring absorption spectra of atomically precise clusters[49] show a decreasing intrinsic linewidth as the size increases in CdSe and PbS. Thus, in samples of colloidal crystals with narrow size distributions the spectral linewidth of the ensemble depends on both the intrinsic linewidth of single particles, the particle size, and the size distribution.

*3.5.2. Transient Hole Burning Spectroscopy*

Given the narrow size distributions evident from the sharp spectral features in Figure 1B, we sought to estimate the single-particle spectral linewidth using transient spectral hole burning measurements.[50] Wavelength-tunable excitation pulses that are narrower than the $1S_e$–$1S_h$ linewidth of our samples (5–40 meV versus 65–320 meV) were used to selectively excite a fraction of the ensemble. Following pump-probe delay times ($t$ = 2 ns) that are much longer than multiexciton lifetimes, we measure induced changes in the absorption spectrum ($\Delta A$) as a function of the pump wavelength.

Typical transient absorption (TA) spectra for an ensemble with $E_g$ = 1.2 eV are plotted in Figure 3.5.1. As the excitation pulse is tuned from the tail of the $1S_e$–$1S_h$ absorption, where only the largest nanocrystals absorb, to higher

energies, we observe a corresponding shift in the minimum of the ground state bleach signal (Figure 3.5.1B). After accounting for this shift (Figure 3.5.1C) and the finite spectral width of the excitation pulses (see Section 3.7),[50] we deconvolute the transient absorption spectrum to determine the average single particle transient absorption linewidth. In all cases, this width is 17–27% narrower than that of the ensemble excited far above the band edge. We therefore estimate that the average single particle linewidth of the $1S_e$–$1S_h$ transition in the steady state absorption spectrum is 73–83% of the ensemble linewidth and conclude that the broadening due to the size distribution accounts for the remaining 17–27%. Using the percent narrowing measured with TA, we calculate the intrinsic absorption linewidths of single sizes and plot them next to the ensemble linewidths in Figure 3.5.2 and Figure 3.5.3. A recent measurement of the intrinsic average single PbSe particle linewidth ($1S_e$–$1S_h$ = 1.1 eV, FWHM = 80 meV) was performed using two-dimensional Fourier transform spectroscopy, and is in good agreement with our measurements.[51]

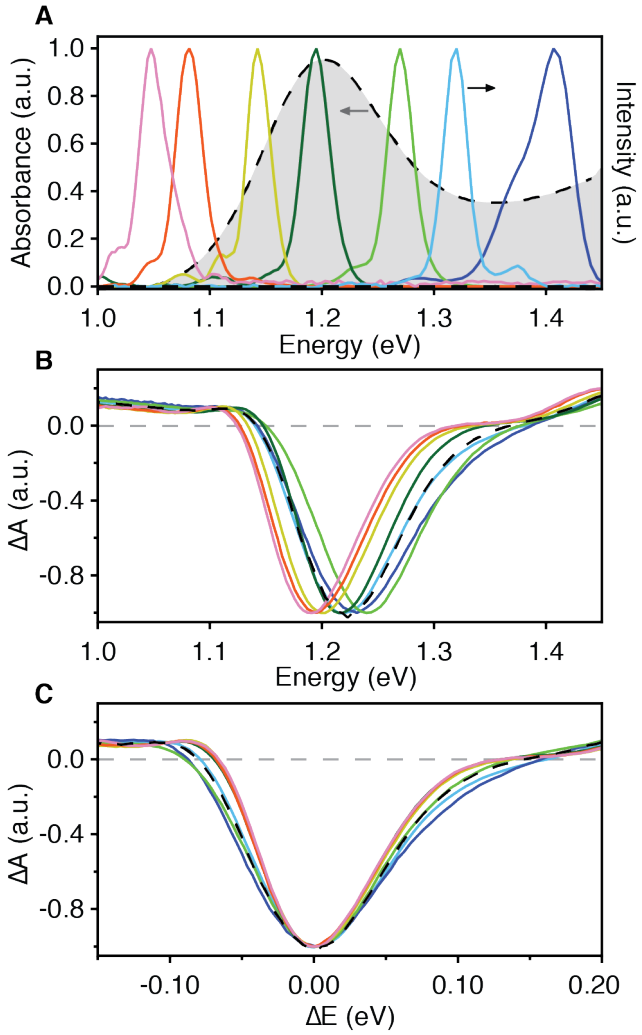


Figure 3.5.1. A) Nanocrystal extinction spectrum for an ensemble with $E_g$ = 1.2 eV (dashed black line) and the spectra of the laser pulses used for photoexcitation. B) Transient spectra recorded at $t$ = 2 ns as a function of photon energy. C) Transient spectra as a function of photon energy, offset to account for changes in the ground state bleach minima.

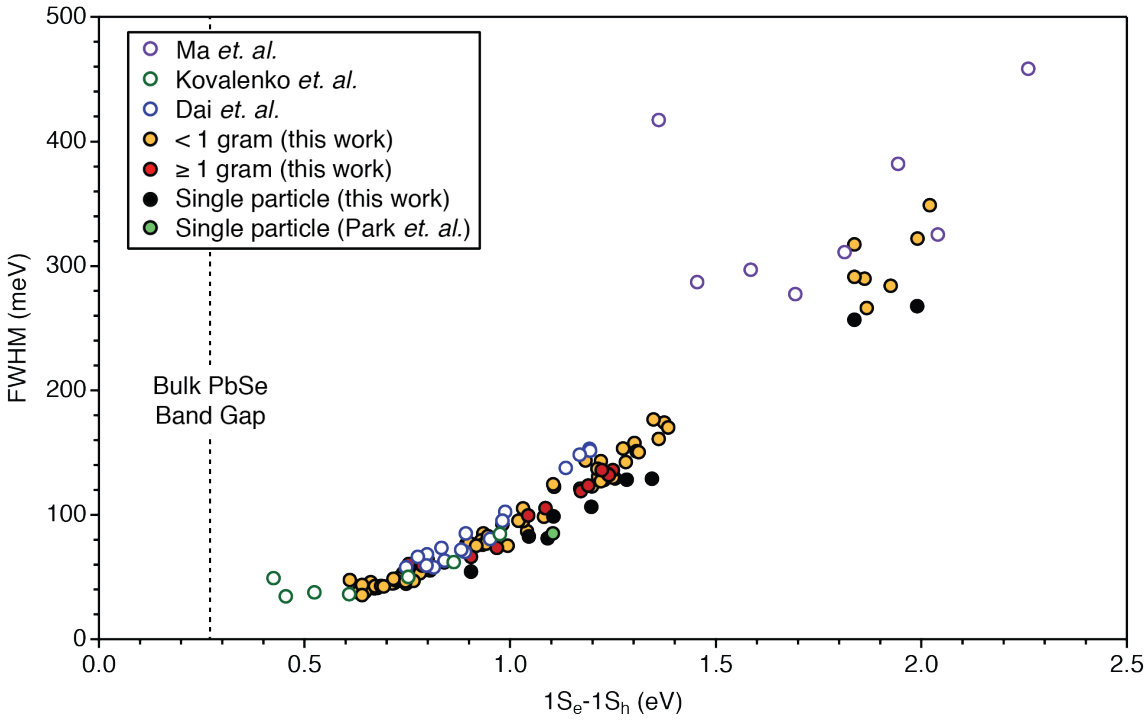


Figure 3.5.2. Results of a reproducibility study showing the FWHM of the lowest energy electronic transition versus its position ($1S_e$–$1S_h$) across 94 reactions using a variety of selenourea precursors and reaction scales (yellow, red). These data are overlaid with data extracted from previously published spectra of PbSe samples (violet,[33] green,[31] blue[32]) and single-particle component linewidths (black, green/black[51]).

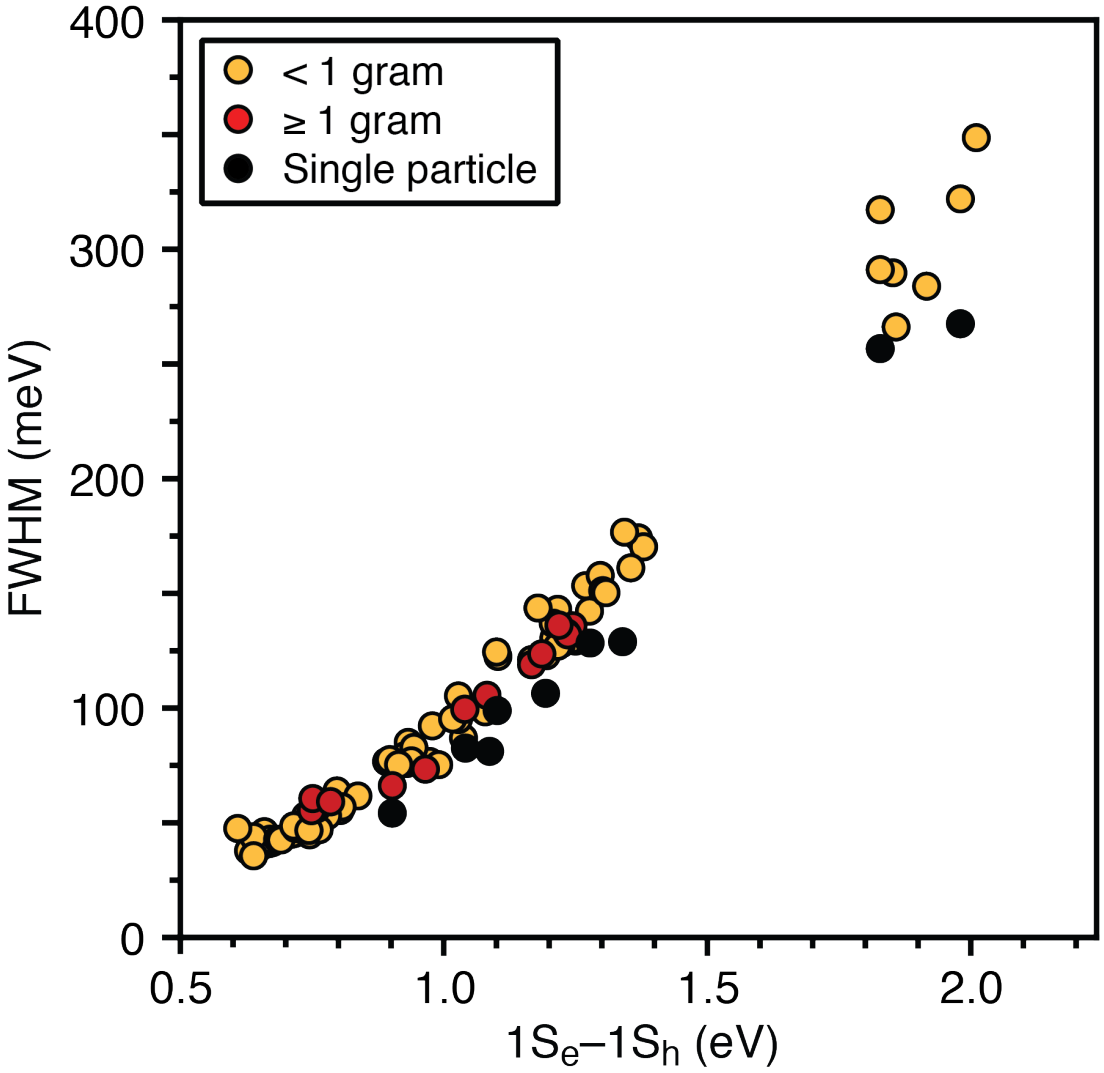


Figure 3.5.3. Subset of data presented in Figure 3.5.2. Measured linewidths of 94 PbSe nanocrystal samples synthesized from trisubstituted selenoureas overlaid with estimated single-particle linewidths.

A significant decrease in the broadening is evident as the size of the nanocrystal increases. The broadening derives mainly from two effects: fine structure in the electronic states and exciton-phonon coupling. Tight binding calculations on a series of PbSe particle sizes indicate that broadening caused by fine structure, including intervalley coupling, is size dependent and can account for roughly half the observed broadening in Figure 3.5.2 and Figure 3.5.3.[52–56] The remainder can be attributed to thermal broadening such as exciton–phonon coupling, which is predicted to be stronger in small nanocrystals, although some disagreement exists over the magnitude of its size dependence.[57–61] Regardless of the source of the intrinsic spectral broadening, the data clearly show that the broadening caused by the size distribution is minor across the wide range of sizes accessible with the selenourea library.

Mechanistic studies of nanocrystal growth often use the spectral linewidth to argue for or against a particular growth mechanism: e.g. spectral broadening with increasing size is signature of Ostwald ripening, while spectral narrowing is signature of size distribution focusing. However, the size dependence of the single particle linewidth evident in Figure 3.5.2, Figure 3.5.3 and in other studies[62,63] must be considered in order to correctly extract the size distribution. In particular, the numerous claims of size distribution focusing should be reevaluated in light of our finding as well as related work on CdSe and PbS

nanocrystals. In the present case, the spectral linewidth is mostly a consequence of the intrinsic broadening of a single size and is not significantly influenced by the size distribution. Indeed, our estimate indicates that the relative standard deviation in the nanocrystal diameter is 0.5–2% for all samples studied here, corresponding to total distributions in the formula of 3–15 PbSe units, assuming a spherical particle shape. These distributions are vanishingly small and unlikely to induce significant differences in the relative growth rates of different radii within the size distribution.

**3.6. Summary**

We report a library of *N*,*N*,*N'*-trisubstituted selenoureas whose conversion kinetics to PbSe nanocrystals can be finely controlled by adjusting their substitution pattern. The nanocrystal concentration, and therefore the final nanocrystal size following complete precursor conversion, is readily tuned by the conversion reactivity. These precursors provide a convenient synthesis of PbSe nanocrystals on large reaction scales whose spectral features are exceptionally narrow and dominated by single-particle spectral broadening rather than the size distribution. This is especially valuable at small sizes where it has proven difficult to access PbSe nanocrystals whose band gap is appropriate for solar photovoltaic devices.

## 3.7. Experimental Details

### *3.7.1. General Methods*

All manipulations were performed using standard air-free techniques on a Schlenk line under argon atmosphere or in a nitrogen-filled glovebox unless otherwise indicated.

### *3.7.2. Chemicals*

Acetonitrile (≥99.5%), hexane (mixture of isomers, ≥98.5%), isopropanol (≥99.5%), methanol (≥99.8%), and toluene (≥99.5%) were obtained from Aldrich and used without further purification. Tetrachloroethylene (anhydrous, ≥99%), tetrahydrofuran (anhydrous, ≥99.9%, inhibitor-free), methyl acetate (99.5%, anhydrous), decane (anhydrous, ≥99%), dibutyl ether (anhydrous, 99.3%), diethylene glycol dimethyl ether ("diglyme," anhydrous, 99.5%) were obtained from Aldrich, transferred to a glovebox, shaken with activated alumina, filtered, and stored over activated 3Å molecular sieves for 24 h prior to use. Toluene (≥99.5), dichloromethane (≥99.5%, contains 40-150 ppm amylene as stabilizer), and diethyl ether (≥99.9%, inhibitor-free) were obtained from Aldrich, degassed, dried in a column packed with activated alumina, and stored in a glovebox over activated 3Å molecular sieves for 24 h prior to use. Pentane (≥98%) was obtained from Fisher Chemical, degassed, dried in a column packed with activated

alumina, and stored in a glovebox over activated 3Å molecular sieves for 24 h prior to use. Diphenyl ether (≥99%), hexadecane (99%), and *n*-octane (≥99%) were obtained from Aldrich, stirred with calcium hydride overnight, distilled and stored in a glove box over activated 3Å molecular sieves for 24 h prior to use. 1-octene (99%) was obtained from Acros Organics, stirred with calcium hydride overnight, distilled and stored in a glove box over activated 3Å molecular sieves for 24 h prior to use. Benzene-$d_6$ (*d*, 99.5%), chloroform-*d* (*d*, 99.8%), dichloromethane-$d_2$ (*d*, 99.8%), tetrahydrofuran-$d_8$ (*d*, 99.5%), and toluene-$d_8$ (*d*, 99.5%) were obtained from Cambridge Isotope Laboratories and stored in a glovebox over activated 3Å molecular sieves for 24 h prior to use.

Diisopropylamine (≥99.5%), dibutylamine (≥99.5%), diethylamine (≥99.5%), pyrrolidine (≥99.5%, purified by distillation), piperidine (≥99.5%, purified by distillation), *N*-*n*-butylmethylamine (96%), diallylamine (99%), dimethylamine (2.0 M in tetrahydrofuran), Dicyclohexylamine (99%), *N*-ethylisopropylamine (98%), *N*-isopropylmethylamine (98%), *N*-ethylmethylamine (97%), 1,2,3,4-tetrahydroisoquinoline (95%), 4-chloro-*N*-methylaniline (97%), and *N*-methylaniline (98%) were obtained from Aldrich, stirred with calcium hydride overnight, distilled and stored in a glove box. 2-methylpyrrolidine (98%) was obtained from Acros Organics, stirred with calcium hydride overnight, distilled and stored in a glove box. 4-methoxy-*N*-

methylaniline (98%) was obtained from Combi-Blocks, stirred with calcium hydride overnight, distilled and stored in a glove box. Dimethyl terephthalate (≥99%), tris(dimethylamino)methane (97%), 4-(methylamino)benzonitrile (97%), and triethylamine (≥99%) were obtained from Aldrich and used without further purification. Selenium (100 mesh, 99.99%) and phosphorus(V) oxychloride (99%) were obtained from Aldrich and used without further purification. Lead(II) oxide (99.999+%) was obtained from Strem or Alfa Aesar and used without further purification. Cyclohexyl isocyanide (99%), *n*-butyl isocyanide (98+%), and *tert*-butyl isocyanide (97%) were obtained from Acros Organics, degassed by the freeze-pump-thaw method, and stored in a glovebox. Trifluoroacetic acid (99%) and trifluoroacetic anhydride (99%) were obtained from Aldrich and used without further purification. *N*-*n*-hexadecylformamide (97%) was obtained from Alfa Aesar and used without further purification. Oleic acid (99%) was obtained from Aldrich or Alfa Aesar, stored in a –20 °C freezer, and used without further purification.

*3.7.3. Instrumentation*

UV-Vis-NIR spectra were obtained using a Perkin-Elmer Lambda 950 spectrophotometer equipped with deuterium and halogen lamps and either a PbS or InGaAs detector. Samples for UV-Vis-NIR and photoluminescence spectroscopies were dissolved in tetrachloroethylene. A background spectrum

was obtained of the same solvent mixture and concentration as the sample to be analyzed. Infrared photoluminescence measurements were conducted using excitation from a 6-picosecond supercontinuum laser. After spectral filtering, the excitation light (590 ± 10 nm, < 25 nJ $cm^{-2}$ per pulse) was focused onto a dilute solution of nanocrystals. The emission was collected using reflective optics, dispersed by a 1/3-meter spectrometer, and detected with an InGaAs photodiode and lock-in amplifier. The grating angle was scanned to acquire spectra. All spectra were corrected for grating and detector efficiency, and the measurements were conducted under inert atmosphere with weak excitation and stirring to prevent experimental artifacts due to oxidation, multiple excitation, and photo-charging.

NMR spectroscopy was performed on Bruker 300, 400, and 500 MHz spectrometers. $^{77}Se$ NMR spectra were referenced to diphenyl diselenide in benzene-$d_6$ (464.10 ppm[26]), which was sealed inside a glass capillary and placed inside the NMR tube. Single crystal XRD analysis was performed on either an Agilent SuperNova SCXRD or a Bruker Apex II diffractometer. Powder XRD analysis (Figure 3.7.1) was performed on a Scintag X-ray diffractometer. Transmission electron microscopy (TEM) was performed on either a JEOL JEM-100CX or a JEOL 2100 TEM. High-resolution TEM images were recorded on a FEI

Talos F200X, operated at 200 kV without a $C_s$ corrector. STEM images were recorded at a nominal spot size of 9 and a 50 μm condenser aperture.

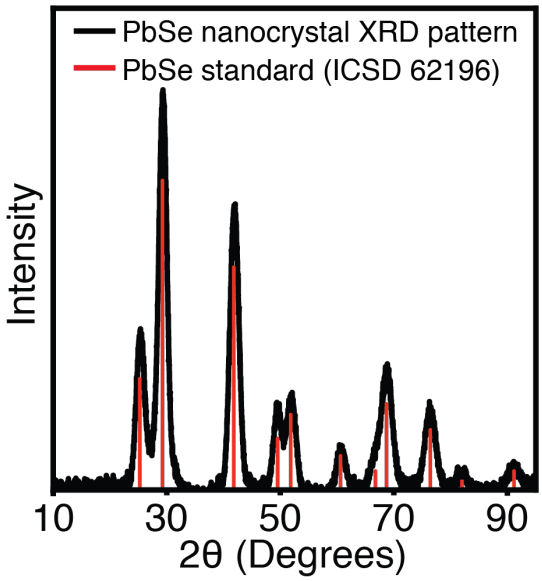


Figure 3.7.1. Powder X-ray diffraction pattern of PbSe nanocrystals. The black curve was obtained from PbSe nanocrystals isolated from a reaction under conditions similar to those described in Section 3.7.11. An exponential baseline correction was applied to remove signal from scattering. The PbSe standard was obtained from the International Crystallographic Structure Database (ICSD) as coll. Code 62196.

Kinetics experiments were carried out under nitrogen at 9 mM in selenourea according to Hendricks *et al*.[13] Kinetics experiments were monitored at 400 nm using a PerkinElmer 316SS dip probe (2 mm path length) attached to a Perkin-Elmer Lambda 650 spectrophotometer equipped with deuterium and halogen lamps.

Transient spectral hole burning experiments were performed using a commercial amplified Ti:sapphire laser system (SpectraPhysics) operating at a repetition rate of 1 kHz. Resonant excitation pulses were generated by a collinear optical parametric amplifier (LightConversion) and the spectrum of each pulse was measured using a fiber coupled commercial miniature spectrometer (Ocean Optics NIRQuest). Near-infrared supercontinuum probe light was generated using a sapphire plate. Cross-polarized pump and probe beams were used to reject the scattered pump light. Transient spectra were recorded on a shot-by-shot basis using a pair of fiber coupled InGaAs (infrared) diode arrays (Ultrafast Systems). The excitation fluence in each measurement was approximately 100 $\mu J/cm^2$.

*3.7.4. Precursor Synthesis*

Lead oleate was prepared from lead trifluoroacetate according to Hendricks *et al*.[13] on 134 mmol scale. It is important to use high-purity, yellow lead(II) oxide in this reaction, as discussed in depth in Chapter 2. *n*-Hexadecyl isocyanide was prepared according to Hoertz *et al*.[64] at 40 mmol scale. *N*,*N*,*N*′,*N*′-tetramethylselenourea was prepared according to Kantlehner, Hauber, and Vettel.[65]

*3.7.5. Synthesis of Selenoureas **1**-**31***

In a glovebox, selenium (3.0 mmol), amine (3.0 mmol), isocyanide (3.0 mmol), and toluene (to a total volume of 3 mL) are sealed under nitrogen and the mixture stirred in an oil bath heated to 100 °C for 1 h. During this time nearly all of the selenium is consumed and the reaction mixture becomes colorless to yellow. The vessel is then transferred to a glovebox and, mixture is passed through a syringe filter (PTFE, 0.2 μm), and the volatiles are removed under vacuum. Solid selenoureas are recrystallized using solvents indicated in the Supplementary Information, isolated by filtration using a glass fritted funnel, and dried under vacuum for >3 h. Liquid and low-melting solid selenoureas area placed under vacuum for 24 h with stirring. Isolated selenoureas are stored at –40 °C in a glove box freezer where they are indefinitely stable. All reactions were performed at a 3.0 mmol scale unless otherwise noted, but can be run at 25 times the scale and twice the above concentrations without significantly impacting the results.

*3.7.6. Example Selenourea Synthesis:* N,N-*dibutyl*-N′-*cyclohexylselenourea (**16**)*

*N*,*N*-dibutyl-*N′*-cyclohexylselenourea is prepared according to the general procedure from dibutylamine (387.7 mg, 3.00 mmol), selenium (236.9 mg, 3.00 mmol), and cyclohexyl isocyanide (327.5 mg, 3.00 mmol) in toluene (2.6 mL). The filtrate is recrystallized by concentration of a saturated solution in toluene under

reduced pressure. The solid is isolated by suction filtration on a fritted glass funnel, washed with pentane (3 x 4 mL), and dried under vacuum for >3 h. White solid. Yield: 727.2 mg (76.4%).

*3.7.7. Example Selenourea Synthesis:* N'-*cyclohexyl*-N-*ethyl*-N-*methylselenourea (**18**)*

*N'*-cyclohexyl-*N*-ethyl-*N*-methylselenourea was prepared according to the general procedure from *N*-ethylmethylamine (177.3 mg, 3.00 mmol), selenium (236.9 mg, 3.00 mL), and cyclohexyl isocyanide (327.5 mg, 3.00 mmol) in toluene (2.6 mL). Pentane (6 mL) is added to the filtrate to induce crystallization, and then the mixture is cooled in a –40 °C freezer for > 2 hours. Following this period, the crystals are isolated by suction filtration on a fritted glass funnel, washed with pentane (3 x 4 mL), and dried under vacuum >3 h. Pale yellow crystals. Yield: 0.5106 g (68.8%).

*3.7.8. Example Selenourea Synthesis:* N,N-*diallyl*-N'-*butylselenourea (**6**)*

*N,N*-diallyl-*N'*-butylselenourea was prepared according to the general procedure from diallylamine (291.5 mg, 3.00 mmol), selenium (236.9 mg, 3.00 mmol), and butyl isocyanide (249.4 mg, 3.00 mmol) in toluene (2.6 mL). Pale yellow, nearly colorless oil. Yield: 757.2 mg (97.4%).

*3.7.9. Synthesis of PbSe Nanocrystals for Absorbance and Photoluminescence Spectroscopies*

In a glove box, lead oleate (231.0 mg, 0.30 mmol, 1.5 equiv) and 1-octene (9.5 mL) are added to a 40 mL scintillation vial equipped with a stir bar that is then sealed with a rubber septum. The selenourea (0.20 mmol) and diglyme (0.5 mL) are added to a 4 mL scintillation vial and sealed with a rubber septum. Both vials are removed from the glove box, the septa pierced with argon inlet needles, and placed in oil baths at 100 °C. After reaching thermal equilibrium (15 minutes), the selenourea solution is injected into the lead oleate solution. An aliquot (100 μL) is removed at the desired time and dissolved in tetrachloroethylene (6 mL) for absorbance spectroscopy. For photoluminescence measurements, the reaction mixture is transferred via syringe into a Schlenk flask under argon, brought into a glove box, and diluted in tetrachloroethylene to an absorbance of 0.1–0.3 at the $1S_e$–$1S_h$ maximum.

*3.7.10. Large-Scale Synthesis of 2.7 nm PbSe Nanocrystals*

In a glove box, lead oleate (2.657 g, 3.45 mmol, 1.5 equiv) and 1-octene (54.6 mL) are added to a 100 mL 3-neck round bottom flask equipped with a stir bar, that is then sealed with two rubber septa and an air-free vacuum adapter. In a 20 mL scintillation vial, *N*,*N*-dibutyl-*N'*-cyclohexylselenourea (0.730 g, 2.30 mmol) and dibutyl ether (2.9 mL) are mixed and the vial sealed with a rubber

septum. Both vessels are transferred to a Schlenk line where they are placed under nitrogen and brought to 100 °C in an oil bath. Once the temperature is stable, the solution of selenourea is quickly injected into the clear colorless solution of lead oleate via a syringe equipped with a wide gauge needle. The reaction is allowed to run for 10 minutes before the flask is removed from the oil bath and allowed to cool to room temperature. The septa are then replaced with glass stoppers under positive argon flow and the volatiles removed under vacuum. After three hours, the flask is sealed and transferred to a nitrogen-filled glovebox. The dark residue is dissolved in 12 mL of a 1:1 pentane/toluene mixture. 50 mL of methyl acetate are added to precipitate the nanocrystals and the mixture is centrifuged (7000 rpm, 10 min), giving a clear, pale brown supernatant. The dark residue remaining is dissolved in 12 mL of a 1:1 pentane/toluene mixture, precipitated with 50 mL of methyl acetate, and centrifuged (7000 rpm, 10 min). This process is repeated three more times (five precipitations in total), and then the nanocrystal solution is dried under vacuum for > 6 hours. The nanocrystal solid is dissolved in benzene-$d_6$ or toluene-$d_8$ for analysis with UV-vis-NIR and NMR spectroscopies. Yield: 83-97%, based on empirical formulas of $(PbSe)(Pb(oleate)_2)_n$ determined spectroscopically. *Commercially available anhydrous octane (b.p. = 125-126°C) may also be used in place of 1-octene*.

*3.7.11. Large-Scale Synthesis of 5.1 nm PbSe Nanocrystals*

In a glove box, lead oleate (10.497 g, 13.63 mmol, 1.2 equiv) and 1-octene (146 mL) are added to a 250 mL 3-neck round bottom flask equipped with a stir bar, that is then sealed with two rubber septa and an air-free vacuum adapter. To a 20 mL scintillation vial, *N*,*N*-diallyl-*N'*-butylselenourea (2.945 g, 11.36 mmol) and diglyme (5 mL), were added and the vial sealed with a rubber septum. Both vessels are transferred to a Schlenk line where they are placed under nitrogen and brought to 100 °C in an oil bath. Once the temperature is stable, the solution of selenourea is quickly injected into the clear colorless solution of lead oleate. The reaction is stirred for 120 minutes before the flask is removed from the oil bath and allowed to cool to room temperature. The septa are then replaced with glass stoppers under positive argon flow and the volatiles removed under vacuum. After two hours, the flask is placed under argon and the glass stoppers replaced with rubber septa. 50 mL of pentane is then added via cannula, and the dark slurry was transferred via cannula to a Teflon-sealable Schlenk flask and taken into a nitrogen glovebox. 70 mL of methyl acetate was added and the mixture was centrifuged (7000 rpm, 10 min.), giving a clear, pale brown supernatant. The dark residue remaining was dissolved in 65 mL of a 1:1 pentane/toluene mixture, precipitated with 135 mL of methyl acetate, and centrifuged (7000 rpm, 10 min.). The process of precipitation, centrifugation, and

redissolution was repeated three more times. The nanocrystal solution was then dried under vacuum for 24 hours and the solid dissolved in a mixture of tetrachloroethylene and benzene-$d_6$ or toluene-$d_8$ for analysis with UV-vis-NIR and NMR spectroscopies. *Commercially available anhydrous octane (b.p. = 125-126°C) may also be used in place of 1-octene*.

*3.7.12. Rate of Ostwald Ripening Experiment*

Ostwald ripening was determined to be negligibly slow by following the same procedure described in Section 3.7.9. *N*,*N*-diallyl-*N'*-butylselenourea was injected into the lead oleate solution at 100 °C. Aliquots (200 μL) were removed at 2 hours, 5 hours, and 8 hours after injection and dissolved in tetrachloroethylene (6 mL) for absorbance spectroscopy.

*3.7.13. Determination of Oleate, PbSe, and Nanocrystal Concentrations*

The concentration of oleate in a given nanocrystal sample is determined by $^1$H NMR spectroscopy. Purified nanocrystals are thoroughly dried under vacuum and dissolved in benzene-$d_6$ or toluene-$d_8$. Dimethyl terephthalate (DMT) dissolved in benzene-$d_6$ or toluene-$d_8$ (100 μL, 50.1 mM) was added to a known volume of the nanocrystal stock solution and its aromatic resonances used as an internal standard for $^1$H NMR spectroscopy. The concentration of ligands was determined relative to the DMT internal standard by integrating the

ligand vinyl and DMT aryl resonances and normalizing for the number of hydrogens, respectively (2:4). $^{1}$H NMR spectra were acquired with sufficient relaxation delay to allow complete relaxation between pulses (T1(oleate vinyl) = 1.0 s; T1(DMT aryl) = 12.0 s; 5 x T1 = 60 s). See Figure S13 for an example $^{1}$H NMR spectrum of isolated PbSe nanocrystals.

The concentration of nanocrystals was determined by UV-vis-NIR absorbance spectroscopy. The molar concentration of PbSe in these stock solutions was determined by diluting 10–50 μL to a known volume with tetrachloroethylene and measuring the absorbance at $\lambda$ = 400 nm. At this wavelength, the extinction coefficient is independent of size:[8]

$$[PbSe] = \frac{A_{400}}{\varepsilon_{400} l}$$

The wavelength of the lowest energy absorption maximum was used to determine the average nanocrystal diameter.[32] Assuming the nanocrystals have a spherical shape and the molar volume of bulk PbSe (0.0584925$N_A$), the number of PbSe units per nanocrystal was calculated from the nanocrystal diameter. The concentration of nanocrystals is determined by dividing the concentration of PbSe by the number of PbSe formula units per nanocrystal.

The number of ligands per nanocrystal is determined by dividing the ligand concentration measured by $^{1}$H NMR by the nanocrystal concentration measured by UV-vis-NIR and the ligand surface density is calculated by dividing

the number of ligands per nanocrystal by the average surface area per nanocrystal.

*3.7.14. Estimation of Single-Particle Linewidths*

To estimate the linewidths of the nanocrystal electronic transitions, we use a modified version of the transient spectral hole burning experiments described in Norris *et al*.[50] Briefly, features in the $t$ = 2 ns transient absorption spectra are fit using a negative amplitude Gaussian function bordered by two positive amplitude Gaussian functions. The positive functions account for spectral shifts associated with the excited state of the quantum dot (also known as the biexciton effect).[50,66,67] A linear baseline was used to account for the background photoinduced absorption signals. A typical spectral decomposition is shown in Figure 3.7.2 and a typical time dependence is shown in Figure 3.7.3. In all cases, the linewidth of the transition is taken to be the width of the negative Gaussian signal component (with variance $\sigma^2_{measured}$).

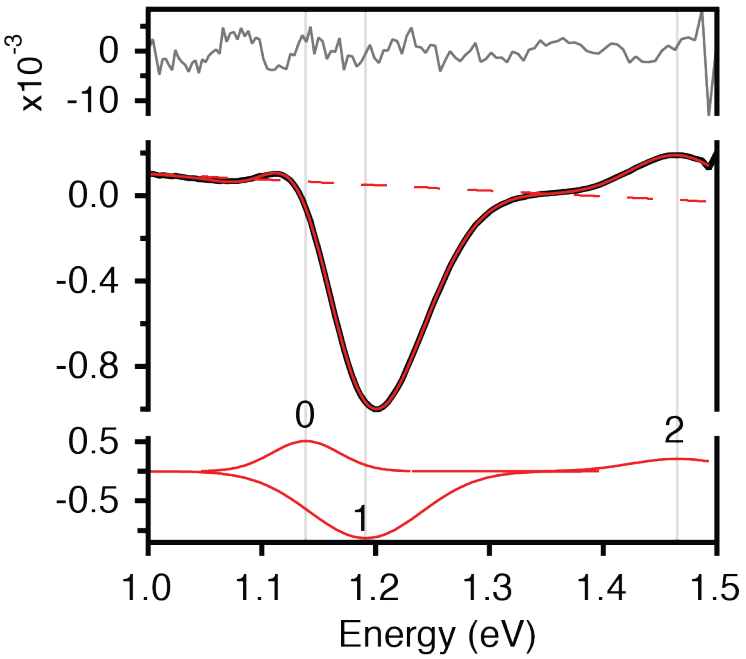


Figure 3.7.2. Example of the fit procedure used to extract the measured nanocrystal linewidths. The top panel is the residual of the fit shown in the middle panel (red = fit, black = data). The bottom panel shows the individual Gaussian components of the fit. A linear baseline (red dashed line) is used to account for the broad photoinduced background signal.

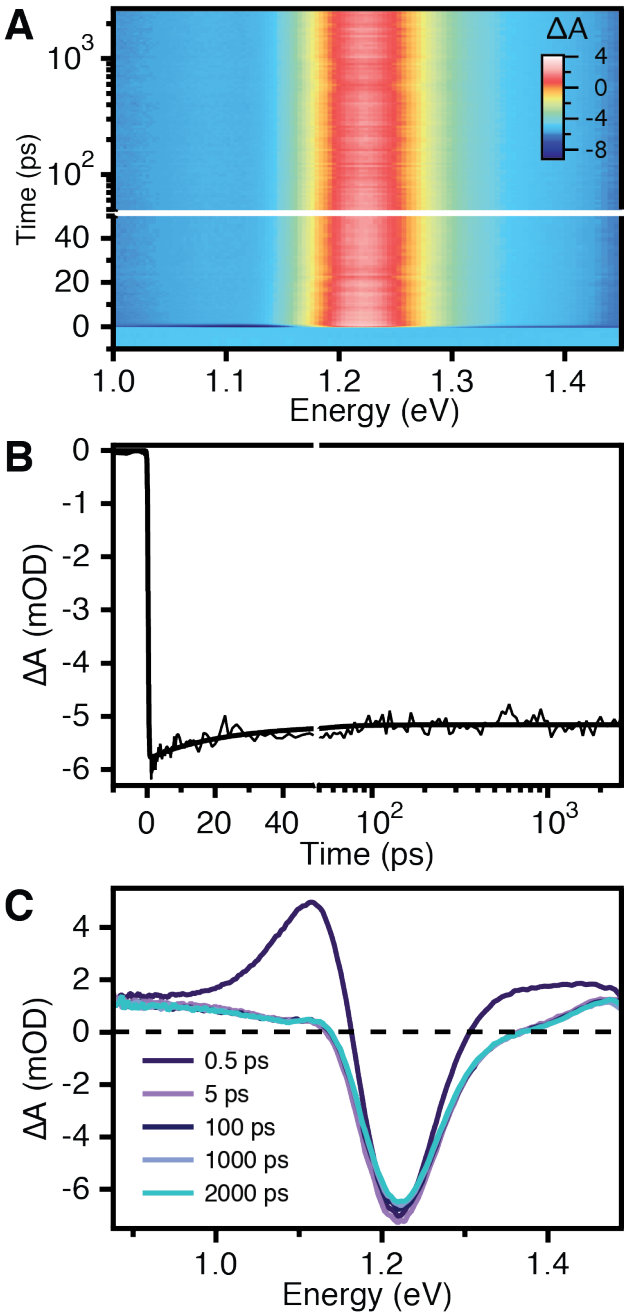


Figure 3.7.3. A) Raw transient absorption data for pumping at 2.2 eV for a sample with $E_g$ = 1.2 eV. B) Kinetic trace through the minima of the ground state bleach signal. The extracted biexponential lifetimes are approximately 25 ps. C) Transient spectra for different time slices.

We account for the finite width of the laser pulse spectrum using by fitting it to a Gaussian lineshape (whose variance is $\sigma_{laser}^2$). Deconvolution is used to obtain the corrected linewidths (with variance of $\sigma_{particle}^2$) as a function of excitation energy:

$$\sigma_{measured}^2 = \sigma_{laser}^2 + \sigma_{particle}^2$$

The finite bandwidth of the laser pulse minimally affects the measured linewidth. For the sample with $E_g$ = 1.2 eV shown in the main text, the measured and deconvoluted linewidths differ by only 5%. This is a typical value for the range of samples reported here (2 – 7% difference). The high excitation energy ensemble linewidth is independent of the laser pulse spectrum since the spectrum is featureless and absorbs roughly equally over the excitation pulse width in that spectral region. As such, no deconvolution of the laser lineshape is used to determine the ensemble widths (extracted using the Gaussian fitting procedure described above).

The $1S_e$–$1S_h$ transition is fit to a Gaussian function on an eV scale. The resulting $c$ (width) parameter is multiplied by the percent narrowing obtained from spectral hole burning measurements, giving the homogeneous linewidth $c_0$. The inhomogeneous broadening is expressed as $c - c_0$ (in eV) and plotted in Figure 3.5.2 and Figure 3.5.3.

*3.7.15. Estimation of Relative Standard Deviation (%RSD)*

The absorption spectrum is converted to nanocrystal diameter according to Dai *et al*.[32]:

$$d = (\lambda - 143.75)/281.25$$

where $d$ is the nanocrystal diameter in nanometers. The $1S_e$–$1S_h$ transition within this plot is fit to a Gaussian function and from which $c$ is multiplied by the percent narrowing obtained from spectral hole burning measurements, giving the single-particle linewidth $c_0$ (in nm). These parameters are used to obtain a relative (%) standard deviation in diameter:

$$\%RSD = \frac{c - c_0}{d}$$

where $d$ is the average nanocrystal diameter. $d$ is also converted to a number of PbSe formula units per nanocrystal at each point:

$$n_{PbSe} = \frac{V_{NC}Z}{V_{UC}} = \frac{\pi d^3 Z}{6V_{UC}}$$

where $n_{PbSe}$ is the average number of PbSe formula units per nanocrystal, $V_{NC}$ is the average nanocrystal volume in $nm^3$ (assuming sphericity), $Z$ is the number of PbSe formula units per unit cell ($Z$ = 4 for rock salt PbSe), and $V_{UC}$ is the volume of the PbSe unit cell (0.0584925 $nm^3$). The $c$ parameter extracted from Gaussian fit on this axis is multiplied by 1 minus the percent narrowing obtained from spectral hole burning measurements, giving the homogeneous linewidth $c_0$ in

terms of $n_{PbSe}$. The inhomogeneous broadening is again expressed as $c - c_0$, giving the standard deviation in $n_{PbSe}$.

*3.7.16. Precursor Characterization*

**N,N-diisopropyl-N'-butylselenourea (1)**

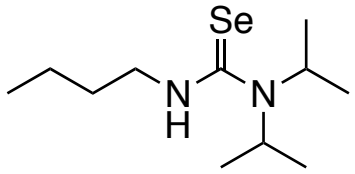


Chemical Formula: $C_{11}H_{24}N_2Se$
Molecular Weight: 263.29

Yield: 94%. Low-melting pale yellow solid. $^1$H NMR (500 MHz, $C_6D_6$): $\delta$ = 5.28 (br, 1H, NH), 5.20-4.30 (br, 2H, isopropyl $\alpha$-CH), 3.88 (m, 2H, butyl $\alpha$-$CH_2$), 1.44 (m, 2H, butyl $\beta$-$CH_2$), 1.19 (qt, $J_{H\text{-}H}$ = 7.4, 7.4 Hz, 2H, $C\underline{H}_2CH_3$), 0.88 (d, $J_{H\text{-}H}$ = 7.0 Hz), 0.80 (t, $J_{H\text{-}H}$ = 7.4 Hz, 3H); $^{13}$C {$^1$H} (125 MHz, $C_6D_6$): $\delta$ = 182.82 ($J_{C\text{-}Se}$ = 216.4 Hz, C=Se), 50.52 (br, isopropyl $\alpha$-CH), 48.73 (butyl $\alpha$-$CH_2$), 31.79 (butyl $\beta$-$CH_2$), 20.64 ($\underline{C}H_2CH_3$), 20.34 (isopropyl $CH_3$), 14.03 (butyl $CH_3$); $^{77}$Se {$^1$H} (95.4 MHz, $C_6D_6$): $\delta$ = 234.98; Anal. Calcd for $C_{11}H_{24}N_2Se$: C, 50.18; H, 9.19; N, 10.64. Found: C, 50.21; H, 9.69; N, 10.62. MS (ASAP) *m*/*z* Calcd for [$C_{11}H_{24}N_2{}^{80}Se + H^+$]: 265.1183. Found: 265.1187.

***N,N,N′*-tributylselenourea (2)**

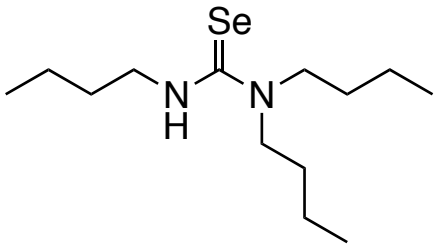

Chemical Formula: $C_{13}H_{28}N_2Se$
Molecular Weight: 291.34

Yield: 97%. Pale yellow oil. $^1$H NMR (400 MHz $C_6D_6$): $\delta$ = 5.26 (br t, 1H, NH), 3.82 (td, $J_{H\text{-}H}$ = 7.3, 5.3 Hz, 2H, NHC$\underline{H}_2$), 3.40 (t, $J_{H\text{-}H}$ = 7.8 Hz, 4H, NC$H_2$), 1.51-1.36 (m, 6H, β-C$H_2$), 1.21 (tq, $J_{H\text{-}H}$ = 7.5, 7.3 Hz, 2H, C$\underline{H}_2$C$H_3$), 1.13 (tq, $J_{H\text{-}H}$ = 7.6, 7.3 Hz, 4H, C$\underline{H}_2$C$H_3$), 0.83 (t, $J_{H\text{-}H}$ = 7.4 Hz, 3H, $CH_3$), 0.82 (t, $J_{H\text{-}H}$ = 7.4 Hz, 6H, $CH_3$); $^{13}$C {$^1$H} (100 MHz, $C_6D_6$): $\delta$ = 181.84 ($J_{C\text{-}Se}$ = 217.87 Hz, C=Se), 52.19 (NHC$H_2$), 48.64 (NC$H_2$), 31.94 (β-C$H_2$), 29.80 (β-C$H_2$), 20.47 (C$\underline{H}_2$C$H_3$), 20.43 (C$\underline{H}_2$C$H_3$), 14.06 ($CH_3$); $^{77}$Se {$^1$H} (76.3 MHz, $C_6D_6$): $\delta$ = 209.97; Anal. Calcd for $C_{13}H_{28}N_2Se$: C, 53.59; H, 9.69; N, 9.62. Found: C, 53.83; H, 9.44; N, 9.55. MS (FAB) *m*/*z* Calcd for [$C_{13}H_{28}N_2{}^{80}Se + H^+$]: 293.15. Found: 293.22.

***N,N*-diethyl-*N′*-butylselenourea (3)**

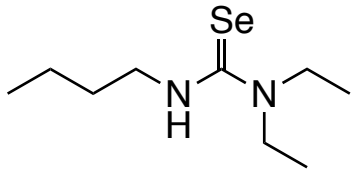

Chemical Formula: $C_9H_{20}N_2Se$
Molecular Weight: 235.23

Yield: 94%. Pale yellow oil. $^{1}$H NMR (500 MHz, $C_6D_6$): $\delta$ = 5.41 (br t, 1H, NH), 3.80 (td, $J_{H\text{-}H}$ = 7.4, 5.3 Hz, 2H, butyl $\alpha$-$CH_2$), 3.32 (q, $J_{H\text{-}H}$ = 7.2 Hz, 4H, ethyl $CH_2$), 1.51 (m, 2H, butyl β-$CH_2$); 1.23 (m, 2H, $C\underline{H}_2$), 0.88 (t, $J_{H\text{-}H}$ = 7.1 Hz, 6H, ethyl $CH_3$), 0.85 (t, $J_{H\text{-}H}$ = 7.4 Hz, 3H, butyl $CH_3$); $^{13}$C {$^{1}$H} (125 MHz, $C_6D_6$): $\delta$ = 180.76 ($J_{C\text{-}Se}$ = 216.4 Hz, C=Se), 48.56 (butyl $\alpha$-$CH_2$), 46.29 (ethyl $\alpha$-$CH_2$), 32.06 (butyl β-$CH_2$), 20.48 (butyl $\underline{C}H_2CH_3$), 14.14 (butyl $CH_3$), 12.67 (ethyl $CH_3$); $^{77}$Se {$^{1}$H} (95.4 MHz, $C_6D_6$): $\delta$ = 193.70; Anal. Calcd for $C_9H_{20}N_2Se$: C, 45.95; H, 8.57; N, 11.91. Found: C, 45.86; H, 8.30; N, 11.76. MS (ASAP) *m*/*z* Calcd for [$C_9H_{20}N_2{}^{80}Se$ + $H^+$]: 237.0870. Found: 237.0872.

**_N_-butylpiperidine-1-carboselenoamide (4)**

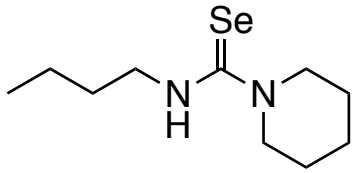


Chemical Formula: $C_{10}H_{20}N_2Se$
Molecular Weight: 247.24

Yield: 95%. Colorless low-melting solid. $^{1}$H NMR (500 MHz, $C_6D_6$): $\delta$ = 6.45 (br t, $J_{H\text{-}H}$ = 5.5 Hz, 1H, NH), 3.91 (m, 2H, butyl $\alpha$-$CH_2$), 3.69 (m, 4H, piperidine $\alpha$-$CH_2$), 1.68 (m, 2H, butyl β-$CH_2$), 1.35-1.23 (m, 8H, butyl $\underline{C}H_2CH_3$ and piperidine $CH_2$), 0.90 (t, $J_{H\text{-}H}$ = 7.4 Hz, 3H, butyl $CH_3$),; $^{13}$C {$^{1}$H} (125 MHz, $C_6D_6$): $\delta$ = 180.96 ($J_{C\text{-}Se}$ = 213.16 Hz, C=Se), 50.80 ($\alpha$-$CH_2$), 48.77 ($\alpha$-$CH_2$), 32.23 ($CH_2$), 25.83 (piperidine $CH_2$), 24.54 ($CH_2$), 20.58 (butyl $\underline{C}H_2CH_3$), 14.28 (butyl $CH_3$); $^{77}$Se {$^{1}$H}

(95.4 MHz, $C_6D_6$): $\delta$ = 185.85; Anal. Calcd for $C_{10}H_{20}N_2Se$: C, 48.58; H, 8.15; N, 11.33. Found: C, 48.23; H, 7.72; N, 11.11. MS (ASAP) *m*/*z* Calcd for [$C_{10}H_{20}N_2{}^{80}Se$ + $H^+$]: 249.0870. Found: 249.0867.

***N,N′*-dibutyl-*N*-methylselenourea (5)**

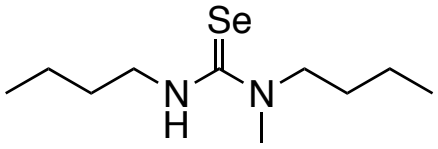


Chemical Formula: $C_{10}H_{22}N_2Se$
Molecular Weight: 249.26

Yield: 98%. Pale yellow oil. $^1$H NMR (400 MHz, $C_6D_6$): $\delta$ = 4.85 (br, 1H, NH), 3.75 (td, $J_{H\text{-}H}$ = 7.4, 5.3 Hz 2H, N′-butyl NHC$\underline{H}_2$), 3.62 (br t, $J_{H\text{-}H}$ =7.6 Hz 2H, N-butyl NC$H_2$), 2.34 (s, 3H, N$CH_3$), 1.45-1.34 (m, 4H, butyl β-$CH_2$), 1.19 (tq, $J_{H\text{-}H}$ = 7.7, 7.4 Hz, 2H, butyl C$\underline{H}_2CH_3$), 1.13 (tq, $J_{H\text{-}H}$ = 7.7, 7.2 Hz, 2H, butyl C$\underline{H}_2CH_3$), 0.85 (t, $J_{H\text{-}H}$ = 7.4 Hz, 3H, butyl $CH_3$); $^{13}$C {$^1$H} (125 MHz, $C_6D_6$): $\delta$ = 182.12 ($J_{C\text{-}Se}$ = 217.43 Hz, C=Se) 55.51 (N-butyl N$CH_2$), 48.62 (N′-butyl NH$CH_2$), 37.30 (N$CH_3$), 32.01 (butyl β-$CH_2$), 29.77 (butyl β-$CH_2$), 20.43 (butyl $\underline{C}H_2CH_3$), 20.25 (butyl $\underline{C}H_2CH_3$), 14.12 (butyl $CH_3$), 14.11 (butyl $CH_3$); $^{77}$Se {$^1$H} (57.2 MHz, $C_6D_6$): $\delta$ = 201.46; Anal. Calcd for $C_{10}H_{22}N_2Se$: C, 48.19; H, 8.90; N, 11.24. Found: C, 48.45; H, 8.47; N, 11.26. MS (FAB) *m*/*z* Calcd for [$C_{10}H_{22}N_2{}^{80}Se$ + $H^+$]: 251.10. Found: 251.19.

***N,N*-diallyl-*N′*-butylselenourea (6)**

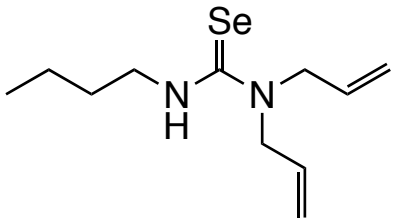


Chemical Formula: $C_{11}H_{20}N_2Se$
Molecular Weight: 259.26

Yield: 97%. Pale yellow oil. $^1$H NMR (400 MHz, $C_6D_6$): $\delta$ = 5.54 (m, 2H, vinyl CH), 5.33 (br s, 1H, NH), 4.90-4.83 (m, 2H, vinyl $CH_2$), 4.88-4.86 (m, 2H, vinyl $CH_2$), 4.00 (br d, 4H, allylic $CH_2$), 3.75 (td, $J_{H\text{-}H}$ = 7.2, 5.2 Hz, 4H, butyl $\alpha$-$CH_2$), 1.42-1.34 (m, 2H, butyl $\beta$-$CH_2$), 1.52-1.43 (qt, $J_{H\text{-}H}$ = 7.5, 7.3, Hz, 2H, $C\underline{H}_2CH_3$), 0.79 (t, $J_{H\text{-}H}$ = 7.3 Hz, 3H, $CH_3$); $^{13}$C {$^1$H} (100 MHz, $C_6D_6$): $\delta$ = 183.47 ($J_{C\text{-}Se}$ = 219.1 Hz, C=Se), 132.94 (vinyl CH), 117.29 (vinyl $CH_2$), 54.65 (butyl $\alpha$-$CH_2$), 54.79 (allylic $CH_2$), 31.66 (butyl $\beta$-$CH_2$), 20.37 ($\underline{C}H_2CH_3$), 14.03 ($CH_3$); $^{77}$Se {$^1$H} (76.3 MHz, $C_6D_6$): $\delta$ = 216.81; Anal. Calcd for $C_{11}H_{20}N_2Se$: C, 50.96; H, 7.78; N, 10.81. Found: C, 50.83; H, 7.56; N, 10.75. MS (ASAP) *m*/*z* Calcd for [$C_{11}H_{20}N_2{}^{80}Se$+ $H^+$]: 261.0870. Found: 261.0864.

***N*-butyl-*N′*,*N′*-dimethylselenourea (7)**

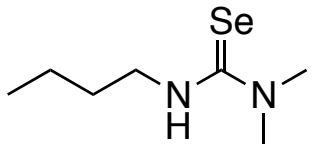


Chemical Formula: $C_7H_{16}N_2Se$
Molecular Weight: 207.18

Yield: 88%. Yellow oil. $^{1}$H NMR (400 MHz, $C_6D_6$): $\delta$ = 5.10 (br, 1H, NH), 3.74 (m, 2H, butyl $\alpha$-C<u>H</u>$_2$), 2.66 (s, 6H, $NCH_3$), 1.51-1.42 (m, 2H, butyl $\beta$-$CH_2$), 1.21 (m, 2H, butyl C<u>H</u>$_2$$CH_3$), 0.85 (t, $J_{H\text{-}H}$ = 7.4 Hz, 3H, butyl $CH_3$); $^{13}$C {$^{1}$H} (125 MHz, $C_6D_6$): $\delta$ = 182.59 ($J_{C\text{-}Se}$ = 217.19 Hz, C=Se), 48.69 ($NCH_3$), 41.18 (butyl $\alpha$-$CH_2$), 31.98 (butyl $\beta$-$CH_2$), 20.40 (butyl <u>C</u>H$_2$$CH_3$), 14.11 (butyl $CH_3$); $^{77}$Se {$^{1}$H} (57.2 MHz, $C_6D_6$): $\delta$ = 212.52; Anal. Calcd for $C_7H_{16}N_2Se$: 40.58; H, 7.78; N, 13.52. Found: C, 41.12; H, 7.80; N, 13.40. MS (FAB) *m*/*z* Calcd for [$C_7H_{16}N_2{}^{80}Se$ + $H^+$]: 209.06. Found: 209.13.

***N*-butypyrrolidine-1-carboselenoamide (8)**

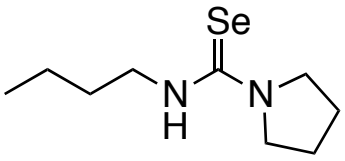


Chemical Formula: $C_9H_{18}N_2Se$
Molecular Weight: 233.22

Yield: 68% (6.6 mmol scale). White powder. Recrystallized by addition of pentane to a saturated toluene solution followed by storage at –40 °C overnight. $^{1}$H NMR (500 MHz, $C_6D_6$): $\delta$ = 5.88 (br t, 1H, NH), 3.84 (dt, $J_{H\text{-}H}$ = 7.3, 5.8 Hz, 2H, butyl $\alpha$-$CH_2$), 4.30-2.50 (br, 4H, pyrrolidine $\alpha$-$CH_2$), 1.66 (m, 2H, butyl $\beta$-$CH_2$), 1.37 (br s, 4H, pyrrolidine $\beta$-$CH_2$), 1.30 (tq, $J_{H\text{-}H}$ = 7.4, 7.4 Hz, 2H, butyl C<u>H</u>$_2$$CH_3$), 0.89 (t, $J_{H\text{-}H}$ = 7.4 Hz, 3H, $CH_3$); $^{13}$C {$^{1}$H} (125 MHz, $C_6D_6$): $\delta$ = 177.88 ($J_{C\text{-}Se}$ = 212.9 Hz, C=Se), 54.68 (br, pyrrolidine $\alpha$-$CH_2$), 47.97 (butyl $\alpha$-$CH_2$), 32.33 (butyl $\beta$-$CH_2$),

25.22 (br, pyrrolidine β-$CH_2$), 20.52 (butyl $\underline{C}H_2CH_3$), 14.24 ($CH_3$); $^{77}$Se {$^1$H} (95.4 MHz, $C_6D_6$): $\delta$ = 219.78; Anal. Calcd for $C_9H_{18}N_2Se$: C, 46.35; H, 7.78; N, 12.01. Found: C, 46.53; H, 7.63; N, 11.98. MS (ASAP) *m*/*z* Calcd for [$C_9H_{18}N_2{}^{80}Se + H^+$]: 235.0714. Found: 235.0718. X-ray quality crystals were grown by addition of pentane to a concentrated solution in tetrahydrofuran.

**_N′_-butyl-_N_-(4-methoxyphenyl)-_N_-methylselenourea (9)**

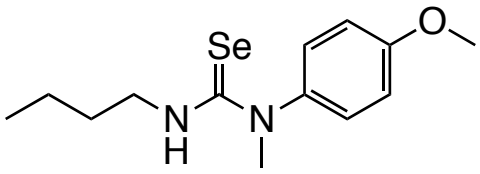


Chemical Formula: $C_{13}H_{20}N_2OSe$
Molecular Weight: 299.28

Yield: 72%. White crystalline solid. Recrystallized by addition of pentane to a saturated toluene solution followed by storage at –40 °C for 30 minutes. $^1$H NMR (500 MHz, $CD_2Cl_2$): $\delta$ = 7.12 (m, 2H, aryl CH), 6.98 (m, 2H, aryl CH), 5.61 (br s, 1H, NH), 3.81 (s, 3H, $CH_3$), 3.67 (s, 3H, $CH_3$), 3.56 (td, $J_{H\text{-}H}$ = 7.2, 5.4 Hz, 2H, butyl $\alpha$-$CH_2$), 1.45-1.39 (m, 2H, butyl β-$CH_2$), 1.21 (tq, $J_{H\text{-}H}$ = 7.4, 7.3 Hz, 2H, butyl $C\underline{H}_2CH_3$) 0.84 (t, $J_{H\text{-}H}$ = 7.4 Hz, 3H, butyl $CH_3$); $^{13}$C {$^1$H} (125 MHz, $CD_2Cl_2$): $\delta$ = 182.23 ($J_{C\text{-}Se}$ = 215.9 Hz, C=Se), 159.79 ($\underline{C}OCH_3$), 135.16 (aryl $\underline{C}$N), 128.29 (aryl CH), 116.02 (aryl CH), 55.88 ($CH_3$ or butyl $\alpha$-$CH_2$) 48.41 ($CH_3$ or butyl $\alpha$-$CH_2$) 46.30 ($CH_3$ or butyl $\alpha$-$CH_2$), 31.45 (butyl β-$CH_2$), 20.24 (butyl $\underline{C}H_2CH_3$) 13.88 (butyl $CH_3$); $^{77}$Se {$^1$H} (95.4 MHz, $CD_2Cl_2$): $\delta$ = 191.06; Anal. Calcd for $C_{13}H_{20}N_2Se$: C,

52.17; H, 6.74; N, 9.36. Found: C, 52.21; H, 6.85; N, 9.34. MS (ASAP) *m*/*z* Calcd for [$C_{13}H_{20}N_2{}^{80}Se + H^+$]: 301.0819. Found: 301.0821.

***N*-cyclohexyl-*N′*-dodecylselenourea (10)**

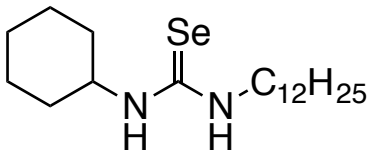


Chemical Formula: $C_{19}H_{38}N_2Se$
Molecular Weight: 373.49

Yield: 90% (10.0 mmol scale). White powder. $^1$H NMR (500 MHz, $CD_2Cl_2$): $\delta$ = 7.20-5.00 (br, 2H, NH), 4.60-2.60 (br, 3H, $\alpha$-CH and $\alpha$-$CH_2$), 2.00 (m, 2H, cyclohexyl $CH_2$), 1.75-1.67 (m, 2H, cyclohexyl or dodecyl $CH_2$) 1.63-1.55 (m, 3H, cyclohexyl or dodecyl $CH_2$), 1.40-1.13 (m, 23H, cyclohexyl and dodecyl $CH_2$) 0.87 (t, $J_{H\text{-}H}$ = 6.8 Hz, 3H, $CH_3$); $^{13}$C {$^1$H} (125 MHz, $CD_2Cl_2$): $\delta$ = 178.03 (br, C=Se), 56.70 (br, $\alpha$-CH or $\alpha$-$CH_2$), 47.97 (br, $\alpha$-CH or $\alpha$-$CH_2$), 44.16 (br, cyclohexyl or dodecyl $CH_2$), 33.14 (br, cyclohexyl or dodecyl $CH_2$), 32.27 (cyclohexyl or dodecyl $CH_2$), 30.02 (cyclohexyl or dodecyl $CH_2$), 29.99 (cyclohexyl or dodecyl $CH_2$), 29.96 (cyclohexyl or dodecyl $CH_2$), 29.91 (cyclohexyl or dodecyl $CH_2$), 29.70 (cyclohexyl or dodecyl $CH_2$), 29.37 (br, cyclohexyl or dodecyl $CH_2$), 27.32 ((cyclohexyl or dodecyl $CH_2$), 25.73 (cyclohexyl or dodecyl $CH_2$), 25.19 (cyclohexyl or dodecyl $CH_2$), 23.04 (dodecyl $\underline{C}H_2CH_3$), 14.25 (dodecyl $CH_3$); $^{77}$Se {$^1$H} (95.4 MHz, $CD_2Cl_2$): $\delta$ = 189.59; Anal. Calcd for $C_{19}H_{38}N_2Se$: C, 61.10; H, 10.26; N, 7.50. Found: C, 61.33;

H, 10.34; N, 7.53. MS (ASAP) *m*/*z* Calcd for [$C_{19}H_{38}N_2{}^{80}Se + H^+$]: 375.2278. Found: 375.2271.

***N,N,N'*-tricyclohexylselenourea (11)**

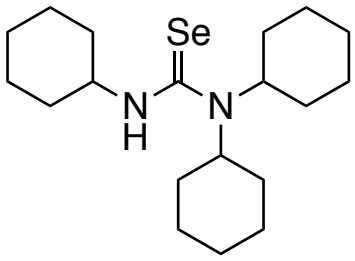


Chemical Formula: $C_{19}H_{34}N_2Se$
Molecular Weight: 369.46

Yield: 65%. Pale yellow crystals. Recrystallized by addition of pentane to a saturated toluene solution followed by storage at –40 °C overnight. $^1$H NMR (500 MHz, $CD_2Cl_2$): $\delta$ = 5.70 (d, $J_{H\text{-}H}$ = 7.8 Hz, 1H, NH), 5.2-3.8 (br, 2H, $N(CH)_2$), 4.50 (m, 1H, NHC<u>H</u>), 2.09 (m, 2H, cyclohexyl $CH_2$), 1.85-1.47 (m, 17H, cyclohexyl $CH_2$), 1.47-1.15 (m, 9H, cyclohexyl $CH_2$), 1.13-1.03 (m, 2H, cyclohexyl $CH_2$); $^{13}$C {$^1$H} (125 MHz, $CD_2Cl_2$): $\delta$ = 179.54 ($J_{C\text{-}Se}$ = 210.9 Hz, C=Se), 61.12 (br, $N(CH)_2$), 56.95 (NHCH), 33.20 (cyclohexyl $CH_2$), 31.29 (br, cyclohexyl $CH_2$), 26.58 (cyclohexyl $CH_2$), 26.00 (cyclohexyl $CH_2$), 25.97 (cyclohexyl $CH_2$), 25.16 (cyclohexyl $CH_2$); $^{77}$Se {$^1$H} (95.4 MHz, $CD_2Cl_2$): $\delta$ = 190.99; Anal. Calcd for $C_{19}H_{34}N_2Se$: C, 61.77; H, 9.28; N, 7.58. Found: C, 61.39; H, 9.44; N, 7.58. MS (ASAP) *m*/*z* Calcd for [$C_{19}H_{34}N_2{}^{80}Se + H^+$]: 371.1965. Found: 371.1970.

***N,N*-diispropyl-*N′*-cyclohexylselenourea (12)**

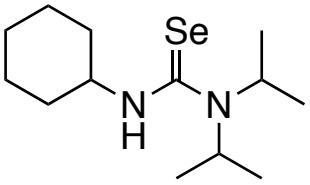


Chemical Formula: $C_{13}H_{26}N_2Se$
Molecular Weight: 289.33

Yield: 57%. Colorless crystals. Recrystallized by addition of pentane to a saturated toluene solution followed by storage at –40 °C overnight. $^{1}$H NMR (500 MHz, $C_6D_6$): $\delta$ = 5.32 (d, $J_{H\text{-}H}$ =7.6 Hz, 1H, NH), 4.95 (tdt, $J_{H\text{-}H}$ = 10.2, 7.8, 3.9 Hz, 1H, cyclohexyl $\alpha$-CH), 4.84 (br, 2H, isopropyl $\alpha$-CH), 2.15 (m, 2H, cyclohexyl $CH_2$), 1.48 (m, 2H, cyclohexyl $CH_2$), 1.40 (m, 1H, cyclohexyl $CH_2$), 1.26 (m, 2H, cyclohexyl $CH_2$), 1.06 (m, 3H, cyclohexyl $CH_2$), 0.94 (d, $J_{H\text{-}H}$ = 7.0 Hz, 12H, $CH_3$); $^{13}$C {$^{1}$H} NMR (125 MHz, $C_6D_6$): $\delta$ = 180.82 ($J_{C\text{-}Se}$ = 216.1 Hz, C=Se), 56.70 (cyclohexyl $\alpha$-CH), 50.40 (br, isopropyl $\alpha$-CH), 33.29 (cyclohexyl $CH_2$), 25.93 (cyclohexyl $CH_2$), 25.14 (cyclohexyl $CH_2$), 20.45 ($CH_3$); $^{77}$Se {$^{1}$H} (95.4 MHz, $C_6D_6$): $\delta$ = 220.95; Anal. Calcd for $C_{13}H_{26}N_2Se$: C, 53.97; H, 9.06; N, 9.68. Found: C, 54.90; H, 9.27; N, 9.62; MS (ESI) *m*/*z* Calcd for [$C_{13}H_{26}N_2{}^{80}Se + H^+$]: 291.29. Found: 291.3. X-ray quality crystals were grown from a concentrated solution in 2:1 pentane/toluene at -40°C.

***N′*-cyclohexyl-*N*-ethyl-*N*-isopropylselenourea (13)**

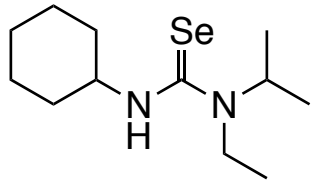


Chemical Formula: $C_{12}H_{24}N_2Se$
Molecular Weight: 275.30

Yield: 79%. White crystalline solid. Recrystallized by addition of pentane to a saturated solution of 2:3 dichloromethane:toluene. $^{1}$H NMR (500 MHz, tetrahydrofuran-$d_8$): $\delta$ = 6.00 (br d, $J_{H\text{-}H}$ = 7.7, 1H, NH), 5.75 (hept, $J_{H\text{-}H}$ = 6.8 Hz, 1H, isopropyl CH), 4.65 (tdt, J = 11.5, 7.9, 3.9, 1H, cyclohexyl $\alpha$-CH), 3.45 (q, 2H, ethyl $CH_2$), 2.10 (m, 2H, cyclohexyl $CH_2$), 1.75-1.67 (m, 3H, cyclohexyl $CH_2$), 1.67-1.60 (m, 1H, cyclohexyl $CH_2$), 1.43-1.33 (m, 2H, cyclohexyl $CH_2$), 1.27-1.18 (m, 3H, cyclohexyl $CH_2$), 1.16 (t, $J_{H\text{-}H}$ = 7.1 Hz, 2H, ethyl $CH_3$), 1.13 (d, $J_{H\text{-}H}$ = 6.8 Hz, 6H, isopropyl $CH_3$); $^{13}$C {$^{1}$H} (125 MHz, tetrahydrofuran-$d_8$): $\delta$ = 180.49 ($J_{C\text{-}Se}$ = 216.4 Hz, C=Se), 57.61 (CH), 53.99 (CH), 37.90 (cyclohexyl $CH_2$), 33.42 (cyclohexyl $CH_2$), 26.50 (cyclohexyl $CH_2$), 26.02 (cyclohexyl $CH_2$), 20.08 (isopropyl $CH_3$), 14.44 (ethyl $CH_3$); $^{77}$Se {$^{1}$H} (95.4 MHz, tetrahydrofuran-$d_8$): $\delta$ = 185.21; Anal. Calcd for $C_{12}H_{24}N_2Se$: C, 52.35; H, 8.79; N, 10.18. Found: C, 52.22; H, 8.82; N, 10.16. MS (ASAP) *m*/*z* Calcd for [$C_{12}H_{24}N_2{}^{80}Se + H^+$]: 277.1183. Found: 277.1187.

***N′*-cyclohexyl-*N*-isopropyl-*N*-methylselenourea (14)**

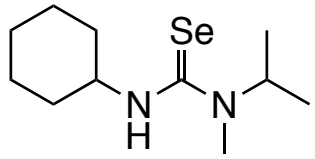


Chemical Formula: $C_{11}H_{22}N_2Se$
Molecular Weight: 261.27

Yield: 90%. White powder. Recrystallized by evaporation of a saturated solution of 2:3 dichloromethane:toluene under reduced pressure. $^{1}$H NMR (500 MHz, tetrahydrofuran-$d_8$): $\delta$ = 6.17, (br, 1H, NH), 5.81 (hept, $J_{H\text{-}H}$ = 6.9 Hz, 1H, isopropyl CH), 4.58 (tdt, $J_{H\text{-}H}$ = 11.5, 7.9, 4.0 Hz, 1H, cyclohexyl $\alpha$-CH), 2.84 (s, 3H, methyl $CH_3$), 2.09 (m, 2H, cyclohexyl $CH_2$), 1.71 (m, 2H, cyclohexyl $CH_2$), 1.63 (m, 1H, cyclohexyl $CH_2$), 1.41-1.31 (m, 2H, cyclohexyl $CH_2$), 1.26-1.12 (m, 3H, cyclohexyl $CH_2$), 1.09 (d, $J_{H\text{-}H}$ = 6.8 Hz, 6H, isopropyl $CH_3$); $^{13}$C {$^{1}$H} (125 MHz, tetrahydrofuran-$d_8$): $\delta$ = 181.15 ($J_{C\text{-}Se}$ = 216.4 Hz, C=Se), 57.62 (CH), 53.99 (CH), 33.53 (methyl $CH_3$), 29.64 (cyclohexyl $CH_2$), 26.49 (cyclohexyl $CH_2$), 26.09 (cyclohexyl $CH_2$), 19.41 (isopropyl $CH_3$); $^{77}$Se {$^{1}$H} (95.4 MHz, tetrahydrofuran-$d_8$): $\delta$ = 174.90; Anal. Calcd for $C_{11}H_{22}N_2Se$: C, 50.57; H, 8.49; N, 10.72. Found: C, 50.47; H, 8.75; N, 10.79. MS (ASAP) *m*/*z* Calcd for [$C_{11}H_{22}N_2{}^{80}Se + H^+$]: 263.1026. Found: 263.1025. X-ray quality crystals were grown by addition of pentane to a saturated solution in dichloromethane.

***N*-cyclohexylpiperidine-1-carboselenoamide (15)**

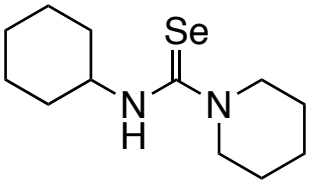


Chemical Formula: $C_{12}H_{22}N_2Se$
Molecular Weight: 273.28

Yield: 82%. White powder. Recrystallized by evaporation of a saturated solution of 1:1 dichloromethane:toluene under reduced pressure. $^{1}H$ NMR (500 MHz, $CD_2Cl_2$): $\delta$ = 5.64 (br d, $J_{H\text{-}H}$ = 8.1 Hz, 1H, NH), 5.64 (tdt, $J_{H\text{-}H}$ = 11.4, 7.9, 4.0 Hz, 1H, cyclohexyl $\alpha$-CH), 3.80 (t, $J_{H\text{-}H}$ = 5.6 Hz, 4H, piperidine $\alpha$-$CH_2$), 2.07 (m, 2H, cyclohexyl/pyrrolidine $CH_2$), 1.75-1.50 (m, 9H, cyclohexyl/pyrrolidine $CH_2$), 1.41-1.31 (m, 2H, cyclohexyl/pyrrolidine $CH_2$), 1.24-1.10 (m, 3H, cyclohexyl/pyrrolidine $CH_2$); $^{13}C$ {$^{1}H$} (125 MHz, $CD_2Cl_2$): $\delta$ = 178.80 ($J_{C\text{-}Se}$ = 212.3 Hz, C=Se), 57.23 (cyclohexyl CH), 50.61 (piperidine $\alpha$-$CH_2$), 33.33 (cyclohexyl/pyrrolidine $CH_2$), 25.82 (cyclohexyl/pyrrolidine $CH_2$), 25.71 (cyclohexyl/pyrrolidine $CH_2$), 25.35 (cyclohexyl/pyrrolidine $CH_2$), 24.56 (cyclohexyl/pyrrolidine $CH_2$); $^{77}Se$ {$^{1}H$} (95.4 MHz, $CD_2Cl_2$): $\delta$ = 176.98; Anal. Calcd for $C_{12}H_{22}N_2Se$: C, 52.74; H, 8.11; N, 10.25. Found: C, 52.88; H, 8.18; N, 10.26. MS (ASAP) *m*/*z* Calcd for [$C_{12}H_{22}N_2{}^{80}Se + H^+$]: 275.1026. Found: 275.1025. X-ray quality crystals were grown by addition of pentane to a saturated solution in dichloromethane.

***N,N*-dibutyl-*N′*-cyclohexylselenourea (16)**

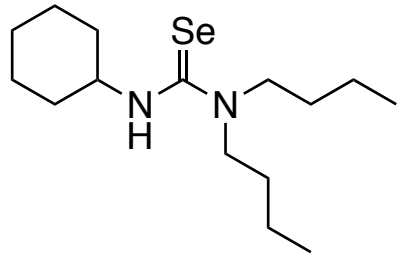


Chemical Formula: $C_{15}H_{30}N_2Se$
Molecular Weight: 317.38

Yield: 77%. White powder. Recrystallized by evaporation of a saturated solution in toluene under reduced pressure. $^1$H NMR (400 MHz, $C_6D_6$): $\delta$ = 5.27 (d, $J_{H\text{-}H}$ = 7.2 Hz, 1H, NH), 4.85 (tdt, $J_{H\text{-}H}$ = 11.4, 7.8, 3.9 Hz, 1H, cyclohexyl $\alpha$-CH), 3.44 (t, $J_{H\text{-}H}$ = 7.4 Hz, 4H, butyl $\alpha$-$CH_2$), 2.16 (m, 2H, cyclohexyl $CH_2$), 1.57-1.40 (m, 7H, butyl and cyclohexyl $CH_2$), 1.35-1.23 (m, 2H, butyl and cyclohexyl $CH_2$), 1.21-0.95 (m, 3H, butyl and cyclohexyl $CH_2$), 1.16 (q, $J_{H\text{-}H}$ = 7.4 Hz, 4H, butyl $C\underline{H}_2CH_3$), 0.83 (t, $J_{H\text{-}H}$ = 7.6 Hz, 6H, $CH_3$); $^{13}$C {$^1$H} (100 MHz, $C_6D_6$): $\delta$ = 180.03 ($J_{C\text{-}Se}$ = 217.6 Hz, C=Se), 56.88 (cyclohexyl $\alpha$-CH), 52.20 (butyl $\alpha$-$CH_2$), 33.43 (cyclohexyl $CH_2$), 29.87 (butyl $\beta$-$CH_2$), 25.93 (cyclohexyl $CH_2$), 25.30 (cyclohexyl $CH_2$), 20.47 (butyl $\underline{C}H_2CH_3$), 14.12 ($CH_3$); $^{77}$Se {$^1$H} (76.3 MHz, $C_6D_6$): $\delta$ = 206.31; Anal. Calcd for $C_{15}H_{30}N_2Se$: C, 56.77; H, 9.53; N, 8.83. Found: C, 56.89; H, 9.21; N, 8.89; MS (FAB) *m*/*z* Calcd for [$C_{15}H_{30}N_2{}^{80}Se$ + $H^+$]: 319.17. Found: 319.25. X-ray quality crystals were grown by vapor diffusion of pentane into a saturated solution in toluene.

***N,N*-diethyl-*N′*-cyclohexylselenourea (17)**

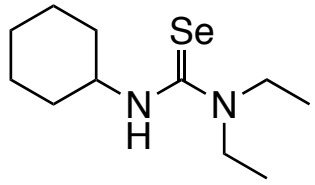


Chemical Formula: $C_{11}H_{22}N_2Se$
Molecular Weight: 261.27

Yield: 85%. White crystalline solid. Recrystallized by addition of pentane to a saturated solution in toluene (2:1 final ratio). $^{1}H$ NMR (400 MHz, $C_6D_6$): $\delta$ = 5.29 (d, $J_{H\text{-}H}$ = 7.9 Hz, 1H, NH), 4.84 (tdt, $J_{H\text{-}H}$ = 11.7, 7.9, 4.0 Hz, 1H, cyclohexyl $\alpha$-CH), 3.37 (q, $J_{H\text{-}H}$ = 7.2 Hz, 4H, ethyl $CH_2$), 2.13 (m, 2H, cyclohexyl $CH_2$), 1.54 (m, 2H, cyclohexyl $CH_2$), 1.44 (m, 1H, cyclohexyl $CH_2$), 1.27 (m, 2H, cyclohexyl $CH_2$), 1.13-0.98 (m, 3H, cyclohexyl $CH_2$), 0.91 (t, $J_{H\text{-}H}$ = 7.2 Hz, 6H, $CH_3$); $^{13}C$ {$^{1}H$} (100 MHz, $C_6D_6$): $\delta$ = 179.11 ($J_{C\text{-}Se}$ = 216.9 Hz, C=Se), 56.99 (cyclohexyl $\alpha$-CH), 46.37 (ethyl $CH_2$), 33.38 (cyclohexyl $CH_2$), 25.90 (cyclohexyl $CH_2$), 25.40 (cyclohexyl $CH_2$), 12.72 ($CH_3$); $^{77}Se$ {$^{1}H$} (76.3 MHz, $C_6D_6$): $\delta$ = 191.25; Anal. Calcd for $C_{11}H_{22}N_2Se$: C, 50.57; H, 8.49; N, 10.72. Found: C, 50.73; H, 8.33; N, 10.75. MS (ASAP) *m*/*z* Calcd for [$C_{11}H_{22}N_2{}^{80}Se + H^+$]: 263.1027. Found: 263.1031. X-ray quality crystals were grown by addition of pentane to a concentrated solution in dichloromethane.

***N′*-cyclohexyl-*N*-ethyl-*N*-methylselenourea (18)**

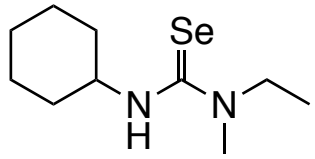


Chemical Formula: $C_{10}H_{20}N_2Se$
Molecular Weight: 247.24

Yield: 69%. White crystalline solid. Recrystallized by addition of pentane to a saturated solution in toluene followed by cooling to –40 °C. $^{1}H$ NMR (500 MHz, $C_6D_6$): $\delta$ = 5.35 (d, $J_{H\text{-}H}$ = 8.0 Hz, 1H, NH), 4.79 (tdt, $J_{H\text{-}H}$ = 11.6, 8.0, 4.0 Hz, 1H, cyclohexyl $\alpha$-CH), 3.66 (q, $J_{H\text{-}H}$ = 7.1 Hz, 2H, ethyl $CH_2$), 2.55 (s, 3H, methyl $CH_3$), 2.14 (m, 2H, cyclohexyl $CH_2$), 1.57 (m, 2H, cyclohexyl $CH_2$), 1.46 (m, 1H, cyclohexyl $CH_2$), 1.27 (m, 2H, cyclohexyl $CH_2$), 1.15 (m, 2H, cyclohexyl $CH_2$), 1.03 (m, 1H, cyclohexyl $CH_2$), 0.91 (t, $J_{H\text{-}H}$ = 7.1 Hz, 3H, ethyl $CH_3$); $^{13}C$ $\{^{1}H\}$ (125 MHz, $C_6D_6$): $\delta$ = 179.63 ($J_{C\text{-}Se}$ = 216.27 Hz, C=Se), 57.21 (cyclohexyl $\alpha$-CH), 50.36 (ethyl $CH_2$), 36.88 (methyl $CH_3$), 33.44 (cyclohexyl $CH_2$), 25.90 (cyclohexyl $CH_2$), 25.49 (cyclohexyl $CH_2$), 12.39 (ethyl $CH_3$); $^{77}Se$ $\{^{1}H\}$ (95.4 MHz, $C_6D_6$): $\delta$ = 190.17; Anal. Calcd for $C_{10}H_{20}N_2Se$: C, 48.58; H, 8.15; N, 11.33. Found: C, 48.73; H, 8.32; N, 11.35. MS (ASAP) *m*/*z* Calcd for $[C_{10}H_{20}N_2{}^{80}Se + H^+]$: 249.0870. Found: 249.0864. X-ray quality crystals were grown by addition of pentane to a saturated solution in toluene.

***N*-cyclohexyl-2-methylpyrrolidine-1-carboselenoamide (19)**

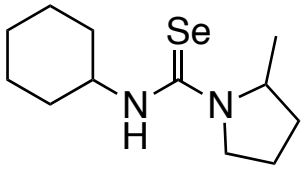


Chemical Formula: $C_{12}H_{22}N_2Se$
Molecular Weight: 273.28

Yield: 88%. White powder. Recrystallized by evaporation of a saturated solution of 2:3 dichloromethane:toluene under reduced pressure. $^{1}H$ NMR (500 MHz, $C_6D_6$): $\delta$ = 4.92-4.80 (m, 2H), 4.40 (br, 1H), 3.04 (br, 1H), 2.92 (br, 1H), 2.20 (m, 2H, cyclohexyl $CH_2$), 1.67-1.50 (m, 2H, cyclohexyl or pyrrolidine $CH_2$), 1.48-1.25 (m, 6H, cyclohexyl and pyrrolidine $CH_2$), 1.10-0.97 (m, 7H, cyclohexyl and pyrrolidine $CH_2$ and $CH_3$); $^{13}C$ $\{^{1}H\}$ (125 MHz, $C_6D_6$): $\delta$ = 177.15 ($J_{C\text{-}Se}$ = 217.31 Hz, C=Se), 57.77 (br), 55.94, 49.17 (br), 33.70, 33.55, 25.98, 25.32, 25.29, 23.04, 19.14; $^{77}Se$ $\{^{1}H\}$ (95.4 MHz, $C_6D_6$): $\delta$ = 229.59; Anal. Calcd for $C_{12}H_{22}N_2Se$: C, 52.74; H, 8.11; N, 10.25. Found: C, 52.50; H, 8.27; N, 10.27. MS (ASAP) *m*/*z* Calcd for [$C_{12}H_{22}N_2{}^{80}Se$ + $H^+$]: 275.1026. Found: 275.1023. X-ray quality crystals were grown by addition of pentane to a saturated solution in dichloromethane.

***N*-cyclohexyl-3,4-dihydroisoquinoline-2(*1H*)-carboselenoamide (20)**

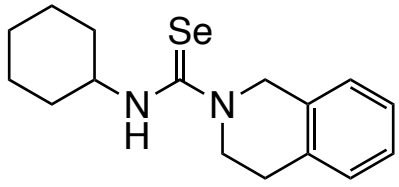


Chemical Formula: $C_{16}H_{22}N_2Se$
Molecular Weight: 321.33

Yield: 95%. White powder. Recrystallized by addition of pentane to a saturated toluene solution followed by storage at –40 °C overnight. $^1$H NMR (500 MHz, tetrahydrofuran-$d_8$): $\delta$ = 7.16-7.09 (m, 4H, aryl CH), 6.56 (br d, $J_{H-H}$ = 7.9 Hz, 1H, NH), 4.93 (s, 2H, NC$\underline{H}_2$C), 4.63 (tdt, $J_{H-H}$ = 11.5, 7.9, 4.0 Hz, 1H, cyclohexyl $\alpha$-CH), 4.05 (t, $J_{H-H}$ = 5.9 Hz, 2H, NC$\underline{H}_2$CH$_2$C), 2.87 (t, $J_{H-H}$ = 5.9 Hz, 2H, NCH$_2$C$\underline{H}_2$C), 2.11 (m, 2H, cyclohexyl CH$_2$), 1.72 (m, 2H, cyclohexyl CH$_2$), 1.64 (m, 1H, cyclohexyl CH$_2$), 1.41-1.31 (m, 2H, cyclohexyl CH$_2$), 1.29-1.19 (m, 2H, cyclohexyl CH$_2$), 1.19-1.09 (m, 1H, cyclohexyl CH$_2$); $^{13}$C {$^1$H} (125 MHz, tetrahydrofuran-$d_8$): $\delta$ = 181.56 ($J_{C-Se}$ = 217.2 Hz, C=Se), 136.45 (aryl C), 134.43 (aryl C), 128.51 (aryl CH), 127.28 (aryl CH), 126.87 (aryl CH), 126.75 (aryl CH), 57.89 (CH$_2$ or cyclohexyl $\alpha$-CH), 51.24 (CH$_2$ or cyclohexyl CH), 48.02 (NCH$_2$ or cyclohexyl CH), 33.45 (cyclohexyl CH$_2$), 29.48 (NCH$_2$C$\underline{H}_2$C), 26.48 (cyclohexyl CH$_2$), 26.12 (cyclohexyl CH$_2$); $^{77}$Se {$^1$H} (95.4 MHz, tetrahydrofuran-$d_8$): $\delta$ = 204.58; Anal. Calcd for $C_{16}H_{22}N_2Se$: C, 59.81; H, 6.90; N, 8.72. Found: C, 59.43; H, 7.09; N, 8.76. MS (ASAP) *m*/*z* Calcd for [$C_{16}H_{22}N_2{}^{80}Se$ + $H^+$]: 323.1026. Found: 323.1031. X-ray

quality crystals were grown by addition of pentane to a saturated solution in dichloromethane.

***N,N*-diallyl-*N'*-cyclohexylselenourea (21)**

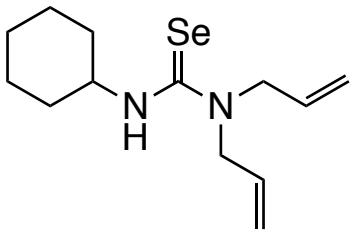


Chemical Formula: $C_{13}H_{22}N_2Se$
Molecular Weight: 285.29

Yield: 98%. Pale yellow low-melting solid. $^{1}H$ NMR (400 MHz, $C_6D_6$): $\delta$ = 5.57 (ddd, $J_{H\text{-}H}$ = 21.3, 10.6, 5.3 Hz, 2H, vinyl CH), 5.38 (d, $J_{H\text{-}H}$ = 7.4 Hz, 1H, NH), 4.91 (ddd, $J_{H\text{-}H}$ = 4.6, 1.5, 1.5 Hz, 1H, vinyl $CH_2$), 4.87 (ddd, $J_{H\text{-}H}$ = 11.1, 1.6, 1.6 Hz, 1H, vinyl $CH_2$), 4.85-4.75 (m, 1H, cyclohexyl $\alpha$-CH), 4.04 (m, 4H, allylic $CH_2$), 2.10 (m, 2H, cyclohexyl $CH_2$), 1.52-1.43 (m, 3H, cyclohexyl $CH_2$), 1.43-1.33 (m, 1H, cyclohexyl $CH_2$), 1.31-1.20 (m, 2H, cyclohexyl $CH_2$), 1.05-0.96 (m, 3H, cyclohexyl $CH_2$); $^{13}C$ {$^{1}H$} (100 MHz, $C_6D_6$): $\delta$ = 181.74 ($J_{C\text{-}Se}$ = 218.8 Hz, C=Se), 133.05 (vinyl CH), 117.44 (vinyl $CH_2$), 57.10 (allylic $CH_2$), 54.79 (cyclohexyl $\alpha$-CH), 33.13 (cyclohexyl $CH_2$), 25.88 (cyclohexyl $CH_2$), 25.10 (cyclohexyl $CH_2$); $^{77}Se$ {$^{1}H$} (76.3 MHz, $C_6D_6$): $\delta$ = 217.25; Anal. Calcd for $C_{15}H_{30}N_2Se$: C, 54.73; H, 7.77; N, 9.82. Found: C, 55.00; H, 7.88; N, 9.74. MS (FAB) *m/z* Calcd for [$C_{15}H_{30}N_2{}^{80}Se + H^+$]: 287.10. Found: 287.19. X-ray quality crystals were grown from the melt.

***N,N*-dimethyl-*N′*-cyclohexylselenourea (22)**

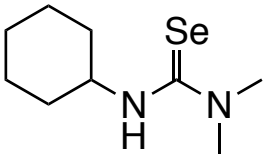


Chemical Formula: $C_9H_{18}N_2Se$
Molecular Weight: 233.22

Yield: 76% (6.6 mmol scale). White crystalline solid. Recrystallized by addition of pentane to a saturated toluene solution followed by storage at –40 °C overnight. $^1$H NMR (400 MHz, $C_6D_6$): $\delta$ = 4.80 (m, 2H, NH and cyclohexyl $\alpha$-CH), 2.59 (s, 6H, $CH_3$), 2.14 (dd, $J_{H\text{-}H}$ = 12.4, 3.8 Hz, 2H, cyclohexyl $CH_2$), 1.52 (m, 2H, cyclohexyl $CH_2$), 1.43 (m, 1H, cyclohexyl $CH_2$), 1.27 (m, 2H, cyclohexyl $CH_2$), 1.03-0.87 m, 3H, cyclohexyl $CH_2$); $^{13}$C {$^1$H} (100 MHz, $C_6D_6$): $\delta$ = 181.27 ($J_{C\text{-}Se}$ = 218.5 Hz, C=Se), 56.84 (cyclohexyl $\alpha$-CH), 40.84 ($CH_3$), 33.50 (cyclohexyl $CH_2$), 25.93 (cyclohexyl $CH_2$), 25.27 (cyclohexyl $CH_2$); $^{77}$Se {$^1$H} (76.3 MHz, $C_6D_6$): $\delta$ = 219.82; Anal. Calcd for $C_9H_{18}N_2Se$: C, 46.35; H, 7.78; N, 12.01. Found: C, 46.32; H, 7.51; N, 11.90. MS (ASAP) *m*/*z* Calcd for [$C_9H_{18}N_2{}^{80}Se + H^+$]: 235.0714. Found: 235.0719. X-ray quality crystals were grown by vapor diffusion of pentane into a concentrated solution in toluene.

***N*-cyclohexylpyrrolidine-1-carboselenoamide (23)**

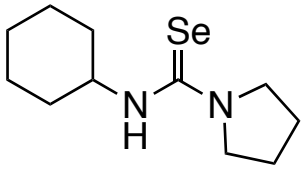


Chemical Formula: $C_{11}H_{20}N_2Se$
Molecular Weight: 259.26

Yield: 89%. White powder. Recrystallized by evaporation of a saturated solution in 1:1 dichloromethane:toluene under reduced pressure. $^{1}H$ NMR (500 MHz, $CD_2Cl_2$): $\delta$ = 5.43 (br d, $J_{H\text{-}H}$ = 8.0 Hz, 1H, NH), 4.44 (tdt, $J_{H\text{-}H}$ = 11.3, 8.0, 4.0 Hz, 1H, cyclohexyl $\alpha$-CH), 4.20-3.00 (br m, 4H, pyrrolidine $\alpha$-$CH_2$), 2.30-1.80 (br, 4H, pyrrolidine $\beta$-$CH_2$), 2.14 (m, 2H, cyclohexyl $CH_2$), 1.79 (m, 2H, cyclohexyl $CH_2$), 1.70 (m, 1H, cyclohexyl $CH_2$), 1.44 (m, 2H, cyclohexyl $CH_2$), 1.28 (m, 3H, cyclohexyl $CH_2$); $^{13}C$ {$^{1}H$} (125 MHz, $CD_2Cl_2$): $\delta$ = 175.40 ($J_{C\text{-}Se}$ = 212.7 Hz, C=Se), 56.39 (cyclohexyl $\alpha$-CH), 54.91 (br, pyrrolidine $\alpha$-$CH_2$), 47.23 (br, pyrrolidine $\beta$-$CH_2$), 33.42 (cyclohexyl $CH_2$), 25.78 (cyclohexyl $CH_2$), 25.55 (cyclohexyl $CH_2$), 25.31 (cyclohexyl $CH_2$); $^{77}Se$ {$^{1}H$} (95.4 MHz, $CD_2Cl_2$): $\delta$ = 206.65; Anal. Calcd for $C_{11}H_{20}N_2Se$: C, 50.96; H, 7.78; N, 10.81. Found: C, 51.19; H, 7.65; N, 10.82. MS (ASAP) *m*/*z* Calcd for [$C_{11}H_{20}N_2{}^{80}Se + H^+$]: 261.0870. Found: 261.0875. X-ray quality crystals were grown by addition of pentane to a concentrated solution in tetrahydrofuran.

***N′*-cyclohexyl-*N*-(4-methoxyphenyl)-*N*-methylselenourea (24)**

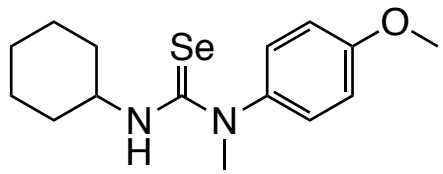


Chemical Formula: $C_{15}H_{22}N_2OSe$
Molecular Weight: 325.31

Yield: 71%. White powder. Recrystallized by addition of pentane to a saturated toluene solution. $^1$H NMR (500 MHz, $C_6D_6$): $\delta$ = 6.60 (s, 4H, aryl CH), 5.39 (d, $J_{H\text{-}H}$ = 8.1 Hz, 1H, NH), 4.77 (tdt, $J_{H\text{-}H}$ = 10.4, 8.0, 4.0 Hz, 1H, cyclohexyl $\alpha$-CH), 3.72 (s, 3H, $NCH_3$), 3.22 (s, 3H, $OCH_3$), 2.01 (m, 2H, cyclohexyl $CH_2$), 1.37-1.24 (m, 3H, cyclohexyl $CH_2$), 1.23-1.13 (m, 2H, cyclohexyl $CH_2$), 0.85-0.70 (m, 3H, cyclohexyl $CH_2$); $^{13}$C {$^1$H} (125 MHz, $C_6D_6$): $\delta$ = 182.14 ($J_{C\text{-}Se}$ = 220.3 Hz, C=Se), 159.10 (aryl CO), 135.46 (aryl CN), 128.22 (aryl CH), 115.77 (aryl CH), 56.44 (cyclohexyl $\alpha$-CH), 55.12 ($OCH_3$), 46.19 ($NCH_3$), 32.78 (cyclohexyl $CH_2$), 25.63 (cyclohexyl $CH_2$), 24.96 (cyclohexyl $CH_2$),; $^{77}$Se {$^1$H} (95.4 MHz, $C_6D_6$): $\delta$ = 218.80; Anal. Calcd for $C_{15}H_{22}N_2Se$: C, 55.38; H, 6.82; N, 8.61. Found: C, 55.38; H, 6.56; N, 8.47. MS (ASAP) *m*/*z* Calcd for [$C_{15}H_{22}N_2{}^{80}Se + H^+$]: 327.0976. Found: 327.0975.

***N′*-cyclohexyl-*N*-methyl-*N*-phenylselenourea (25)**

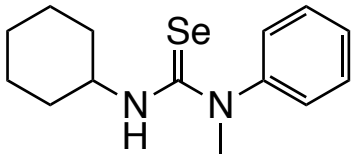


Chemical Formula: $C_{14}H_{20}N_2Se$
Molecular Weight: 295.29

Yield: 64%. Pale yellow-orange powder. Recrystallized by addition of pentane to a saturated tetrahydrofuran solution followed by storage at –40 °C overnight. $^{1}$H NMR (500 MHz, $C_6D_6$): $\delta$ = 6.96 (t, $J_{H\text{-}H}$ = 7.6 Hz, 2H, *o*-CH), 6.90 (t, $J_{H\text{-}H}$ = 7.4 Hz, 1H, *p*-CH), 6.65 (t, $J_{H\text{-}H}$ = 7.7 Hz, 2H, *m*-CH), 5.31 (d, $J_{H\text{-}H}$ = 7.9 Hz 1H, NH), 4.76 (tdt, $J_{H\text{-}H}$ = 11.4, 8.3, 4.0, 1H, cyclohexyl $\alpha$-CH), 3.67 (s, 3H, methyl $CH_3$), 1.97 (m, 2H, cyclohexyl $CH_2$), 1.45-1.10 (m, 5H, cyclohexyl $CH_2$), 0.90-0.64 (m, 3H, cyclohexyl $CH_2$); $^{13}$C {$^{1}$H} (125 MHz, $C_6D_6$): $\delta$ = 182.01 ($J_{C\text{-}Se}$ = 220.8 Hz, C=Se), 143.25 (*ipso*-C), 130.53 (*m*-CH), 128.24 (*p*-CH), 127.05 (*o*-CH), 56.44 (cyclohexyl $\alpha$-CH), 45.97 (methyl $CH_3$), 32.62 (cyclohexyl $CH_2$), 25.58 (cyclohexyl $CH_2$), 24.89 (cyclohexyl $CH_2$); $^{77}$Se {$^{1}$H} (95.4 MHz, $C_6D_6$): $\delta$ = 227.43; Anal. Calcd for $C_{14}H_{20}N_2Se$: C, 56.95; H, 6.83; N, 9.49. Found: C, 56.67; H, 6.84; N, 9.23. MS (ASAP) *m*/*z* Calcd for [$C_{14}H_{20}N_2{}^{80}Se + H^+$]: 297.0870. Found: 297.0869.

**_N_-(4-chlorophenyl)-_N'_-cyclohexyl-_N_-methylselenourea (26)**

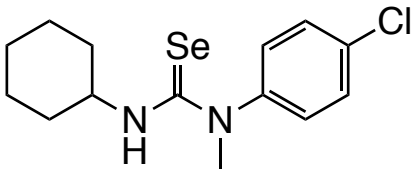


Chemical Formula: $C_{14}H_{19}ClN_2Se$
Molecular Weight: 329.73

Yield: 27%. Pale yellow powder. Recrystallized by addition of pentane to a saturated toluene solution followed by storage at –40 °C overnight. $^{1}$H NMR (500 MHz, $C_6D_6$): $\delta$ = 6.88 (m, 2H, aryl CH), 6.32 (m, 2H, aryl CH), 5.15 (d, $J_{H\text{-}H}$ = 8.0

Hz, 1H, NH), 4.71 (m, 1H, cyclohexyl $\alpha$-CH), 3.55 (s, 3H, $CH_3$), 1.98 (m, 2H, cyclohexyl $CH_2$), 1.38-1.27 (m, 3H, cyclohexyl $CH_2$), 1.22-1.13 (m, 2H, cyclohexyl $CH_2$), 0.86-0.77 (m, 1H, cyclohexyl $CH_2$), 0.74-0.65 (m, 2H, cyclohexyl $CH_2$); $^{13}C$ {$^1H$} (125 MHz, $C_6D_6$): $\delta$ = 182.18 ($J_{C\text{-}Se}$ = 221.51 Hz, C=Se), 141.59 (aryl NC), 133.91 (aryl CCl), 130.61 (aryl CH), 128.46 (aryl CH), 56.64 (cyclohexyl $\alpha$-CH), 45.80 ($CH_3$), 32.65 (cyclohexyl $CH_2$), 25.98 (cyclohexyl $CH_2$), 24.95 (cyclohexyl $CH_2$); $^{77}Se$ {$^1H$} (95.4 MHz, $C_6D_6$): $\delta$ = 239.92.

***N'*-hexadecyl-*N*-isopropyl-*N*-methylselenourea (27)**

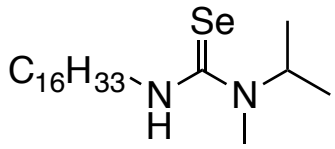


Chemical Formula: $C_{21}H_{44}N_2Se$
Molecular Weight: 403.56

Yield: 45%. White powder. Recrystallized by evaporation of a saturated toluene solution under reduced pressure. $^1H$ NMR (500 MHz, $C_6D_6$): $\delta$ = 6.00 (br, 1H, NH or isopropyl CH), 5.35 (br, 1H, NH or isopropyl CH), 3.86 (dt, $J_{H\text{-}H}$ = 7.3, 5.7 Hz, 2H, hexadecyl $\alpha$-$CH_2$), 2.2 (s, 3H, methyl $CH_3$), 1.59 (m, 2H, hexadecyl $\beta$-$CH_2$), 1.37-1.24 (m, 26H, hexadecyl $CH_2$), 0.91 (t, $J_{H\text{-}H}$ = 6.9 Hz, 3H, hexadecyl $CH_3$), 0.85 (d, $J_{H\text{-}H}$ = 6.8 Hz, 6H, isopropyl $CH_3$); $^{13}C$ {$^1H$} (125 MHz, $C_6D_6$): $\delta$ = 181.93 ($J_{C\text{-}Se}$ = 216.1 Hz, C=Se), 53.81 (isopropyl CH), 48.87 (hexadecyl $\alpha$-$CH_2$), 32.39 (methyl $CH_3$), 30.27 (br, hexadecyl $CH_2$), 30.26 (br, hexadecyl $CH_2$), 30.20 (br, hexadecyl $CH_2$), 30.18 (hexadecyl $CH_2$), 30.10 (hexadecyl $CH_2$), 29.97 (hexadecyl

$CH_2$), 29.89 (hexadecyl $CH_2$), 27.44 (hexadecyl $CH_2$), 23.17 (hexadecyl $CH_2$), 19.49 (isopropyl $CH_3$), 14.44 (hexadecyl $CH_3$); $^{77}Se$ {$^1H$} (95.4 MHz, $C_6D_6$): $\delta$ = 189.01; Anal. Calcd for $C_{21}H_{44}N_2Se$: C, 62.50; H, 10.99; N, 6.94. Found: C, 62.97; H, 11.27; N, 6.89. MS (ASAP) *m*/*z* Calcd for [$C_{21}H_{44}N_2{}^{80}Se + H^+$]: 405.2748. Found: 405.2747.

**_N,N_-diallyl-_N'_-_n_-hexadecylselenourea (28)**

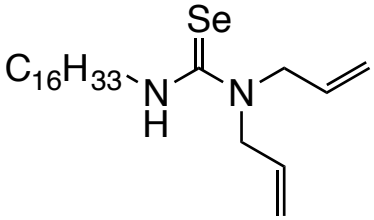


Chemical Formula: $C_{23}H_{44}N_2Se$
Molecular Weight: 427.58

Yield: 63%. White powder. Recrystallized by evaporation of a saturated toluene solution under reduced pressure. $^1H$ NMR (500 MHz, $C_6D_6$): $\delta$ = 5.56 (ddt, $J_{H-H}$ = 16.0, 10.4, 5.3 Hz, 2H, vinyl CH), 5.47 (br t, $J_{H-H}$ = 5.3 Hz, 1H, NH), 4.90 (m, 4H, vinyl $CH_2$), 4.03 (br s, 4H, allylic $CH_2$), 3.78 (td, $J_{H-H}$ = 7.3, 5.3 Hz, 2H, hexadecyl $\alpha$-$CH_2$), 1.49 (m, 2H, hexadecyl $\beta$-$CH_2$), 1.37-1.15 (m, 26H, hexadecyl $CH_2$), 0.91 (t, $J_{H-H}$ = 6.9 Hz, 3H, hexadecyl $CH_3$); $^{13}C$ {$^1H$} (125 MHz, $C_6D_6$): $\delta$ = 183.62 ($J_{C-Se}$ = 217.7 Hz, C=Se), 132.96 (vinyl CH), 117.25 (vinyl $CH_2$), 54.63 (allylic $CH_2$), 49.15 (hexadecyl $\alpha$-$CH_2$), 32.38 (hexadecyl $\beta$-$CH_2$), 30.25 (br, hexadecyl $CH_2$), 30.22 (hexadecyl $CH_2$), 30.19 (hexadecyl $CH_2$), 30.12 (hexadecyl $CH_2$), 30.11 (hexadecyl $CH_2$), 29.88 (hexadecyl $CH_2$), 29.82 (hexadecyl $CH_2$), 29.67 (hexadecyl $CH_2$), 27.30 (hexadecyl $CH_2$), 23.17 (hexadecyl $CH_2$), 14.43 (hexadecyl $CH_3$); $^{77}Se$

{$^1$H} (95.4 MHz, $C_6D_6$): $\delta$ = 221.81; Anal. Calcd for $C_{23}H_{44}N_2Se$: C, 64.61; H, 10.37; N, 6.55. Found: C, 63.83; H, 10.54; N, 6.48. MS (ASAP) *m*/*z* Calcd for [$C_{23}H_{44}N_2{}^{80}Se$ + $H^+$]: 429.2748. Found: 429.2744.

***N′-n*-hexadecyl-*N*-methyl-*N*-phenylselenourea (29)**

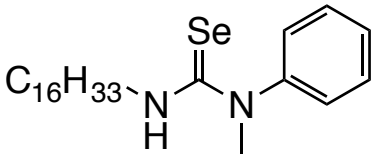


Chemical Formula: $C_{24}H_{42}N_2Se$
Molecular Weight: 437.57

Yield: 73%. Pale yellow powder. Recrystallized by evaporation of a saturated toluene solution under reduced pressure. $^1$H NMR (500 MHz, $C_6D_6$): $\delta$ = 6.94 (m, 2H, *o*-CH), 6.87 (m, 1H, *p*-CH), 6.64 (m, 2H, *m*-CH), 5.36 (br t, $J_{H\text{-}H}$ = 5.4 Hz, 1H, NH) 3.67 (s, 3H, methyl $CH_3$), 3.62 (td, $J_{H\text{-}H}$ = 7.4, 5.6 Hz, 2H, hexadecyl $\alpha$-$CH_2$), 1.38-1.00 (m, 28H, hexadecyl $CH_2$), 0.91 (t, $J_{H\text{-}H}$ = 6.5 Hz, 3H, hexadecyl $CH_3$); $^{13}$C {$^1$H} (125 MHz, $C_6D_6$): $\delta$ = 183.73 ($J_{C\text{-}Se}$ = 221.0 Hz, C=Se), 143.09 (*ipso*-C), 130.50 (*o*- or *m*-CH), 128.21 (*p*-CH), 127.14 (*o*- or *m*-CH), 48.65 (methyl $CH_3$ or hexadecyl $\alpha$-$CH_2$), 46.15 (methyl $CH_3$ or hexadecyl $\alpha$-$CH_2$), 32.38 (hexadecyl $CH_2$), 30.23 (br, hexadecyl $CH_2$), 30.18 (hexadecyl $CH_2$), 30.05 (hexadecyl $CH_2$), 30.02 (hexadecyl $CH_2$), 29.87 (hexadecyl $CH_2$), 29.67 (hexadecyl $CH_2$), 29.42 (hexadecyl $CH_2$), 27.14 (hexadecyl $CH_2$), 23.15 (hexadecyl $CH_2$), 14.41 (hexadecyl $CH_3$); $^{77}$Se {$^1$H} (95.4 MHz, $C_6D_6$): $\delta$ = 233.46; Anal. Calcd for $C_{24}H_{42}N_2Se$: C, 65.88;

H, 9.68; N, 6.40. Found: C, 65.85; H, 9.54; N, 6.38. MS (ASAP) *m*/*z* Calcd for [$C_{24}H_{42}N_2{}^{80}Se + H^+$]: 439.2591. Found: 439.2589.

**_N,N_-dimethyl-_N′_-_tert_-butylselenourea (30)**

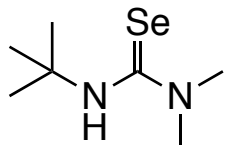


Chemical Formula: $C_7H_{16}N_2Se$
Molecular Weight: 207.18

Yield: 72%. White powder. Recrystallized by addition of pentane to a saturated toluene solution followed by storage at –40 °C overnight. $^1$H NMR (500 MHz, $C_6D_6$): $\delta$ = 4.93 (br s, 1H, NH), 2.56 (s, 6H, N($CH_3$)$_2$), 1.55 (s, 9H, C($CH_3$)$_3$); $^{13}$C {$^1$H} (125 MHz, $C_6D_6$): $\delta$ = 179.65 ($J_{C\text{-}Se}$ = 220.5 Hz), 54.93 (C(CH$_3$)$_3$), 41.16 (N($CH_3$)$_2$), 29.68 (C($CH_3$)$_3$); $^{77}$Se {$^1$H} (95.4 MHz, $C_6D_6$): $\delta$ = 266.53; Anal. Calcd for $C_7H_{16}N_2Se$: C, 40.58; H, 7.78; N, 13.52. Found: C, 40.91; H, 7.65; N, 13.54. MS (ASAP) *m*/*z* Calcd for [$C_7H_{16}N_2{}^{80}Se + H^+$]: 209.0557. Found: 209.0560. X-ray quality crystals were grown by addition of pentane to a concentrated solution in diethyl ether.

**_N_-_tert_-butylpyrrolidine-1-carboselenoamide (31)**

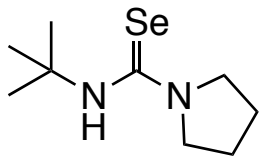


Chemical Formula: $C_9H_{18}N_2Se$
Molecular Weight: 233.22

Yield: 68%. White crystalline solid. Recrystallized by addition of pentane to a saturated toluene solution followed by storage at –40 °C overnight. $^{1}$H NMR (500 MHz, THF-$d_8$): $\delta$ = 3.86 (s, 1H, NH), 1.69 (m, 4H, pyrrolidine $\alpha$-$CH_2$), 0.08 (m, 4H, pyrrolidine β-$CH_2$), -0.27 (s, 9H, $CH_3$); $^{13}$C {$^{1}$H} (125 MHz, THF-$d_8$): $\delta$ = 176.36 ($J_{C\text{-}Se}$ = 219.1 Hz, C=Se) 54.90 (pyrrolidine $\alpha$-$CH_2$), 51.09 (br, $\underline{C}(CH_3)_3$), 29.69 ($CH_3$), 26.01 (pyrrolidine β-$CH_2$); $^{77}$Se {$^{1}$H} (95.4 MHz, THF-$d_8$): $\delta$ = 288.15; Anal. Calcd for $C_9H_{18}N_2Se$: C, 46.35; H, 7.78; N, 12.01. Found: C, 46.59; H, 7.59; N, 12.06. MS (ASAP) *m*/*z* Calcd for [$C_9H_{18}N_2{}^{80}Se + H^+$]: 235.0714. Found: 235.0715. X-ray quality crystals were grown by addition of pentane to a concentrated solution in dichloromethane.

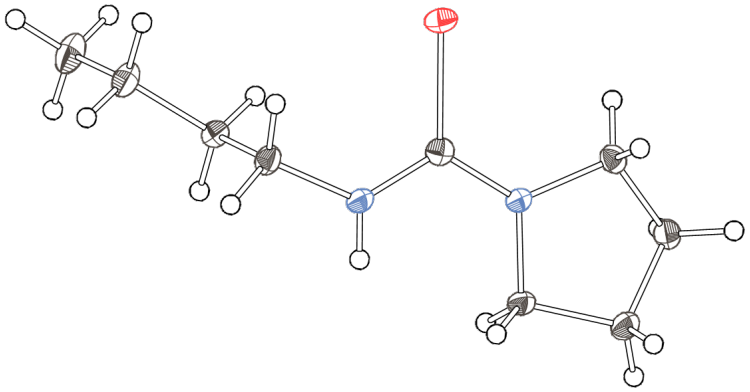

Figure 3.7.4. *N*-butylpyrrolidine-1-carboselenoamide (**8**)

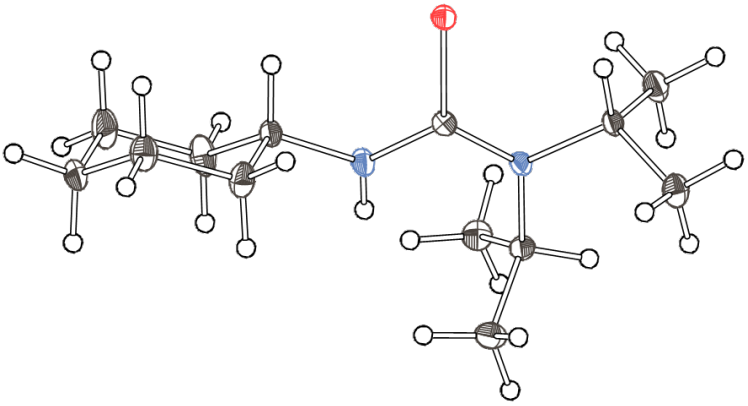

Figure 3.7.5. *N'*-cyclohexyl-*N*,*N*-diisopropylselenourea (**12**)

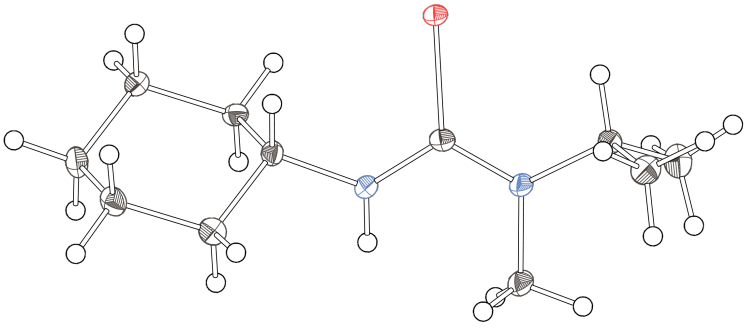

Figure 3.7.6. *N'*-cyclohexyl-*N*-methyl-*N*-isoproylselenourea (**14**)

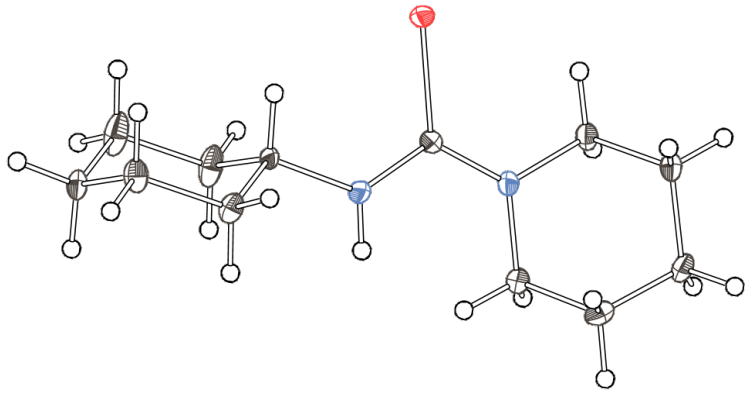

Figure 3.7.7. *N*-cyclohexylpiperidine-1-carboselenoamide (**15**)

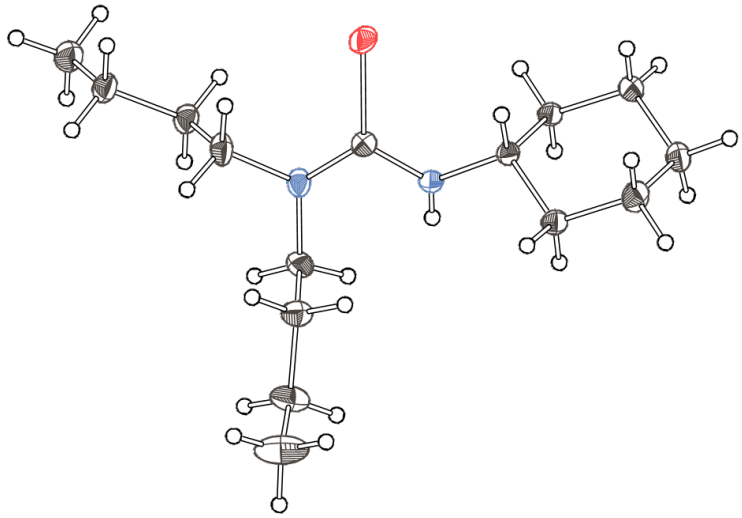

Figure 3.7.8. *N,N*-dibutyl-*N'*-cyclohexylselenourea (**16)**

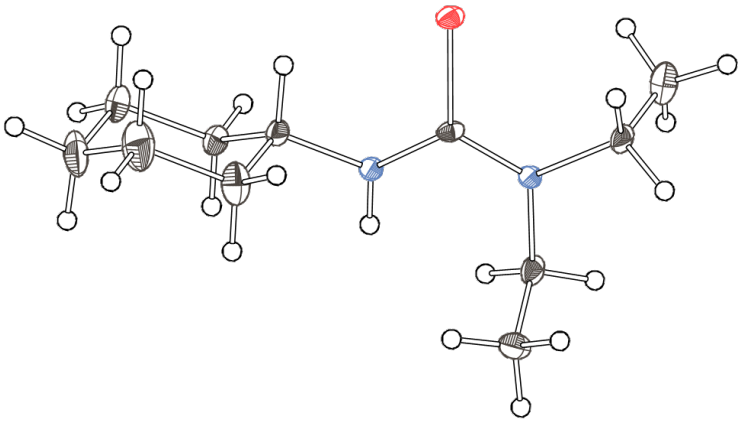

Figure 3.7.9. *N'*-cyclohexyl-*N*,*N*-diethylselenourea (**17**)

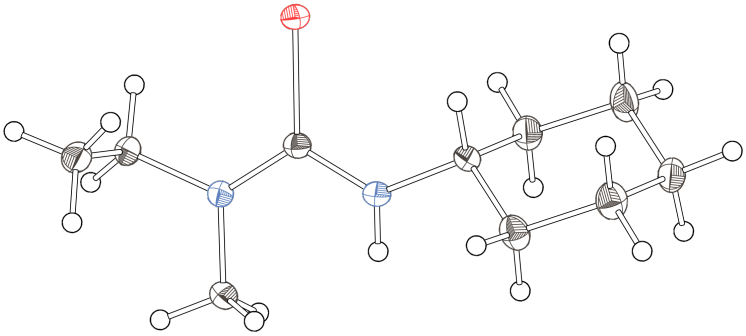

Figure 3.7.10. *N'*-cyclohexyl-*N*-ethyl-*N*-methylselenourea (**18**)

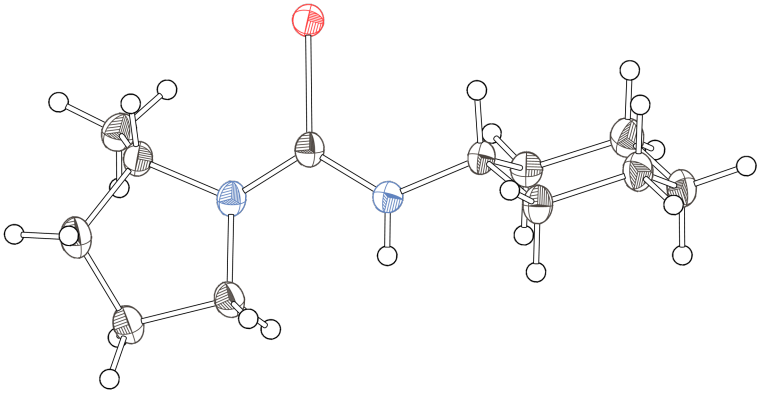

Figure 3.7.11. *N*-cyclohexyl-2-methylpyrrolidine-1-carboselenoamide (**19**)

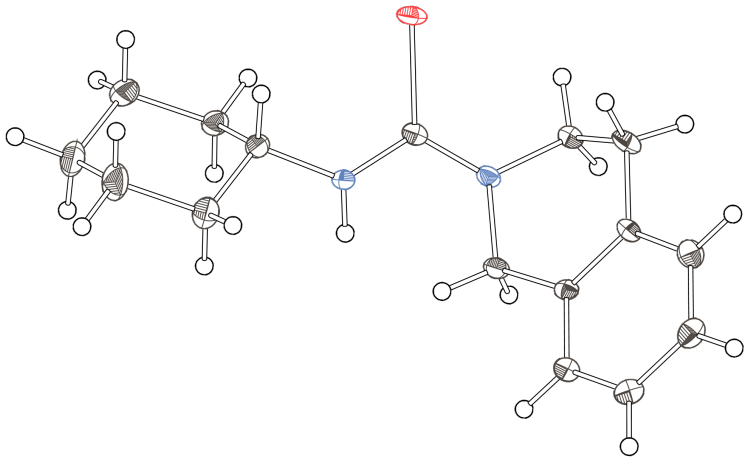

Figure 3.7.12. *N*-cyclohexyl-3,4-dihydroisoquinoline-2(1*H*)-carboselenoamide (**20**)

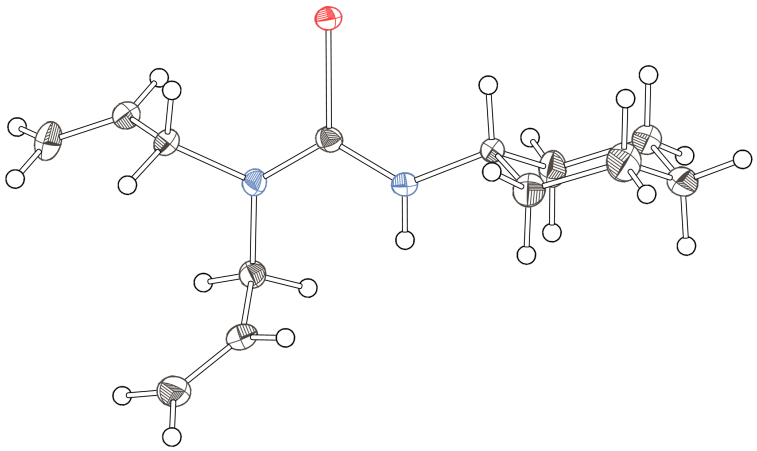

Figure 3.7.13. *N,N*-diallyl-*N'*-cyclohexylselenourea (**21**)

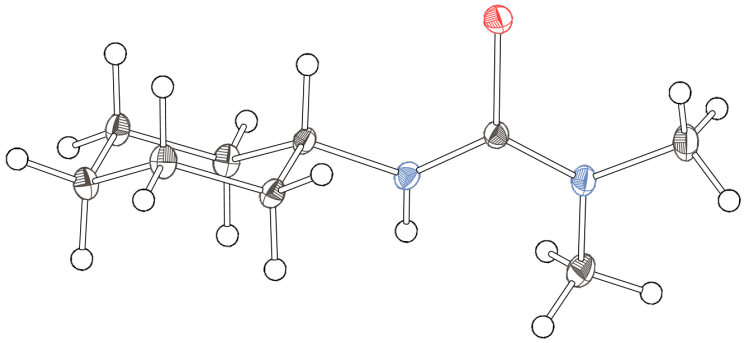

Figure 3.7.14. *N'*-cyclohexyl-*N*,*N*-dimethylselenourea (**22**)

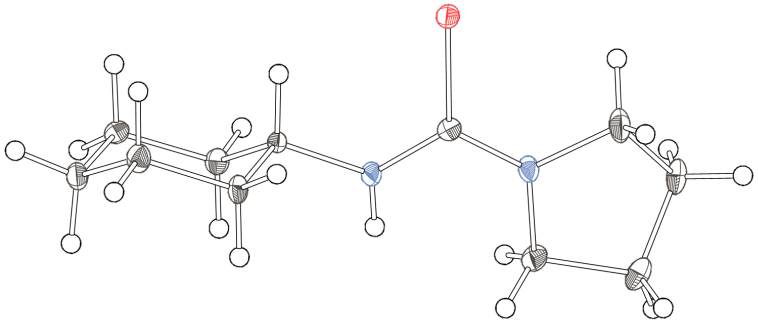

Figure 3.7.15. *N*-cyclohexylpyrrolidine-1-carboselenoamide (**23**)

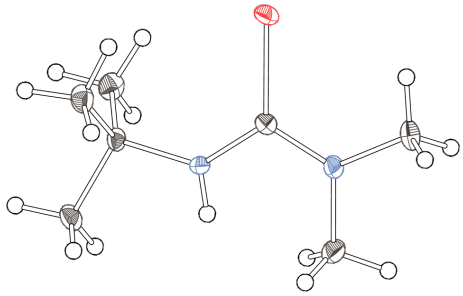

Figure 3.7.16. *N'*-(*tert*-butyl)-*N*,*N*-dimethylselenourea (**30**)

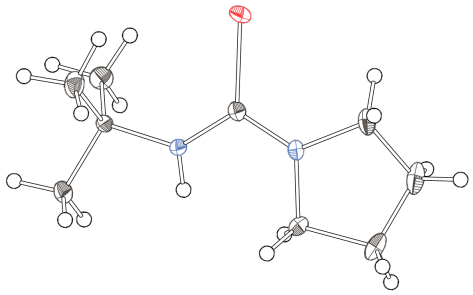

Figure 3.7.17. *N*-(*tert*-butyl)pyrrolidine-1-carboselenoamide (**31**)

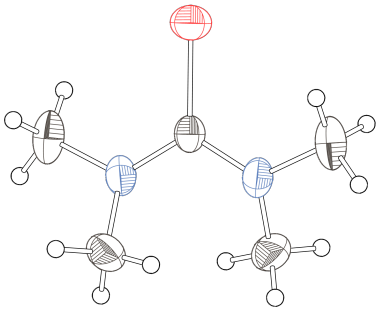

Figure 3.7.18. *N,N,N′,N′*-tetramethylselenourea

Table 3.7.1. Structural parameters extracted from single-crystal x-ray diffraction analysis of trisubstituted selenoureas.

| | **Compound Name** | ***d* C-Se (Å)** | **< NCN (°)** |
|---|---|---|---|
| **8** | N-butylpyrrolidine-1-carboselenoamide | 1.868(17) | 117.40(15) |
| **12** | N'-cyclohexyl-N,N-diisopropylselenourea | 1.8697(12) | 117.02(10) |
| **14** | N'-cyclohexyl-N-methyl-N-isoproylselenourea | 1.881(4) | 117.5(4) |
| **15** | N-cyclohexylpiperidine-1-carboselenoamide 1 | 1.883(4) | 118.3(4) |
| **15** | N-cyclohexylpiperidine-1-carboselenoamide 2 | 1.882(4) | 118.2(4) |
| **16** | N,N-dibutyl-N'-cyclohexylselenourea | 1.871(3) | 117.5(2) |
| **17** | N'-cyclohexyl-N,N-diethylselenourea | 1.872(4) | 118.4(3) |
| **18** | N'-cyclohexyl-N-ethyl-N-methylselenourea | 1.8711(19) | 116.43(17) |
| **19** | N-cyclohexyl-2-methylpyrrolidine-1-carboselenoamide | 1.876(3) | 116.9(3) |
| **20** | N-cyclohexyl-3,4-dihydroisoquinoline-2(1*H*)-carboselenoamide | 1.873(3) | 117.5(3) |
| **21** | N,N-diallyl-N'-cyclohexylselenourea | 1.877(3) | 118.6(2) |
| **22** | N'-cyclohexyl-N-N-dimethylselenourea | 1.873(15) | 117.24(13) |
| **23** | N-cyclohexylpyrrolidine-1-carboselenoamide | 1.868(2) | 117.06(19) |
| **30** | N'-(*tert*-butyl)-N,N-dimethylselenourea | 1.863(14) | 115.16(12) |
| **31** | N-(*tert*-butyl)pyrrolidine-1-carboselenoamide | 1.863(2) | 115.1(2) |
| | Average of trisubstituted selenoureas | 1.873 | 117.2 |
| | Standard Deviation | 0.006 | 1.0 |
| | N,N,N',N'-tetramethylselenourea | 1.844(4) | 116.6(3) |

*3.7.18. Crystallographic Data*

Table 3.7.2. Crystal, intensity collection, and refinement data for **8**.

| | |
|---|---|
| Empirical formula | $C_9H_{18}N_2Se$ |
| Formula weight | 233.21 |
| Temperature/K | 100 |
| Crystal system | Monoclinic |
| Space group | $P2_1/c$ |
| a/Å | 11.4123(3) |
| b/Å | 9.6891(2) |
| c/Å | 9.8300(2) |
| $\alpha$/° | 90 |
| $\beta$/° | 95.698(2) |
| $\gamma$/° | 90 |
| Volume/Å$^3$ | 1081.58(4) |
| Z | 4 |
| $\varrho_{calc}$g/cm$^3$ | 1.432 |
| $\mu$/mm$^{-1}$ | 3.426 |
| F(000) | 480.0 |
| Crystal size/mm$^3$ | 0.137 × 0.0832 × 0.0448 |
| Radiation | MoK$\alpha$ ($\lambda$ = 0.71073) |
| 2$\Theta$ range for data collection/° | 6.704 to 59.316 |
| Index ranges | -15 ≤ h ≤ 15, -12 ≤ k ≤ 13, -13 ≤ l ≤ 13 |
| Reflections collected | 29636 |
| Independent reflections | 2871 [$R_{int}$ = 0.0571, $R_{sigma}$ = 0.0290] |
| Data/restraints/parameters | 2871/1/113 |
| Goodness-of-fit on $F^2$ | 1.079 |
| Final R indexes [I>=2$\sigma$ (I)] | $R_1$ = 0.0294, $wR_2$ = 0.0612 |
| Final R indexes [all data] | $R_1$ = 0.0365, $wR_2$ = 0.0635 |
| Largest diff. peak/hole / e Å$^{-3}$ | 0.55/-0.26 |

Table 3.7.3. Crystal, intensity collection, and refinement data for **12**.

| | |
|---|---|
| Empirical formula | $C_{13}H_{26}N_2Se$ |
| Formula weight | 289.32 |
| Temperature/K | 100.0 |
| Crystal system | Monoclinic |
| Space group | $P2_1/n$ |
| a/Å | 11.35852(9) |
| b/Å | 12.23104(6) |
| c/Å | 11.94506(11) |
| $\alpha$/° | 90 |
| $\beta$/° | 117.1228(11) |
| $\gamma$/° | 90 |
| Volume/Å$^3$ | 1477.00(2) |
| Z | 4 |
| $\varrho_{calc}$g/cm$^3$ | 1.301 |
| $\mu$/mm$^{-1}$ | 3.258 |
| F(000) | 608.0 |
| Crystal size/mm$^3$ | 0.2729 × 0.1987 × 0.1437 |
| Radiation | CuK$\alpha$ ($\lambda$ = 1.54184) |
| 2$\Theta$ range for data collection/° | 11.026 to 143.046 |
| Index ranges | $-13 \le h \le 13$, $-15 \le k \le 15$, $-14 \le l \le 14$ |
| Reflections collected | 35837 |
| Independent reflections | 2869 [$R_{int}$ = 0.0235, $R_{sigma}$ = 0.0087] |
| Data/restraints/parameters | 2869/1/152 |
| Goodness-of-fit on $F^2$ | 1.076 |
| Final R indexes [I>=2$\sigma$ (I)] | $R_1$ = 0.0183, $wR_2$ = 0.0469 |
| Final R indexes [all data] | $R_1$ = 0.0184, $wR_2$ = 0.0470 |
| Largest diff. peak/hole / e Å$^{-3}$ | 0.30/-0.27 |

Table 3.7.4. Crystal, intensity collection, and refinement data for **14**.

| | |
|---|---|
| Empirical formula | $C_{11}H_{22}N_2Se$ |
| Formula weight | 261.26 |
| Temperature/K | 99.9(4) |
| Crystal system | Orthorhombic |
| Space group | $Pna2_1$ |
| a/Å | 20.94407(19) |
| b/Å | 9.68682(10) |
| c/Å | 6.18700(6) |
| $\alpha$/° | 90 |
| $\beta$/° | 90 |
| $\gamma$/° | 90 |
| Volume/Å$^3$ | 1255.23(2) |
| Z | 4 |
| $\varrho_{calc}$g/cm$^3$ | 1.383 |
| $\mu$/mm$^{-1}$ | 3.776 |
| F(000) | 544.0 |
| Crystal size/mm$^3$ | 0.2869 × 0.0461 × 0.034 |
| Radiation | CuK$\alpha$ ($\lambda$ = 1.54184) |
| 2$\Theta$ range for data collection/° | 10.06 to 142.996 |
| Index ranges | $-24 \le h \le 25$, $-11 \le k \le 11$, $-7 \le l \le 7$ |
| Reflections collected | 28148 |
| Independent reflections | 2294 [$R_{int}$ = 0.0802, $R_{sigma}$ = 0.0342] |
| Data/restraints/parameters | 2294/2/133 |
| Goodness-of-fit on $F^2$ | 1.034 |
| Final R indexes [I>=2$\sigma$ (I)] | $R_1$ = 0.0394, $wR_2$ = 0.0990 |
| Final R indexes [all data] | $R_1$ = 0.0400, $wR_2$ = 0.1001 |
| Largest diff. peak/hole / e Å$^{-3}$ | 0.91/-0.50 |
| Flack parameter | -0.05(2) |

Table 3.7.5. Crystal, intensity collection, and refinement data for **15**.

| | |
|---|---|
| Empirical formula | $C_{12}H_{22}N_2Se$ |
| Formula weight | 273.27 |
| Temperature/K | 100.15 |
| Crystal system | Monoclinic |
| Space group | $P2_1/c$ |
| a/Å | 24.2552(5) |
| b/Å | 9.97679(19) |
| c/Å | 10.9577(2) |
| $\alpha$/° | 90 |
| $\beta$/° | 102.715(2) |
| $\gamma$/° | 90 |
| Volume/Å$^3$ | 2586.61(9) |
| Z | 8 |
| $\varrho_{calc}$g/cm$^3$ | 1.403 |
| $\mu$/mm$^{-1}$ | 3.693 |
| F(000) | 1136.0 |
| Crystal size/mm$^3$ | 0.1503 × 0.0846 × 0.0282 |
| Radiation | CuK$\alpha$ ($\lambda$ = 1.54184) |
| 2$\Theta$ range for data collection/° | 8.864 to 142.442 |
| Index ranges | $-29 \le h \le 29$, $-12 \le k \le 12$, $-13 \le l \le 13$ |
| Reflections collected | 53336 |
| Independent reflections | 5008 [$R_{int}$ = 0.0515, $R_{sigma}$ = 0.0262] |
| Data/restraints/parameters | 5008/2/278 |
| Goodness-of-fit on $F^2$ | 1.116 |
| Final R indexes [I>=2$\sigma$ (I)] | $R_1$ = 0.0329, $wR_2$ = 0.0842 |
| Final R indexes [all data] | $R_1$ = 0.0342, $wR_2$ = 0.0860 |
| Largest diff. peak/hole / e Å$^{-3}$ | 1.05/-1.05 |

Table 3.7.6. Crystal, intensity collection, and refinement data for **16**.

| | |
|---|---|
| Empirical formula | $C_{15}H_{30}N_2Se$ |
| Formula weight | 317.37 |
| Temperature/K | 130.03 |
| Crystal system | Orthorhombic |
| Space group | $Pna2_1$ |
| a/Å | 13.4556(14) |
| b/Å | 20.0405(6) |
| c/Å | 6.243(2) |
| $\alpha$/° | 90 |
| $\beta$/° | 90 |
| $\gamma$/° | 90 |
| Volume/Å$^3$ | 1683.5(6) |
| Z | 4 |
| $\varrho_{calc}$g/cm$^3$ | 1.252 |
| $\mu$/mm$^{-1}$ | 2.219 |
| F(000) | 672.0 |
| Crystal size/mm$^3$ | 1.17 × 0.73 × 0.56 |
| Radiation | MoK$\alpha$ ($\lambda$ = 0.71073) |
| 2$\Theta$ range for data collection/° | 3.646 to 61.06 |
| Index ranges | $-19 \le h \le 19$, $-28 \le k \le 28$, $-8 \le l \le 8$ |
| Reflections collected | 26325 |
| Independent reflections | 5113 [$R_{int}$ = 0.0447, $R_{sigma}$ = 0.0396] |
| Data/restraints/parameters | 5113/6/198 |
| Goodness-of-fit on $F^2$ | 1.025 |
| Final R indexes [I>=2$\sigma$ (I)] | $R_1$ = 0.0301, $wR_2$ = 0.0672 |
| Final R indexes [all data] | $R_1$ = 0.0389, $wR_2$ = 0.0697 |
| Largest diff. peak/hole / e Å$^{-3}$ | 0.93/-0.39 |
| Flack parameter | 0.022(5) |

Table 3.7.7. Crystal, intensity collection, and refinement data for **17**.

| | |
|---|---|
| Empirical formula | $C_{11}H_{22}N_2Se$ |
| Formula weight | 261.26 |
| Temperature/K | 100.0 |
| Crystal system | Orthorhombic |
| Space group | $Pca2_1$ |
| a/Å | 11.9340(3) |
| b/Å | 9.8566(3) |
| c/Å | 11.2837(3) |
| $\alpha$/° | 90 |
| $\beta$/° | 90 |
| $\gamma$/° | 90 |
| Volume/Å$^3$ | 1327.29(7) |
| Z | 4 |
| $\varrho_{calc}$g/cm$^3$ | 1.307 |
| $\mu$/mm$^{-1}$ | 2.800 |
| F(000) | 544.0 |
| Crystal size/mm$^3$ | 0.4621 × 0.0808 × 0.0356 |
| Radiation | MoK$\alpha$ ($\lambda$ = 0.71073) |
| 2$\Theta$ range for data collection/° | 6.828 to 59.048 |
| Index ranges | $-15 \le h \le 16$, $-13 \le k \le 13$, $-14 \le l \le 15$ |
| Reflections collected | 24645 |
| Independent reflections | 3424 [$R_{int}$ = 0.0689, $R_{sigma}$ = 0.0486] |
| Data/restraints/parameters | 3424/2/132 |
| Goodness-of-fit on $F^2$ | 1.080 |
| Final R indexes [I>=2$\sigma$ (I)] | $R_1$ = 0.0344, $wR_2$ = 0.0583 |
| Final R indexes [all data] | $R_1$ = 0.0457, $wR_2$ = 0.0616 |
| Largest diff. peak/hole / e Å$^{-3}$ | 0.36/-0.43 |
| Flack parameter | 0.011(9) |

Table 3.7.8. Crystal, intensity collection, and refinement data for **18**.

| | |
|---|---|
| Empirical formula | $C_{10}H_{20}N_2Se$ |
| Formula weight | 247.24 |
| Temperature/K | 100.0(4) |
| Crystal system | Orthorhombic |
| Space group | Pbca |
| a/Å | 11.42330(9) |
| b/Å | 10.80265(8) |
| c/Å | 18.95402(15) |
| $\alpha$/° | 90 |
| $\beta$/° | 90 |
| $\gamma$/° | 90 |
| Volume/Å$^3$ | 2338.96(3) |
| Z | 8 |
| $\varrho_{calc}$g/cm$^3$ | 1.404 |
| $\mu$/mm$^{-1}$ | 4.022 |
| F(000) | 1024.0 |
| Crystal size/mm$^3$ | 0.0966 × 0.0703 × 0.0291 |
| Radiation | CuK$\alpha$ ($\lambda$ = 1.54184) |
| 2$\Theta$ range for data collection/° | 9.332 to 143.692 |
| Index ranges | $-13 \le h \le 14$, $-13 \le k \le 13$, $-23 \le l \le 23$ |
| Reflections collected | 68521 |
| Independent reflections | 2282 [$R_{int}$ = 0.0692, $R_{sigma}$ = 0.0168] |
| Data/restraints/parameters | 2282/1/123 |
| Goodness-of-fit on F$^2$ | 1.079 |
| Final R indexes [I>=2$\sigma$ (I)] | $R_1$ = 0.0377, w$R_2$ = 0.1017 |
| Final R indexes [all data] | $R_1$ = 0.0395, w$R_2$ = 0.1040 |
| Largest diff. peak/hole / e Å$^{-3}$ | 0.60/-0.39 |

Table 3.7.9. Crystal, intensity collection, and refinement data for **19**.

| | |
|---|---|
| Empirical formula | $C_{12}H_{22}N_2Se$ |
| Formula weight | 273.27 |
| Temperature/K | 99.9(4) |
| Crystal system | Monoclinic |
| Space group | $P2_1/c$ |
| a/Å | 11.94130(17) |
| b/Å | 10.41973(13) |
| c/Å | 10.4300(2) |
| $\alpha$/° | 90 |
| $\beta$/° | 98.2799(17) |
| $\gamma$/° | 90 |
| Volume/Å$^3$ | 1284.22(4) |
| Z | 4 |
| $\varrho_{calc}$g/cm$^3$ | 1.413 |
| $\mu$/mm$^{-1}$ | 3.719 |
| F(000) | 568.0 |
| Crystal size/mm$^3$ | 0.237 × 0.0637 × 0.0299 |
| Radiation | CuK$\alpha$ ($\lambda$ = 1.54184) |
| 2$\Theta$ range for data collection/° | 11.322 to 145.034 |
| Index ranges | $-14 \le h \le 14$, $-12 \le k \le 12$, $-12 \le l \le 12$ |
| Reflections collected | 4704 |
| Independent reflections | 4704 [$R_{int}$ = ?, $R_{sigma}$ = 0.0216] |
| Data/restraints/parameters | 4704/1/141 |
| Goodness-of-fit on $F^2$ | 1.028 |
| Final R indexes [I>=2$\sigma$ (I)] | $R_1$ = 0.0506, $wR_2$ = 0.1294 |
| Final R indexes [all data] | $R_1$ = 0.0559, $wR_2$ = 0.1348 |
| Largest diff. peak/hole / e Å$^{-3}$ | 1.61/-0.57 |

Table 3.7.10. Crystal, intensity collection, and refinement data for **20**.

| | |
|---|---|
| Empirical formula | $C_{16}H_{22}N_2Se$ |
| Formula weight | 321.31 |
| Temperature/K | 99.9(4) |
| Crystal system | Monoclinic |
| Space group | $P2_1/n$ |
| a/Å | 14.2487(5) |
| b/Å | 6.03760(15) |
| c/Å | 17.5143(5) |
| $\alpha$/° | 90 |
| $\beta$/° | 95.262(3) |
| $\gamma$/° | 90 |
| Volume/Å$^3$ | 1500.37(8) |
| Z | 4 |
| $\varrho_{calc}$g/cm$^3$ | 1.422 |
| $\mu$/mm$^{-1}$ | 3.279 |
| F(000) | 664.0 |
| Crystal size/mm$^3$ | 0.079 × 0.0371 × 0.0307 |
| Radiation | CuK$\alpha$ ($\lambda$ = 1.54184) |
| 2$\Theta$ range for data collection/° | 8.386 to 144.88 |
| Index ranges | $-17 \le h \le 17$, $-6 \le k \le 7$, $-21 \le l \le 21$ |
| Reflections collected | 33648 |
| Independent reflections | 2938 [$R_{int}$ = 0.1010, $R_{sigma}$ = 0.0418] |
| Data/restraints/parameters | 2938/1/175 |
| Goodness-of-fit on $F^2$ | 1.090 |
| Final R indexes [I>=2$\sigma$ (I)] | $R_1$ = 0.0475, $wR_2$ = 0.1264 |
| Final R indexes [all data] | $R_1$ = 0.0530, $wR_2$ = 0.1308 |
| Largest diff. peak/hole / e Å$^{-3}$ | 1.20/-0.65 |

Table 3.7.11. Crystal, intensity collection, and refinement data for **21**.

| | |
|---|---|
| Empirical formula | $C_{13}H_{22}N_2Se$ |
| Formula weight | 285.28 |
| Temperature/K | 100.0(3) |
| Crystal system | Orthorhombic |
| Space group | $Pna2_1$ |
| a/Å | 10.16777(7) |
| b/Å | 13.46789(10) |
| c/Å | 10.18040(10) |
| $\alpha$/° | 90 |
| $\beta$/° | 90 |
| $\gamma$/° | 90 |
| Volume/Å$^3$ | 1394.09(2) |
| Z | 4 |
| $\varrho_{calc}$g/cm$^3$ | 1.359 |
| $\mu$/mm$^{-1}$ | 3.451 |
| F(000) | 592.0 |
| Crystal size/mm$^3$ | 0.251 × 0.1042 × 0.0917 |
| Radiation | CuK$\alpha$ ($\lambda$ = 1.54184) |
| 2$\Theta$ range for data collection/° | 10.894 to 143.278 |
| Index ranges | $-12 \le h \le 12$, $-16 \le k \le 16$, $-11 \le l \le 12$ |
| Reflections collected | 39550 |
| Independent reflections | 2539 [$R_{int}$ = 0.0503, $R_{sigma}$ = 0.0160] |
| Data/restraints/parameters | 2539/2/164 |
| Goodness-of-fit on $F^2$ | 1.088 |
| Final R indexes [I>=2$\sigma$ (I)] | $R_1$ = 0.0299, $wR_2$ = 0.0804 |
| Final R indexes [all data] | $R_1$ = 0.0300, $wR_2$ = 0.0805 |
| Largest diff. peak/hole / e Å$^{-3}$ | 0.43/-0.35 |
| Flack parameter | -0.039(12) |

Table 3.7.12. Crystal, intensity collection, and refinement data for **22**.

| | |
|---|---|
| Empirical formula | $C_9H_{18}N_2Se$ |
| Formula weight | 233.21 |
| Temperature/K | 100.0 |
| Crystal system | Monoclinic |
| Space group | $P2_1/c$ |
| a/Å | 10.58561(17) |
| b/Å | 10.51744(17) |
| c/Å | 9.66073(16) |
| $\alpha$/° | 90 |
| $\beta$/° | 96.1599(15) |
| $\gamma$/° | 90 |
| Volume/Å$^3$ | 1069.35(3) |
| Z | 4 |
| $\varrho_{calc}$g/cm$^3$ | 1.449 |
| $\mu$/mm$^{-1}$ | 3.465 |
| F(000) | 480.0 |
| Crystal size/mm$^3$ | 0.2505 × 0.1828 × 0.0791 |
| Radiation | MoK$\alpha$ ($\lambda$ = 0.71073) |
| 2$\Theta$ range for data collection/° | 6.668 to 59.248 |
| Index ranges | $-14 \le h \le 14$, $-14 \le k \le 14$, $-13 \le l \le 13$ |
| Reflections collected | 29160 |
| Independent reflections | 2832 [$R_{int}$ = 0.0429, $R_{sigma}$ = 0.0246] |
| Data/restraints/parameters | 2832/1/114 |
| Goodness-of-fit on $F^2$ | 1.068 |
| Final R indexes [I>=2$\sigma$ (I)] | $R_1$ = 0.0238, $wR_2$ = 0.0489 |
| Final R indexes [all data] | $R_1$ = 0.0291, $wR_2$ = 0.0507 |
| Largest diff. peak/hole / e Å$^{-3}$ | 0.40/-0.28 |

Table 3.7.13. Crystal, intensity collection, and refinement data for **23**.

| | |
|---|---|
| Empirical formula | $C_{11}H_{20}N_2Se$ |
| Formula weight | 259.25 |
| Temperature/K | 100.15 |
| Crystal system | Orthorhombic |
| Space group | Pbca |
| a/Å | 9.1761(3) |
| b/Å | 10.9659(3) |
| c/Å | 23.4534(8) |
| $\alpha$/° | 90 |
| $\beta$/° | 90 |
| $\gamma$/° | 90 |
| Volume/Å$^3$ | 2359.98(13) |
| Z | 8 |
| $\varrho_{calc}$g/cm$^3$ | 1.459 |
| $\mu$/mm$^{-1}$ | 3.149 |
| F(000) | 1072.0 |
| Crystal size/mm$^3$ | 0.1543 × 0.0611 × 0.0247 |
| Radiation | MoK$\alpha$ ($\lambda$ = 0.71073) |
| 2$\Theta$ range for data collection/° | 6.752 to 59.322 |
| Index ranges | $-12 \le h \le 12$, $-14 \le k \le 14$, $-32 \le l \le 32$ |
| Reflections collected | 33357 |
| Independent reflections | 3139 [$R_{int}$ = 0.0628, $R_{sigma}$ = 0.0397] |
| Data/restraints/parameters | 3139/1/130 |
| Goodness-of-fit on F$^2$ | 1.139 |
| Final R indexes [I>=2$\sigma$ (I)] | $R_1$ = 0.0399, w$R_2$ = 0.0589 |
| Final R indexes [all data] | $R_1$ = 0.0555, w$R_2$ = 0.0620 |
| Largest diff. peak/hole / e Å$^{-3}$ | 0.35/-0.59 |

Table 3.7.14. Crystal, intensity collection, and refinement data for **30**.

| | |
|---|---|
| Empirical formula | $C_7H_{16}N_2Se$ |
| Formula weight | 207.18 |
| Temperature/K | 100.0 |
| Crystal system | Monoclinic |
| Space group | $P2_1/n$ |
| a/Å | 6.22247(10) |
| b/Å | 10.03939(18) |
| c/Å | 15.0636(2) |
| $\alpha$/° | 90 |
| $\beta$/° | 100.3451(15) |
| $\gamma$/° | 90 |
| Volume/Å$^3$ | 925.72(3) |
| Z | 4 |
| $\varrho_{calc}$g/cm$^3$ | 1.487 |
| $\mu$/mm$^{-1}$ | 3.992 |
| F(000) | 424.0 |
| Crystal size/mm$^3$ | 0.4309 × 0.1552 × 0.0811 |
| Radiation | MoK$\alpha$ ($\lambda$ = 0.71073) |
| 2$\Theta$ range for data collection/° | 6.73 to 59.414 |
| Index ranges | -8 ≤ h ≤ 8, -14 ≤ k ≤ 13, -20 ≤ l ≤ 20 |
| Reflections collected | 25414 |
| Independent reflections | 2445 [$R_{int}$ = 0.0391, $R_{sigma}$ = 0.0205] |
| Data/restraints/parameters | 2445/1/99 |
| Goodness-of-fit on $F^2$ | 1.062 |
| Final R indexes [I>=2$\sigma$ (I)] | $R_1$ = 0.0216, w$R_2$ = 0.0451 |
| Final R indexes [all data] | $R_1$ = 0.0262, w$R_2$ = 0.0465 |
| Largest diff. peak/hole / e Å$^{-3}$ | 0.37/-0.36 |

Table 3.7.15. Crystal, intensity collection, and refinement data for **31**.

| | |
|---|---|
| Empirical formula | $C_9H_{18}N_2Se$ |
| Formula weight | 233.21 |
| Temperature/K | 100.15 |
| Crystal system | Monoclinic |
| Space group | $P2_1/n$ |
| a/Å | 6.2032(2) |
| b/Å | 9.9913(5) |
| c/Å | 17.2951(7) |
| $\alpha$/° | 90 |
| $\beta$/° | 92.004(4) |
| $\gamma$/° | 90 |
| Volume/Å$^3$ | 1071.26(8) |
| Z | 4 |
| $\varrho_{calc}$g/cm$^3$ | 1.446 |
| $\mu$/mm$^{-1}$ | 3.459 |
| F(000) | 480.0 |
| Crystal size/mm$^3$ | 0.0858 × 0.0475 × 0.0268 |
| Radiation | MoK$\alpha$ ($\lambda$ = 0.71073) |
| 2$\Theta$ range for data collection/° | 6.904 to 59.182 |
| Index ranges | $-7 \le h \le 8$, $-13 \le k \le 10$, $-23 \le l \le 21$ |
| Reflections collected | 11134 |
| Independent reflections | 2661 [$R_{int}$ = 0.0434, $R_{sigma}$ = 0.0444] |
| Data/restraints/parameters | 2661/1/115 |
| Goodness-of-fit on $F^2$ | 1.076 |
| Final R indexes [I>=2$\sigma$ (I)] | $R_1$ = 0.0350, $wR_2$ = 0.0602 |
| Final R indexes [all data] | $R_1$ = 0.0474, $wR_2$ = 0.0639 |
| Largest diff. peak/hole / e Å$^{-3}$ | 0.56/-0.34 |

Table 3.7.16. Crystal, intensity collection, and refinement data for N,N,N′,N′-tetramethylselenourea.

| | |
|---|---|
| Empirical formula | $C_5H_{12}N_2Se$ |
| Formula weight | 179.13 |
| Temperature/K | 200.00(10) |
| Crystal system | Monoclinic |
| Space group | C2/c |
| a/Å | 5.4557(2) |
| b/Å | 12.6064(3) |
| c/Å | 11.1113(3) |
| $\alpha$/° | 90 |
| $\beta$/° | 94.681(3) |
| $\gamma$/° | 90 |
| Volume/Å$^3$ | 761.65(4) |
| Z | 4 |
| $\varrho_{calc}$g/cm$^3$ | 1.562 |
| $\mu$/mm$^{-1}$ | 5.936 |
| F(000) | 360.0 |
| Crystal size/mm$^3$ | 0.1039 × 0.0736 × 0.0475 |
| Radiation | CuK$\alpha$ ($\lambda$ = 1.54184) |
| 2$\Theta$ range for data collection/° | 14.05 to 143.12 |
| Index ranges | $-6 \le h \le 6$, $-15 \le k \le 15$, $-13 \le l \le 13$ |
| Reflections collected | 9238 |
| Independent reflections | 748 [$R_{int}$ = 0.0540, $R_{sigma}$ = 0.0192] |
| Data/restraints/parameters | 748/0/40 |
| Goodness-of-fit on $F^2$ | 1.086 |
| Final R indexes [I>=2$\sigma$ (I)] | $R_1$ = 0.0423, $wR_2$ = 0.1099 |
| Final R indexes [all data] | $R_1$ = 0.0432, $wR_2$ = 0.1112 |
| Largest diff. peak/hole / e Å$^{-3}$ | 0.73/-0.34 |

### 3.8. References


(1) Nozik, A. J. *Phys. E Low-Dimens. Syst. Nanostructures* **2002**, *14* (1), 115.
(2) Carey, G. H.; Abdelhady, A. L.; Ning, Z.; Thon, S. M.; Bakr, O. M.; Sargent, E. H. *Chem. Rev.* **2015**, *115* (23), 12732.
(3) Semonin, O. E.; Luther, J. M.; Choi, S.; Chen, H.-Y.; Gao, J.; Nozik, A. J.; Beard, M. C. *Science* **2011**, *334* (6062), 1530.
(4) Boneschanscher, M. P.; Evers, W. H.; Geuchies, J. J.; Altantzis, T.; Goris, B.; Rabouw, F. T.; Rossum, S. A. P. van; Zant, H. S. J. van der; Siebbeles, L. D. A.; Tendeloo, G. V.; Swart, I.; Hilhorst, J.; Petukhov, A. V.; Bals, S.; Vanmaekelbergh, D. *Science* **2014**, *344* (6190), 1377.
(5) Evers, W. H.; Schins, J. M.; Aerts, M.; Kulkarni, A.; Capiod, P.; Berthe, M.; Grandidier, B.; Delerue, C.; van der Zant, H. S. J.; van Overbeek, C.; Peters, J. L.; Vanmaekelbergh, D.; Siebbeles, L. D. A. *Nat. Commun.* **2015**, *6*, 8195.
(6) Kalesaki, E.; Delerue, C.; Morais Smith, C.; Beugeling, W.; Allan, G.; Vanmaekelbergh, D. *Phys. Rev. X* **2014**, *4* (1).
(7) Delerue, C. *Nat. Mater.* **2016**, *15* (5), 498.
(8) Moreels, I.; Lambert, K.; De Muynck, D.; Vanhaecke, F.; Poelman, D.; Martins, J. C.; Allan, G.; Hens, Z. *Chem. Mater.* **2007**, *19* (25), 6101.
(9) Steckel, J. S.; Yen, B. K. H.; Oertel, D. C.; Bawendi, M. G. *J. Am. Chem. Soc.* **2006**, *128* (40), 13032.
(10) Evans, C. M.; Evans, M. E.; Krauss, T. D. *J. Am. Chem. Soc.* **2010**, *132* (32), 10973.
(11) Zhang, J.; Gao, J.; Miller, E. M.; Luther, J. M.; Beard, M. C. *ACS Nano* **2014**, *8* (1), 614.
(12) Joo, J.; Pietryga, J. M.; McGuire, J. A.; Jeon, S.-H.; Williams, D. J.; Wang, H.-L.; Klimov, V. I. *J. Am. Chem. Soc.* **2009**, *131* (30), 10620.
(13) Hendricks, M. P.; Campos, M. P.; Cleveland, G. T.; Plante, I. J.-L.; Owen, J. S. *Science* **2015**, *348* (6240), 1226.
(14) Sugimoto, T. *J. Colloid Interface Sci.* **1992**, *150* (1), 208.
(15) Sugimoto, T.; Shiba, F.; Sekiguchi, T.; Itoh, H. *Colloids Surf. Physicochem. Eng. Asp.* **2000**, *164* (2), 183.
(16) Sugimoto, T.; Shiba, F. *Colloids Surf. Physicochem. Eng. Asp.* **2000**, *164* (2), 205.
(17) Owen, J. S.; Chan, E. M.; Liu, H.; Alivisatos, A. P. *J. Am. Chem. Soc.* **2010**, *132* (51), 18206.
(18) Abe, S.; Čapek, R. K.; De Geyter, B.; Hens, Z. *ACS Nano* **2012**, *6* (1), 42.
(19) Kuhn, N.; Verani, G. In *Handbook of Chalcogen Chemistry*; Royal Society of Chemistry: Cambridge, 2007; pp 107–144.
(20) Lipp, M.; Dallacker, F.; Köcker, I. M. zu. *Monatshefte Für Chem. Verwandte Teile Anderer Wiss.* **1959**, *90* (1), 41.

(21) Sonoda, N.; Yamamoto, G.; Tsutsumi, S. *Bull. Chem. Soc. Jpn.* **1972**, *45* (9), 2937.
(22) Blum, T.; Ermert, J.; Coenen, H. H. *J. Label. Compd. Radiopharm.* **2001**, *44* (S1), S140.
(23) Mamedov, V. A.; Zhukova, N. A.; Gubaidullin, A. T.; Beschastnova, T. N.; Rizvanov, I. K.; Levin, Y. A.; Litvinov, I. A. *Russ. Chem. Bull.* **2009**, *58* (6), 1294.
(24) Palmer, J. H.; Parkin, G. *Polyhedron* **2013**, *52*, 658.
(25) Zakrzewski, J.; Huras, B.; Kie\lczewska, A. *Synthesis* **2016**, *48* (1), 85.
(26) *The Chemistry of organic selenium and tellurium compounds*; Patai, S., Rappoport, Z., Eds.; The Chemistry of functional groups; Wiley: Chichester [Sussex] ; New York, 1986.
(27) Landry, V. K.; Minoura, M.; Pang, K.; Buccella, D.; Kelly, B. V.; Parkin, G. *J. Am. Chem. Soc.* **2006**, *128* (38), 12490.
(28) Anderson, N. C.; Hendricks, M. P.; Choi, J. J.; Owen, J. S. *J. Am. Chem. Soc.* **2013**, *135* (49), 18536.
(29) Murray, C. B.; Sun, S.; Gaschler, W.; Doyle, H.; Betley, T. A.; Kagan, C. R. *IBM J. Res. Dev.* **2001**, *45* (1), 47.
(30) Yu, W. W.; Falkner, J. C.; Shih, B. S.; Colvin, V. L. *Chem. Mater.* **2004**, *16* (17), 3318.
(31) Kovalenko, M. V.; Talapin, D. V.; Loi, M. A.; Cordella, F.; Hesser, G.; Bodnarchuk, M. I.; Heiss, W. *Angew. Chem. Int. Ed.* **2008**, *47* (16), 3029.
(32) Dai, Q.; Wang, Y.; Li, X.; Zhang, Y.; Pellegrino, D. J.; Zhao, M.; Zou, B.; Seo, J.; Wang, Y.; Yu, W. W. *ACS Nano* **2009**, *3* (6), 1518.
(33) Ma, W.; Swisher, S. L.; Ewers, T.; Engel, J.; Ferry, V. E.; Atwater, H. A.; Alivisatos, A. P. *ACS Nano* **2011**, *5* (10), 8140.
(34) Choi, J. J.; Lim, Y.-F.; Santiago-Berrios, M. B.; Oh, M.; Hyun, B.-R.; Sun, L.; Bartnik, A. C.; Goedhart, A.; Malliaras, G. G.; Abruña, H. D.; Wise, F. W.; Hanrath, T. *Nano Lett.* **2009**, *9* (11), 3749.
(35) Evans, C. M.; Guo, L.; Peterson, J. J.; Maccagnano-Zacher, S.; Krauss, T. D. *Nano Lett.* **2008**, *8* (9), 2896.
(36) Hendricks, M. P.; Cossairt, B. M.; Owen, J. S. *ACS Nano* **2012**, *6* (11), 10054.
(37) Campos, M. P.; Owen, J. S. *Chem. Mater.* **2016**, *28* (1), 227.
(38) Rodrigues, M. O.; Cantos, J. B.; D'Oca, C. R. M.; Soares, K. L.; Coelho, T. S.; Piovesan, L. A.; Russowsky, D.; da Silva, P. A.; D'Oca, M. G. M. *Bioorg. Med. Chem.* **2013**, *21* (22), 6910.
(39) Ghosh, H.; Sarkar, S.; Ali, A. R.; Patel, B. K. *J. Sulfur Chem.* **2010**, *31* (1), 1.
(40) Busby, E.; Anderson, N. C.; Owen, J. S.; Sfeir, M. Y. *J. Phys. Chem. C* **2015**, *119* (49), 27797.
(41) Peng, X.; Wickham, J.; Alivisatos, A. P. *J. Am. Chem. Soc.* **1998**, *120* (21), 5343.

(42) Weidman, M. C.; Beck, M. E.; Hoffman, R. S.; Prins, F.; Tisdale, W. A. *ACS Nano* **2014**, *8* (6), 6363.
(43) Cui, J.; Beyler, A. P.; Marshall, L. F.; Chen, O.; Harris, D. K.; Wanger, D. D.; Brokmann, X.; Bawendi, M. G. *Nat. Chem.* **2013**, *5* (7), 602.
(44) Cui, J.; Beyler, A. P.; Coropceanu, I.; Cleary, L.; Avila, T. R.; Chen, Y.; Cordero, J. M.; Heathcote, S. L.; Harris, D. K.; Chen, O.; Cao, J.; Bawendi, M. G. *Nano Lett.* **2016**, *16* (1), 289.
(45) Chen, O.; Zhao, J.; Chauhan, V. P.; Cui, J.; Wong, C.; Harris, D. K.; Wei, H.; Han, H.-S.; Fukumura, D.; Jain, R. K.; Bawendi, M. G. *Nat. Mater.* **2013**, *12* (5), 445.
(46) Mittleman, D. M.; Schoenlein, R. W.; Shiang, J. J.; Colvin, V. L.; Alivisatos, A. P.; Shank, C. V. *Phys. Rev. B* **1994**, *49* (20), 14435.
(47) Peterson, J. J.; Krauss, T. D. *Nano Lett.* **2006**, *6* (3), 510.
(48) Zhou, J.; Pu, C.; Jiao, T.; Hou, X.; Peng, X. *J. Am. Chem. Soc.* **2016**, *138* (20), 6475.
(49) Beecher, A. N.; Yang, X.; Palmer, J. H.; LaGrassa, A. L.; Juhas, P.; Billinge, S. J. L.; Owen, J. S. *J. Am. Chem. Soc.* **2014**, *136* (30), 10645.
(50) Norris, D. J.; Sacra, A.; Murray, C. B.; Bawendi, M. G. *Phys. Rev. Lett.* **1994**, *72* (16), 2612.
(51) Park, S. D.; Baranov, D.; Ryu, J.; Cho, B.; Halder, A.; Seifert, S.; Vajda, S.; Jonas, D. M. *Nano Lett.* **2017**, *17* (2), 762.
(52) Caram, J. R.; Bertram, S. N.; Utzat, H.; Hess, W. R.; Carr, J. A.; Bischof, T. S.; Beyler, A. P.; Wilson, M. W. B.; Bawendi, M. G. *Nano Lett.* **2016**, *16* (10), 6070.
(53) Grodzińska, D.; Evers, W. H.; Dorland, R.; van Rijssel, J.; van Huis, M. A.; Meijerink, A.; de Mello Donegá, C.; Vanmaekelbergh, D. *Small* **2011**, *7* (24), 3493.
(54) Allan, G.; Delerue, C. *Phys. Rev. B* **2004**, *70* (24).
(55) An, J. M.; Franceschetti, A.; Zunger, A. *Nano Lett.* **2007**, *7* (7), 2129.
(56) Franceschetti, A. *Phys. Rev. B* **2008**, *78* (7).
(57) Kelley, A. M. *J. Phys. Chem. Lett.* **2010**, *1* (9), 1296.
(58) Kelley, A. M. *ACS Nano* **2011**, *5* (6), 5254.
(59) Lin, C.; Gong, K.; Kelley, D. F.; Kelley, A. M. *J. Phys. Chem. C* **2015**, *119* (13), 7491.
(60) Salvador, M. R.; Graham, M. W.; Scholes, G. D. *J. Chem. Phys.* **2006**, *125* (18), 184709.
(61) Sagar, D. M.; Cooney, R. R.; Sewall, S. L.; Dias, E. A.; Barsan, M. M.; Butler, I. S.; Kambhampati, P. *Phys. Rev. B* **2008**, *77* (23).
(62) Bullen, C. R.; Mulvaney, P. *Nano Lett.* **2004**, *4* (12), 2303.
(63) Clark, M. D.; Kumar, S. K.; Owen, J. S.; Chan, E. M. *Nano Lett.* **2011**, *11* (5), 1976.

(64) Hoertz, P. G.; Niskala, J. R.; Dai, P.; Black, H. T.; You, W. *J. Am. Chem. Soc.* **2008**, *130* (30), 9763.
(65) Kantlehner, W.; Hauber, M.; Vettel, M. *Adv. Synth. Catal.* **1996**, *338* (1), 403.
(66) Hu, Y. Z.; Koch, S. W.; Lindberg, M.; Peyghambarian, N.; Pollock, E. L.; Abraham, F. F. *Phys. Rev. Lett.* **1990**, *64* (15), 1805.
(67) Klimov, V.; Hunsche, S.; Kurz, H. *Phys. Rev. B* **1994**, *50* (11), 8110.

# CHAPTER 4. Understanding the Nucleation and Growth of II-VI, IV-VI, and Graded Alloy Nanocrystals

## Table of Contents




Some of the experiments described herein were performed by B. Abécassis, S. Jana, N. Castro, C. Goldman, J. De Roo, I. Rreza, and L. S. Hamachi. Their collaboration in this endeavor is gratefully acknowledged.

## 4.1. Abstract

This chapter discusses my major ongoing projects at the time of this writing, which break down into two categories: 1) nucleation and growth studies, and 2) red-emitting nanocrystals for solid-state lighting. Our nucleation and growth studies take advantage of the modularity of thio- and selenourea-based reactions to carefully isolate parameters like temperature, reaction rate, and S vs. Se. In this process, we have developed a toolbox for these studies, including dip probe measurements (discussed in Chapters 2 and 3), small-angle X-ray scattering (SAXS), and high-throughput infrared photoluminescence spectroscopy. Our red-emitting nanocrystal studies have involved broader surveys of reaction conditions to achieve large, graded alloy structures that are only attainable through thio-/selenourea mixtures. After honing in on CdS/CdSe/CdS "spherical quantum well" structures, we rapidly developed highly fluorescent materials and tested them under accelerated aging conditions.

## 4.2. Nucleation and Growth Studies

### *4.2.1. Theoretical Framework*

The studies discussed in this section draw upon the theoretical frameworks discussed in Chapter 2. In this section, we will focus on the early

time points in nanocrystal synthesis reactions, in which the dynamics of solute can be described by Figure 4.2.1:

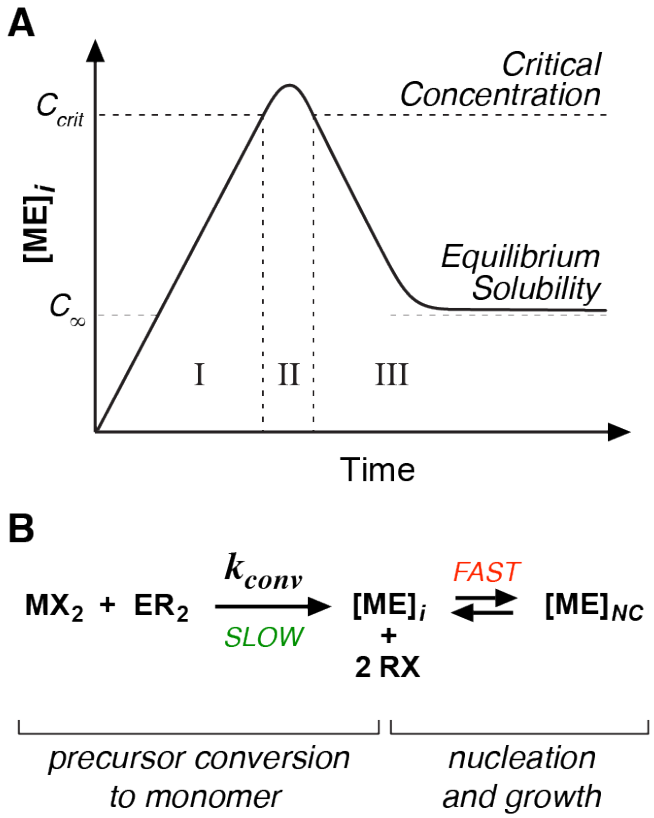


Figure 4.2.1. A) The three stages of the La Mer model, I: solute accumulation, II: nucleation, and III: solute consumption. B) Reaction scheme showing the formation of solute by precursor conversion and consumption of solute by nucleation and growth. This figure also appears in Chapter 2.

To get a bit more granular, Sugimoto proposed the following mass balance equation to describe solute flux during nucleation:[1,2]

$$Q_0 V_M = v_0 \frac{dn}{dt} + \dot{v} n$$

Equation 4.2.1

Where:

- $Q_0$ is the solute production rate (mol $sec^{-1}$)
- $V_M$ is the molar volume of the solid ($nm^3$ $mol^{-1}$)
- $v_0$ is the volume of the initial stable nucleus ($nm^3$)
- $\frac{dn}{dt}$ is the nucleation rate ($sec^{-1}$)
- $\dot{v}$ is the per-particle nucleus growth rate ($nm^3$ $sec^{-1}$)
- $n$ is the number of nuclei (unitless)

$Q_0 V_m$ represents solute formation; $v_0 \frac{dn}{dt}$ represents solute consumption by nucleation; $\dot{v}n$ represents solute consumption by growth. In other words, any incremental solute must be consumed by nucleation of new nuclei or consumption by existing nuclei.

After nucleation, the $v_0 \frac{dn}{dt}$ term goes to zero and the equation can be rewritten as:

$$n = \frac{Q_0 V_M}{\dot{v}}$$

Equation 4.2.2

from which it is clear that the number of nanocrystals increases as precursor conversion rate increases and as per-particle growth rate decreases.

By in situ and ex situ UV-vis-NIR spectroscopic methods discussed in Chapters 2 and 3, we are able to measure $n$, estimate $Q_0$ from $k_{obs}$, and infer $\dot{\nu}$. A schematic describing how these values are extracted is shown in Figure 4.2.2.

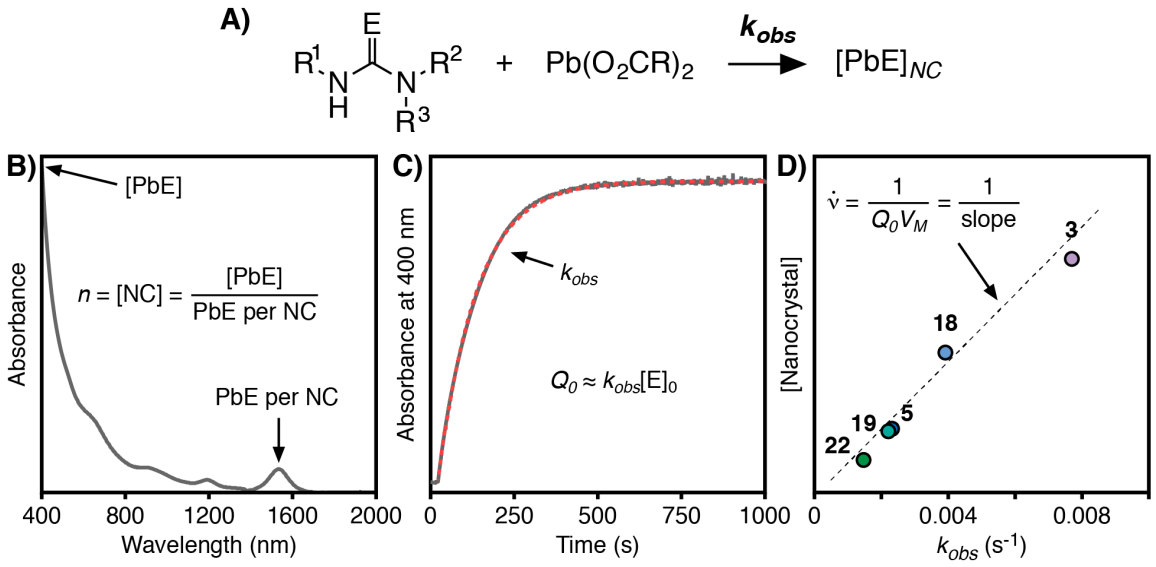


Figure 4.2.2. A) Reaction between thio-/selenoureas and lead(II) carboxylate. B) Example UV-vis-NIR spectrum, from which [PbE] is proportional to the absorbance at 400 nm and the number of PbE formula units per nanocrystal (PbE per NC) is related to the peak position of the lowest energy electronic transition. By dividing [PbE] by PbE per NC, the nanocrystal concentration ($n$, [NC]) is obtained. C) Example trace of absorbance at 400 nm versus time obtained by in situ measurement using a fiber optic dip probe. The curve is fit to a single exponential function, from which $k_{obs}$ is extracted. $k_{obs}$ times the thio-/selenourea concentration is assumed to be equal to the solute production rate $Q_0$. C) Plot of [nanocrystal] versus $k_{obs}$ fit to a linear function. The inverse of the slope is

proportional to the per-particle growth rate during nucleation as laid out by Sugimoto.

These data, particularly the latter two, are powerful. Measuring $k_{obs}$ enables detailed synthetic and mechanistic studies correlating molecular structure with reactivity and nanomaterial properties. Estimating $\dot{v}$ across a variety of conditions will lead us to fundamental material insights, such as the temperature, concentration, and material dependence of nanocrystal growth rates.

However, these studies offer no insight into the nucleation term of Sugimoto's mass balance equation, since the critical nucleus ($v_0$) is likely too small and transient to directly measure and nucleation rates ($\frac{dn}{dt}$) are assumed to be rapid. In the following sections, we will introduce methods to study these processes more directly in colloidal PbS, PbSe, CdS, and CdSe crystallizations.

*4.2.2. Induction Period Measurement*

All dip probe traces shown up to this point have taken a wide view, focusing on the gradual increase in [PbE] over time in order to extract $k_{obs}$ rate constants. However, these traces offer a much richer dataset than just $k_{obs}$. By carefully studying the early times in PbS and PbSe synthesis, we reliably observe two additional phenomena (Figure 4.2.3): 1) a rapid fluctuation in absorbance coincident with precursor injection, which we attribute to a brief inhomogeneity

in the reaction mixture's index of refraction that is quickly resolved, and 2) an induction period with low absorbance prior to the rapid onset of absorbance due to the formation of crystalline PbE formula units ($\varepsilon_{400nm,\ PbS\ unit}$ = 2320 $cm^{-1}$ $M^{-1}$; $\varepsilon_{400nm,\ PbSe\ unit}$ = 3090 $cm^{-1}$ $M^{-1}$; precursors have negligible absorbance at 400 nm).[3,4]

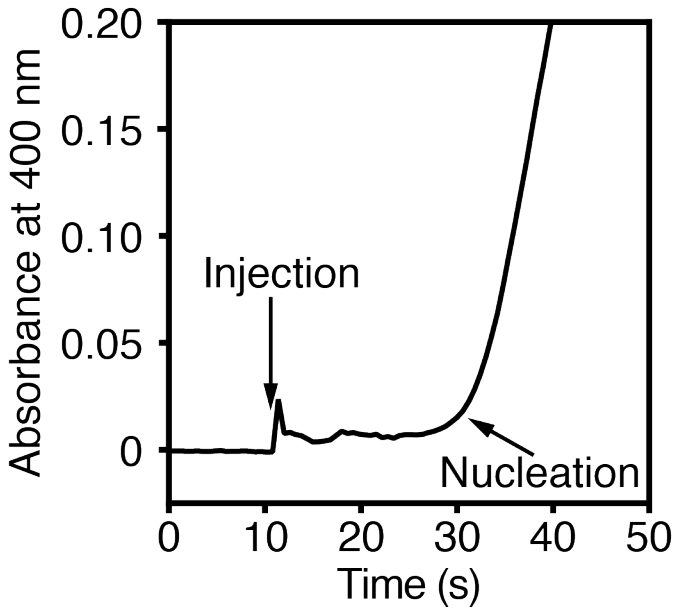


Figure 4.2.3. Example plot showing the early times of a PbS nanocrystal synthesis reaction monitored using a fiber-optic dip probe. The time of injection is reliably marked by the beginning of a rapid fluctuation in absorbance, while the time of nucleation is estimated by the onset of absorbance.

We can use the length of this induction period to estimate the buildup of solute prior to nucleation. If we assume that the reaction is first-order throughout its entirety, we can extrapolate an appropriate single exponential backwards to the time of injection (Figure 4.2.4).

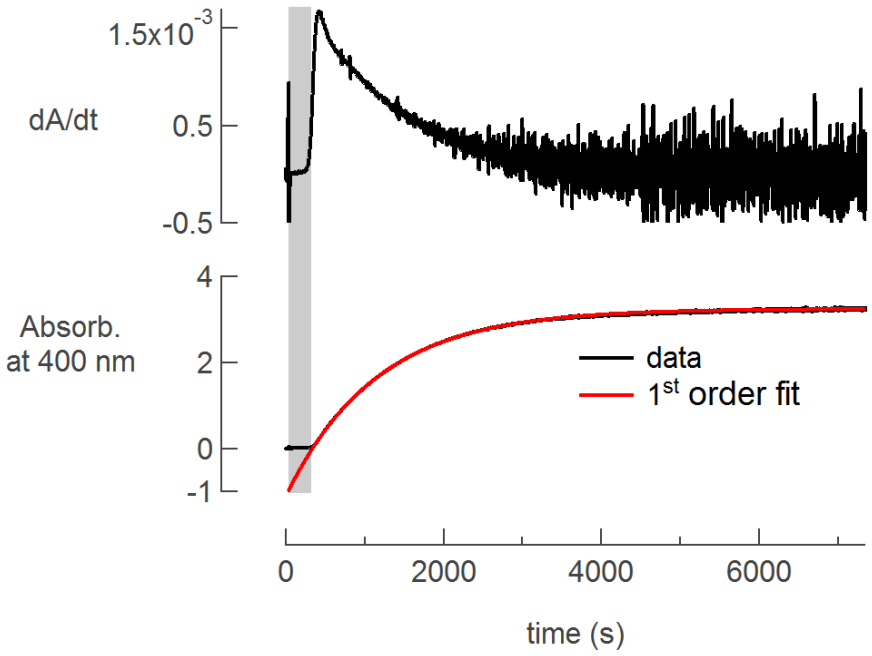


Figure 4.2.4. Bottom: backward extrapolation of single exponential fit (red line) to the time of injection (t = 0). Top: first derivative of data shown in black.

We wrote an automated IGOR routine to identify the maximum in the derivative, which corresponds to the greatest rate of nucleation ($t_{growth}$), and fit the data with a single exponential function:

$$= A_{max}(1 - e^{-k_{obs}(t-t_0)})$$

Equation 4.2.3

Where $A_{max}$ is the maximum absorption reached, $k_{obs}$ is the observed rate constant ($sec^{-1}$), and $t_0$ is the onset of the exponential since the reaction does not start at $t$ = 0. The time between injection and the actual start of the reaction is called the induction time $t_{ind}$, and is defined as:

$$t_{ind} = t_0 - t_{injection}$$

Equation 4.2.4

Since the fit at early times has an outsized impact on $t_0$, a second fit is applied to the data where $A_{max}$ is fixed to the earlier determined value and only the early time points are considered. This "early time" fit still describes all the data points very well but insures that $t_o$ is correctly identified. This approach is especially advantageous in cases where the overall fit fails to adequately predict the early time points, as demonstrated in Figure 4.2.5.

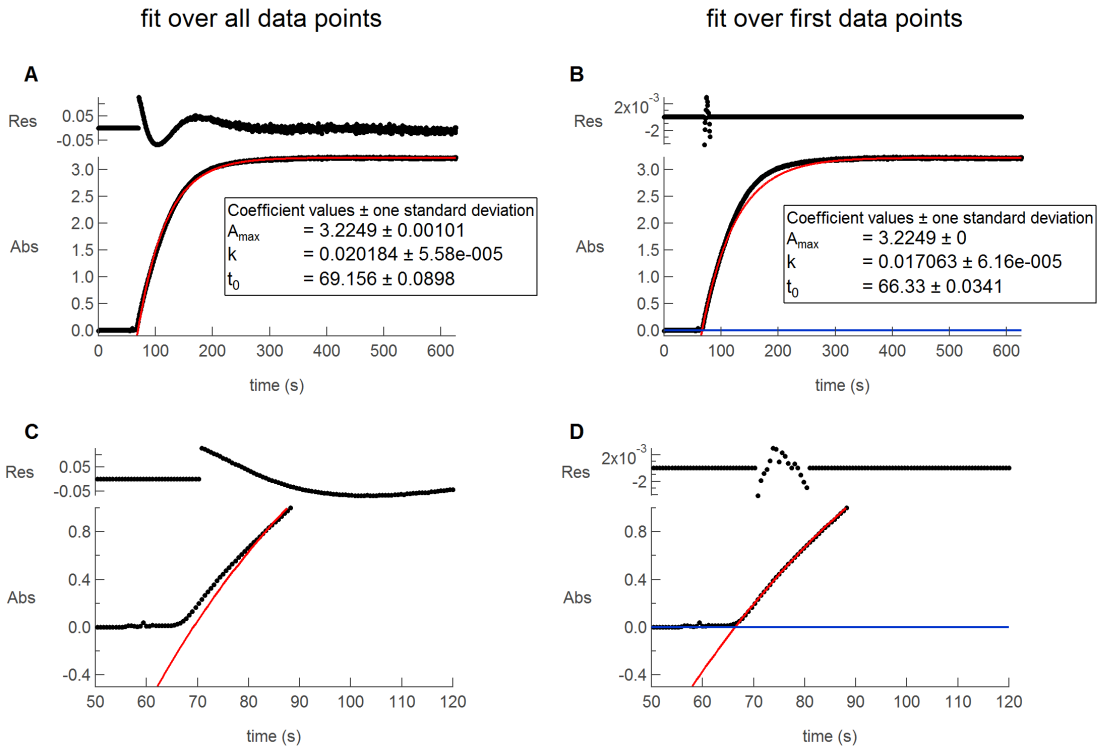


Figure 4.2.5. Data fits to a PbS synthesis from lead(II) oleate and *N*-dodecyl-*N'*-(4-(trifluoromethyl)phenyl)thiourea at 110 °C. A) Fit over all data points following $t_{ind}$. B) Fit applied to the early time points between $A(t_{growth})$ to $3A(t_{growth})$, showing much better agreement at early times

at the expense of slightly worse fitting as later times. C) Expanded view of early times in A. D) Expanded view of early times in B.

The absolute value of the early time fit at $t_{injection}$ is negative; its absolute value represents the fraction of conversion ($f_{con}$) that took place prior to nucleation ($t_0$):

$$f_{con} = \frac{-A(t_{inj})}{A_{max} - A(t_{inj})} = \frac{-A_{max}(1 - e^{-k(t_{inj} - t_0)})}{A_{max} - A_{max}(1 - e^{-k(t_{inj} - t_0)})}$$

Equation 4.2.5

If $f_{con}$ is multiplied by the concentration PbE measured by UV-vis-NIR spectroscopy (Figure 4.2.2B), the "critical" concentration of solute at nucleation ($[PbE]_{i,crit}$) is readily determined:

$$[PbE]_{i,crit} = [PbE]_{\infty} f_{con}$$

Equation 4.2.6

If $[PbE]_{i,crit}$ is divided by the nanocrystal concentration measured at the end of the reaction ($n$), we can estimate the upper limit of the critical nucleus size ($v_0$). This is an upper limit because 1) not all solute is consumed during nucleation, and 2) not all solute is consumed over the entire reaction since the equilibrium solubility of solute is greater than zero. Nonetheless, it is useful to place upper bounds on the critical nucleus size in order to better understand the energetics of these nanostructures, to understand what factors influence solute solubility, and to optimize the synthesis of small PbE nanocrystals useful for

quantum dot photovoltaics. This analysis is possible because Ostwald ripening is negligible under our conditions (see Chapters 2 and 3).

Further, we can adapt Equation 4.2.2 to model $Q_0$ during nucleation in terms of the instantaneous precursor concentration $[P]$ and $f_{con}$, again assuming first-order behavior:

$$Q_0 = \frac{d[PbE]_i}{dt} = -\frac{d[P]}{dt} = k[P] = k(1 - f_{con})[P]_i$$

Equation 4.2.7

In all reactions studied here, $[P]_i$ is the injected thio-/selenourea concentration, 9 mM.

According to the La Mer model, solute builds up beyond its equilibrium solubility $[PbE]_{i,eq}$, to give a supersaturated solution with the supersaturation, $S$, given by:

$$S = \frac{[PbE]}{[PbE]_{i,eq}}$$

Equation 4.2.8

Assuming that the same supersaturation must be reached to induce nucleation in all reactions for a given material and set of conditions, one should expect $t_{ind}$ to vary with precursor conversion (solute supply) rate, since slower reactions should take more time to reach $[PbE]_{i,crit}$. Figure 4.2.6A shows this to be true; at 80 °C, slower-converting thioureas exhibit longer induction periods.

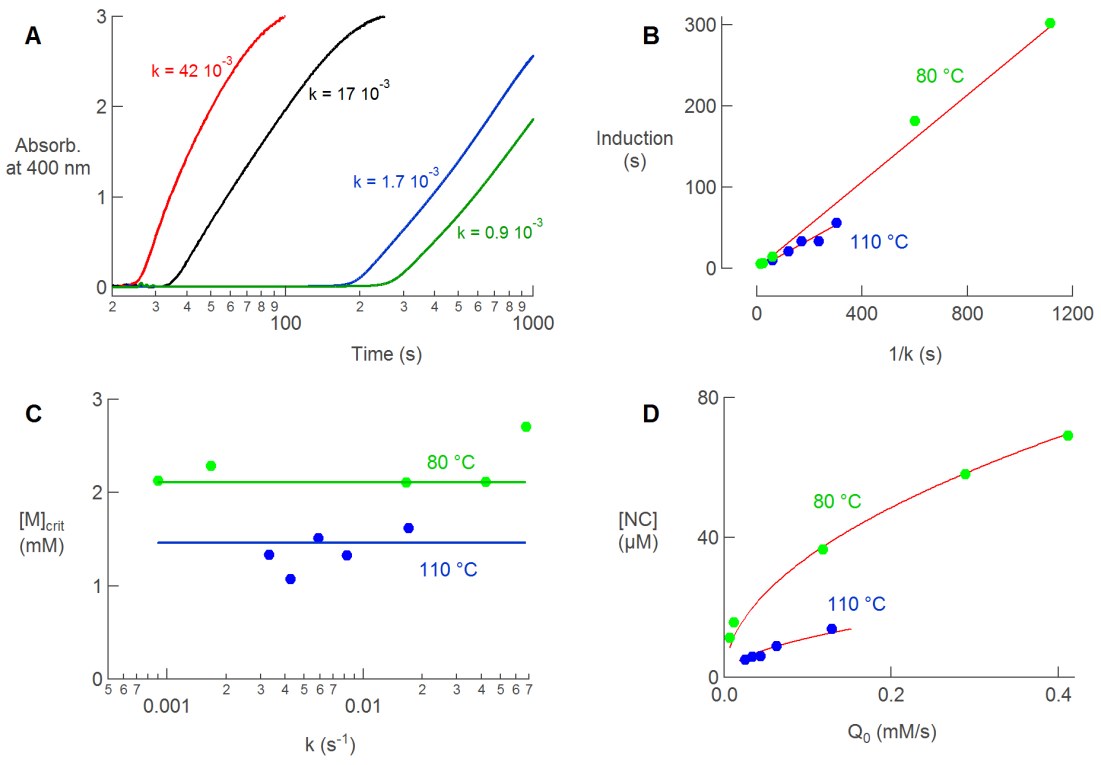


Figure 4.2.6. A) thioureas with increasing conversion rates yield shorter induction times at 80 °C. B) The induction time varies approximately linearly with respect to 1/*k*, both at 80 °C and 110 °C. C) The critical concentration is largely independent of $k$ but is lower at higher temperatures. D) The amount of NCs formed in a reaction increases with $Q_0$, although not linearly. The data shown are fitted to a square root function.

To give this relationship a more quantitative treatment, we can express $f_{con}$ at nucleation as:

$$f_{con} = [P]_0 - [P] = 1 - e^{-kt_{ind}}$$

Equation 4.2.9

which rearranges to:

$$t_{ind} = \frac{\ln (1 - f_{con})}{k}$$

Equation 4.2.10

In Figure 4.2.6B we can see that this linear relationship between $t_{ind}$ and $k$ holds true. This implies that $f_{con}$ is constant; indeed, Figure 4.2.6C shows this to be a reasonable conclusion ($f_{con}$ has been converted to solute concentration in mM), although with some scatter. To make a more affirmative conclusion, it will be necessary to 1) expand the range of rate constants studied here as wide as possible, and 2) generate better statistics to mitigate scatter.

From these data we can start to see that $[PbS]_{i,crit}$ is largely independent of $k$, but dependent on temperature. In the present case, the critical concentration is significantly lower at 110 °C ($[PbS]_{i,crit}$ = 1.46 mM) than at 80 °C ($[PbS]_{i,crit}$ = 2.11 mM). Since the equilibrium solute solubility ($[PbS]_{i,eq}$) likely increases with temperature (like most dissolved solids), this result is highly suggestive that the $[PbS]_{i,crit}$ at 80 °C is at least 1.4x greater than $[PbS]_{i,crit}$ at 110 °C.

This could have dramatic implications for the crystallization of monodisperse colloids. In the classical "burst nucleation" model, low polydispersity is afforded by rapid nucleation rates ($J$) giving rise to short nucleation periods:[5]

$$J = Aexp\left(-\frac{16\pi\gamma^3 V_M^2}{3k_B^3 T^3 (ln\, S)^2}\right)$$

Equation 4.2.11

Where:

- $A$ is a pre-exponential factor
- $\gamma$ is surface tension
- $V_M$ is the molar volume
- $k_B$ is Boltzmann's constant
- $T$ is temperature
- $S$ is supersaturation

This equation indicates that there are three potential experimental levers to increase the rate of nucleation: $\gamma$, $T$, and $S$. Since $\gamma$ is difficult to measure (but likely decreases with increasing $T$), this leaves $T$ and $S$; increases to $T$ and $S$ should lead to more rapid nucleation. In our case, however, high $T$ leads to lower $S$; the two work in opposite directions. Thus, there is likely an optimal balance between $T$ and $S$, but at present this relationship will require further study to understand.

Figure 4.2.6D shows the relationship between $n$ and $k_{obs}$ at 80 °C and 110 °C. Although Equation 4.2.2 predicts a linear relationship, there is a systematic plateauing effect at high rates that has also been observed in prior studies on

PbS[6] and CdSe.[7] In our case, this relationship is better described by a square root dependence:

$$n = V_M \sqrt{\frac{Q_0}{\dot{v}}}$$

Equation 4.2.12

The precise reason for this drop-off is unclear, but there are three reasonable hypotheses that merit further study (Scheme 4.2.1). The first is simple acid-catalyzed Ostwald ripening following precursor conversion. Both disubstituted thioureas and trisubstituted selenoureas liberate oleic acid upon reaction with lead(II) oleate (in the case of thioureas, more so as substituent acidity increases), and while Ostwald ripening is demonstrably slow under conditions shown in Chapters 2 and 3, its effects become more important as substituent acidity increases and nanocrystal size decreases (i.e. surface tension increases). This should be straightforward assess by nanocrystal concentration and size measurements by absorbance spectroscopy. The second hypothesis is that aggregation occurs during and/or shortly after nucleation to reduce the particle number. This could be promoted by low concentrations of $Pb(O_2CR)_2$. This could be tested by reproducing some of the data in Figure 4.2.6D at various Pb:S ratios. The third hypothesis is that nucleation is not nearly as fast a process as assumed in most colloidal synthesis. This would result in $[PbS]_{i,crit}$ being dependent upon

$k_{obs}$, which cannot definitively be ruled out due to the scatter in Figure 4.2.6C, but appears unlikely given the results in Figure 4.2.6A and B.

Scheme 4.2.1. Potential explanations for sub-linear deviation from $n$ vs. $k_{obs}$ linearity in PbS. A) Acid-catalyzed Ostwald ripening, which effectively transfers PbS monomers from smaller nanocrystals with higher surface tension to larger, more bulk-like nanocrystals. Nanocrystal ligands are omitted for clarity. B) Aggregation during nucleation due to incomplete surface passivation and high surface tension. C) Slow nucleation, in which nucleation and growth cannot keep up with solute formation, and the critical concentration $[PbS]_{i,crit}$ varies with $k_{obs}$.

***A) Ostwald Ripening***

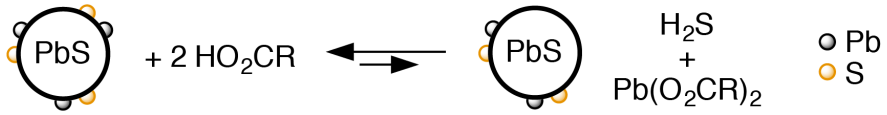


***B) Aggregation during nucleation***

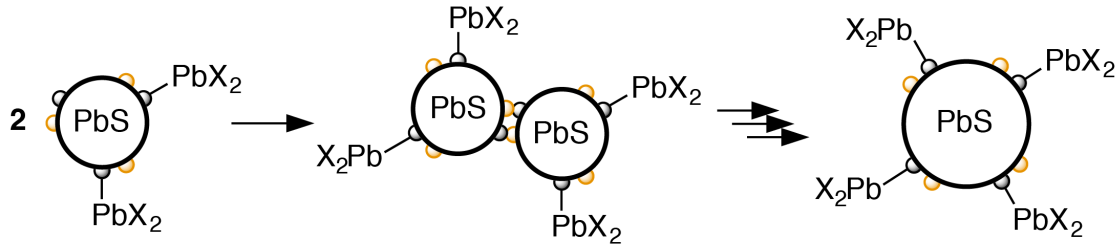


***C) Slow nucleation***

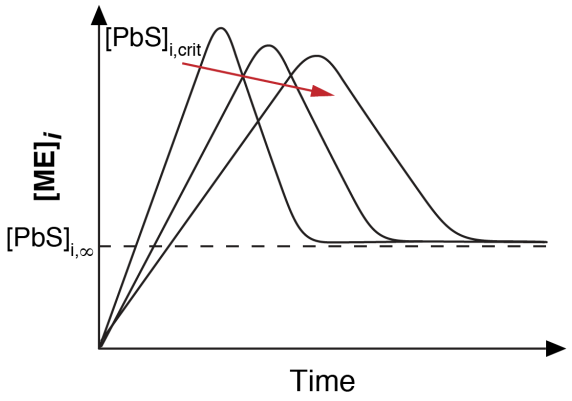

We performed the same analysis on an extensive dataset of PbSe nanocrystal syntheses (Figure 4.2.7). All the same conclusions hold from the PbS study, with the exception of the dependence of $n$ vs. $k_{obs}$ (Figure 4.2.7C), which remains approximately linear across a wide range of rates and temperatures. Whatever process is depleting the nanocrystal concentration in PbS does not seem to be operative in PbSe synthesis, which raises the question: what is different between the two?

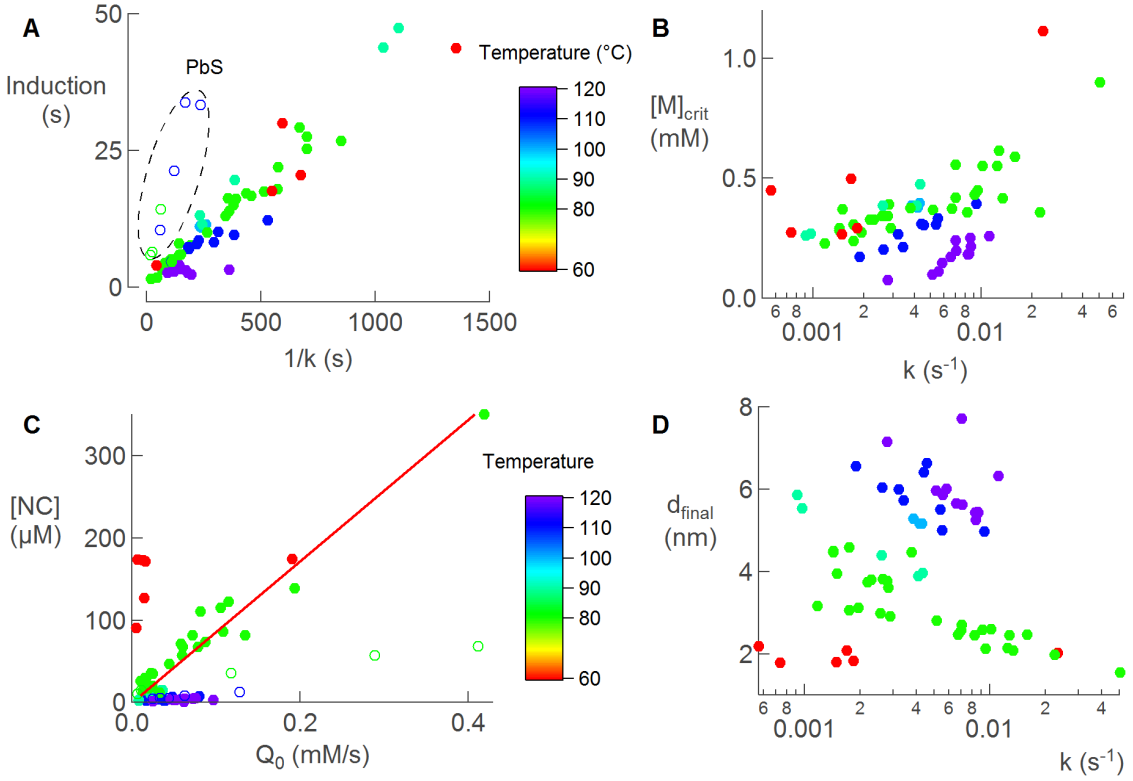


Figure 4.2.7. A) Induction times for PbSe (closed circles) and PbS (empty circles) at various temperatures. B) The corresponding critical concentrations. C) The number of PbSe (closed circles) and PbS (empty circles) nanocrystals formed at various temperatures. D) The

corresponding nanocrystal diameter. The temperature scale applies to all four graphs.

PbS and PbSe are two of the most analogous binary semiconductors imaginable. Both take the rock salt crystal structure with only a 3% lattice mismatch ($a_{PbS}$ = 5.936 Å, $a_{PbSe}$ = 6.12 Å),[8] both have similar Pauling electronegativity differences (PbS: 0.53, PbSe: 0.50), both are infrared absorbers that are strongly quantum confined as nanocrystals (Bohr exciton radii: 18 nm for PbS, 46 nm for PbSe), and both may be synthesized under otherwise identical conditions using thio- and selenourea precursors.

We propose that differences in chalcogen orbital energies could explain both the observed difference between PbS and PbSe and the sub-linearity of $n$ vs. $k_{obs}$ for PbS in terms of Ostwald ripening. Given that Ostwald ripening is acid-catalyzed and acid is a co-product of PbE synthesis, the likely intermediate is a small quantity of $H_2E$, which may coordinate to $Pb(O_2CR)_2$ (Table 4.2.1). Despite the similarities between PbS and PbSe, $H_2S$ and $H_2Se$ have markedly different behavior that can be explained by periodic trends. From $H_2O$ to $H_2Te$, the H-E orbital overlap becomes worse and worse, which is exhibited in four ways: 1) more positive heats of formation, 2) longer bond lengths, 3) bond angles approaching 90°, which signals greater *p*-character than *s*-character in bonding,

and 4) lower $pK_a$s, despite smaller and smaller electronegativity differences from O to Te.

Table 4.2.1. (Top) Acid-catalyzed Ostwald Ripening of PbS and PbSe nanocrystals. (Bottom) Comparison of selected thermodynamic properties of hydrogen chalcogenides.[9,10]


| Compound | $H_2O$ | $H_2S$ | $H_2Se$ | $H_2Te$ |
|---|---|---|---|---|
| $\Delta H°_f$ (kJ mol$^{-1}$) | –285.9 | +20.1 | +73.0 | +99.6 |
| Bond length (pm) | 95.7 | 133.6 | 146 | 169 |
| Bond angle | 104.5° | 92.1° | 91° | 90° |
| $pK_{a,H2O}$ | 14 | 7.05 | 3.89 | 2.6 |

Because of the weak H-E bonding in $H_2E$ equivalents, H-E bond formation likely dictates the position of the above equilibrium. Thus, the more stable intermediate, $H_2S$, should lead to faster ripening rates, all other factors being equal. Although direct evidence for this phenomenon will be difficult to obtain given the infinitesimally small quantities likely involved, it may be fruitful to test this hypothesis by first finding conditions that lead to rapid Ostwald ripening in PbS but not PbSe, then repeat those experiments in the presence of a non-nucleophilic Brønsted base strong enough to deprotonate oleic acid in nonpolar

solution, such as 1,8-Diazabicyclo[5.4.0]undec-7-ene or perhaps *N*,*N*-diisopropylethylamine.

This analysis is very likely an oversimplification given the extreme reactivity of $H_2S$ and $H_2Se$ in the presence of lead(II) salts. However, a similar argument is likely to apply in less extreme cases, such as the formation of Pb-coordinated $H_2E$, $Pb(EH)(O_2CR)$, or mixed polymeric/hydrogen-bonded intermediates. Further, while it may just be coincidence, this difference is also consistent with the ~5x smaller per-particle growth rate during nucleation of PbSe as compared to PbS (inferred from Figure 4.2.7).

*4.2.3. Nanocrystal Formation and Evolution*

Given this exciting data, we sought to obtain more direct measurements of nanocrystal evolution during synthesis through small-angle X-ray scattering (SAXS) experiments. Broadly speaking, SAXS is an X-ray technique that probes structural features in the several-nanometer range, while traditional X-ray diffraction, or wide-angle X-ray scattering (WAXS), probes atomic-scale features such as crystal lattice planes. There is an extraordinarily well-developed literature on the use of SAXS for nanoscience[11,12] to which the reader is directed for a thorough theoretical treatment of the subject and its applications.

In the present case, we built an apparatus and developed protocol to carry out in situ monitoring of PbS nanocrystal synthesis by SAXS/WAXS as well as

UV-visible absorbance spectroscopy at a synchrotron X-ray source (Figure 4.2.8). This apparatus combines the standard dip probe apparatus described in Chapter 2 with an adapter to flow a small amount of solution through a glass capillary and back into the reaction mixture.

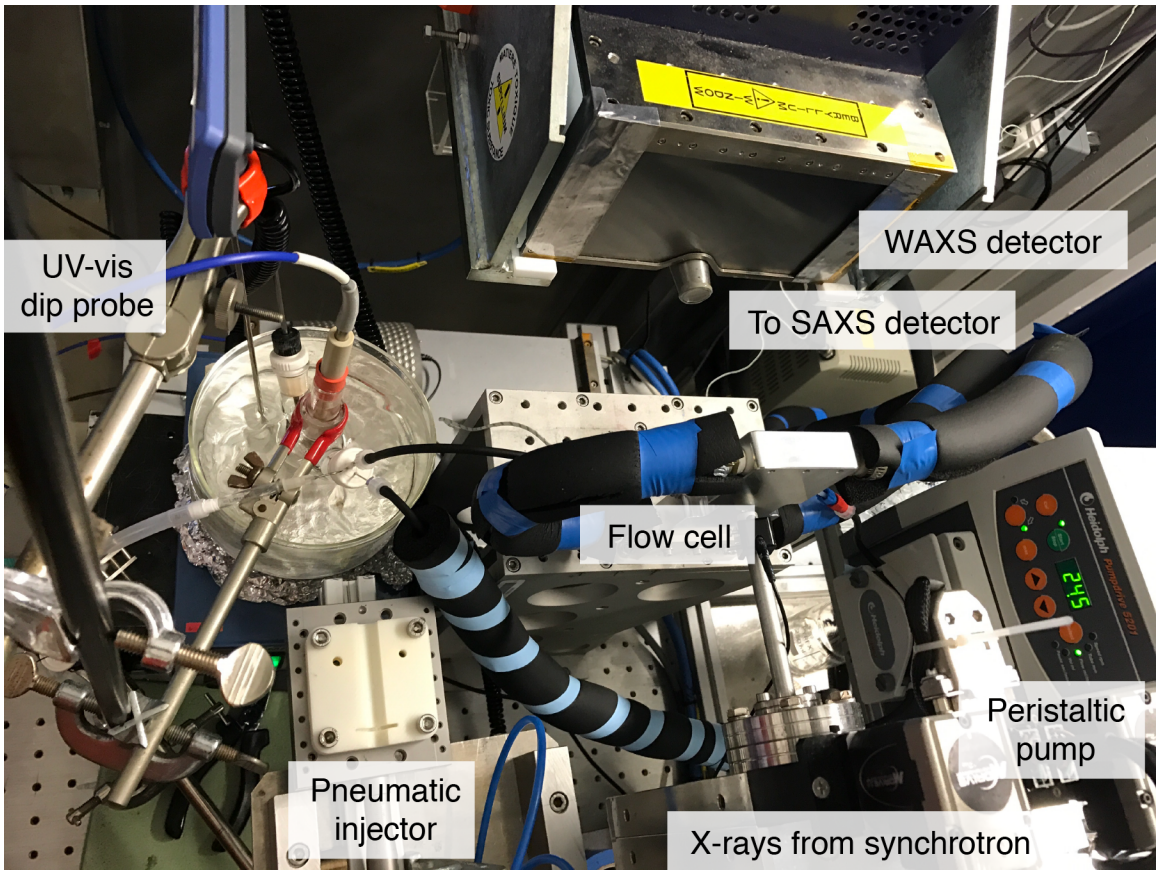


Figure 4.2.8. Photograph of synchrotron X-ray experiment apparatus.

Figure 4.2.9 shows SAXS patterns from the synthesis of PbS nanocrystals from 1 s to 1199 s (the beginning to the end of a 20 minute reaction). The first SAXS patterns (violet and blue curves) are consistent with lead(II) oleate micelles dispersed in hexadecane. Similar patterns were observed during preliminary

non-synchrotron SAXS experiments. After approximately 10 s, the intensity at small $q$ ($I_0$) begins to increase. This corresponds to the onset of nanoparticle formation. As the reaction proceeds, the intensity at high $q$ (2.8 – 5 $nm^{-1}$) decreases with time, which shows a decrease in signal from micellular aggregates of lead(II) oleate as Pb is gradually incorporated into the nanocrystals. The intensity at low $q$ increases by more than two orders of magnitude, showing the appearance of scattering objects in solution. The large oscillation visible near 2 $nm^{-1}$ at the end of the reaction indicates that the objects formed in solution are highly monodisperse.

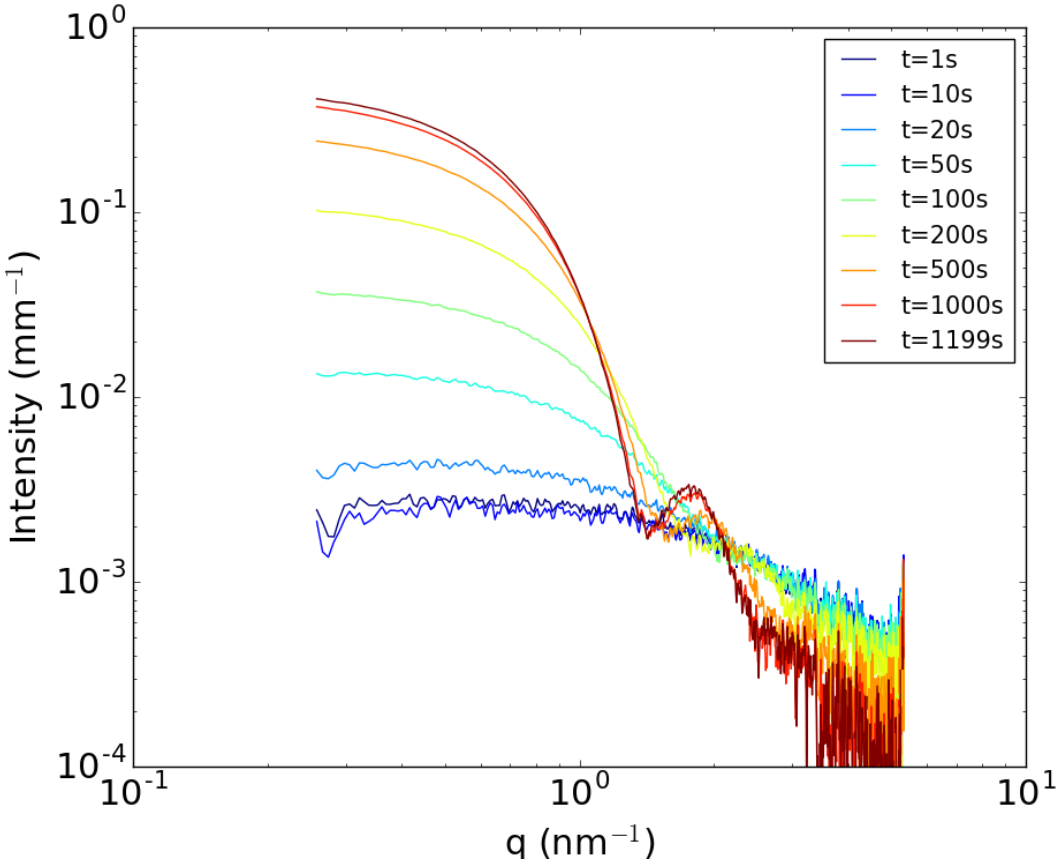


Figure 4.2.9. SAXS patterns during the formation of PbS nanocrystals at 110 °C.

To build a more quantitative view, we modeled the SAXS intensity as the a linear combination of two components: micelles and nanoparticles (see Section 4.4.8). From these fits we can extract nanocrystal size, polydispersity, yield, and nanocrystal concentration over the course of the reaction. An example dataset from this analysis is shown in Figure 4.2.10.

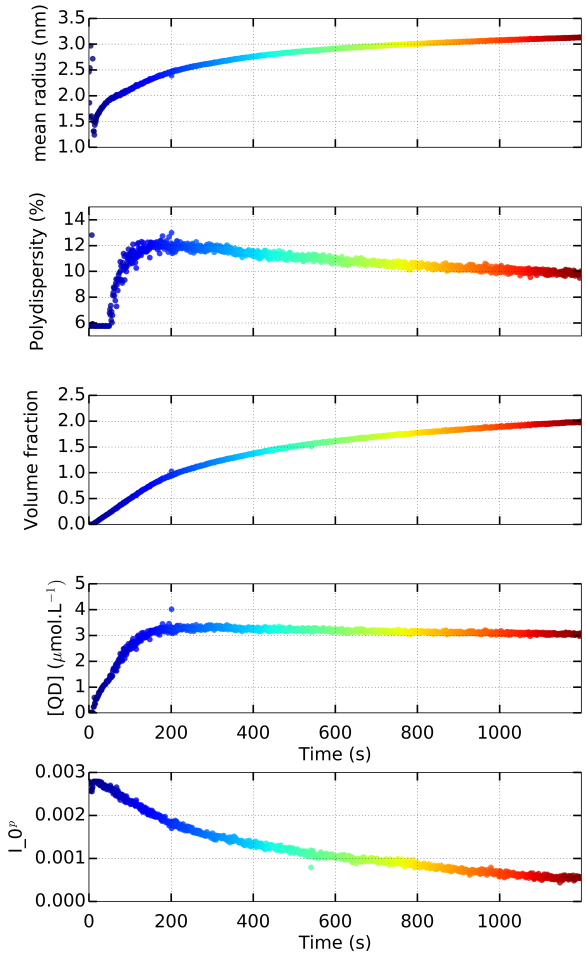


Figure 4.2.10. Results of data fitting. The parameters from the fits are displayed as a function of time elapsed after injection of the thiourea. Fitting procedures are described in Sections 4.4.6 – 4.4.8.

From Figure 4.2.10, we can see that the radius and yield increase smoothly with time as expected. The polydispersity jumps to ~12% during particle nucleation and then decreases to ~10% over the course of the reaction. It is unclear whether this apparent size distribution focusing is real or an artifact of the fitting method, which assumes sphericity. It is also worth noting that at early times, a lower bound of 6% is imposed on the polydispersity to aid the fitting routine.

However, most importantly, we see a gradual onset of nanocrystal nucleation starting at $t = 0$ and ending nearly 180 seconds later. This is a highly unexpected result given our prior data showing the La Mer model to be operative. A 3-minute nucleation period during a reaction that takes ~20 minutes to complete represents 6% of the total reaction time and approximately 35% of the total solute generated during the formation of nuclei. To put this in context, two prior studies show nucleation periods for CdSe[13] and Au[14] lasting for ~0.6% and < 3% of the total reaction time, respectively. It is difficult to imagine how such a long nucleation period could lead to such monodisperse samples. One possibility is that the per-particle growth rates of small, new nuclei are much faster than those of larger, older nuclei. This would allow the small ones to catch up to the larger ones and could lead to a narrow size distribution. This argument is often invoked in the literature on size distribution focusing.[15–17] It is also difficult to reconcile the different onset behavior during nucleation exhibited in dip probe experiments and SAXS/WAXS experiments, since the former shows a much sharper onset of intensity. Do, for example, absorbance measurements capture signal from solute? If true, this would be an exciting opportunity to study the nature of the solute.

In order to tackle this question, we performed experiments combining optical dip probe measurements with SAXS/WAXS collection. An example dataset is shown in Figure 4.2.11.

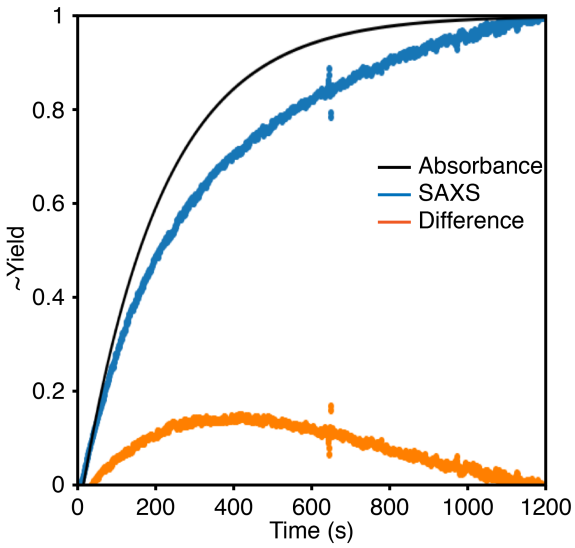


Figure 4.2.11. Results of a nanocrystal reaction monitored simultaneously by in situ absorbance using a dip probe (fit shown in black) and in situ SAXS (blue) and WAXS (not shown). The difference plot (orange) clearly shows a disconnect between the two datasets.

From this data we can see that this discrepancy persists under identical collection conditions. If the difference in signal is due to solute, we can see a gradual buildup and depletion of solute over the course of the reaction that roughly corresponds with what would be expected in a slowed-down version of the La Mer model. However, this is still an indirect dataset and a difficult experiment to reproduce given the complexity involved in the apparatus and operation, so

more detailed, and ideally, direct observation of solute will be necessary to make stronger conclusions about nucleation.

*4.2.4. Secondary Nucleation Measurement*

To make orthogonal measurements on nucleation thresholds, we sought to induce and monitor nucleation processes in the presence of existing PbS nanocrystals. The relationship between [nanocrystal] on the $k_{obs}$ gives important information about how to control nanocrystal size (Figure 4.2.12; see Chapter 2 for more), but also implies that if [nanocrystal] and $k_{obs}$ can be independently varied, nucleation can be turned on or off in the presence of a population of nanocrystals.

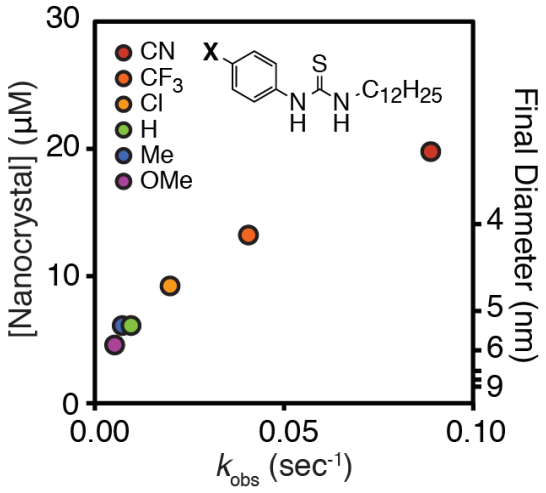


Figure 4.2.12. Dependence of [nanocrystal] on $k_{obs}$.

Given the importance of epitaxial growth and avoiding secondary nucleation in core-shell nanocrystal synthesis, it is crucial to understand these

nucleation thresholds. However, little in the way of controlled studies have been carried out on this topic; further, data analysis can quickly become complicated because of overlapping absorbance/photoluminescence spectra, the limited resolving power of TEM below few-nanometer distances, and difficult deconvolution of other bulk techniques such as dynamic light scattering and SAXS.

We approached this challenge using high-throughput PbS nanocrystal synthesis and infrared photoluminescence spectroscopy to track the growth of existing populations and nucleation of new populations. By pre-synthesizing nanocrystals samples using a selection of thiourea precursors, we were able to vary [nanocrystal] and $k_{obs}$ independently. Our hypothesis was that if a given ([nanocrystal], $k_{obs}$) coordinate fell above the data shown in Figure 4.2.12, no secondary nucleation would take place. In other words, the collective maximum growth rate of the existing particles would be sufficiently rapid to keep the solute concentration below $[PbS]_{i,crit}$ and avoid nucleation. If, however, the ([nanocrystal], $k_{obs}$) coordinate fell below the line, secondary nucleation should take place because not enough particles are present to keep the solute concentration below $[PbS]_{i,crit}$.

Example datasets in Figure 4.2.13 show typical results from experiments and Figure 4.2.14 shows the aggregated results of 16 experiments. When

secondary nucleation occurs, a new peak appears at short wavelengths, which is usually well separated from the peak arising from the initial nanocrystal population. When these results are compared with the [nanocrystal] vs. rate data collected from our previous study[6] and shown in Figure 4.2.12, we can see a close match between expectation and reality. For the most part, ([nanocrystal], $k_{obs}$) coordinates are predictive of secondary nucleation behavior. While these data are fairly qualitative, it should be possible to extract more detailed insight into per-particle growth rates from these and similar experiments that feed precursor to the reaction mixture in a slow addition. The caveat to this study is that we intentionally held the starting nanocrystal diameter constant at 5.9 nm, which gives us a degree of experimental control but fails to completely capture the results of Figure 4.2.12, in which the numbers of nanocrystals are determined when the nanocrystals are much smaller, near the critical radius.

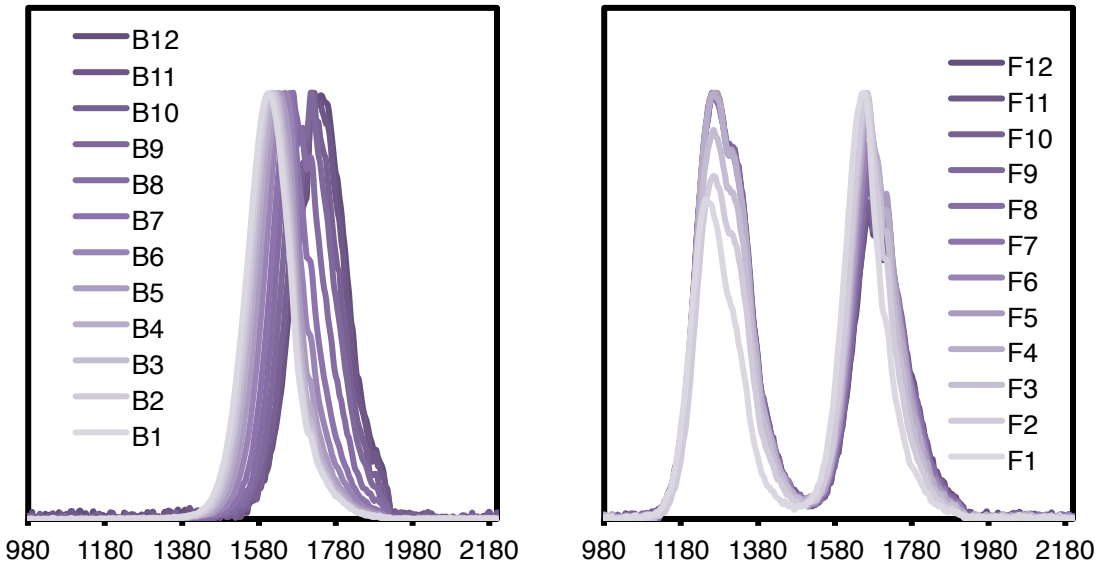


Figure 4.2.13. Example photoluminescence spectra of aliquots removed from (left) a reaction in which secondary nucleation did not occur and (right) a reaction in which secondary nucleation occurred. X-axes are both wavelength (nm).

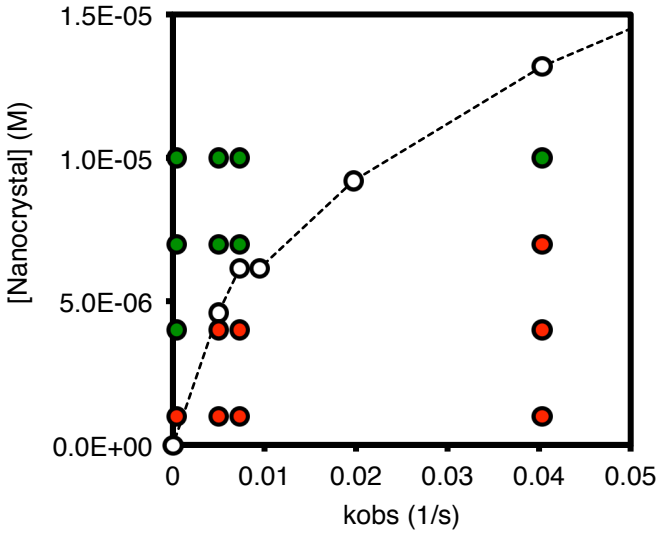


Figure 4.2.14. Results of secondary nucleation study overlaid with [nanocrystal] vs. $k_{obs}$ data shown in Figure 4.2.12 (white). Green circles represent experiments where no secondary nucleation was observed,

while red circles represent experiments where secondary nucleation was observed.

While PbS is a convenient model system, and PbSe shows dramatically different behavior than PbS, it will be much more practically impactful to carry out similar studies on mixed CdSe/CdS systems relevant for solid-state lighting. Preliminary data from single-component reactions show that [nanocrystal] vs. $k_{obs}$ has a much steeper dependence for CdS than CdSe, corresponding with slower growth rates for CdS than CdSe. Ignoring lattice mismatch and wettability, this suggests that CdS shell growth in CdSe/CdS heterostructures is prone to secondary nucleation.

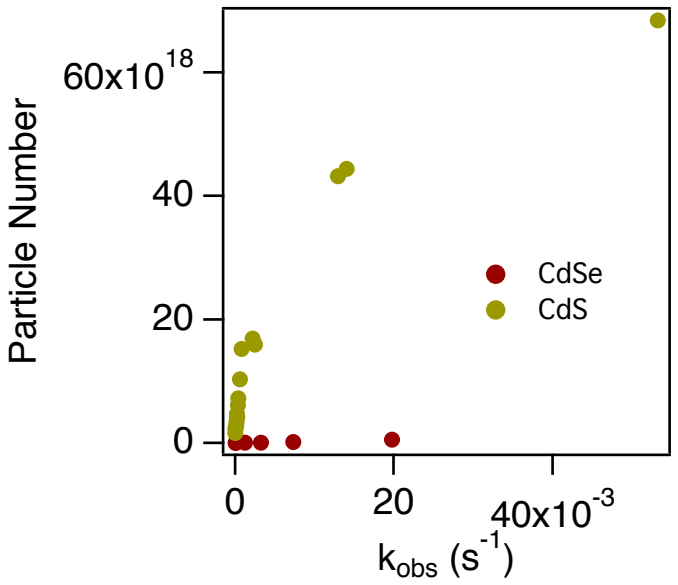


Figure 4.2.15. [nanocrystal] vs. $k_{obs}$ for CdS and CdSe. All reactions are carried out at 240 °C, 10 mM in chalcogenourea, 1.2 equivalents of

cadmium oleate, and 2.4 equivalents of oleic acid, in 95% 1-octadecene, 5% tetraglyme.

*4.2.5. Conclusions, Outlook, and Next Steps*

Studying the nucleation and growth processes fundamental to colloidal crystallization has long been difficult and relegated to speculation. By leveraging the clean reactivity and modularity of thio- and selenourea-based nanocrystal synthesis, we have unlocked previously impossible studies into the induction period preceding nucleation, nucleation itself, and growth rates of colloidal nanocrystals, uncovering insights such as the critical solute concentration for nucleation, the surprisingly lengthy nucleation period, and the thresholds for secondary homogeneous nucleation. These fundamental processes, once properly understood, will greatly accelerate the rational design of nanocrystals for technological applications including solid-state downconversion, biological labeling, and photovoltaics.

## 4.3. Red-Emitting Nanocrystals for Solid-State Lighting

*4.3.1. Theoretical Framework*

The final project we will discuss attempts to apply some of the fundamentals learned in the nucleation and growth studies to red-emitting nanocrystal downconverters.

The two major mechanisms that reduce nanocrystal downconversion efficiency in high-flux applications are trap-assisted recombination and Auger recombination (Figure 4.3.1). Trap-assisted recombination occurs in the presence of one or more midgap states accessible to holes and/or electrons. Trap-assisted recombination is often nonradiative and at best significantly red-shifted from the band edge. In many cases, trap states are long-lived, leading to prolonged "dark" periods for individual nanocrystals. Auger recombination is a nonradiative recombination pathway in which the energy from recombination is not emitted as light but rather transferred to a valence band hole or conduction band electron, which is pushed far into its band to relax thermally.

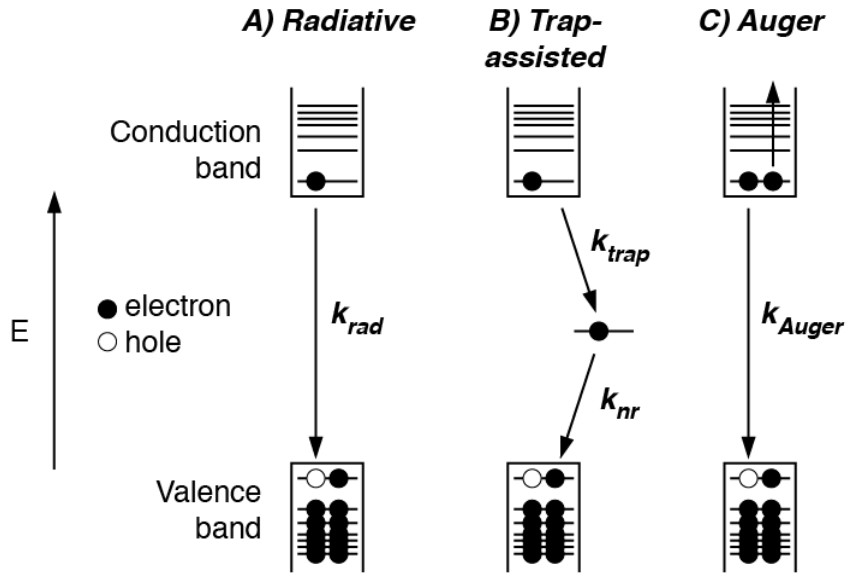


Figure 4.3.1. Three major recombination pathways operative in semiconductor nanocrystals. A) Radiative recombination resulting in band-edge photoluminescence. B) Trap-assisted recombination resulting

in red-shifted trap luminescence and/or heat energy. C) Auger recombination resulting in promotion of a hole or electron (electron shown here) to a deep band state, followed by release of heat energy.

To date, several synthetic strategies for $CdSe_{1-x}S_x$ nanocrystals have effectively eliminated trap-assisted recombination at room temperature and low light flux (< 0.1 W $cm^{-2}$).[18] However, the conditions in an operative LED (1 – 30 W $cm^{-2}$, 60 – 150 °C) rapidly trigger Auger recombination, leaving it as the major problem standing between nanocrystals and efficient, stable LED lighting. The nanocrystal properties most often proposed to mitigate Auger recombination are 1) large size and 2) a smoothly graded energetic landscape between narrow-gap core and wide-gap shell material, although there is some disagreement over their effectiveness.[19–30] In reality, it is quite possible that no sample to date actually achieves a smooth, defect-free graded alloy because of difficulties in kinetic control using legacy methods and characterization capable of distinguishing S from Se with sub-nanometer resolution.

We set out to use the control over precursor conversion afforded by thioureas and selenoureas to smoothly grade $CdSe_{1-x}S_x$ nanocrystals. This would serve two purposes: 1) testing this hypothesis using a method much more able to to demonstrate smooth grading and 2) these materials would be brightly emissive.

*4.3.2. Initial Attempts: Wurtzite Graded Alloys*

Our initial attempts focused on the synthesis of large ($d$ > 10 nm), wurtzite $CdSe_{1-x}S_x$ graded alloy nanocrystals. Since neither CdSe nor CdS are strongly quantum confined at 10 nm diameters, the color would be determined by the alloy composition of the emissive area of the nanocrystal. Further, synthesizing nanocrystals in the wurtzite phase would require high temperatures (> ~300 °C) and relatively acidic crystallization media that lead to facile recrystallization and "anneal out" defects. Most commercialized nanocrystal emitters are wurtzite samples, which is perhaps not a coincidence.

Most wurtzite syntheses prepare cadmium alkylphosphonate ($Cd(H_{x-1}O_3PR)_x$) solutions in situ by reacting CdO with alkylphosphonic acids in tri-*n*-octylphosphine oxide (TOPO) at > 100 °C under vacuum. This is followed by injection of a selenium precursor, typically tri-*n*-octylphosphine selenide at > 300 °C.

Scheme 4.3.1. Typical synthesis of wurtzite CdSe nanocrystals.

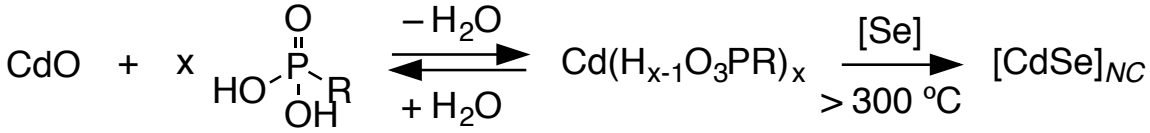


Given the issues with in situ metal precursor syntheses from metal oxides discussed in detail in Chapter 2, we sought to develop an alternate route to ($Cd(H_{x-1}O_3PR)_x$). However, metal phosphonates are notoriously insoluble until

high temperatures,[7] making synthesis, isolation, and characterization nearly impossible. Thus, we developed a cleaner in situ preparation of cadmium *bis*(octadecylphosphonate) from cadmium triflate ($Cd(O_3SCF_3)_2$) in the presence of primary amine:

Scheme 4.3.2. Synthesis of CdE nanocrystals from cadmium octadecylphosphonate formed in situ from $Cd(O_3SCF_3)_2$.

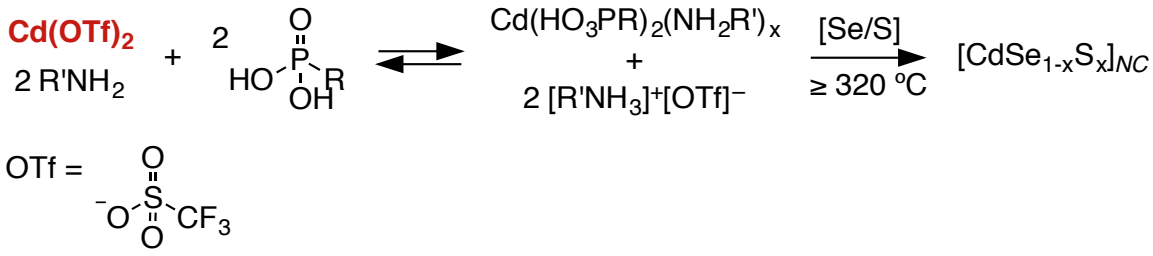


Notably, triflate is an excellent leaving group and extremely poorly coordinating anion, making this reaction favorable in the presence of phosphonate anions. The co-product of this salt exchange is ammonium triflate, which we hypothesize also helps us achieve our goals: the triflate anion should be inert at high temperature, while the additional ammonium ions increase the solution acidity and promote recrystallization in CdSe/CdS.

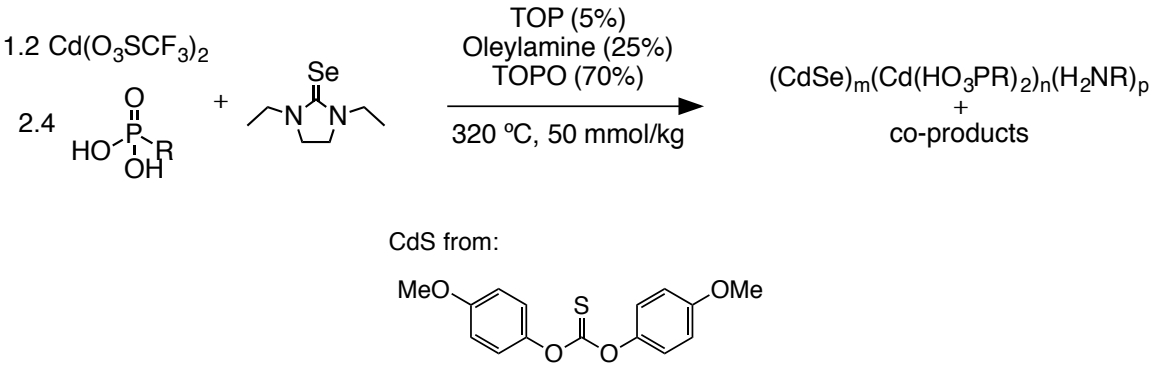

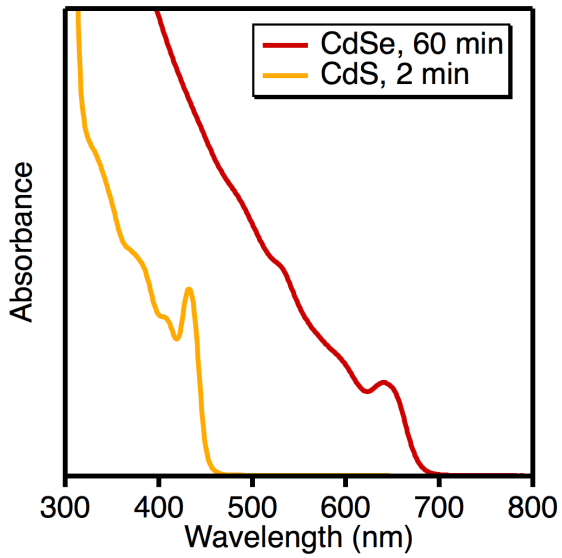


Figure 4.3.2. Synthesis of wurtzite CdSe and CdS nanocrystals from 1,3-diethylimidazolidine-2-selenone and *O*,*O*′-bis(4-methoxyphenyl)thiocarbonate using $Cd(O_3SCF_3)_2$ as the Cd precursor.

Initial single-component reactions produced high-quality CdSe and CdS samples. However, myriad other issues prevented this from becoming a practical method for graded alloy synthesis. First and foremost, quantum yields were less than 1%, which is low even for bare CdSe, and all attempts to synthesize CdSe/CdS heterostructures led to inconclusive results and in some cases obvious secondary nucleation. Second, a quantized-growth cluster persisted across a range of reactions, which acts as a local thermodynamic minimum between precursors and nanocrystals and mutes the effects of kinetic control in nanocrystal synthesis. While we were able to suppress this cluster species to a degree by increasing the concentration to 50 mmol/kg, clusters could easily

defeat the purpose of using precursors with different rates. Third, these reaction conditions are poorly compatible with much of our precursor library. Our precursor library consists primarily of polar compounds, requiring polar injection solvents. Most polar aprotic injection solvent candidates are either unstable at reaction temperatures or solid at low temperatures, leaving us with relatively nonpolar options such as oleylamine or tri-*n*-octylphosphine that exclude many potential compounds that are insoluble in these liquids. Further, when either oleylamine or tri-*n*-octylphosphine is used as the injection solvent, *O,O'*-bis(4-methoxyphenyl)thiocarbonate decomposes at 100 °C and turns deep brown over the course of 30 minutes to an hour. Fourth and lastly, this chemistry is difficult to scale given the stringent purity requirements of the octadecylphosphonic acid and TOPO, as well as difficulties in processing semisolids following cooling of the reaction mixture. We decided to pivot to an alternate strategy.

*4.3.3. Zinc Blende Spherical Quantum Wells*

Although we will not discuss it in detail here, we have extensively demonstrated the use of our precursor libraries in the synthesis of the lower temperature phase of CdSe and CdS, zinc blende. This chemistry is readily carried out at 240 °C in well-established 1-octadecene/tetraglyme mixtures using pre-synthesized cadmium oleate, making it much more accessible.

Adding to the appeal of zinc blende is a recent report describing the synthesis of large ($d$ = ~15 nm) "spherical quantum well" (SQW) nanocrystals having a CdS/CdSe/CdS radial structure that relieves strain associated with heteroepitaxy and leads to photoluminescence quantum yields (PLQYs) near 100%.[31] Their key data are shown in Figure 4.3.3.

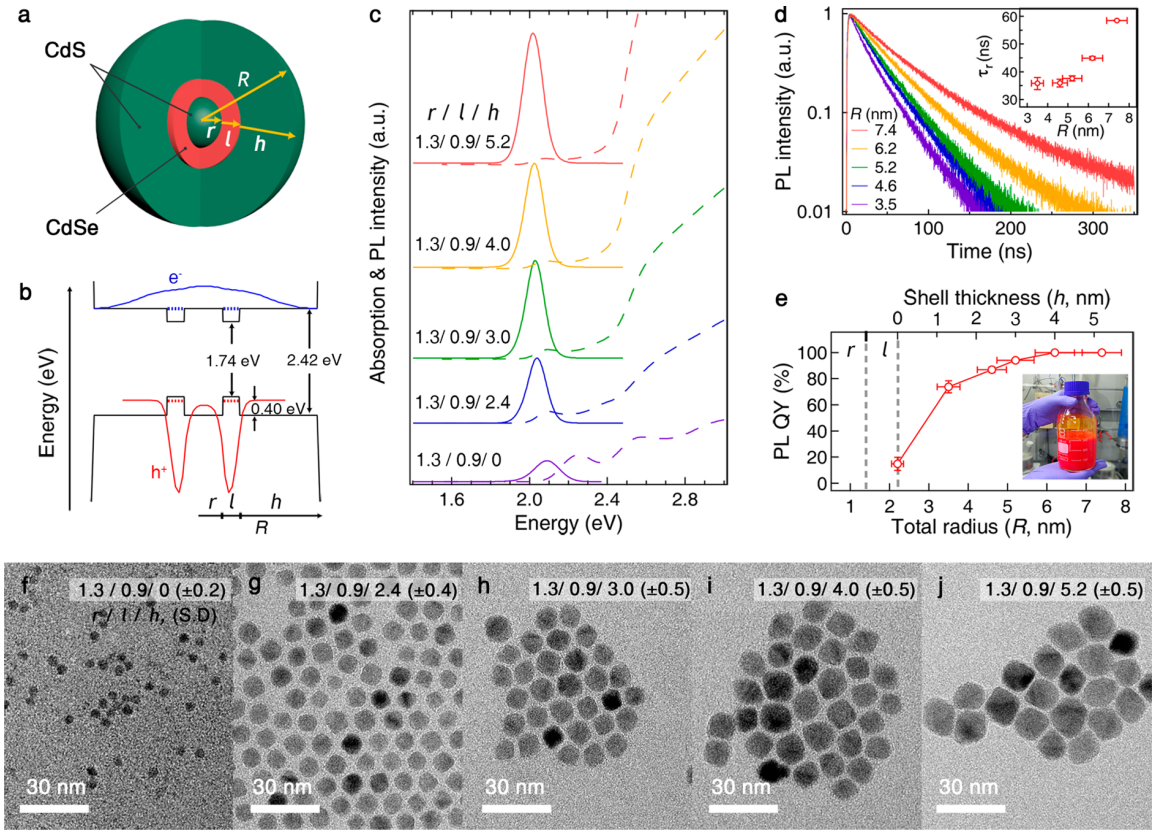


Figure 4.3.3. Structural and optical characteristics of CdS/CdSe/CdS SQW nanocrystals with varying shell thicknesses. A) Schematic illustration and B) energy band diagram of CdS/CdSe/CdS SQW nanocrystals. $r$, $l$, $h$, and $R$ denote the radius of the CdS seed, the thickness of the CdSe emissive layer, the exterior CdS shell thickness, and the total radius, respectively. C) Absorption and PL spectra, D) ensemble PL decay dynamics (inset:

single-exciton radiative recombination lifetime ($\tau_r$)), E) PLQYs excited at 450 nm (inset: photograph of concentrated SQW NC dispersion (300 mg/mL) taken under room light), and F-J) TEM images of CdS/CdSe/CdS SQW nanocrystal with varying CdS shell thickness ($r$ = 1.3 nm, $l$ = 0.9 nm, $h$ = 0, 2.4, 3.0, 4.0, and 5.2 nm). Figure reproduced from literature.[31]

We sought to synthesize analogous structures using mixtures of thio- and selenourea precursors, while controlling the alloy composition and grading. As a first pass, we targeted an abrupt heterostructure with $r$ = 1.25 nm, $l$ = 1.0 nm, $h$ = 5.5 nm. Using rate constants measured in single-component reactions, we hypothesized that we could synthesize the first two layers relatively simply with a fast thiourea and a slow selenourea. Initial simulations (Figure 4.3.4) predicted this should be possible if the ratio of $k_S/k_{Se}$ is maintained above ~64, which, at a 1:9 S:Se ratio should lead to deposition rate ratios of 64/9 ≈ 7. Further, assuming that the fast precursor dominates the nucleation chemistry and determines the number of nuclei, we expected a CdS-rich core with a $r$ = 1.25. Indeed, this reaction worked as predicted, showing at early times CdS-like absorption features too blue to be CdSe, but yielding a final product whose optical features look mostly like CdSe (Figure 4.3.5) and whose TEM shows quasi-spherical shape and low polydispersity (Figure 4.3.6).

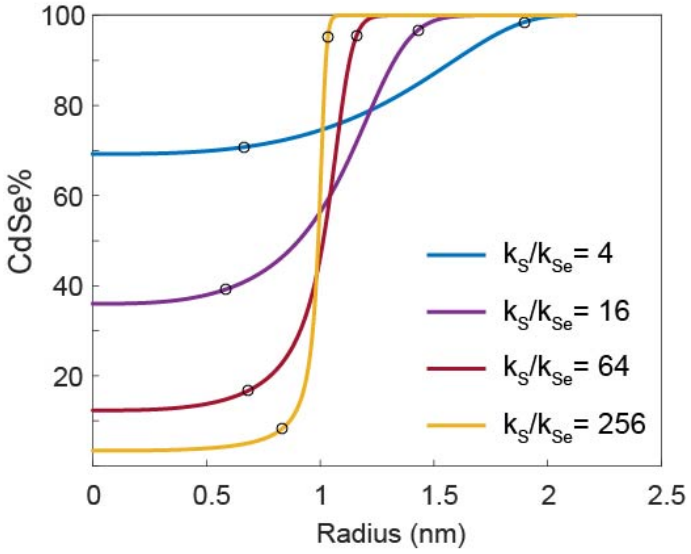


Figure 4.3.4. Simulation of the effect of two-component kinetics on nanocrystal radial composition. The overall Se:S ratio in the nanocrystal is held constant at 9:1 and the final radius is held constant at 5 nm. Deposition rates of CdSe and CdS are assumed to follow first-order kinetics limited by precursor conversion. Small black circles represent regions of grading (> 5% relative increase from particle center and > 5% relative decrease from particle edge).

Scheme 4.3.3. Synthesis of SQWs in a single step from *N*-dodecyl-*N*′-hexylthiourea ($k_{obs}$ = 3.0 x $10^{-2}$ $s^{-1}$)and 1,3-diisopropylimidazolidine-2-thione ($k_{obs}$ = 1.2 x $10^{-4}$ $s^{-1}$).

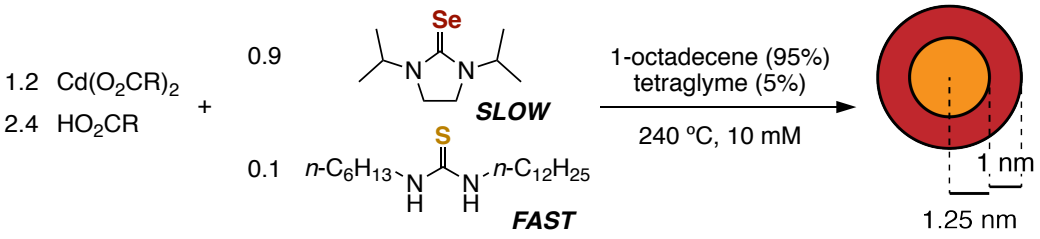

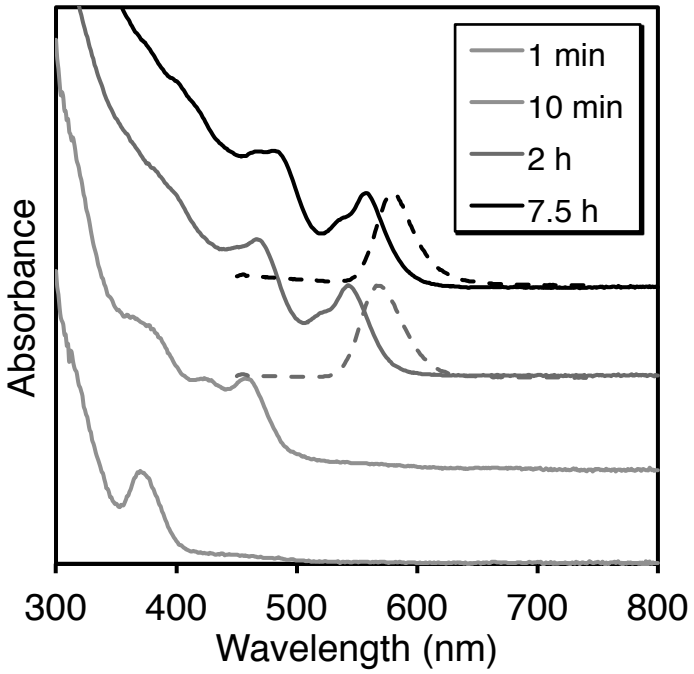


Figure 4.3.5. Time-dependent UV-vis and photoluminescence spectra of aliquots removed from a typical SQW synthesis shown in Scheme 4.3.3.

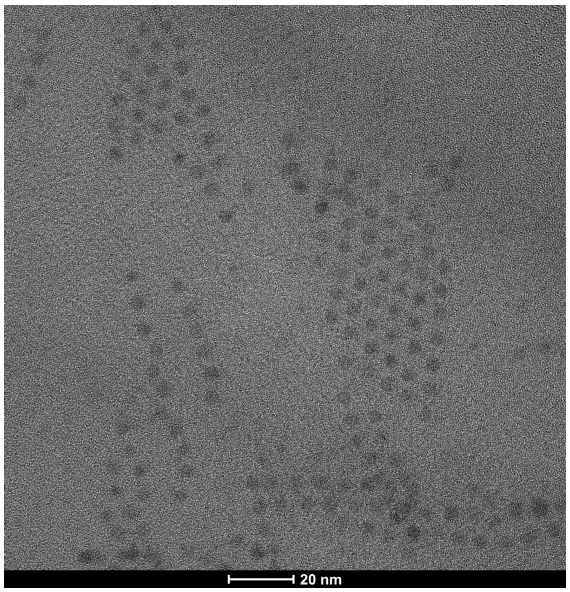


Figure 4.3.6. Transmission electron micrograph of SQWs synthesized from thio- and selenoureas as shown in Scheme 4.3.3. The measured diameter of ~4.2 nm is close to the expected final diameter of 4.5 nm.

For practical reasons, the thick CdS layer would need to be added in a separate step following complete CdSe deposition. The selenourea shown in Scheme 4.3.3 requires approximately 11 hours to convert completely ($k_{obs}$ = 1.2 x $10^{-4}$ $s^{-1}$, 7 half-lives). If an outer CdS shell is to be deposited with virtually no alloying between layers, let's assume that a Se:S deposition rate ratio of > 7 must be maintained, as written above. In order to achieve this, it would require a reaction time of at least 77 hours, which is beginning to become unreasonable. Further, since the CdS shell comprises ~97% of the nanocrystal, and the CdSe layer ~2%, this would require a thiourea $k_{obs}$ of at most 3.4 x $10^{-7}$ $s^{-1}$. To date, our slowest tested precursors fall into the range of $10^{-6}$ $s^{-1}$. Further still, synthesizing nanocrystals of such large size would require a much lower nanocrystal concentration, and therefore, precursor concentration, than that produced in the standard 10 mM case. While in principle $k_{obs}$ should not depend on concentration, this often turns out to be untrue and the system gets complicated even further. Suffice it to say that a second shelling step is much simpler and more practical.

Scheme 4.3.4. Growth of thick CdS shells onto SQWs by syringe-pumping a mixture of $Cd(O_2CR)_2$, $HO_2CR$, and *N*,*N*,*N*′,*N*′-tetramethylthiourea.

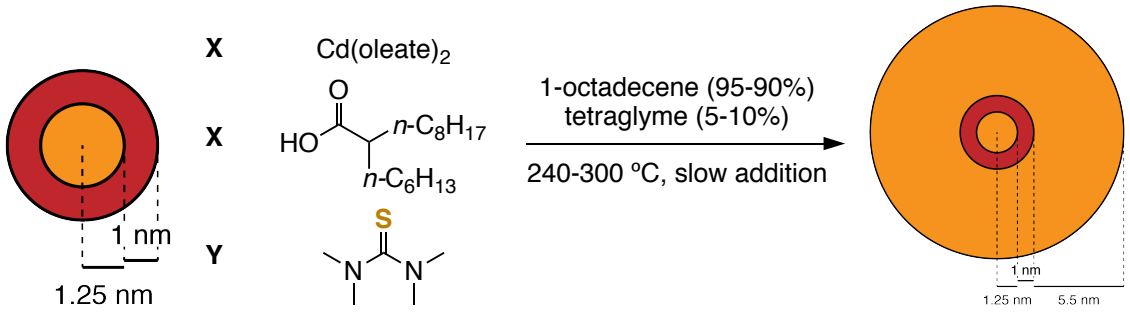


We decided to grow the CdS shell by slow injection via syringe pump (Scheme 4.3.4). Initial attempts gave dramatically brightened (64-72% PLQY), red-emitting ($\lambda$ = 625 ± 5 nm) samples, but resulted in nanocrystal precipitation from the reaction mixture at $d \approx 10$ nm. This decomposition mostly is due to insolubility rather than crystalline aggregation because the nanocrystals are well-soluble when diluted at room temperature and do not exhibit extreme polydispersity in TEM images (Figure 4.3.7). However, we cannot completely rule out aggregation. Additionally, the resulting nanocrystal residues were highly viscous, intractable gels due to the excess $Cd(O_2CR)_2$ employed in synthesis, presenting a kinetic barrier to dissolution even in coordinating solvents like tetrahydrofuran. We thus began to pursue additives to help obtain larger, more easily processible nanocrystal emitters.

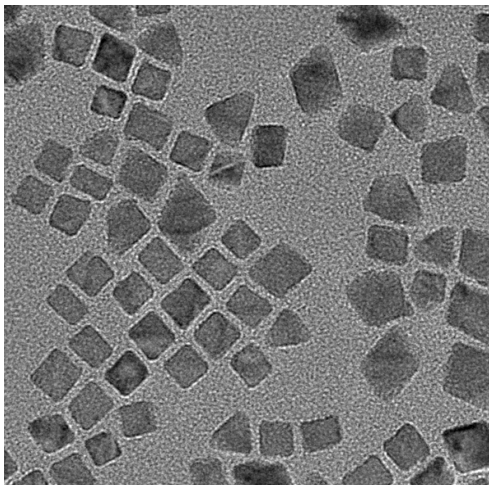

Figure 4.3.7. Transmission electron micrograph of SQWs

Table 4.3.1. Conditions surveyed in CdS shell growth. Page refers to notebook page in MPC-6. ODPA: *n*-octadecylphosphonic acid. $Ph_2O$: diphenyl ether. $Oct_3N$: tri-*n*-octylamine. $Oct_3P$: tri-*n*-octylphosphine. PLT: Pacific Light Technologies, Portland, OR.

| Page | Cd:S | Additional reagent | Temp. (°C) | Max PLQY | Precip.? | Notes |
|---|---|---|---|---|---|---|
| 226 | 1.5 | - | 240 | 72% | Yes | Sent to PLT |
| 232 | 1.5 | ODPA (10 mol %) | 240 | Low | Yes | Ripened |
| 236 | 1.5 | $Ph_2O$ (50 vol. %) | 255 | 37% | Yes, then no | Decreasing PLQY |
| 240 | 3 | - | 240, 265, 300 | 89% | Yes | CdO formation |
| 244 | 3 | - | 265, 290 | 93% | Yes | - |
| 250 | 3 | $Oct_3N$ (150 mol %) | 290 | High | Yes | Cd formation |
| 252 | 3 | $Oct_3P$ (150 mol %) | 290 | 92-95% | No | $d \approx 10$ nm<br>Ran out of precursor |
| 254 | 1.5 | $Oct_3P$ (150 mol %) | 290 | High | Yes | - |
| 256 | 3 | $Oct_3P$ (150 mol %) | 290 | 92-93% | No | $d = 20$-25 nm<br>Sent to PLT |

After surveying a wide range of options, we arrived at the results shown in

Table 4.3.1. The two most helpful changes we made were the addition of tri-*n*-octylphosphine and increasing the reaction temperature. Tri-*n*-octylphosphine had the largest effect, increasing nanocrystal solubility and coordinating $Cd(O_2CR)_2$ to decrease its degree of polymerization, eliminating the intractable gel issue and improving workup. Tri-*n*-octylphosphine may also promote the formation of ion-pairs during growth, which can bind tightly to stoichiometric nanocrystal surfaces.[32] These effects are shown in Scheme 4.3.5. Interestingly, despite these arguments about surface stability during growth, the faceting does change noticeably with the addition of phosphine.

Scheme 4.3.5. Potential reactions of trialkylphosphines under conditions studied here.

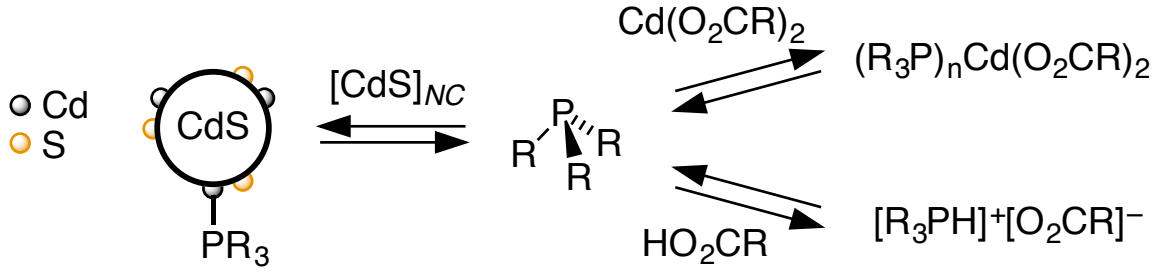


Increasing the reaction temperature above 240 °C has a moderately positive effect on nanocrystal solubility as well. However, above ~295 °C, precipitation of brown-to-gray solid begins (CdO is brown, Cd is gray), likely signifying $Cd(O_2CR)_2$ decomposition. Thus, we arrived at an optimal temperature of 290 °C.

This decomposition threshold is substantially higher than the previously reported values of 200 – 226 °C[33–36] and is likely due to stabilizing effects of tri-*n*-octylphosphine on $Cd(O_2CR)_2$.

Two variables tested had little to no observable impact on synthesis. The first was switching the carboxylate from oleate to 2-hexyldecanoate. Recent reports have shown dramatically improved nanocrystal solubility at room temperature with branched chain carboxylate ligands,[37] but in our high-temperature synthetic conditions, this did not result in noticeably less precipitation. The second was adjusting the addition rate of the syringe pump. Faster addition rates can dramatically cut reaction times but can also induce secondary nucleation of CdS. In our experiments, however, adjusting the rate from 2.0 mL/h to 8.0 mL/h had little observable effect on the nanocrystal properties, and none showed obvious secondary nucleation. For reference, a typical starting reaction mixture is 5 mL; the larger the amount of starting nanocrystals, the more precursor needs to be added per unit time. However, it is very possible that slower addition rates could promote anisotropic growth, particularly if wetting of CdSe surfaces by CdS solute is imperfect.

The three additives that actively harmed CdS shell growth were *n*-octadecylphosphonic acid, diphenyl ether, and tri-*n*-octylamine. Adding *n*-Octadecylphosphonic acid to the SQW stock solution prior to CdS growth led to

rapid ripening and poor photoluminescence. Adding diphenyl ether into the CdS shell growth mixture seemed to marginally improve nanocrystal solubility, albeit with some hysteretic effects, but ultimately failed as an additive because its presence harmed nanocrystal PLQY. It is unclear why this should happen; diphenyl ether is inert and often used as a high-temperature reaction solvent. Tri-*n*-octylamine had little effect on solubility, but led to Cd metal formation at 290 °C. Since tri-*n*-octylamine and tri-*n*-octylphosphine are isoelectronic and isostructural but the phosphine is more nucleophilic while the amine is more Brønsted basic, this result shows that the ion-pair formation proposed in Scheme 4.3.5 is not very important to nanocrystal solubility under our conditions.

After optimization, we arrived at a set of reaction conditions that reliably gives nanocrystals in the 90-95% PLQY range at up to 2.5 gram scale (Scheme 4.3.6, Figure 4.3.8). The fluorescence is narrow in addition to being bright (FWHM = 32 nm), and the peak emission falls within the acceptable range for blue LED downconversion to red ($\lambda$ = 625 ± 5 nm) (at the time of this writing, these are the highest recorded PLQYs ever measured in the Owen Lab!).

Scheme 4.3.6. Optimized synthesis of red-emitting SQW nanocrystals.

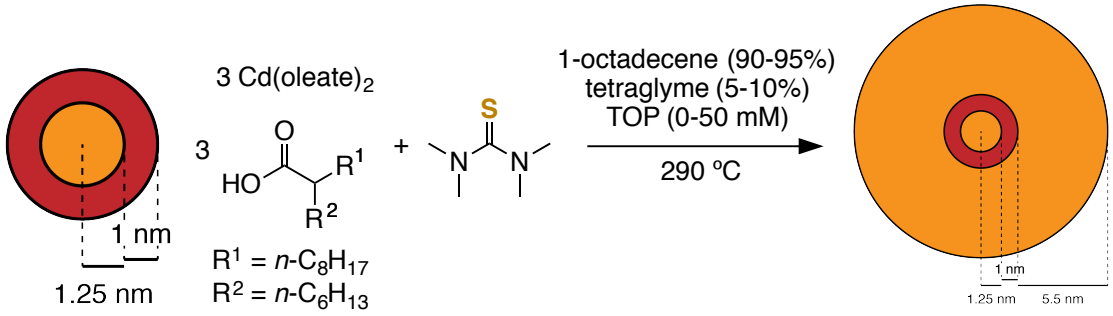


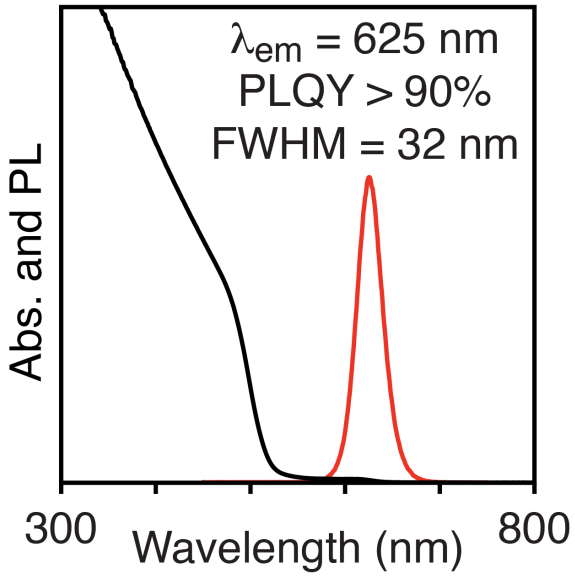


Figure 4.3.8. Optical properties of SQWs synthesized in the presence of tri-*n*-octylphosphine.

*4.3.4. Structural characterization*

Given the large, faceted shapes exhibited by the ~10 nm SQWs, we were interested in understanding the structure of these larger nanocrystals. By TEM, we see that the nanocrystals have transformed from roughly cubic to roughly octahedral, consistent with the results in Jeong *et al.*[31] However, when we conduct elemental mapping by STEM-EDX (Figure 4.3.10), the apparent

distribution of Se and S are quite surprising. CdSe appears to be concentrated at the tips the octahedra, and possibly even being exposed to the surface. Given the bright photoluminescence of these samples, it is strange that CdSe would be exposed or even shelled by a thin CdS layer; these structural features do not effectively insulate electrons and holes from surface states and should lead to high degrees of trap-assisted recombination and low PLQYs. It is unlikely that the image in Figure 4.3.10 is the result of simple drift, since the tip-located CdSe seems to hold true across particles of different orientations. However, this is a complex measurement that bears repeating before concluding too much.

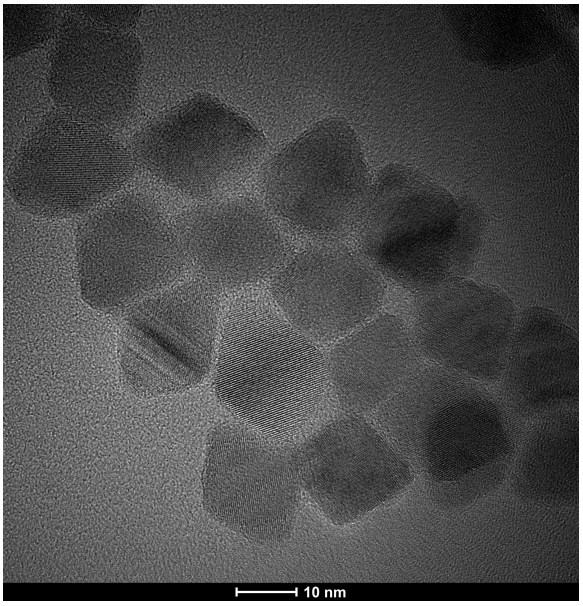


Figure 4.3.9. Transmission electron micrograph of SQWs with $d$ = 20-25 nm.

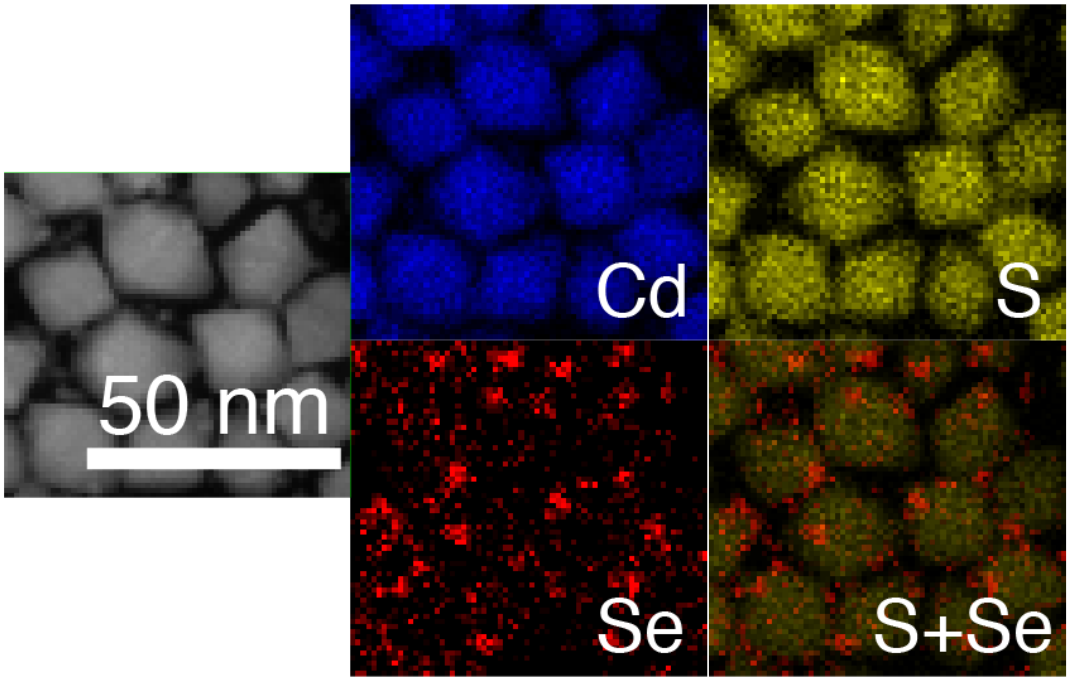


Figure 4.3.10. Results of elemental mapping of SQWs by STEM-EDX.

*4.3.5. Conclusions, Outlook, and Next Steps*

In this section we have demonstrated that the concept of precursor tuning can lead to control over nanocrystal heterostructure, although it has important limits. Our first targets have been fairly abrupt heterostructures that do not take full advantage of the fine alloy gradations possible using thio- and selenoureas, but importantly, these materials have remarkable optical properties for downconverting applications. We are currently collaborating with Pacific Light Technologies (Portland, OR) to complete advanced photophysical characterization and performance metrics under high flux, temperature, and humidity. This collaboration will lead to a virtuous cycle, in which we rapidly

gain insight into not only what properties lead to bright, narrow emission at room temperature, but also under practical conditions necessary for widespread adoption of nanocrystals into LEDs lighting.

## 4.4. Experimental Details

### *4.4.1. General Methods*

All manipulations were performed using standard air-free techniques on a Schlenk line under argon atmosphere or in a nitrogen-filled glovebox unless otherwise indicated.

### *4.4.2. Chemicals*

Cadmium oxide (99.99%) was obtained from Strem. *Note: CdO should be red-brown in color, not dark brown, which may indicate oxide vacancies and residual Cd metal*. Trifluoroacetic acid (99%), trifluoroacetic anhydride (99%), trifluoromethanesulfonic acid (≥ 99%), trifluoromethanesulfonic anhydride (≥ 99%), oleic acid (99%), Triethylamine (≥ 99%), acetonitrile (≥ 99.5%), and dichloromethane (≥ 99.5%, contains 50 ppm amylene as stabilizer) were obtained from Aldrich and used as received. Tri-*n*-octylphosphine oxide (99%) was obtained from Aldrich and recrystallized from hot acetonitrile.[38] 1-Octadecene, tetraethylene glycol dimethyl ether ("tetraglyme," ≥ 99%), diphenyl ether (≥ 99%) oleylamine (98% primary amine), tri-*n*-octylamine (98%) were obtained from

Aldrich, stirred over calcium hydride overnight, vacuum distilled, and stored under nitrogen prior to use. 2-Hexyldecanoic acid (> 98.0%) was obtained from TCI America and vacuum distilled prior to use.

Lead(II) oleate and thiourea syntheses were carried out according to Hendricks *et al*.[6] Selenourea syntheses were carried out according to Campos *et al*.[39] *n*-Octadecylphosphonic acid was synthesized according to Anderson.[40]

*4.4.3. Instrumentation*

Kinetics experiments were monitored at 400 nm using an Ocean Optics TP300 dip probe (2 mm path length) attached to a Perkin-Elmer Lambda 650 spectrophotometer equipped with deuterium and halogen lamps. UV-visible absorbance spectra were obtained using a PerkinElmer Lambda 950 spectrophotometer equipped with deuterium and halogen lamps and either a PbS or InGaAs detector. Photoluminescence measurements in the range 300-800 nm were performed using a Fluoromax 4 from Horiba Scientific, and quantum yields were determined using a quanta-phi integrating sphere accessory. Samples for UV-vis absorbance and photoluminescence spectroscopies were dissolved in hexanes or cyclohexane, and quartz cuvettes were cleaned with aqua regia between uses. Transmission electron microscopy was performed on a FEI Talos F200X transmission / scanning transmission electron microscope

(S/TEM). Powder X-ray diffraction (XRD) was measured on a PANalytical X'Pert Powder X-ray diffractometer.

*4.4.4. PbS and PbSe Kinetics Experiments*

PbS and PbSe nanocrystal synthesis reactions were carried out at 9 mM in chalcogenourea and 10.8 mM in lead(II) oleate according to Hendricks *et al*.[6] and Campos *et al*.[39] with minor adjustments. In a nitrogen-filled glovebox, three vessels are prepared: 1) Lead oleate (166.3 mg, 0.216 mmol, 1.2 equiv.) and hexadecane (19.0 mL) are added to a three-neck round-bottom flask equipped with a 19/22 middle neck and a stir bar. The flask is sealed with three rubber septa. 2) The desired thio- or selenourea (0.216 mmol, 1.2 equiv.) and diphenyl ether (1.288 g, 1.2 mL) are added to a 4 mL scintillation vial, which is sealed with a rubber septum. 3) Tetrachloroethylene (3.895 g, 2.4 mL) is added to a 1 cm x 1 cm quartz cuvette, which is then sealed with a septum cap. The vessels containing lead oleate and thio- or selenourea are then attached to a Schlenk line via argon inlet needles. Under positive argon flow, the middle septum of the lead oleate flask is replaced with a home-built airfree adapter for an in situ optical dip probe. Both vessels are immersed in silicon oil baths set to the desired temperature and allowed to reach thermal equilibrium with stirring (1000 rpm, > 15 minutes). After equilibration, the absorbance at 400 nm is set to zero and then recording of the absorbance at 400 nm is initiated, collecting one data point every

600 milliseconds. A portion of the thio- or selenourea solution (1 mL, 1.0 equiv) is injected into the lead oleate solution to initiate the reaction. This results in 20 mL of total solution with a lead oleate concentration of 10.8 mM and a thio- or selenourea concentration of 9.0 mM. The reaction is run for 7-9 times $t_{1/2}$, at which time the absorbance has plateaued. At this time, a 100 μL aliquot was removed and dissolved in the cuvette containing tetrachloroethylene to measure the full UV-vis-NIR spectrum. The kinetics data was corrected by setting t=0 as the beginning of the small fluctuation in absorbance corresponding to injection (see Figure 4.2.3). The data were fit to single exponential functions, allowing first-order rate constants to be extracted.

*4.4.5. Time-Resolved SAXS, WAXS, and UV-vis Experiments*

The SAXS/WAXS experiments were performed on the ID02 beamline of the ESRF (European Synchrotron Radiation Facility) at an energy of 11.5 keV (wavelength of 1.08 °A). The sample-to-SAXS detector distance was 1.29707 m which yields a $q$-range of 0.067 to 5.33 $nm^{-1}$. In the experiments presented here, 19 mL of a 9.47 mM solution lead(II) oleate in hexadecane are transferred via syringe into a three-neck round bottom flask equipped with a fiber-optic dip probe and thermocouple under argon. An oil bath is used to set the internal flask temperature to 110 °C. The lead(II) oleate solution is pumped through a glass capillary using a peristaltic pump equipped with Viton tubing and the

temperature is allowed to equilibrate for > 15 minutes. The absorbance spectrum of the solution is continuously recorded at 100-250 millisecond intervals.

During this time, 1 mL of 180 mM thiourea solution in tetraglyme is loaded into a syringe and clamped to a stand. The injection of this solution is controlled remotely from outside the beamline hutch with a pneumatic piston to which a TTL signal is sent. This time defines $t = 0$ of the sequence. At this point, SAXS/WAXS acquisitions are triggered. A decrease of a few degrees is observed after the thiourea injection but the temperature quickly reaches back the set value. In the sequence shown here, 1200 SAXS and WAXS patterns each with a duration of 300 milliseconds are taken every second (i.e. there is a 700 millisecond waiting time between each two acquisitions).

After each sequence, the whole pumping circuit is purged with clean hexadecane. The circuit is then detached and the capillary is cleaned with acetone followed by dilute aqua regia. The aqua regia is left in the capillary for 5 minutes, leading to recovery of the signal of the clean capillary. The capillary is then cleaned with additional acetone and hexadecane.

*4.4.6. Data Normalization, Background Signal Subtraction, and Data Handling*

The size of the capillary was determined by scanning it with the X-ray beam before the start of the experiment. After the acquisition, beamline-specific corrections are applied to the SAXS and WAXS images and the intensity is

radially averaged to yield intensity as a function of wavevector $q = 4\pi/\lambda sin(\theta/2)$, where $\theta$ is the scattering angle. The final intensity is divided by the thickness to yield the scattering signal in absolute units ($mm^{-1}$). Before each experiment at a given temperature, hexadecane is flowed through the capillary at the same temperature and SAXS patterns are acquired at the same acquisition time than during the sequence. This background is then subtracted from all the patterns of the kinetic sequence since the X-ray beam hits the capillary exactly at the same place for background acquisition and during the kinetic sequence.

Starting from the intensity-versus-wavelength wavevector files, all data handling was performed using Ipython Notebooks. The non-linear fits were performed using the Levenberg-Marquardt algorithm implemented in the LMFit module in Python.

*4.4.7. Modeling the SAXS Pattern of Lead(II) Oleate Micelles*

The micellular lead(II) oleate solution was modeled to a Schultz distribution of polydisperse spheres:

$$I = I_0 \times P_s(q, R_{av}, z)$$

Equation 4.4.1

This yields a mean radius of $R_{av}$ = 0.25 nm. The model is agnostic to the precise shape and composition (e.g. monomers, dimers, etc.) of the micelles, but it is

clear that this organization does not change with time during the reaction. Hence, during the formation of nanocrystals, the signal of the micelles is:

$$I = I_0(t) \times P_s(q, R_{av}, z)$$

Equation 4.4.2

Where $R_{av}$ and $Z$ do not depend on time. An example is shown in Figure 4.4.1.

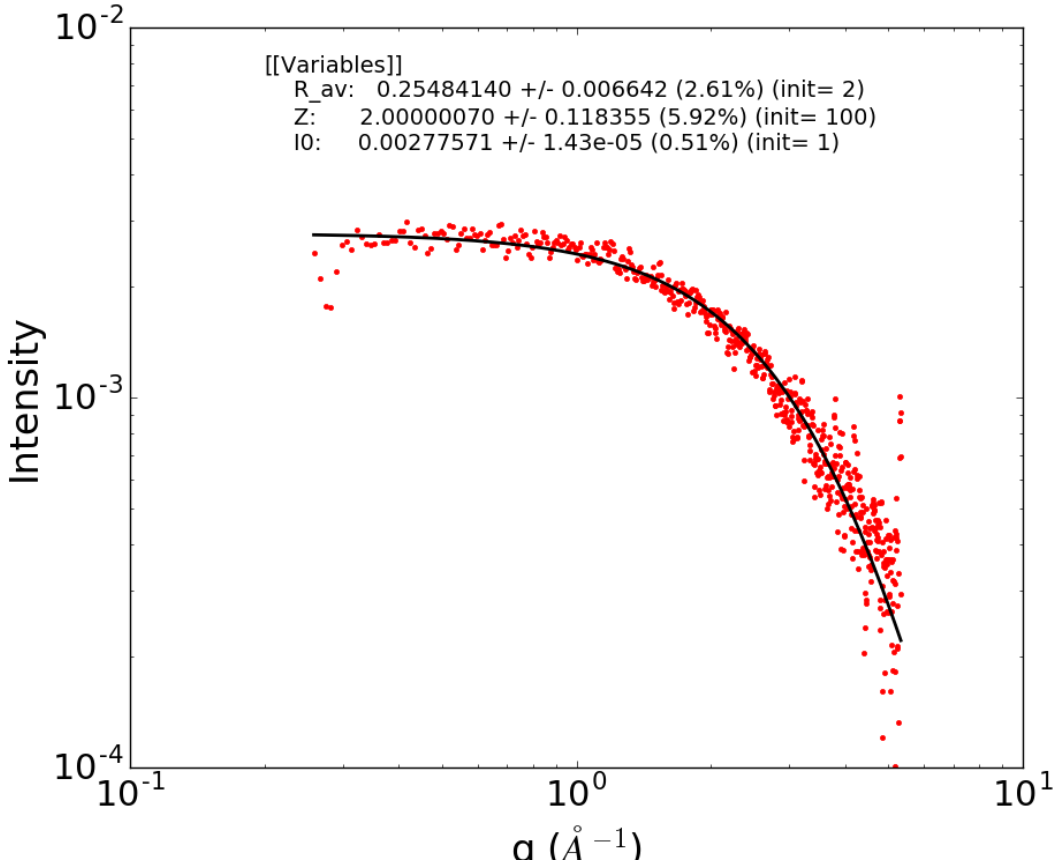


Figure 4.4.1. SAXS pattern of the reaction mixture prior to nucleation. The fir corresponds to a distribution of polydisperse spheres.

*4.4.8. Modeling the SAXS Pattern of PbS Nanocrystals*

After the onset of nanocrystal formation, the signal is fitted by:

$$I(q,t) = I_0^{NP}(t) \times P_s\left(q, R_{av}^{NP}, Z^{NP}(t)\right) + I_0^{p}(t) \times P_s(q, R_{av}^{p}, Z^{p})$$

Equation 4.4.3

where superscript *NP* designates the parameters for the nanoparticles and $p$ for the precursors. There are 4 unknown parameters: $I_0^{NP}$, $R_{av}^{NP}$, $Z^{NP}$, and $I_0^{p}$. We impose $I_0^{p}(t = 0)$ as an upper bound to the determination of $I_0^{p}(t)$ because the signal of the precursor decreases with time. We start the fitting procedure by the last SAXS pattern of the sequence and pass the values of the parameters found for the fit at instant t as initial guesses for the fit at instant t – 1. Starting at the end is justified by the fact that the signal to noise ratio is the highest at this point and also because the large oscillations present ensure a precise determination of the polydispersity at this point. From $I_0^{NP}$, we can extract the nanocrystal concentration:

$$n^{NP}(t) = \frac{I_0^{NP}}{\Delta\rho^2 \langle V^2 \rangle}$$

Equation 4.4.4

Where:

$$\langle V^2 \rangle = \frac{16\pi^2 R_0^6}{9\gamma}$$

Equation 4.4.5

Example fits are shown in Figure 4.4.2:

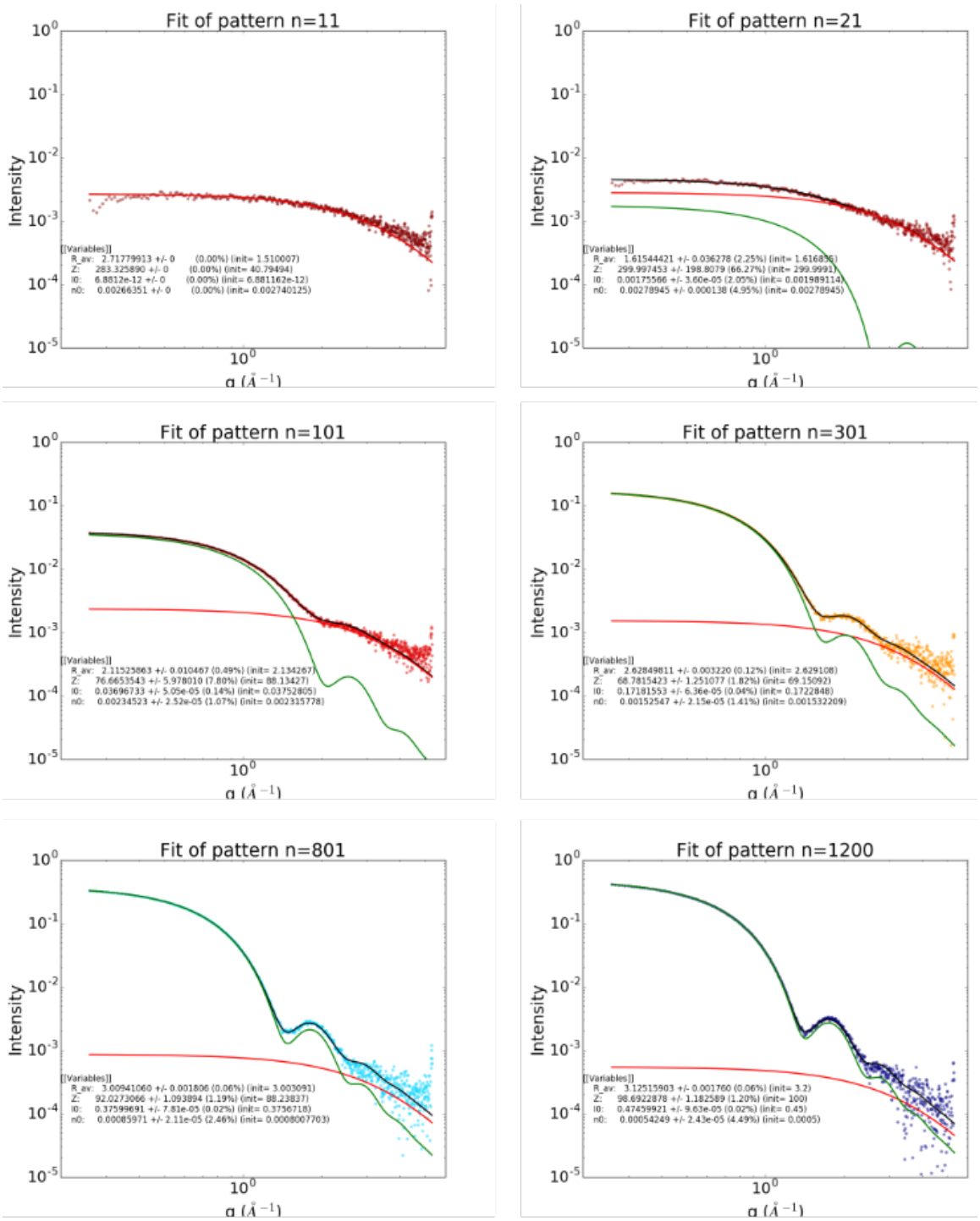


Figure 4.4.2. SAXS patterns at several instants during the formation of PbS nanocrystals and their corresponding fits to the model described above. The green line corresponds to the nanocrystals, while the red line

corresponds to the signal of the precursors. The black line is the sum of the two.

Scattering length densities of 7.510 x $10^{-6}$ $Å^{-2}$ and 49.973 x $10^{-6}$ $Å^{-2}$ were used for hexadecane and PbS, respectively, for an X-ray wavelength of 0.995 Å (12.36 keV).

*4.4.9. Secondary Nucleation Experiments*

Secondary nucleation experiments were carried out using an automated synthesis and characterization protocol at the Workstation for Automated Nanomaterial Discovery and Analysis (WANDA) at the Molecular Foundry. Stock solutions of nanocrystals (0.1 – 1.1 mM) at desired sizes ($d$ = 3 – 6 nm) and lead(II) oleate ligand coverages (3 – 5 $nm^2$) were prepared according to Hendricks *et al*.[6] A desired volume of nanocrystal stock solution (88 – 880 μL, 10 – 100 nmol) was added to an empty 40 mL vial and the pentane or toluene solvent was removed by evaporation. The dried nanocrystals were diluted in hexadecane to 9.5 mL and sufficient lead(II) oleate to give 10.8 mM solutions. 180 mM stock solutions of the desired thiourea in diphenyl ether were prepared and heated to 100 °C prior to injection. Thioureas used in these experiments include *N*-dodecyl-*N*′-4-(trifluoromethyl)phenylthiourea, N-dodecyl-N′-phenylthiourea, *N*-dodecyl-*N*′-4-methoxyphenylthiourea, and *N*-dodecyl-*N*′-hexylthiourea.

After the temperature of the lead(II) oleate solution stabilized at 120 °C, a 0.5 mL portion of the thiourea solution was carried out by an automated robotic injection at 1.5 mL/sec. The reaction was monitored by sequential aliquots (100 μL), which were later diluted in tetrachloroethylene (1400 μL) and transferred to a 96-well quartz plate (Hellma) for infrared photoluminescence spectroscopy.

*4.4.10. Synthesis of Cadmium Oleate*

In a 100 mL round-bottom flask, cadmium oxide (3.852 g, 30.0 mmol) and acetonitrile (40 mL) are stirred and cooled to 0 °C. To this mixture, trifluoroacetic acid (0.46 mL, 6.0 mmol, 0.2 equiv) and trifluoroacetic anhydride (4.24 mL, 30.0 mmol, 1 equiv) are added dropwise, allowed to warm up to room temperature, and stirred overnight to give a clear, colorless solution of cadmium trifluoroacetate.

In a separate 1 L Erlenmeyer flask, dichloromethane (300 mL), triethylamine (9.46 mL, 67.8 mmol, 2.26 equiv), and oleic acid (17.030 g, 60.3 mmol, 2.01 equiv) are mixed together, giving a clear, colorless solution of triethylammonium oleate.

The cadmium trifluoroacetate solution is added dropwise to the triethylammonium oleate solution with stirring, giving a colorless solution. Acetonitrile (70 mL) is slowly added to precipitate cadmium oleate as a white solid, and then the solution is stored overnight in a freezer. The solid is collected

by suction filtration on a fritted glass funnel and washed with acetonitrile (3 x 150 mL), breaking up any large chunks, and dried under vacuum overnight. Theoretical yield: 20.260 g. This procedure may be scaled up 6x with no observable changes.

*4.4.11. Synthesis of Abrupt CdS/CdSe Spherical Quantum Wells*

Cadmium oleate (40.5 mg, 0.06 mmol, 1.2 equiv.), 2-hexyldecanoic acid (30.8 mg, 0.12 mmol, 2.4 equiv.), and 1-octadecene (3.748 g, 4.75 mL) are loaded into a 100 mL 3-neck round-bottom flask equipped with a thermowell and two rubber septa. *N*-dodecyl-*N'*-hexylthiourea (1.6 mg, 0.005 mmol, 0.1 equiv.), *N*,*N'*-diisopropylimidazolidine-2-selone (10.5 mg, 0.045 mmol, 0.9 equiv.), and tetraglyme (0.25 mL) are loaded into a scintillation vial and sealed with a rubber septum. Both are transferred to a Schlenk line via argon inlet needles and the cadmium oleate solution is heated to 240 °C under rapid stirring. As soon as the flask first reaches 240 °C, the thio/selenourea solution is injected and the reaction is allowed to proceed for 8 h. Note: this reaction is typically scaled up 10x and split into 5 mL fractions for further shelling. The reaction mixture is stable for months at room temperature under nitrogen.

*4.4.12. Preparation of CdS Shell Growth Mixture*

Cadmium oleate (4.558 g, 6.75 mmol, 3 equiv.), 2-hexyldecanoic acid (1.731 g, 1.98 mL, 6.75 mmol, 3 equiv.), tri-*n*-octylphosphine (1.194 g, 1.44 mL, 3.38 mmol, 1.5 equiv.), and 1-octadecene (48.819 g, 61.88 mL) are loaded into a Schlenk flask equipped with a large stir bar. *N*,*N*,*N'*,*N'*-tetramethylthiourea (0.298 g, 2.25 mmol, 1 equiv.) and tetraglyme (5.676 g, 5.63 mL) are loaded into a 20 mL scintillation vial equipped with a stir bar. The cadmium oleate solution is transferred to a Schlenk line and briefly submerged in a 150 °C oil bath until a clear, colorless solution is obtained. The solution is allowed to cool completely to room temperature, at which point the thiourea solution is added, thoroughly mixed, and then loaded into a syringe. This mixture is stable indefinitely at room temperature (> 7 days).

*4.4.13. CdS Shell Growth*

Following the spherical quantum well synthesis reaction, the reaction mixture is heated to 240 – 290 °C and then the shelling mixture is added at 2.0 – 8.0 mL/h using a syringe pump. If necessary, the syringe pump is paused, the reaction mixture is cooled to < 100 °C and transferred to a larger flask, then re-heated to 290 °C for 20 minutes, at which point the addition is resumed. Note: quartz cuvettes used for spectroscopy of aliquots must be cleaned with aqua regia between uses.

## 4.5. References


(1) Sugimoto, T.; Shiba, F.; Sekiguchi, T.; Itoh, H. *Colloids Surf. Physicochem. Eng. Asp.* **2000**, *164* (2), 183.
(2) Sugimoto, T.; Shiba, F. *Colloids Surf. Physicochem. Eng. Asp.* **2000**, *164* (2), 205.
(3) Moreels, I.; Lambert, K.; Smeets, D.; De Muynck, D.; Nollet, T.; Martins, J. C.; Vanhaecke, F.; Vantomme, A.; Delerue, C.; Allan, G.; Hens, Z. *ACS Nano* **2009**, *3* (10), 3023.
(4) Moreels, I.; Lambert, K.; De Muynck, D.; Vanhaecke, F.; Poelman, D.; Martins, J. C.; Allan, G.; Hens, Z. *Chem. Mater.* **2007**, *19* (25), 6101.
(5) Mullin, J. W. In *Crystallization (Fourth Edition)*; Butterworth-Heinemann: Oxford, 2001; pp 181–215.
(6) Hendricks, M. P.; Campos, M. P.; Cleveland, G. T.; Plante, I. J.-L.; Owen, J. S. *Science* **2015**, *348* (6240), 1226.
(7) Owen, J. S.; Chan, E. M.; Liu, H.; Alivisatos, A. P. *J. Am. Chem. Soc.* **2010**, *132* (51), 18206.
(8) Zhao, H.; Liang, H.; Vidal, F.; Rosei, F.; Vomiero, A.; Ma, D. *J. Phys. Chem. C* **2014**, *118* (35), 20585.
(9) In *Chemistry of the Elements (Second Edition)*; Butterworth-Heinemann: Oxford, 1997; pp 747–788.
(10) Perrin, D. D. In *Ionisation Constants of Inorganic Acids and Bases in Aqueous Solution (Second Edition)*; Pergamon, 1982; pp 1–138.
(11) Li, T.; Senesi, A. J.; Lee, B. *Chem. Rev.* **2016**, *116* (18), 11128.
(12) Guinier, A. *Small-angle scattering of X-rays*; Wiley: New York, 1955.
(13) Abécassis, B.; Bouet, C.; Garnero, C.; Constantin, D.; Lequeux, N.; Ithurria, S.; Dubertret, B.; Pauw, B. R.; Pontoni, D. *Nano Lett.* **2015**, *15* (4), 2620.
(14) Abécassis, B.; Testard, F.; Spalla, O.; Barboux, P. *Nano Lett.* **2007**, *7* (6), 1723.
(15) Peng, X.; Wickham, J.; Alivisatos, A. P. *J. Am. Chem. Soc.* **1998**, *120* (21), 5343.
(16) Rempel, J. Y.; Bawendi, M. G.; Jensen, K. F. *J. Am. Chem. Soc.* **2009**, *131* (12), 4479.
(17) Abe, S.; Čapek, R. K.; De Geyter, B.; Hens, Z. *ACS Nano* **2012**, *6* (1), 42.
(18) Chen, O.; Zhao, J.; Chauhan, V. P.; Cui, J.; Wong, C.; Harris, D. K.; Wei, H.; Han, H.-S.; Fukumura, D.; Jain, R. K.; Bawendi, M. G. *Nat. Mater.* **2013**, *12* (5), 445.
(19) Cragg, G. E.; Efros, A. L. *Nano Lett.* **2010**, *10* (1), 313.
(20) Hollingsworth, J. A. *Chem. Mater.* **2013**, *25* (8), 1318.
(21) Chen, Y.; Vela, J.; Htoon, H.; Casson, J. L.; Werder, D. J.; Bussian, D. A.; Klimov, V. I.; Hollingsworth, J. A. *J. Am. Chem. Soc.* **2008**, *130* (15), 5026.
(22) Jain, A.; Voznyy, O.; Hoogland, S.; Korkusinski, M.; Hawrylak, P.; Sargent, E. H. *Nano Lett.* **2016**, *16* (10), 6491.

(23) Park, Y.-S.; Bae, W. K.; Padilha, L. A.; Pietryga, J. M.; Klimov, V. I. *Nano Lett.* **2014**, *14* (2), 396.
(24) Park, Y.-S.; Bae, W. K.; Baker, T.; Lim, J.; Klimov, V. I. *Nano Lett.* **2015**, *15* (11), 7319.
(25) Park, Y.-S.; Bae, W. K.; Pietryga, J. M.; Klimov, V. I. *ACS Nano* **2014**, *8* (7), 7288.
(26) Vaxenburg, R.; Rodina, A.; Lifshitz, E.; Efros, A. L. *Nano Lett.* **2016**, *16* (4), 2503.
(27) Beane, G. A.; Gong, K.; Kelley, D. F. *ACS Nano* **2016**, *10* (3), 3755.
(28) García-Santamaría, F.; Brovelli, S.; Viswanatha, R.; Hollingsworth, J. A.; Htoon, H.; Crooker, S. A.; Klimov, V. I. *Nano Lett.* **2011**, *11* (2), 687.
(29) Bae, W. K.; Padilha, L. A.; Park, Y.-S.; McDaniel, H.; Robel, I.; Pietryga, J. M.; Klimov, V. I. *ACS Nano* **2013**, *7* (4), 3411.
(30) Javaux, C.; Mahler, B.; Dubertret, B.; Shabaev, A.; Rodina, A. V.; Efros, A. L.; Yakovlev, D. R.; Liu, F.; Bayer, M.; Camps, G.; Biadala, L.; Buil, S.; Quelin, X.; Hermier, J.-P. *Nat. Nanotechnol.* **2013**, *8* (3), 206.
(31) Jeong, B. G.; Park, Y.-S.; Chang, J. H.; Cho, I.; Kim, J. K.; Kim, H.; Char, K.; Cho, J.; Klimov, V. I.; Park, P.; Lee, D. C.; Bae, W. K. *ACS Nano* **2016**, *10* (10), 9297.
(32) Chen, P. E.; Anderson, N. C.; Norman, Z. M.; Owen, J. S. *J. Am. Chem. Soc.* **2017**, *139* (8), 3227.
(33) Stamatatos, T. C.; Katsoulakoua, E.; Nastopoulos, V.; Raptopoulou, C. P.; Manessi-Zoupa, E.; Perlepes, S. P. *Z. Für Naturforschung B* **2003**, *58* (11), 1045.
(34) Akanni, M. S.; Okoh, E. K.; Burrows, H. D.; Ellis, H. A. *Thermochim. Acta* **1992**, *208*, 1.
(35) Yang, Y. A.; Wu, H.; Williams, K. R.; Cao, Y. C. *Angew. Chem. Int. Ed.* **2005**, *44* (41), 6712.
(36) García-Rodríguez, R.; Hendricks, M. P.; Cossairt, B. M.; Liu, H.; Owen, J. S. *Chem. Mater.* **2013**, *25* (8), 1233.
(37) Yang, Y.; Qin, H.; Jiang, M.; Lin, L.; Fu, T.; Dai, X.; Zhang, Z.; Niu, Y.; Cao, H.; Jin, Y.; Zhao, F.; Peng, X. *Nano Lett.* **2016**, *16* (4), 2133.
(38) Owen, J. S.; Park, J.; Trudeau, P.-E.; Alivisatos, A. P. *J. Am. Chem. Soc.* **2008**, *130* (37), 12279.
(39) Campos, M. P.; Hendricks, M. P.; Beecher, A. N.; Walravens, W.; Swain, R. A.; Cleveland, G. T.; Hens, Z.; Sfeir, M. Y.; Owen, J. S. *J. Am. Chem. Soc.* **2017**, *139* (6), 2296.
(40) Anderson, N. C. The Surface Chemistry of Metal Chalcogenide Nanocrystals. Ph.D., Columbia University: United States -- New York, 2014.